Mild Chemical H-insertion into γ-Manganese Dioxides

Ahmed O. Mohameden

A thesis submitted to Middlesex University
in partial fulfilment of the requirements for the degree of
Doctor of Philosophy

October 2001

The work was carried out at the Energy Technology Centre, Middlesex University, Bounds Green Road, London N11 2NQ

(In The Name of Allah, The Most Gracious, The Most Merciful)

« ... and say: «My Lord! Increase me in knowledge»»
English Translation of The Holy Qur'an 20:114

«A path to knowledge is a path to Paradise»

Prophet Mohammad Peace be upon him

ACKNOWLEDGEMENT

It is my great pleasure to express my deep thanks and gratitude to my Director of Studies, Professor Frank Tye. He provided me with his help and guidance whenever I wanted or needed them. He also arranged for me a studentship to support myself financially during this study. Without Professor Tye's help this thesis would have never been completed.

I also thank very warmly my second supervisor Dr. Lachlan MacLean whose help was immeasurable particularly at the start of the study. With my supervisors, I had stimulating discussions during many Tuesday evening meetings and some telephone calls.

I would like to thank all my colleagues at the Energy Technology Centre particularly Julian Page for his computer programme which I used (and modified) for temperature monitoring during part of my experiments. Other colleagues are fully thanked for their support and advice: Dr. Aboubaker Lasebae, Dr. Hassan Ipakchi, Deepak Gopaul, Noor Salehin and Louis Egbe.

I am also very grateful to the technical staff at Bounds Green particularly Paul Kershaw for his help with SEM, Mick Carroll, Dave Court, Peter Burn and Martin Scott.

Thanks are equally due to Stephen Watts, Helen Ryan and Brenda Smith for their help in the admin side.

I am also very much indebted to my family members for their patience, encouragement and support throughout my student life.

Abstract

About a hundred samples of γ-manganese dioxide covering three materials coded SBP-A, Faradiser M and R2 have been reduced chemically by insertion of H through controlled additions of hydrazine hydrate solutions at about 1°C. The H-inserted samples and the starting materials were subjected to chemical analysis for oxidation state, X-ray diffraction (XRD) for structure study and Fourier Transform Infrared (FTIR) spectroscopy to gain information on OH bonding. Additional techniques including FTIR spectroscopy at low temperature (≥ –180 °C), electrode potential measurement and scanning electron microscopy (SEM) have also been applied.

The intergrowth structure of the starting materials consisted of ramsdellite intercepted with pyrolusite layers, known as de Wolff faults, and quantified by the fraction of pyrolusite layers Pr. An additional structural parameter for these materials was the amount of microtwinning (Tw) across the 021/061 ramsdellite planes. This parameter, introduced by Pannetier, is given in percent. Values of (Pr , Tw) have been given as (0.41 , 17) for SBP-A, (0.70 , 10) for Faradiser M and (0.41 , ~100) for R2.

Upon H-insertion, the structure of the starting materials expanded homogeneously in a direction and to an extent which depended on the Pr and Tw parameters. Faradiser M, with high Pr and very low Tw, expanded homogeneously in the direction of the *b* lattice dimension up to an insertion level of 0.69 of s in MnO_nH_s. Above this level, the initial structure changed suddenly into the structure of the final product: the insertion then proceeded homogeneously in the new phase. The main changes were an expansion of the octahedra and a rotation leading to hinged tunnels. This is the first time that the existence of two solid solutions in the MnO_2/H system has been noted. With SBP-A, the amount of microtwinning restricted the homogeneous expansion of SBP-A to s = 0.28, which occurred predominantly in the *a* direction. Further insertion broke the twinning boundary and formed a demicrotwinned phase of composition $MnO_nH_{0.68}$ in which the tunnels were also hinged. Thereafter H-insertion proceeded heterogeneously from 0.28 to 0.68 in s. Above s = 0.68, the structure developed homogeneously towards that of the fully H-inserted product. The extensive microtwinning in R2 allowed for a homogeneous expansion, thought to be isotropic to maintain the microtwinned structure, up to s = 0.39. Higher insertion levels led to the expansion to proceed heterogeneously to a composition of $MnO_nH_{0.63}$. Above s = 0.63,

a new phase, the final product, was formed with fully demicrotwinned structure and fully hinged tunnels. H-insertion into γ-manganese dioxide has never been reported to occur in three stages previously.

The FTIR study at room temperature has shown absence of OH bond vibrations at insertion levels prior to the hinging of the tunnels, in contrast to their presence after the structure has rotated and the tunnels had hinged. This is seen as a strong indication of H mobility in the initial structure. The hinging is necessary for OH bonding as it brings the O2 an O1 oxygens closer allowing the proton to bond both covalently and by H-bonding.

At low temperature, initially mobile hydrogen could be trapped and OH bonds formed only in H-inserted R2. This was linked to 061-microtwinning. The absence of OH bond at low temperature in SBP-A and Faradiser M led to the conclusion that these materials have no 061 microtwinning faults. The absence of OH bonds at low temperature in the starting materials, particularly in R2, strongly questions the postulated OH groups in the structure of γ-MnO_2, according to the cation vacancy model.

Electrode potential data supported the above conclusions in terms of the stages of the H-insertion. The battery activity of the materials seemed to be related to the extent at which the materials kept the initial structure with non-hinged tunnels.

Comparison with previous works on the same materials suggested that the differences could be accounted for by the kinetics of the H-insertion. While protons in this work were released spontaneously on the surface of the MnO_x, their diffusion into the bulk was slow due to the low temperature. In the compared literature, the reverse applies.

TABLE OF CONTENTS

1 Introduction

1.1 Background

G. Leclanché[1] was the first to use manganese dioxide, in 1866, as positive active material in his battery. This material has undergone considerable studies since, and still attracts the interest of researchers for battery applications because of its performance, low cost and non-toxicity. Leclanché[2] recommended choosing high purity manganese dioxide with good electric conductivity. These criteria remained the basis of selection of battery grade manganese dioxide from the only sources then available; ores (in particular Nikopol, Caucasus)[3]. Alternative mines of interest were discovered later in other parts of the world including Brazil, USA, Ghana, Gabon and Morocco[3]. This grade is known as Natural Manganese Dioxide (NMD) because of its origin.

It was only after World War II that synthetic manganese dioxide appeared in the market as a better choice (more battery active) than NMD. If the synthesis is through a chemical route, the material is termed Chemical Manganese Dioxide (CMD) and if it is prepared by electrolysis, it is labelled Electrodeposited Manganese Dioxide (EMD). More and more manganese dioxide varieties were discovered and/or prepared and were classified by labelling each set of materials sharing similar structure with a Greek alphabet prefix α–, β–, γ–, ε–,.....

The γ-MnO_2 variety is known to be the best battery grade and several techniques including X-Ray Diffraction (XRD), Infra-Red spectroscopy (IR) and potential measurement have been applied to characterise these materials.

Unfortunately, the γ-MnO_2 variety is not a simple one-phase compound; it is rather a series of phases characterised mainly by their poor XRD patterns[4]. Examples of these patterns are given in Fig. 1.1. which covers the starting materials studied in this work and shows that γ-MnO_2's are not perfectly crystallised; note the broadness and asymmetry of the lines. More details about the XRD patterns presented in Fig. 1.1 are given in the following chapters. Crystalline deficiency shows also in the chemical formula as γ- manganese dioxide is not really stoichiometric and the ratio of oxygen to manganese lies between 1.9 and 2 for most materials. Gabano et al.[5] suggested that this deviation from stoichiometry was due to some incorporated water and the formula

of γ-manganese dioxide was proposed to be $MnO_x(2-x)H_2O$. Of course, this was not the only formulation; and it seemed that each author adopted a formula that suited best the conclusions derived from their research. A simpler formula, $MnOOH_r$, proposed by Valand[126] and Atlung[127] for this material suggested that the non-stoichiometry was due to a slight amount of inactive hydrogen. The term "inactive hydrogen" was used to distinguish this initial hydrogen from the one inserted into the γ-MnO_2 (in the course of the battery discharge) which is discussed in section 1.4.

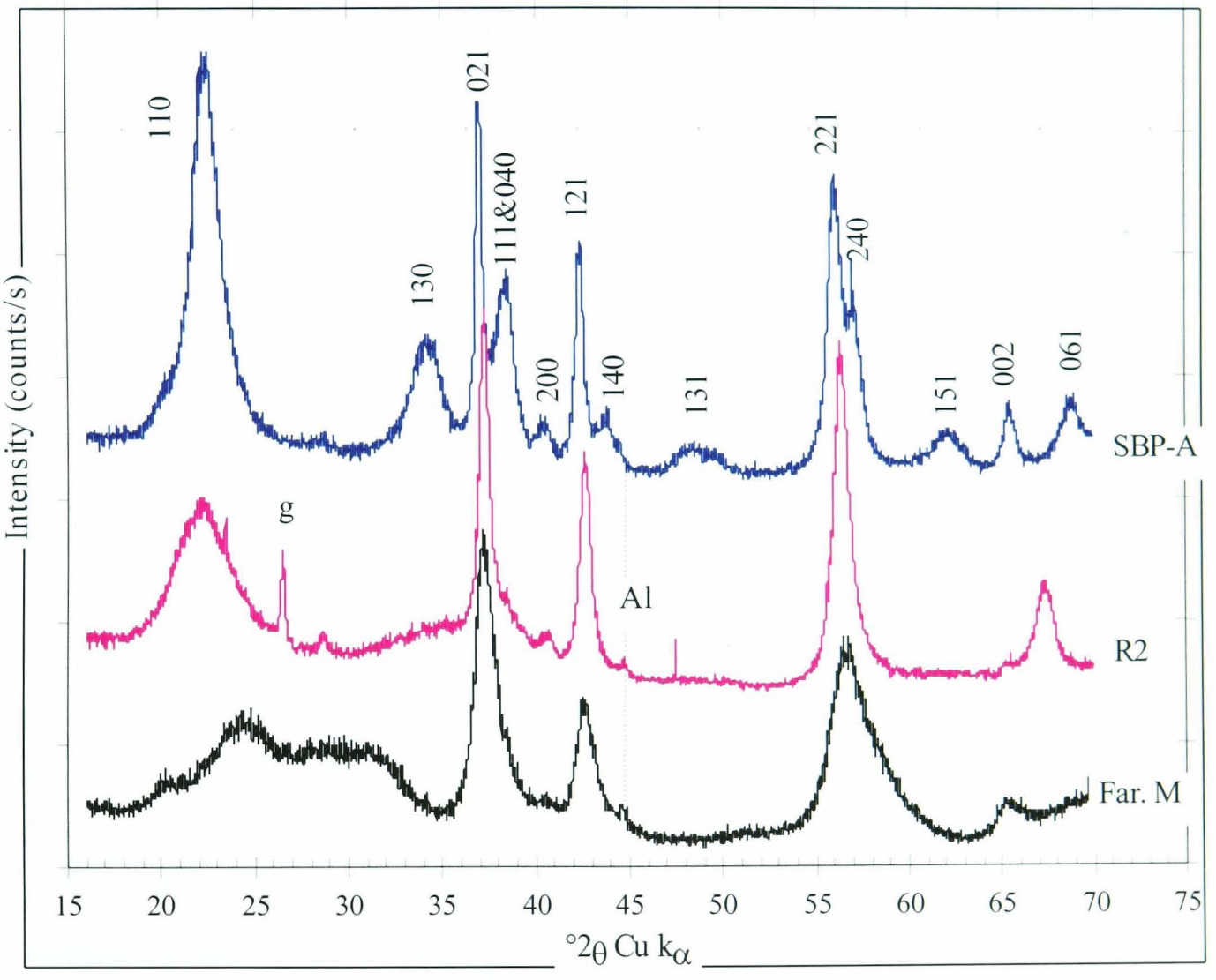

Fig. 1.1 The XRD patterns of the three γ-MnO_x studied in this work. Note the broad peaks 110, 130, 131, 151,... of SBP-A material. The other materials have less peaks which are asymmetric and generally broad. Al marks a peak from the almunium sample holder and g marks a graphite impurity peak in R2.

Another formulation given by Ruetschi[11,12,35] is discussed in section 1.3.3. Thus, there is disagreement about the formula of γ-manganese dioxide. This highlights the conflict in the literature about this material in terms of its composition and behaviour in batteries. However, a more recent formulation, by Tye and Tye[86], seems more

reasonable in the sense that it reports the deviation from stoichiometry as an oxygen deficiency rather than assuming the presence of an initial H impurity. Thus, γ-manganese dioxide is represented as MnO_x where $x < 2$. This formulation has been adopted in this work. More details on this formula are given in Appendix 2.

The next main characterisation technique and study tool of manganese dioxide is Infra-Red spectroscopy. Glemser's school was probably one of the first to study manganese dioxide by IR spectroscopy[14]. Eighteen years later, in 1979, Potter and Rossman[10] published several IR spectra intended to be references covering a wide range of manganese dioxides. This technique has since been used for the study of manganese dioxide but not as widely as XRD. In this work, however, Fourier Transform IR (FTIR) demonstrated a considerable usefulness for the study of manganese dioxide H-inserted samples. It provided unambiguous information about the product of the H-insertion process and clues on the mechanism of the insertion. These results are presented and discussed for each material separately in Chapters 3 to 6.

Additional experimental studies have been carried out in order to gain an insight of the H-insertion. These include low temperature FTIR, electrode potential measurement and Scanning Electron Microscopy (SEM). Details of all the techniques are given in Chapter 2.

To account for the structural defects of γ-MnO_x, derived from the XRD, some models have been developed and are reviewed in section 1.3 below. As most of these models invoke perfectly crystalline forms of manganese dioxide as a platform to map out structures of γ-MnO_x, these perfectly crystalline forms are described first.

1.2 Crystalline Forms of MnO_2 and MnOOH

Perfectly crystalline forms of MnO_2 and MnOOH, within which the structures of γ-manganese dioxide and H-inserted forms lie are described in the following sections. These forms are the limit structures of γ-MnO_x. An additional crystalline form of manganese dioxide (not treated in this thesis) is the λ-MnO_2 variety. This phase was synthesised by Hunter[128] and has a spinel structure.

1.2.1 Pyrolusite, β-MnO_2

This material can be represented by octahedra made of six oxygen anions around a central manganese cation. The octahedra share edges in the *c* direction while connected

by corners in the *ab* plane. This arrangement, in a 3-dimensional framework, yields an alternate of two types of octahedra: one, undistorted, contains the manganese cation and the other heavily distorted constitutes the tunnels. The distortion is accounted for by "primitive tetragonal packing"[9,17] (p.t.p.) of the oxygen anions. Here, the undistorted octahedra are projected as parallelograms in the *ab* plane; while the heavily distorted ones appear as squares in the *ab* plane of the structure. These representations are shown in Fig. 1.2a. Although Potter and Rossman[10] reported an orthorhombic pyrolusite phase with a = 4.36 Å, b = 4.44 Å and c = 2.87 Å, the generally accepted structure of pyrolusite remains, however, the rutile structure with tetragonal symmetry[8] of unit cell of a = 4.3983 Å and c = 2.8730 Å[7].

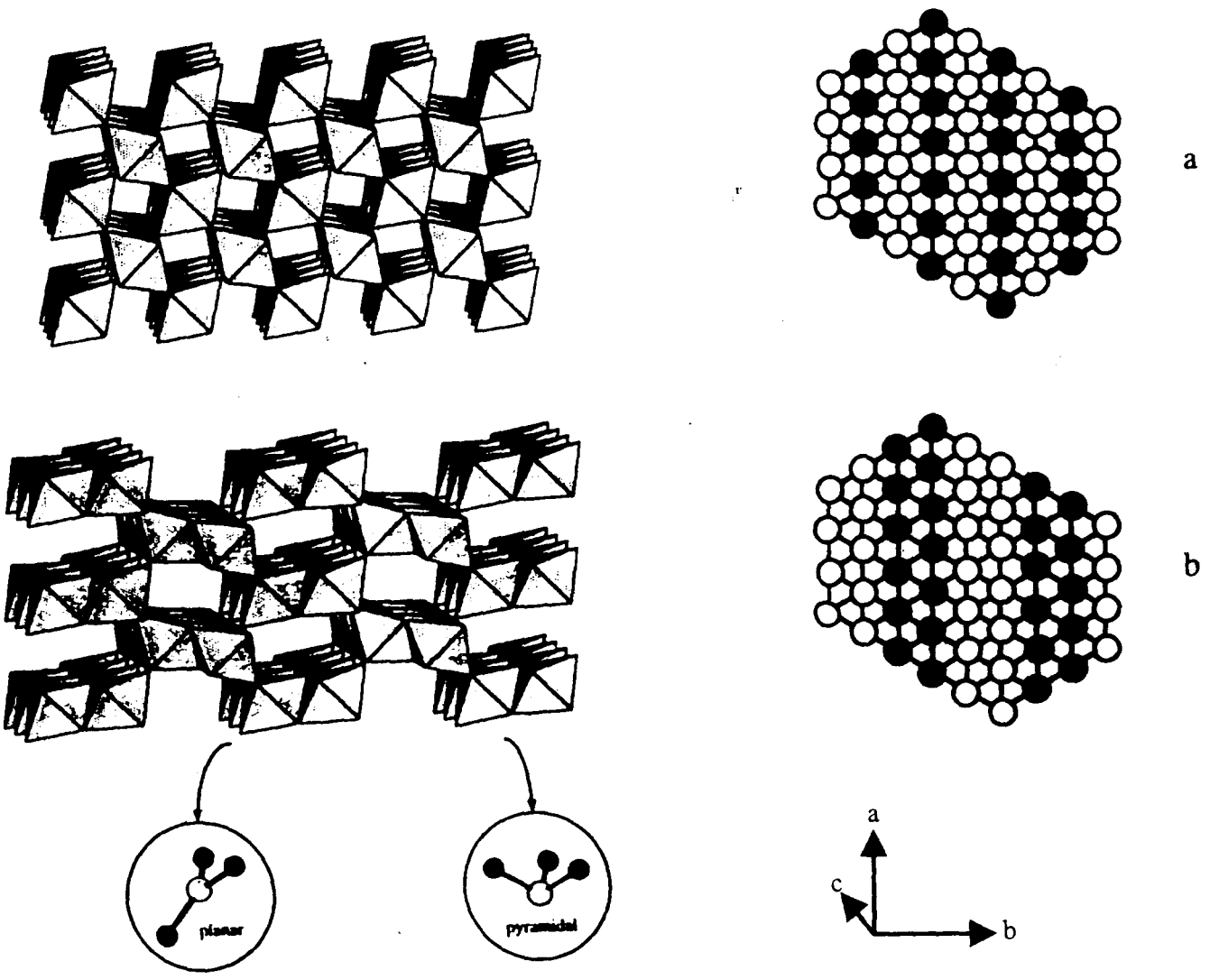

Fig. 1.2 (a) Polyhedral representation (left) and the Mn lattice in the *ab* plane (right) of pyrolusite as drawn by Pannetier (Fig. 1 of ref. 18). Filled circles represent atoms at ½*c*. (b) Polyhedral representation (left) and the Mn lattice in the *ab* plane (right) of ramsdellite as drawn by Pannetier (Fig. 1 of ref. 18). Filled circles represent atoms at ½*c*. Planar and pyramidal oxygens (noted O1 and O2 respectively) are shown in the ramsdellite structure. The (1x1) and (1x2) tunnels are also clearly shown.

Baur[7] also reported that this phase is the most dense (density 5.19) and thermodynamically stable form of MnO_2. Byström[19] reported a close set of lattice parameters a = 4.40 Å and c = 2.87 Å for tetragonal pyrolusite. All oxygen anions in pyrolusite are equivalent as well as the Mn cations.

1.2.2 Ramsdellite

Byström was the first to show that ramsdellite has a diaspore structure with orthorhombic symmetry and of unit cell dimensions a = 4.533 Å, b = 9.27 Å and c = 2.866 Å[19]. This material is constructed in the same way as pyrolusite except that here double chains of octahedra replace single chains in pyrolusite, giving rise to 2x1 tunnels. Each double chain is connected by corners to its neighbours in the *ab* plane but share edges in the c direction. Again, the octahedra are slightly distorted. In ramsdellite, the oxygen anions are arranged slightly differently yielding two types of oxygens[19]: three planar and three pyramidal oxygen atoms. The planar oxygen, noted O1 thereafter, "is the centre of an almost equilateral triangle, which has the metal atom at its corners"[19] and is consistent with an sp^2 hybridisation of the oxygen atom[18]. The Mn-O distances are 1.86, 1.86 and 1.91 Å[19]. This type is similar to the oxygen in pyrolusite. The pyramidal oxygen, noted O2 throughout this thesis, is located at the apex of a trigonal pyramid, which has Mn cations at its base[19], indicating an sp^3 hybridisation[18]. The Mn-O distances are 1.92, 1.92 and 1.89 Å[19]. These two types of oxygen are shown along with the ramsdellite structure in Fig. 1.2b.

1.2.3 Manganite, γ-MnOOH

Manganite is a reduced form of pyrolusite in which the valency of Mn is reduced from +4 to +3. Buerger[15] suggested that manganite has a rutile-like structure as early as 1936. Recently it has been described as a "distorted derivative from pyrolusite"[16] and this distortion is "caused by the Jahn-Teller effect (Mn^{4+} is replaced by Mn^{3+}) and hydrogen bonding"[16]. This is to account for the fact that the change from pyrolusite to manganite occurs when a proton locates in the 1x1 tunnel simultaneously with the capture of 1 e by the Mn^{4+} in the centre of the octahedron. This location (the H-insertion) yields some changes of the initial structure to accommodate both the proton and the larger cation (Mn^{3+}). Essentially, these changes distort the octahedra. Thus, the structure is no longer tetragonal, due to the alteration of the angles, and an orthorhombic unit cell of dimensions a = 4.458 Å, b = 5.277 Å and c = 2.874 Å has

been suggested to account for the distortion observed in manganite[16]. A representation of manganite structure is shown in Fig. 1.3a.

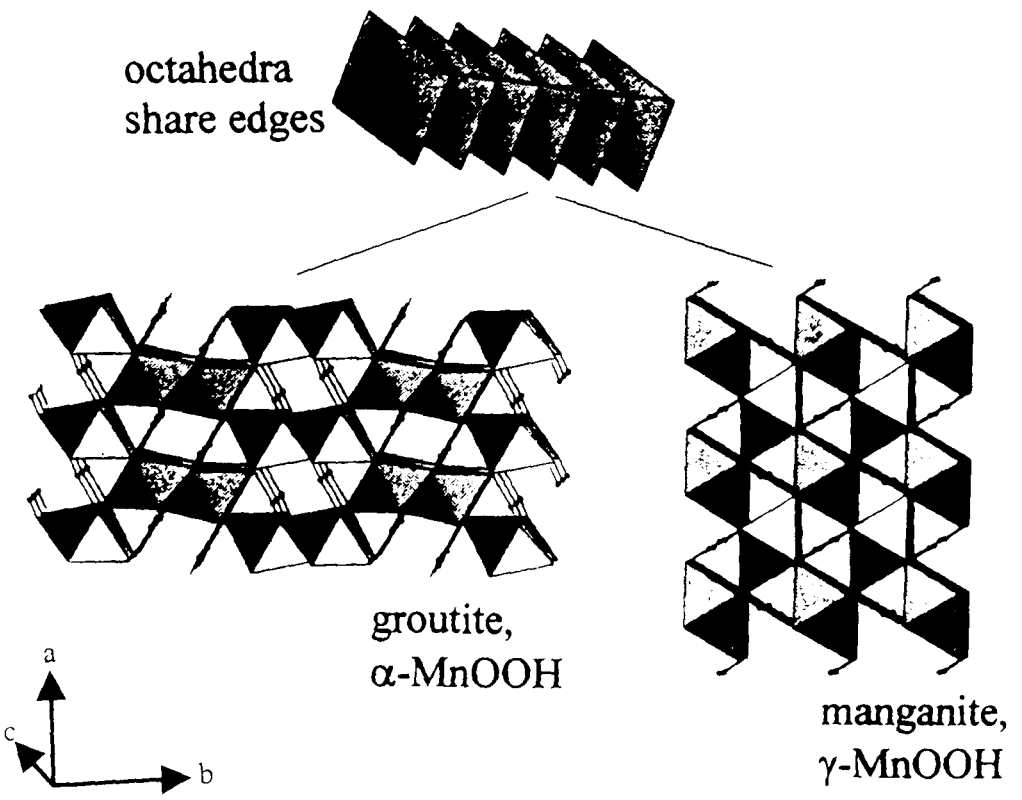

Fig. 1.3 Polyhedral representation of groutite (left) and manganite (right) showing H (small spheres) located in the tunnels. Figure reproduced from Fig. 1 of reference 16. Also note the shape of the tunnels compared with the shapes in Fig. 1.2 above.

1.2.4 Groutite, α-MnOOH

Groutite is a reduced form of ramsdellite in which the valency of Mn is reduced from +4 to +3. Glasser and Ingram[20] studied this phase of oxyhydroxymanganese and found that it crystallises in the diaspore structure (similar to ramsdellite) but with a slight Jahn-Teller distortion due to the replacement of Mn^{4+} by Mn^{3+} in the centre of the octahedron. Here, the two types of oxygen atoms present in ramsdellite (i.e. O1 and O2) are also distinguishable. The O2 oxygens have been reported to be the site of the H-insertion[6,18]. This is understandable since the O2s are slightly risen above the three co-ordinated manganese atoms resulting in a reduced repulsion between the manganeses and the inserted proton. Groutite is thus iso-structural with ramsdellite and the two phases have approximately the same *a* and *c* unit cell values but *b* is about 15% larger in groutite[16,18,20]. A representation of groutite structure is shown in Fig. 1.3b.

1.3 Models of γ-MnO_2

1.3.1 de Wolff's Model, the Layers Model

Byrstöm[19] suggested that γ–manganese dioxide can be described as an intermediate between pyrolusite and ramsdellite. Ten years later, de Wolff[22] confirmed this description when he studied the XRD patterns of γ-manganese dioxide and linked the broadening and shift of some XRD lines with the amount of pyrolusite in γ-manganese dioxide. He suggested the concentration of pyrolusite, p, as a characterisation factor so that $p = 0$ for pure ramsdellite and $p = 1$ for pure pyrolusite. For small p values, de Wolff described γ-MnO_x as blocks of ramsdellite interrupted at random in the b direction by single layers of pyrolusite of half unit cell thickness. This model can be summarised as follows: starting from a ramsdellite framework, a ramsdellite block is replaced by a pyrolusite layer (Fig. 1.4). This will cause a shortening of the lattice in the b direction, and the new value is:

$$b' = 0.75b + 0.5c \qquad (1.1)$$

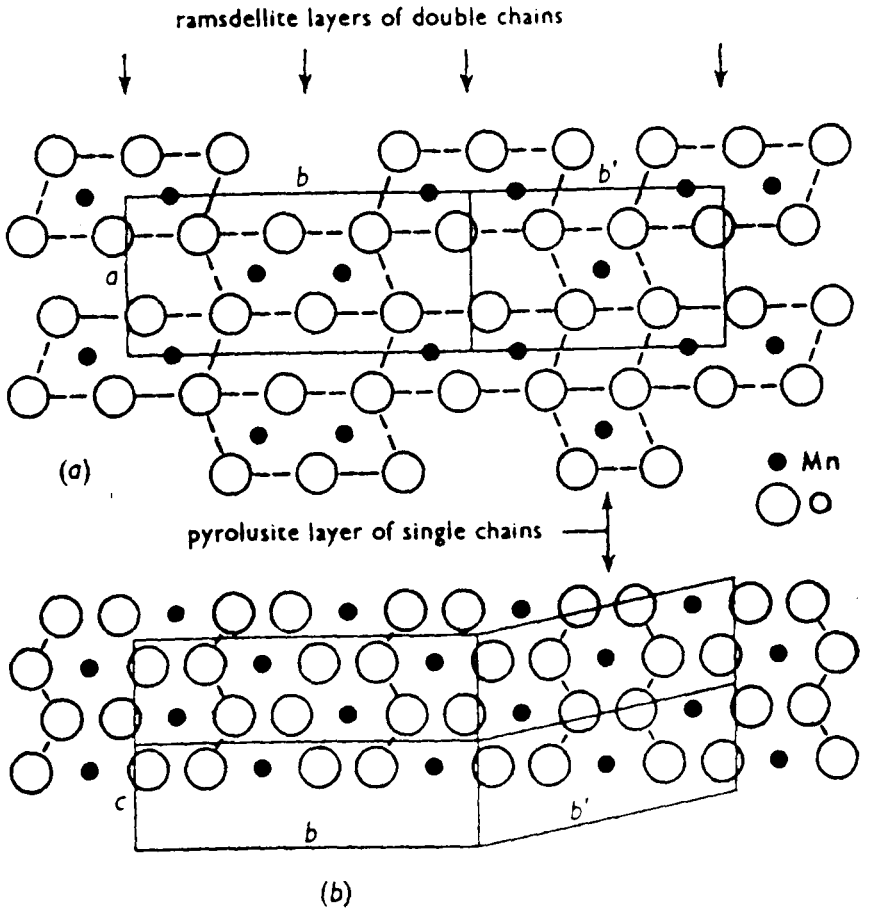

Fig. 1.4 Schematic drawing of de Wolff's model for γ–MnO_x in the *ab* plane (a) and the *bc* plane (b). Drawings by de Wolff, reproduced from Fig. 2 of ref. 22.

a and c remain the same (i.e. $a = a'$ and $c = c'$).

Thus, two sets of planes (hkℓ) and (h'k'ℓ'), leading possibly to different XRD lines, are expected. The XRD patterns will therefore depend on the relative values of hkℓ and h'k'ℓ'.

- When (½k + ℓ) is even h'k'ℓ' lines are almost in the same positions as hkℓ's with a slight weakness compared to the lines of pure ramsdellite. In fact the two sets of lines are supposed to coincide, therefore no shift or broadening is expected; in particular this is the case for k = 2ℓ.
- For k odd, hkℓ's are considerably broadened and shifted towards the nearest h'k'ℓ'
- When (½k + ℓ) is odd, these lines are not shifted but considerably broadened.

Note that this model applies only for small p values and that no consecutive pyrolusite layers are allowed[22], i.e. each pyrolusite fault has a ramsdellite neighbour on both side in the b direction. Thus, only the lines of (½k + ℓ) even can be satisfactorily assigned to the ramsdellite structure as they are not broadened or displaced. De Wolff referred to this set of lines as "the sharp lines" and relied on them for lattice parameters calculation. A summary of the consequences of de Wolff's model on diffraction lines of γ-MnO_x is presented in Table 1.1.

Table 1.1 Effects of de Wolff's model on the XRD lines of γ-MnO_x

k	ℓ	**k/2**	**½k+ℓ**	**effect on diffraction lines**
even	even	Even	even	this set of lines is not shifted or broadened
even	even	Odd	odd	these lines are not shifted but broadened
even	odd	Even	odd	these lines are not shifted but broadened
even	odd	Odd	even	this set of lines is not shifted or broadened
odd	even	X	X	lines broadened and shifted towards nearest h'k'ℓ's
odd	odd	X	X	lines broadened and shifted towards nearest h'k'ℓ's

1.3.2 Pannetier et al.'s Model

Pannetier and co-workers[18,25-29] carried out further developments of de Wolff's model and showed its limitations. They also introduced the new concept of extensive microtwinning across the 061 and/or 021 ramsdellite planes causing peaks to merge

together reducing thereby the number of reflections to the patterns observed for EMD (see for example the patterns of R2 in Fig. 1.1). A recapitulation of their work is presented here while a fully detailed version is available in reference 18. They showed in particular that the unique parameter in de Wolff's model is not sufficient to account for the possible combinations of pyrolusite (r)/Ramsdellite (R) arrangements in the framework of γ-MnO_x. Thus, a second parameter, *the junction probability*, has been introduced. Denoted $P_{r\text{-}r}$, $P_{r\text{-}R}$, $P_{R\text{-}r}$ or $P_{R\text{-}R}$ this parameter accounts for the probability of a pyrolusite layer followed by a ramsdellite one ($P_{r\text{-}R}$), ...etc. They also proposed a method of estimating this probability. Ripert[29] suggested an equation based on the displacement of k odd lines. In the reciprocal lattice, such a displacement, rb*, is related to P_r by minimising Mering's equation for r[29]:

$$\left| 1 - (1 - 2P_r)\exp[2\pi i(1 + r)] - 2P_r^{*}\exp[3\pi i(1+r)/2] \right| \qquad (1.2)$$

For samples close to the ramsdellite side, Pannetier[25] gave an approximate polynomial for the above equation based on displacement of the 110 line:

$$P_r = 2.471\ \Delta(d) - 2.332\Delta^2(d) \qquad (1.3)$$

where $\Delta(d)$ is the displacement of 110 line from its theoretical orthorhombic position.

Another limitation of de Wolff's model is that it does not account for the observed coalescence of h21 and h40 (e.g. 021 & 040 in Fig. 1.1) lines which are not supposed to be modified (½k + ℓ even). This model does not account either for the asymmetry observed in some XRD lines of γ-MnO_x (e.g. lines 221, 061, 021 in Fig. 1.1), nor for the poor resolution characteristic of XRD patterns of most γ- MnO_x samples[3,18].

In addition to these observations, the work of Preisler[30] on fibrous EMD has shown that the axis of the fibres corresponds either to the (061) or (021) direction; and that the EMD crystallites grew perpendicular to these faces. Thus, these planes would also be the sites to check for anomalies in the crystallite growth. Taking these facts into account along with the fact that twinning occurs often in natural samples of rutile[18], Pannetier suggested that extensive *microtwinning* of the intergrowth, across these planes (021 and 061), must have occurred during the growth of γ- MnO_x samples. A schematic representation of the microtwinning is given in Fig. 1.5.

This defect causes some pairs of lines to merge together as a single broad line instead of two separate lines. Other lines are shifted towards either higher or lower angles with respect to their position in perfect ramsdellite (see Table 1.2). The main achievement of this model was that it predicted a reduction of the number of lines observed in the XRD pattern; explaining therefore the poor pattern of EMD (see Chapter 5). Pannetier[18,26] has shown that as the amount of microtwinning (expressed in % and noted Tw) increases, the symmetry of γ-MnO_x changes from orthorhombic to a pseudo hexagonal, except from the presence of a 110 line.

Although the calculation of both types of defects (P_r & Tw) involves complex computing, the same papers[18,26] present a simple procedure for estimating these two parameters: "using the parameters of natural ramsdellite as a reference (Tw = 0) and setting the value of $b/2c$ at $\sqrt{3}$* for Tw = 100, one finds:[18]

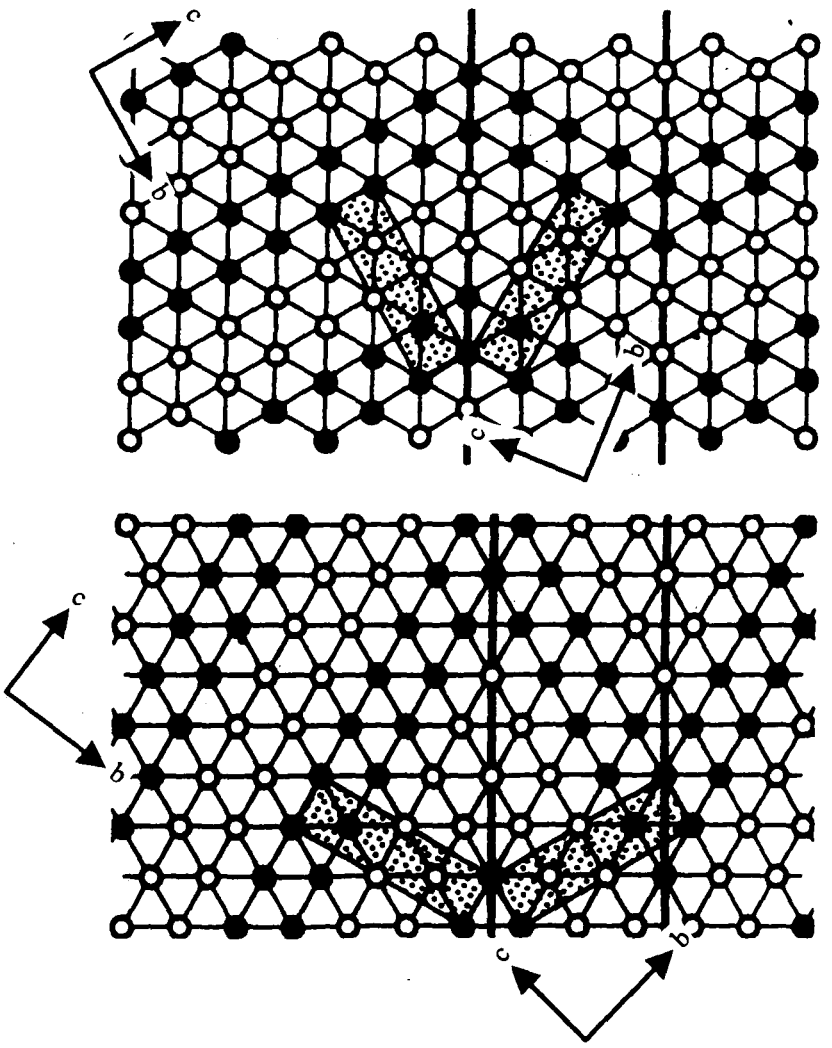

Fig. 1.5 Schematic representation of the microtwinning across the 061 (top) and 021 (bottom) ramsdellite planes according to Pannetier et al.'s model in a ramsdellite structure. Only the manganese lattice is shown; the filled and open circles represent Mn at 0 and ½c. Twinning planes are drawn as thick lines and the ramsdellite unit cell is shaded. This figure was reproduced from Fig. 11 of ref. 18.

* b and c are noted b_T and c_T in the original paper and are refined from the set of lines 021, 200, 121, 140, 221 and 240.

- Tw (in %) = 871($b/2c$) - 1409 (1.4)
- Calculate the shift due to the microtwinning, δ(Tw), from:

$$\delta(Tw) = -0.0054Tw - 8.9\times10^{-5}Tw^2 \quad (1.5)$$

- Calculate the concentration of de Wolff fault, P_r, as:

$$P_r = 0.602\delta(DW) - 0.198\,\delta(DW)^2 + 0.026\delta(DW)^3 \quad (1.6)$$

where $\delta(DW) = 2\theta(110)_{exp} - 21.808°$ and $2\theta(110)_{exp}$ is the experimental position of 110 line and 21.808 °2θ the position of the same line in perfect ramsdellite.

Table 1.2: Effects of de Wolff disorder and microtwinning on the XRD lines of γ-MnO_x (Table 2-3 of ref.18)

				effects of		
Code	**h**	**k**	*ℓ*	**μTw**	**de Wolff**	
E	1	1	0	brd	θ↑	
	1	3	0	brd	θ↓	brd: line broadened
D	0	2	1	θ↑	n/a	θ↑: line shifted towards
I	1	1	1	brd	θ↓	higher angles
J	0	4	0	θ↓	n/a	θ↓: line shifted towards
F	2	0	0	n/a	n/a	lower angles
C	1	2	1	θ↑	n/a	n/a: not affected
H	1	4	0	θ↓	n/a	
	1	3	1	brd	θ↑	
B	2	2	1	θ↑	n/a	
B	2	4	0	θ↓	n/a	
	3	1	0	brd	θ↑	
	1	5	1	θ↑	θ↓	
A	0	0	2	θ↑	n/a	
G	0	6	1	θ↓	n/a	
	3	3	0	brd	θ↓	
	1	1	2	brd	θ↑	
	3	0	1	brd	n/a	
	3	1	1	brd	θ↓	

This two-parameter model (Pr and Tw) provides a useful tool to characterise the structures of γ-MnO_x samples and makes comparison easier. Thus, it was this model that defined the choice of the γ-MnO_x materials studied in this work aiming to cover elements of the range of Tw and Pr (see Chapter 2).

1.3.3 Cation-Vacancy Model

Vosburg[23] linked the battery activity of γ-MnO_x to the water incorporated in the structure. Preisler[24] related this same water to the electrical conductivity and electrode potential. In an attempt to explain several properties of γ-MnO_x (including the above), Ruetschi[11] suggested a model in which the structural water is in the form of OH^- anions. This model also postulates the presence of a fraction of Mn^{3+} and some Mn^{4+} vacancies in the structure of γ- MnO_x. The negative charge of these vacancies is compensated by protons in the form of OH. The overall formula of γ-MnO_x, according to this model, is:

$$\mathbf{Mn_{(1-x-y)}^{4+} \bullet Mn_y^{3+} \bullet O_{(2-4x-y)}^{2-} \bullet OH_{(4x+y)}^{-}}$$

where x is the fraction Mn^{4+} vacancies and y the fraction Mn^{3+} ions.

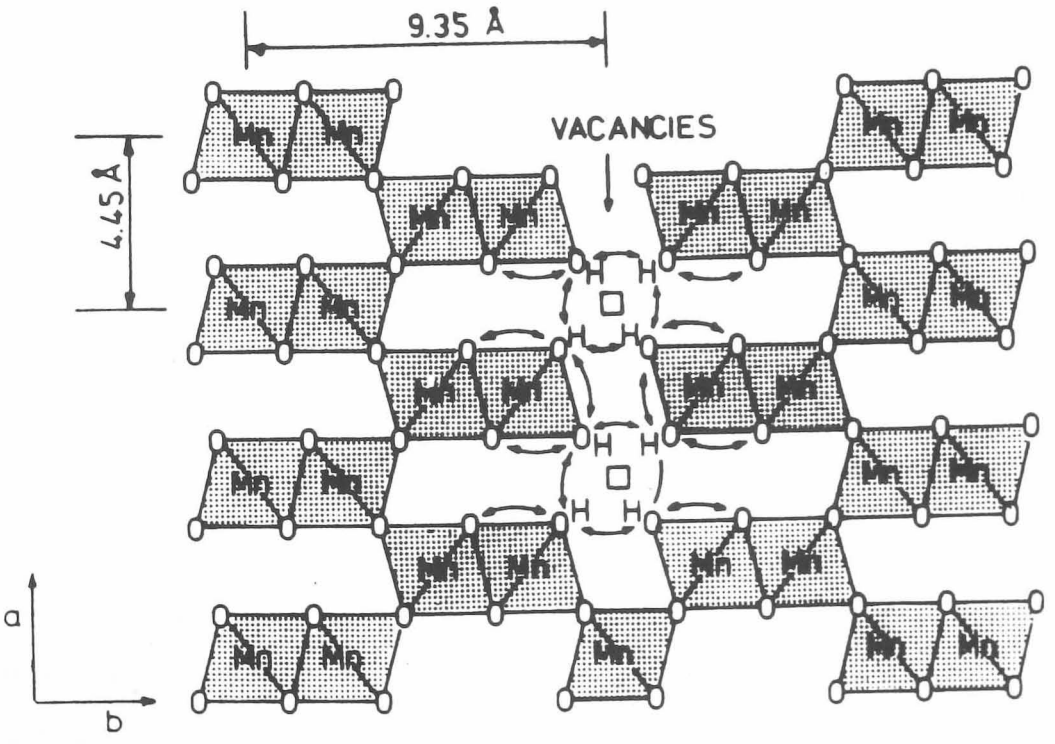

Fig. 1.6 Schematic representation of γ-MnO_x according to the Cation Vacancy model as introduced by Ruetschi (Fig. 3 of ref. 12)

1.4 The H-insertion

Vosburgh[23] was the first to suggest that the depolarisation of γ-MnO_x occurs through the capture of a proton by the γ-MnO_x host, and formulated this capture into an insertion reaction, which can be written for a stoichiometric compound as:

$$MnO_2 + H^+ + e \rightarrow MnOOH \qquad (1.7)$$

Reaction (1.7) is now widely accepted as the electrode reaction of γ-MnO_x cathode in Leclanché and alkaline batteries. The insertion of hydrogen into the manganese dioxide structure causes it to dilate as revealed by XRD studies. Brenet et al.[32] was the first to report this dilation. As it can be seen from Eq. (1.7), the H-insertion reduces the Mn cation from +4 to +3 in valence and intercalates (inserts) a proton in the initial structure. The proton bonds to the O2 oxygen and hydrogen-bonds to the O1-type[6]. In the light of the intergrowth of ramsdellite and pyrolusite blocks present in the starting material, as well as the thermodynamic data (essentially derived from potentiometry), considerable debate dominates the literature as to the mechanism of reaction (1.7). It is noteworthy that the potential measurement, which constituted a main source of information on the H-insertion, was not always satisfactory (see section 2.7). The debate on the H-insertion ranges between two mechanisms. The first, suggested initially by Tye[85] and supported by many subsequent works[e.g.6,21,33,37,38,42-47], states that protons and electrons are independently mobile in the structure of γ-MnO_x up to an insertion level (which depends on the material) at which the proton locates in the tunnels of the host structure and the electron reduces the valence of the Mn. The second mechanism was suggested by Pannetier and co-workers[e.g.18,26-29], and states that the H-insertion occurs first through H location in the ramsdellite blocks of the intergrowth before proceeding in the pyrolusite part. These mechanisms will be reviewed with further details in Chapters 3-6. Nevertheless, it can be seen that each author (or set of authors) interpreted their own results and generalised their conclusion to the γ-MnO_x series.

Such an approach would have been reasonable if enough precautions were taken to ensure that the H-insertion product was not contaminated by any unwanted material whatsoever; as impurities might have influenced the γ-MnO_x data.

Unfortunately, the abundant literature on manganese dioxide fails to provide a set of 'uncontaminated' H-inserted sample and the XRD of reduced samples always comprise a more or less strong (but never negligible) peak at ~ 26.1 °2θ Cu Kα, characteristic of pure manganite[93]. Also, a satisfactory description of experimental details is not always provided to help prevent repetition of previous errors that might have happened during sample preparation. This impurity problem caused a concern at the start of this work and contributed largely to the design of the experimental procedures used in this work for mild H-insertion.

1.5 Aims of this Study

The previous section shows that there is disagreement in the literature about the interpretation of the H-insertion into γ-manganese dioxide. This disagreement also extends to the structure of the products of the H-insertion. However, before engaging in this debate, it seemed crucial to ensure the "purity" of the H-insertion product. That is to ensure that no unwanted product was formed. Hence, it was an aim of this work to produce such a "pure" product, especially manganite-free. The next task was to characterise these uncontaminated samples in order to establish the nature of the H-insertion. In addition, the literature presents some views which have been postulated regarding the H-insertion, and further research is needed to examine them. This is the case for hydrogen mobility and the demicrotwinning[33]. Due to the lengthy and demanding research requirements, demicrotwinning could not be investigated. Clues on H mobility were, however, sought through FTIR spectroscopy investigations. This work aimed to:

- Develop an experimental procedure for mild chemical H-insertion into γ-MnO_x.
- Produce manganite-free MnOOH compounds by mild H-insertion, or minimise the manganite impurity.
- Produce sets of materials with many levels of H-insertion in order to pinpoint changes in process of insertion and in product.
- Develop a procedure for satisfactory electrode potential measurement. That is stable and reproducible electrode potential.
- Characterise the H-inserted compounds of all γ-MnO_x materials by XRD, FTIR and electrode potential
- Investigate H bonding and mobility by FTIR at low temperature.

- Correlate any information on the H-insertion that can be deduced from the characterisation techniques in order to derive some clues on the mechanism of the H-insertion.

2 Experimental

2.1 Materials Studied

Section 1.3.2 has established that γ-manganese dioxide can be characterised by two parameters P_r- the concentration of pyrolusite and Tw – the % microtwinning across the 061 and/or 021 planes of the ramsdellite part. Hence, to cover all γ-manganese dioxide materials, four possible limits can be envisaged: low P_r low Tw, high P_r low Tw, low P_r high Tw, and high P_r high Tw. No material belonging to the last case is known (to the author's knowledge), while examples of the three remaining cases were studied in this work. These are:

Table 2.1 Examples of the possible kinds of γ-manganese dioxide

Tw	P_r	Example Material	Reference
Low	Low	SBP-A (EMD)	ref. 33, 37
Low	High	Faradiser M (CMD)	ref. 18, 38
High	Low	R2 (EMD)	ref. 18, 33
High	High	none known	-

2.1.1 SBP-A

Preisler[34] found that the addition of fine particles into the electrolyte when EMD is deposited (**S**uspension **B**ath **P**rocess), can influence the structure of the EMD. In fact, the anode adsorbs the added particles increasing thereby its active surface and correspondingly decreasing the current density. The larger the amount of added particles, the lower the current density, and the milder is the deposition. So, at large concentrations of particles (low current density) the crystal has time to grow in a uniform way. Preisler[34] prepared different samples by varying the amount of added particles. His samples are coded SBP-A...F with descending amounts of suspended particles i.e. SBP-F has no particles added and SBP-A the highest amount (about 2 g/l). It was speculated as a first approximation that the deposition conditions of SBP-A minimised the possibility of structural defects (Tw & P_r) so the material SBP-A was chosen for this study. Estimation of these parameters from eq.s (1.4) and (1.6) for SBP-

A gives Tw ~ 16.5% and P_r ~ 0.40. MacLean & Tye[33,37] reported for the same material 17% Tw and 0.41% P_r.

2.1.2 Faradiser M (IBA N° 12)

This material is a CMD extensively produced by SEDEMA S.A. for use in Leclanché cells[36]. Faradiser M is prepared by precipitation from $MnSO_4$ solution at ~ 95 °C[35]; this step controls the particle size[36] saving thereby the grinding step necessary for EMD. The XRD patterns of this material exhibit only a few broad lines (see Fig. 1.1) making accurate determination of its structural parameters (Tw and P_r) more difficult than for SBP-A. An attempt to estimate these parameters led to Tw ~ 7.5% and P_r ~ 0.78. Pannetier[18] reported 10% and 0.70 respectively for this material acknowledging that their results were of limited accuracy. For the sake of consistency, the results of Pannetier are used here. The sample of Faradiser M used exhibited an XRD close to that for sample N° 12 of the International Battery Association (IBA)[18].

2.1.3 R2

R2 is the code for a Japanese EMD deposited on a graphite electrode from a hot acidified Mn(II) solution. The usual deposition temperature ranges between 90 and 95 °C, and the acid is sulphuric[34]. The deposition conditions result in slabs of EMD which are ground for use in batteries. R2 has been used in the battery industry and undergone substantial number of studies[39-47]. In terms of the structural parameters, it has been described as heavily microtwinned[18,33]. The defect estimates are Tw ~ 100% and P_r ~ 0.41. Owing to the high microtwinning of this material (Fig. 1.1), estimation of lattice parameters from the peaks position is not reliable due to the shift introduced by microtwinning. Therefore, no attempt was made to work the lattice parameters of R2.

2.2 Development of a New Mild H-insertion Method

2.2.1 Sampling

Before starting any experiment, care is needed to choose representative samples. According to Allan[48], the accuracy of sampling from a powder must meet the so-called "Golden Rules" of sampling. These are: a) collection of samples when powder is in motion and b) collection during many short increments of time. These rules help to avoid biased or selective samples.

The following procedure was adopted to respect them. The manganese dioxide powder (about 500g) to be H-inserted was poured into a large clean tray so as to form a few piles (8 to 10). Each pile was then poured again and a sample collected by moving a scoop through the powder stream, slowly and always in the same direction. These samples were gathered together and mixed and then passed through a sample divider (from Endcotts Ltd.) to obtain two identical halves. One half was passed through the sample divider again and the operation repeated until a final sample of suitable size was achieved (usually 2.5g).

2.2.2 Background to H-insertion Method

Chemical H-insertion into manganese dioxides is a familiar practice in this Centre. However, the "true" H-inserted manganese dioxides have not been achieved as impurities and unwanted side products were always present under the experimental conditions used. A particularly unwanted impurity, believed to precipitate from soluble manganese species, is manganite. Soluble manganese species are enhanced in aqueous and alkaline media[49]. This is why many previous H-insertion studies have been carried out using organic substances as sources of proton. Fitzpatrick[42] used xylene, cinnamyl alcohol and acetone in temperatures of up to 40°C. Under these conditions, high H-insertion levels required very long times of immersion of the manganese dioxide in the organic substance- 9 months immersion of manganese dioxide in xylene at room temperature yielded $MnOOH_{0.89}$[42]. Beside the considerable reaction time required, the products formed were also contaminated by unwanted manganite. Later studies applied reflux in propanols and acetone[21,51] in order to reduce reaction times. The reaction times for full H-insertion was reduced to 33 hours of reflux in 1-propanol for a material coded IBA19 (close to R2) but for SBP-A six weeks were required under the same conditions[37]. Larcin[50] used hydrazine hydrate as a solution in 2-propanol as a source of protons, for his PhD. study in order to reduce the reaction time even further as the long time was believed to be due to the difficulty of extracting protons from the alcohols. Reducing the time period of contact between manganese dioxide and the reaction medium is also believed to reduce chances of solubility of manganese species thought to be responsible for undesired side products such as manganite. Larcin carried out this set of experiment at room temperature and succeeded in producing H-inserted manganese dioxide samples with lower manganite content.

Further development of this method is reported here. Larcin's work was carried out at

room temperature and his H-insertion consisted of adding sufficient hydrazine hydrate to increase inserted H by 0.1s (in MnO_nH_s) per hour. This work sought milder conditions and emphasis was: a) to carry out the H-insertion at controlled low temperature (≤ 1°C) and b) to keep the system very close to equilibrium so that only a small disturbance occurred. Small samples were chosen to reduce the reaction time and the time of contact between the manganese dioxide and the reaction medium in order to reduce chances of unwanted side products. The temperature was also lowered for the same purpose. However, it was necessary to produce samples large enough to carry out experimental studies; 2.5 g was found to be sufficient. A suitable cell was designed (Fig. 2.1) to meet these conditions and diluted solutions of hydrazine hydrate were used in small additions.

2.2.3 The Solutions and Reactions

The theoretical reaction of H-insertion into manganese dioxide using hydrazine hydrate is:

$$4\,MnO_2 + N_2H_4{\cdot}H_2O \rightarrow 4MnOOH + N_2\uparrow + H_2O \qquad (2.1)$$

Manganese dioxide was suspended in hexane (AnalaR 95%, from BDH) as a non-aqueous medium which showed negligible solubility for Mn(II)[42]. Hydrazine hydrate solutions were made in 2-propanol because of the total solubility of hydrazine hydrate in alcohols[52]; 2-propanol was chosen on the basis that the H in secondary alcohols is more stable and less likely to cause side reactions involving the solvent.

It is clear, from reaction 2.1, that each mole of hydrazine hydrate fully reduces 4 moles of MnO_2. In practice, an aliquot (Al 1) was first made of concentration 0.29 mol/l such that 1ml of this aliquot could fully reduced (H-insert) 1g of MnO_2. A set of solutions was prepared from this aliquot, by dilution in 2-propanol, so that 1ml was enough to reduce 1 mg of MnO_2 to s = 0.1, 0.05, 0.01 and 0.005.

This set of solutions ensured the required mild conditions and the insertion levels required. Glass syringes were used to handle all the hydrazine hydrate solutions, including the delivery of the appropriate amount to the samples for H-insertion.

2.2.4 Effect of Solvents

The influence of the reaction medium (n-hexane & 2-propanol) on the H-insertion reaction has been examined. Samples of manganese dioxide were placed in the H-

insertion arrangement (section 2.2.5) but no hydrazine was used. Instead, a large excess of 2-propanol was added as reagent in order to investigate how far this solvent contributed in the manganese dioxide H-insertion under the experimental conditions. 2.5 g of MnO_x were suspended into ~30ml hexane and 20 ml of 2-propanol were added gradually ml by ml so long as the temperature did not rise. Six hours time of reaction was allowed. The maximum H-insertion reached was 0.041 in s in MnO_nH_s for R2 material. These samples are coded ?00; where ? denotes the material code (A for SBP-A, M for Faradiser M and R for R2).

2.2.5 The H-insertion Arrangement

A schematic diagram of the H-insertion assembly is given in Fig. 2.1. It consisted of the following elements:

- *The vessel*: a three-necked round bottom flask in which the manganese dioxide was put together with a magnetic stirrer bar and ~ 30 ml of n-hexane as suspension medium. Two of the three necks had suitable fitted Teflon stoppers for secure connection with the other components of the cell. The middle neck was left open for the released nitrogen to escape [reaction (2.1)].
- *Temperature measurement*: two thermocouples K-code were used for the temperature measurement. One immersed in ice water and used as *reference* (0 °C); the second, *inner* thermocouple, was introduced into the vessel. The thermocouples were connected to a Digital Voltmeter (DVM) such that the DVM *inner - reference* readings were collected through a GPIB* card, converted into temperatures by a QBasic program (Appendix 1) and displayed on a PC. When experiments were running, the QBasic program enabled the temperature traces to be visualised on the computer screen (Fig. 2.1) so that variations in temperature could be followed.
- *The insulator*: a polystyrene box was used as the overall container of the cell. It accommodated the vessel and the cooling ice-water.
- *To cool the sample,* ice water was added around the vessel and renewed when necessary to maintain the desired temperature.
- *Glass syringe* was used to deliver controlled amounts of hydrazine hydrate solution into the vessel through a lateral stopper of the vessel. This stopper had been drilled

* General Purpose Interface Board

to half thickness for this purpose.

2.2.6 The H-insertion

Sampled manganese dioxide samples of about 2.5 g were stored in bottles before undergoing H-insertion. The H-insertion consisted of introducing the sample in question into the round bottom flask (Fig. 2.1), addition of 30 ml of hexane, vigorous stirring and monitoring of the temperature. When the temperature had fallen below 1 °C, an appropriate amount (usually a few drops) of the appropriate hydrazine hydrate solution was added via the glass syringe to reach a fraction (~ 10%) of a predefined H-insertion level. Care was taken when adding hydrazine hydrate solution not to cause a high increase in temperature (typically not above 4 °C, for a short time). Only when the temperature had fallen back below 1 °C, was the next addition of hydrazine hydrate solution made.

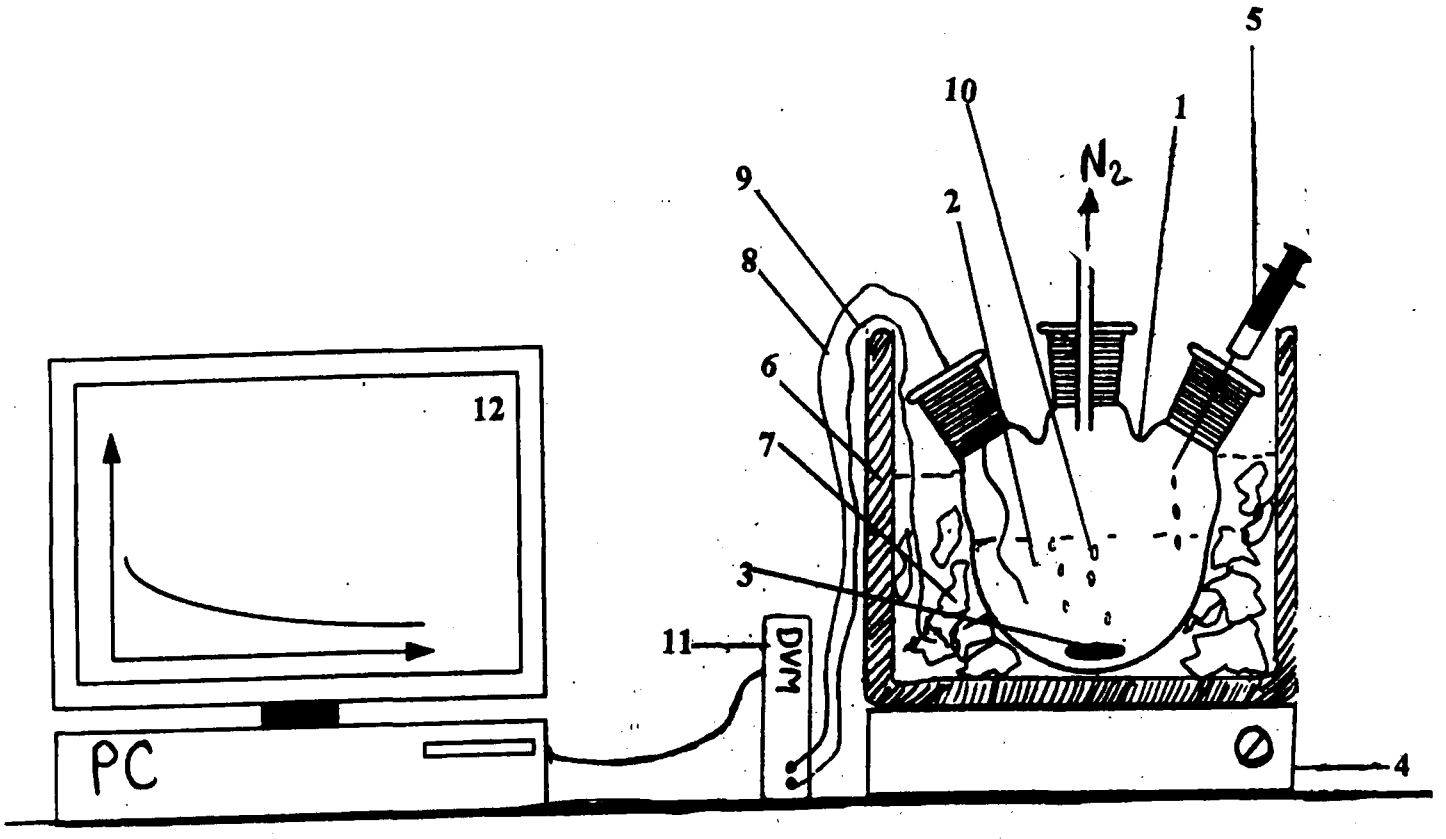

Fig. 2.1: Schematic drawing of the assembly used to prepare H-inserted manganese dioxide samples. 1 three-necked round bottom flask, 2 manganese dioxide suspended in hexane, 3 stirring bar, 4 magnetic stirrer, 5 syringe containing $N_2H_4H_2O$ in 2-propanol, 6 isolating polystyrene container, 7 ice pieces in water, 8 inner thermocouple, 9 outer thermocouple, 10 nitrogen bubbles, 11 digital voltmeter, 12 PC monitor displaying temperature trace.

The reaction was monitored by the bubbles of nitrogen released. When the last addition of hydrazine hydrate had been made and no more bubbles of nitrogen could be seen, the sample was filtered and air-dried in a fume cupboard for two weeks to allow the organic substances to volatilise. Samples were then analysed for oxidation state, and characterised by XRD and FTIR as described below. The reaction time took up to six hours to reach near maximum H-insertion values. However, chemical analysis showed that full H-insertion was not achieved in 6 hours. This suggested that that further contact between the samples and the reaction medium was required. Two samples were stored at ~ 1 °C overnight and for 4 days. Both reached higher H-insertion levels but were contaminated with precipitated manganite. These samples are shown in Fig. 2.2.

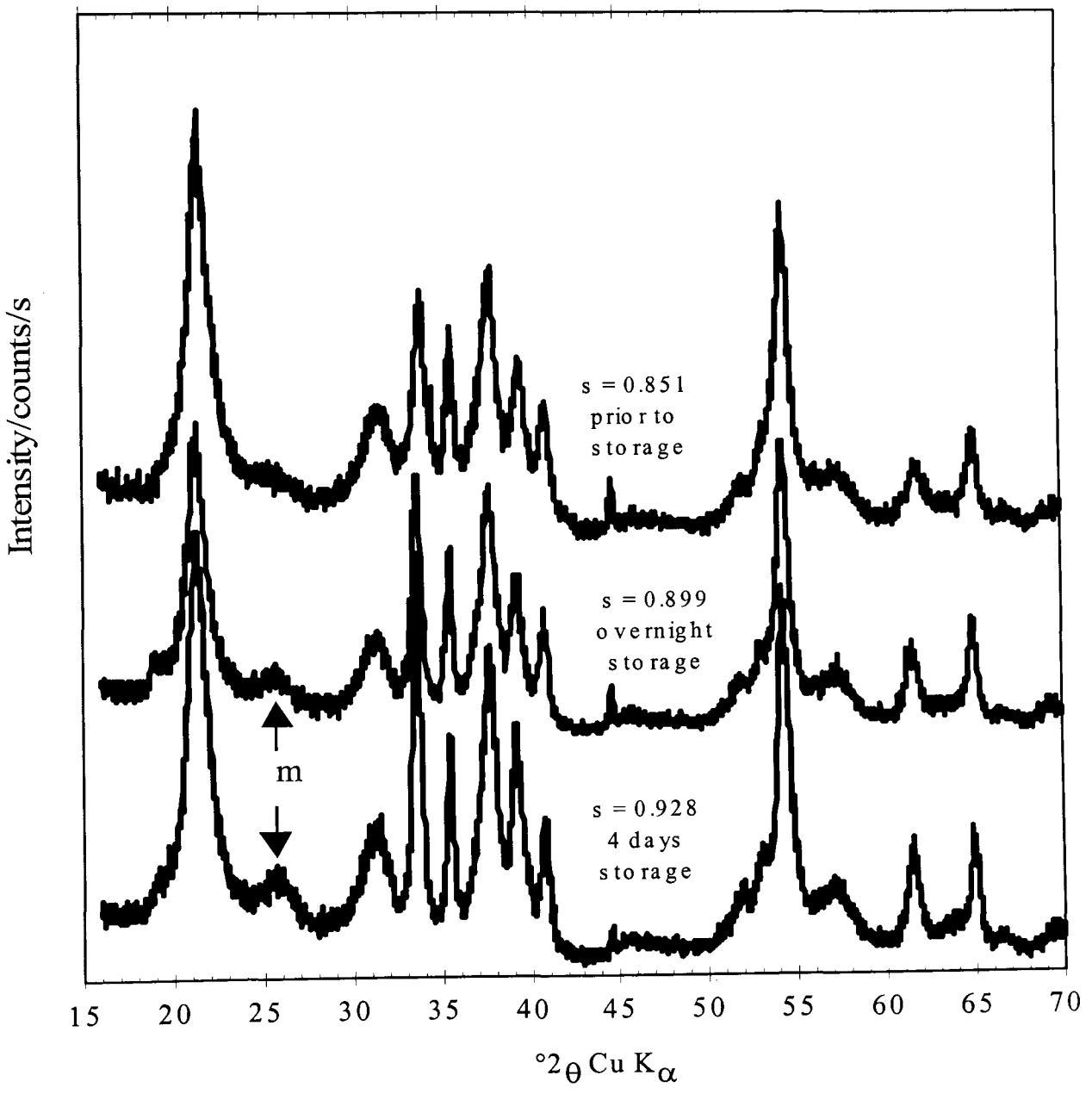

Fig. 2.2 XRD patterns of three H-inserted SBP-A samples stored at 1 °C, in the reaction medium, overnight and for 4 days with the patterns prior to storage. Storage clearly caused precipitation of manganite impurity marked m in the figure.

2.3 Chemical Analysis

The aim of the chemical analysis was to determine the average oxidation state of manganese in manganese dioxide. This oxidation state is noted x in MnO_x or n in MnO_nH_s: n expresses the deviation from stoichiometry of the starting materials. The inter-relationships of these variables are $r = 4 - 2x$ and $s = r - r_0$ where r_0 is the initial value of r in the starting material and expresses the deviation from stoichiometry (see Appendix 2). The method of determination of the average oxidation state followed in this work is well known and often quoted in the literature and is due to Vetter and Jeager[53].

All chemicals used in this investigation were of AnalaR grade (from MERCK Ltd.). The same experimental conditions were kept for all samples. All determinations were carried out three times and the average values are presented.

2.3.1 Preparation of Solutions

- Acidified Mohr's Salt Solution (AMSS) 0.05 M was prepared by dissolving 39.2g of $FeSO_4(NH_4)_2SO_4H_2O$ and 40 ml of concentrated sulphuric acid in a 2l volumetric flask. This solution dissolves manganese dioxide.
- 0.01 M solution of $KMnO_4$ was prepared by dissolving 0.316g of $KMnO_4$ in a 2l volumetric flask. The solution was filtered to eliminate precipitated Mn(IV) and then stored in a dark bottle and kept in a cupboard.

2.3.2 Reactions Involved and Procedure

- 50 ml of the AMSS solution was titrated by $KMnO_4$ potentiometrically and the equivalent volume V_0 recorded. The reaction was:

$$MnO_4^- + 5Fe^{2+} + 8H^+ \rightarrow Mn^{2+} + 5Fe^{3+} + 4H_2O \qquad (2.2)$$

- 80 mg of manganese dioxide was weighed into a 250 ml beaker and dissolved in an excess of AMSS (50 ml) by stirring for 20-25 minutes. The reaction was:

$$MnO_x + (2x-2)Fe^{2+} + 2xH^+ \rightarrow Mn^{2+} + (2x-2)Fe^{3+} + xH_2O \qquad (2.3)$$

Once reaction (2.3) had taken place, the excess ferrous was titrated as in (2.2) and the equivalent volume V_1 recorded. At this stage, the manganese in solution was in the form Mn^{2+} only.

- Lingane & Karplus[54] found that at $6.5 < pH < 6.6$, the complex $Mn(P_2O_7)_3^{3-}$ was

stable and that in this region of pH, the titration of the couple Mn^{2+}/Mn^{3+} has the maximum potential jump in the presence of $P_2O_7^{2-}$ ion. Therefore, sufficient sodium pyrophosphate was added to the solution to adjust the pH to the above region. The reaction was:

$$4Mn^{2+} + MnO_4^- + 15P_2O_7^{2-} + 8H^+ \rightarrow 5Mn(P_2O_7)_3^{3-} + 4H_2O \qquad (2.4)$$

The equivalent volume V_2 of this titration was recorded.

- It is shown in Appendix 2 that x in MnO_x can be calculated from the equation:

$$x = 1 + \frac{5}{8}\left[\frac{V_0 - V_1}{V_2 - \frac{V_1}{4}}\right] \qquad (2.5)$$

2.3.3 The Titration Method

The reactions were followed potentiometrically; a classical arrangement was used including a saturated calomel electrode (SCE) as a reference electrode and a platinum wire as working electrode. The potential difference between the two electrodes was obtained with a digital voltmeter. When appropriate, the SCE was filled up with saturated KCl solution, while the Pt wire was kept in a diluted H_2SO_4 solution when not in use to ensure a clean platinum surface.

2.3.4 Check of the Method

Prior to each series of chemical analyses, the reliability of the procedure and the chemicals was established by carrying out a blank analysis without addition of any manganese dioxide.

- 25 ml AMSS was titrated exactly as in reaction (2.2), the equivalent volume V_0' noted.
- 25 ml AMSS was stirred for 20 minutes and titrated by the same $KMnO_4$ solution; and V_1' determined. Only reaction (2.2) was expected to occur.

Thus $V_0' = V_1'$ as there would be no difference in composition between the two solutions. Any significant difference $V_0' \neq V_1'$, would indicate that the AMSS solution was not stable (e.g. oxidation of Fe^{2+} by air) or that the concentration of the potassium permanganate had been affected (e.g. by precipitation of Mn(IV)), but the former possibility was more likely to result from the stirring. The $KMnO_4$ solution had already been filtered to remove precipitated Mn(IV). When the difference $V_0' - V_1'$ exceeded

the experimental error, the solutions were not considered to be suitable for accurate analysis and new solutions were made up.

- When V_0' = V_1', within the experimental error, the pH was adjusted to the range 6.5-6.6 by addition of sodium pyrophosphate so that reaction (2.4) occurred and V_2' was determined.

Since each mole of MnO_4^- titrates 4 moles of Mn^{2+} (formed by reaction 2.2 or 2.3), only V_0'/4 or (V_1'/4) is required for this titration. It follows that V_2' is expected to be close to V_0'/4 or (V_1'/4) within the experimental error. This is a double check of the method. Examples of successful values of V_0', V_1' and V_2' are 25.2, 24.6 and 6.4 ml respectively.

2.4 X-Ray Diffraction Procedure

2.4.1 Sample preparation

In addition to being representative of the material studied, samples for XRD analysis must have appropriate particle size (the mean should be less than 45 μm), and the preparation procedure should not distort the lattice[55]. In this study, the material with largest particle was the SBP-A starting material (mean particle size ~ 60 μm)*. It was thus, necessary to reduce the particle size in order to obtain smooth diffraction lines. About 1g of each dry H-inserted manganese dioxide sample was ground in an agate pestle and mortar for 5 minutes instead of 3 minutes previously chosen[33]. The ground powder was then mounted by a backloading procedure into a flat aluminium X-ray sample holder fixed on a glass slide in order to obtain a flat sample surface for X-ray examination. No pressure was exerted on the sample to avoid preferential orientation of the crystallites[56]. Gentle tamping of excess powder, with the edge of a spatula, ensured complete filling of the sample holder cavity and a flat sample surface with minimum pressure[57].

2.4.2 The Instrument

The XRD measurements were carried out using a Philips PW1710 diffractometer with the following specifications: High voltage constant potential generator (PW1710), vertical goniometer (PW1050/81), graphite monochromator, automatic sample changer

* Particle size measurement of the starting and most H-inserted materials has been carried out courtesy of Javier Alday from CEGASA, Spain.

(1170).

The diffractometer was monitored by a PC through the Philips *Automated Powder Diffraction* (APD) software. The instrument was set up as follows using a copper target broad focus tube: 1° divergence slit, 1° scatter slit and 0.1 mm receiving slit. The generator was set at 45 kV and 55 mA for analysis throughout this work. The scans were measured generally between 15-70^0 2θ. Outside this range, MnO_2 does not have important reflections and the reflections observed would be mostly second order[21]. Small particle size would also render higher order reflections negligible.

A typical scan programme was as follows:

Type of scan:	*STEP*	*Step size [°2θ]:*	*0.010*
Start angle [°2θ]:	*15.000*	*Maximum d-value [Å]:*	*5.901*
End angle [°2θ]:	*70.000*	*Minimum d-value [Å]:*	*1.343*
Scan time [h:m:s]:	*6:06:40*		
Number of steps:	*5500*	*Time per step [s]:*	*4.00*

The above scan speed of 0.01°2θ per 4s meets the recommendation of Gehain et al.[56] of < 0.01° of 2θ per second for consistent intensity. In fact, the intensity of the incident beam is sampled over an increment of time, and the relative standard deviation (σ_{rel}) of the total number of photons collected (N) is given by[58]:

$$\sigma_{rel} = \frac{1}{\sqrt{N}} \tag{2.6}$$

Under the above scanning conditions, the intensity of the peak maxima of the reference (see section 2.4.3) exceeded 10,000 counts which means a relative standard deviation of less than 1%.

2.4.3 Normalisation of Intensity

As the X-ray tube ages, the intensity of the incident beam weakens. Therefore, XRD patterns taken at sufficiently long gap of time require a normalisation procedure to make them comparable. For this purpose, the main line of an α-quartz sample (known as Arkansas Stone) at 26.8 °2θ has been used as a reference in this work and is shown in Fig. 2.3. Fig. 2.4 reports the variation of this peak area against time and clearly

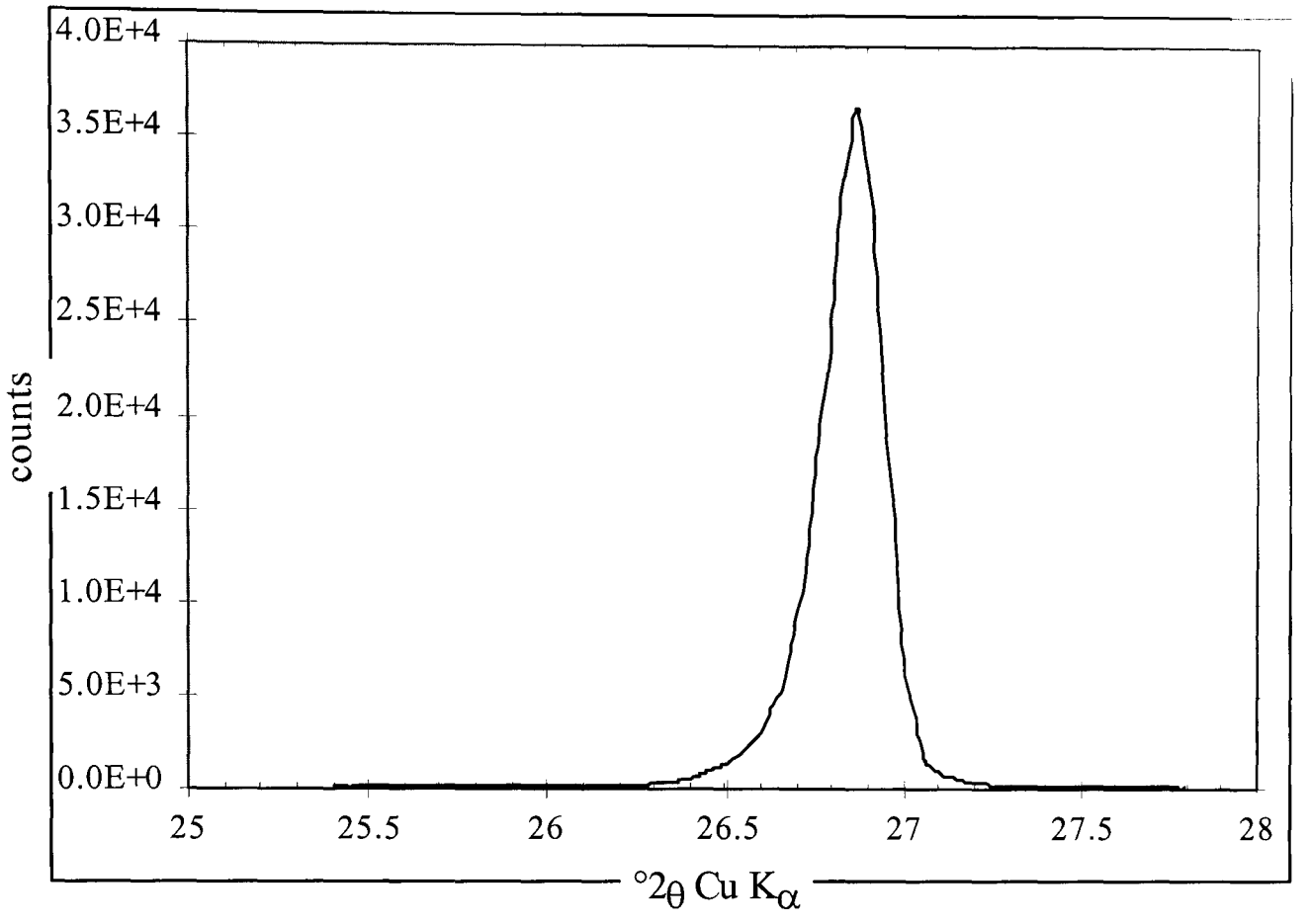

Fig. 2.3 XRD pattern of the main Arkansas Stone peak at 26.8°2θ.

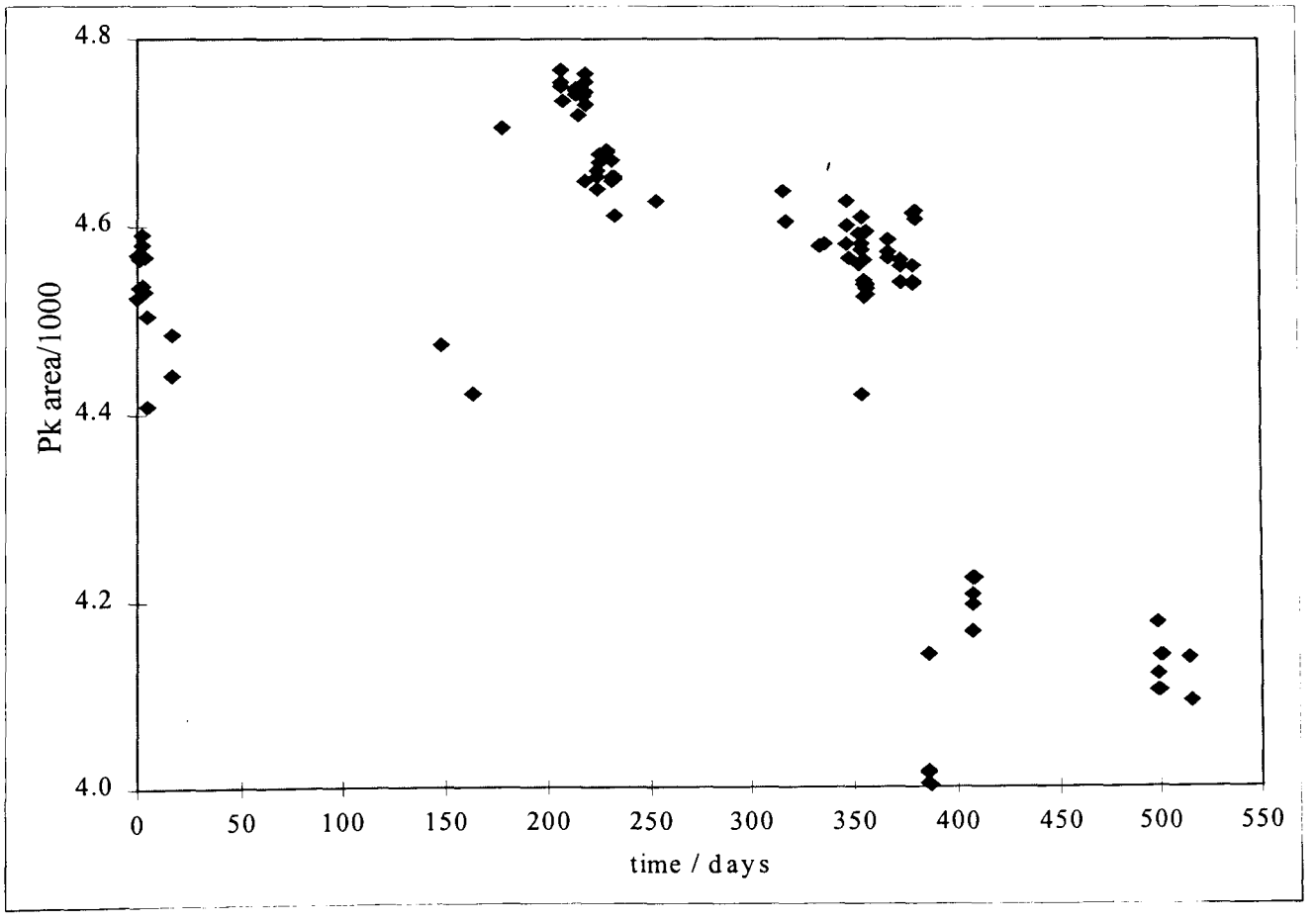

Fig. 2.4 Variation of the peak area of the main *Arkansas Stone* line against time (since Feb. 1997).

shows variations, which are sometimes considerable. The procedure used to correct for these variations was to scan the reference material, before and after scanning each MnO_x sample. Measure the peak areas of the reference and take the average, which was then used to establish a *normalisation factor*. The normalisation factor was simply the ratio of a nominal peak area of 5000 recommended by Philips* to the average value obtained. The experimental peak areas were easily obtained from APD.

This normalisation procedure generated a normalisation factor for every manganese dioxide sample. The factors ranged between 1.04 and 1.25 for extreme cases but were mostly about 1.15. Furthermore, when samples were scanned in batches, the normalisation factors were found almost identical within the batch.

The normalisation process was carried out in an appropriate software from Philips, SIMULATE. So, all XRD patterns presented here have been normalised to an incident intensity which gives 5000 arbitrary units for the area of the main Arkansas stone peak at 26.8 °2θ.

The scatter observed in Fig. 2.4 is very probably due to changing atmospheric conditions.

2.4.4 Normalisation of Position

A second normalisation concerned the position of the XRD lines. The purpose was to avoid errors due to diffractometer assignment of °2θ. The position of the lines in XRD determines d-spacing and hence, the precision of lattice parameters. Therefore, it is necessary to achieve as much accuracy as possible in the position of diffraction lines. Using the position of the 111 line of a standard XRD sample of silicon at 28.442° as a reference, it was possible to calibrate the diffractometer each time a batch of samples was to be analysed. Two different methods were employed to determine the position of the 111 line:

- **Profile Fit:** This method consisted of scanning the silicon standard then fitting the profile in order to determine the peak position (using Fit Profile function, APD program). This process was repeated, with varying the line position, until a fully reproducible value of 2θ, say V, as close to 28.442° as possible was obtained. Then (V - 28.442) was taken as the zero 2θ correction of the diffractometer.

* Telephone call to the Technical Team at Philips Analytical, Cambridge.

- **Peak Maxima:** In this method, the maximum count was searched around the theoretical peak position; first by choosing wide steps on either side of the peak. When a satisfactory value had been obtained, the steps were narrowed down and the time per step increased to collect more counts. This process was repeated until a precise and consistent (3 times) value was obtained. This value was taken and the correction of zero 2θ made as above.

Both methods were used for zero 2θ correction and usually yielded similar results. The differences in their values did not exceed 0.005°, which was the resolution of the equipment. The value yielded by the peak maxima procedure was taken for the data in this work.

2.4.5 Normalisation of Position for SBP-A and Faradiser M

The Arkansas Stone reference was scanned immediately before and after each sample. The average position of the main peak before and after, as defined by the Profile Fit method, was compared to the expected position at 26.8° 2θ. The differences could presumably be used to adjust the XRD patterns of the manganese dioxide samples to their "real" positions. These differences ranged between -0.057 and 0.069° 2θ for the samples of SBP-A and –0.048 and 0.78° 2θ for Faradiser M and are plotted against the insertion levels in Fig. 2.5.

The scatter in fig. 2.5 was not convincing to adjust the XRD patterns since only very few samples were far from the zero difference. In other words, since the "as received" data is more representatives of the samples, minor adjustments seemed unnecessary. The fact that these minor adjustments were derived from a separate material (the reference Arkansas Stone), is an additional reason to disregard them. Thus, the XRD patterns of SBP-A and Faradiser M H-inserted samples have not been corrected for position.

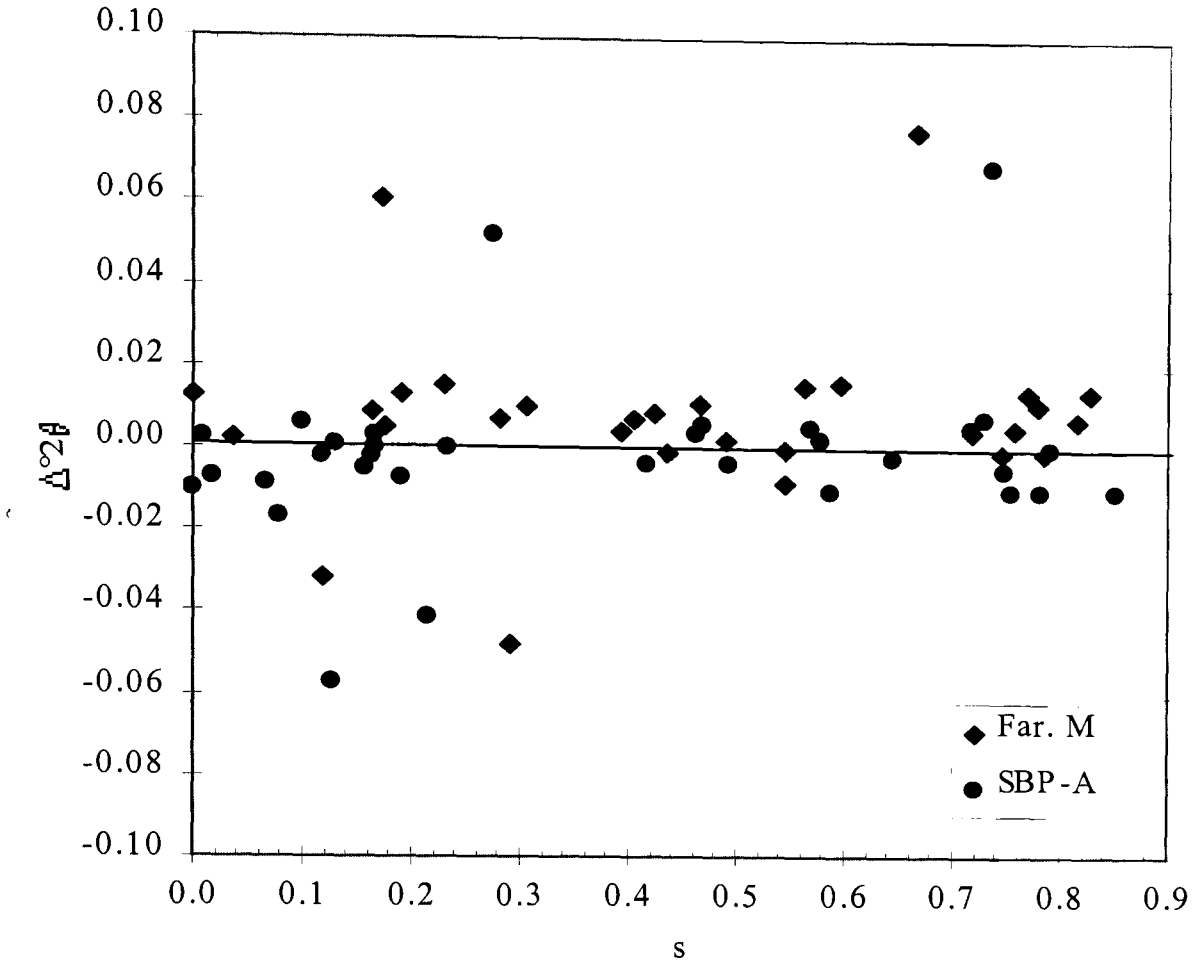

Fig. 2.5 Differences between the experimental and expected peak position of the main Arkansas Stone line at 28.6° 2θ measured with the SBP-A and Faradiser M samples.

2.4.6 Normalisation of Position of R2

Unlike SBP-A and Faradiser M, the patterns of R2 include an additional graphite impurity peak from the manufacture. Fortunately, this graphite peak can serve as an internal standard to normalise position of the entire XRD patterns of R2. The position of this additional line was determined by the following three methods and corrected, when appropriate, to the graphite position of 26.51° for 2θ Cu Kα[61]. The whole pattern was then shifted accordingly.

- **Peak Search:** This facility was available on the APD software. It consisted of detecting peaks across an XRD pattern, with regard to relevant parameters defined by the user. These include peak width (max. & min.), peak base and how the peaks are detected. In this work the following setting was chosen to detect graphite lines in R2 diffractograms.

Peak Positions defined by:	*minimum of 2nd derivative of peak*		
Minimum peak tip width:	*0.00*	*Maximum peak tip width:*	*1.00*
Peak base width:	*2.00*	*Minimum significance:*	*0.75*

The last parameter "is inversely proportional to the number of "phantom" peaks that could be found"[59]. This means simply that the smaller the value entered for this parameter then the greater the number of false peaks detected; it is a limit resolution that the user sets: 0.75 is the typical recommended value for the instrument used in this work. Greater values of the minimum significance have also been investigated, but no further improvement of the graphite line position was noted. This method which is appropriate to sharp lines was judged the most suitable for the determination of graphite line position[59].

- **Profile Fit:** This was a second facility of APD. It consisted of fitting a curve through a selected set of data points using the χ^2 goodness-of-fit test[59,60]. In this case, 300 data points around the graphite peak were chosen. Curve was fitted through the experimental data points, after specifying the tip of the peak. The program examined how far the fitting agreed with the experimental data. The number of peaks defined restricted the degrees of freedom of the test. In this procedure, one peak was searched over a sample of 300 data points, that is having 299 degrees of freedom. At only 100 degree of freedom, the fit is not significantly different at 0.5% from the experimental data, if $\chi^2 \leq 140.2$. At higher degrees of freedom, and for the same level of significance, χ^2 would take greater values.

- **Running Averages:** The XRD data was first saved in a spreadsheet and then a running average over 5 points of the counts-column calculated. This procedure aimed to minimise errors due to scattering of the XRD and helped location of the position of the maximum intensity, which was assigned, to the graphite peak. Although running averages was used previously for this purpose[42,51], the method was found to be of low reliability in this work.

From a paired comparison of the three methods using the *t*-test[60], the values of *t* (Table 2.3) showed that only Profile Fit and Peak Search could be used if a 95% confidence were sought. As the Peak Search method was more suitable and did not yield significantly different results from those obtained by the Profile Fit method, the Peak Search method were chosen.

All R2 XRD patterns presented here were shifted by the appropriate amounts, yielded by the Peak Search method, so that their graphite peaks were brought to the expected position of 26.51° for 2θ Cu Kα[61].

Table 2.3 Peak position of graphite as calculated by the three methods and their comparison for normalisation of R2.

1	2	3	4	5	6	7	8	9	10	11
Sample Code	s in MnO_nH_s	Prof. Fit	Peak. Srch.	Mov. Av.	Pr Fit –Pk Sr	Pk Sr -M Ave	Pr Fit -M Ave	PF-PS $(d-\overline{d})^2$	PS-MA $(d-\overline{d})^2$	PF-MA $(d-\overline{d})^2$
RSM	0.000	26.296	26.305	26.260	-0.009	0.045	0.036	0.000	0.010	0.005
R00	0.041	26.404	26.430	26.420	-0.026	0.010	-0.016	0.000	0.004	0.000
R06	0.181	26.326	26.355	26.280	-0.029	0.075	0.046	0.000	0.016	0.006
R07	0.316	26.217	26.215	26.160	0.002	0.055	0.057	0.001	0.012	0.008
R05	0.317	26.455	26.475	26.410	-0.020	0.065	0.045	0.000	0.014	0.006
R08	0.368	26.463	26.485	26.420	-0.022	0.065	0.043	0.000	0.014	0.006
R09	0.406	26.299	26.325	26.270	-0.026	0.055	0.029	0.000	0.012	0.004
R10	0.434	26.255	26.225	26.180	0.030	0.045	0.075	0.003	0.010	0.011
R17	0.466	26.285	26.290	26.20	-0.005	0.090	0.085	0.000	0.020	0.014
R11	0.467	26.471	26.495	26.430	-0.024	0.065	0.041	0.000	0.014	0.005
R12	0.518	26.384	26.395	26.340	-0.011	0.055	0.044	0.000	0.012	0.006
R14	0.536	26.453	26.480	26.420	-0.027	0.060	0.033	0.000	0.013	0.004
R13	0.584	26.519	26.550	26.490	-0.031	0.060	0.029	0.000	0.013	0.004
R16	0.624	26.293	26.355	26.290	-0.062	0.065	0.003	0.002	0.014	0.001
R15	0.637	26.401	26.380	26.360	0.021	0.020	0.041	0.002	0.005	0.005
R03	0.717	26.490	26.510	26.450	-0.020	0.060	0.040	0.000	0.013	0.005
R01	0.719	26.509	26.530	26.440	-0.021	0.090	0.069	0.000	0.020	0.010
R02	0.742	26.339	26.315	26.260	0.024	0.055	0.079	0.002	0.012	0.012
R04	0.823	26.599	26.655	26.580	-0.056	0.075	0.019	0.001	0.016	0.003
AVERAGES					-0.021	0.053	0.032			
VARIANCES								0.001	0.012	0.007
STANDARD DEVIATIONS								0.03064	0.11079	0.08158
							t	**-3.0577**	**2.1373**	**1.75413**

2.4.7 Deconvolution of Overlapping Peaks

As it can be seen from Fig. 1.1, the quality of the diffraction patterns of all three materials is poor compared with those of well-crystallised materials. The lines are broad and generally asymmetric. Both defects, particularly the asymmetry, are an indication of hidden lines. Hence, the observed XRD patterns cannot be relied upon for accurate analysis. It was thus essential to deconvolute the lines into their constituent peaks.

For this purpose, WinFit!, a program developed by S. Krumm* for XRD patterns analysis was employed.

*This program was a freeware available from
http://www.geol.uni-erlangen.de/html/software/Winfit/winfitnews.html

Prior to deconvolution, background scattering was subtracted from the XRD patterns. This step was important as it removed the effect of changing background on peak position and made the assumption of a constant or linear background of low slope reasonable. The deconvolution used a symmetrical Pearson VII profile for the peaks. Peak parameters such as position, width, intensity and a background function were initially specified and then adjusted when the output yielded non satisfactory results. The output of this process consisted of a set of separate peaks whose sum gave the initial XRD patterns; this output was called a *fit*.

Once the fit of a starting material was available, its peak positions were used as the starting point for deconvolution of the next more H-inserted sample and so on as long as the successive samples exhibited similar XRD patterns. This procedure allowed account to be taken of the shift of the H-inserted samples away from the original patterns of predominantly ramsdellite-like material (i.e. the starting material).

For the most H-inserted samples, the highest s value sample was first deconvoluted. The peak positions of the resulting fit were then used to start the fit of the immediately lower H-inserted samples, again as long as the samples exhibited similar XRD patterns.

2.4.8 Lattice Parameters Evaluation

Selected peak positions of ideal ramsdellite[61] were taken to deconvolute the lines of the starting material. This choice was partly justified by the fact that each ramsdellite units contain twice the number of manganese atoms as those occurring in a pyrolusite unit and partly by the values of P_r. For $P_r \sim 40\%$ (the case for SBP-A and R2), for example, there are 120 Mn atoms belonging to ramsdellite against 40 in the pyrolusite part of the intergrowth. This point is reviewed further in the following chapters (3-5).

The lattice parameters of the manganese dioxide samples were refined based on orthorhombic symmetry, as for ramsdellite. The refinement was carried out by linear multiregression on five XRD lines which are not affected by De Wolff disorder[22,18]. These are 061, 002, 221, 121 and 021 and have all (½k + l) even. The position of these lines was obtained for each sample by the deconvolution procedure described in section 2.4.7. The peak positions for all samples as well as the lattice parameters are listed in Appendices 3-5.

2.5 FTIR at Room Temperature

Since 1952, when the solid disc technique was introduced for IR spectroscopy[62,63],

there has not been an " agreed" standard procedure for the preparation of such discs. However, some common points can be gleaned from the literature. This technique involves dispersing a small amount of the sample to be examined (typically 0.5 to 1 mg) into a much larger amount (typically 100 – 200 mg) of an IR-inert salt, the matrix, usually an alkali halide and the pressing of this mixture to obtain a suitable solid disc. The choice of the matrix and the preparation of the discs are discussed in the following sections.

2.5.1 Matrix

KBr is commonly used for the preparation of solid IR discs and to such an extent that this technique is sometimes referred to as *the KBr disc technique*. The good resistance to thermal and mechanical shocks of this material[64] justified choosing it as a matrix for the study of manganese dioxide samples instead of CsI which was previously chosen (e.g. see ref. 65). Discs were made by pressing about 100 mg of spectroscopy-grade KBr (MERCK Ltd) as received with about 1 mg of the manganese dioxide sample according to the procedures described below. Discs were clear, dry and solid. When not in use the KBr was kept in an oven at 50 °C to avoid contamination from moisture. Also kept in the oven was the desiccant (di-phosphorus pentoxide Analar grade, from Merck Ltd)

2.5.2 Grinding

The sample particle size must be less than the shortest wavelength investigated, for KBr discs the recommended range is one fifth to one tenth of the shortest wavelength[66]. Larger particles lead to high background absorption, especially at high frequencies, along with skewing of normally symmetric bands at low frequencies[67,68]. Grinding of the samples was the way to meet these requirements. The grinding vessel must be stable and chemically inert vis-à-vis to the material of study. Agate pestle and mortar are widely used for grinding IR samples and are fairly easy to clean and dry after each sample; also there is no evidence of contamination to the manganese dioxide samples. By a matter of trial and error, it was found that hand grinding the manganese dioxide samples for 10 minutes in the agate pestle and mortar led to satisfactory results and this was therefore adopted in this work.

2.5.3 Mixing

About 3 mg of the ground MnO_x sample was weighed on a Cahn C-31 microbalance, with 1 μg resolution, using aluminium foil as a container. The Al foil was weighed again after tipping the MnO_x gently into a clean single-use antistatic weighing boat (from Merck Ltd), so that the exact weight could be noted. The MnO_x was then transfered into a clean and dry agate mortar. On another antistatic weighing boat, about 300 mg of KBr Spectrosol grade (from Merck Ltd) was weighed on a 1773 Sartorius analytical balance of 0.1 mg resolution. An amount of this KBr approximately equal in volume to the MnO_x, was added in the mortar and they were mixed gently WITHOUT grinding using the agate pestle.

It is very important not to grind the matrix as this may activate the alkali halide surface thereby encouraging absorption of moisture as pointed out by Faubert Maunder[69]. It is perhaps surprising that this important fact is hardly mentioned in the literature and even in more recent textbooks, the authors still advise of grinding the mixture sample-KBr[70].

When fully mixed, a further addition of KBr of similar volume to the content of the mortar was mixed as previously until the entire KBr was used. The KBr vessel was reweighed to record the exact weight mixed.

2.5.4 Pressing

The mix was then divided into three vessels with ~ 100 mg in each for making pellets-the IR discs. Discs of pure KBr were also made and have been used as reference. Their preparation procedure consisted of simply weighing ~ 300 mg of Spectrosol-grade and dividing it into three equal quantities to make the pellets as follows.

This was carried out using an evacuable pellet dies (EPD) available from Specac Ltd (Kent) and a Denison T.I.A/MC motor driven hydraulic pressure unit available from Denison & Sons Ltd (Leeds). The adopted routine, based on both the literature[66-72] and experimentation was as follows:

- Wipe the EPD with clean tissue and set up the cell.
- Fold the diamond-shaped boat containing ~100 mg of the mix and introduce it into the EPD. Tip the boat to transfer all the powder.
- Using the plunger, tap gently the EPD to level off the powder.
- Put the top die gently on the powder

- Put the plunger and press it slightly to ensure the EPD is secure.
- Connect the EPD to a vacuum line for ~3 minutes.
- Apply pressure smoothly and slowly until ~1.5 tons (0.3 ton/cm^2) was reached, then release the pressure slowly back to atmospheric condition.
- Re-apply the pressure again smoothly and slowly until ~5 tons (1 ton/cm^2) then release slowly until atmospheric.
- Re-apply the pressure again smoothly and slowly until ~10 tons (2 ton/cm^2). Keep this pressure for 2 minutes
- Remove the vacuum gently.
- Release the pressure slowly.
- Dismount the EPD and collect the pellet. Weigh and scan as soon as possible.

2.5.5 Storage

Immediately after dismounting the EPD, the disc if clear and uniform (optical microscope was used when appropriate), was stored over freshly heated silica gel in a desiccator bowl using specially designed cells. Each disc, in a cell, was weighed and scanned and the cell transferred to another desiccator bowl and stored over di-phosphorus pentoxide Analar grade (Merck Ltd) for longer periods.

2.5.6 Scanning

The pellets were scanned in a 1710 Perkin-Elmer FTIR spectrometer with the following main specifications: 1700 series optical module containing a He-Ne laser beam with a maximum output power of 5 mW, 1700 series intelligent controller module with a visual display unit (VDU) and a key pad, temperature stabilised ceramic source operating at 1400K, ordinate precision better than 0.1%, abscissa accuracy of 0.01 cm^{-1}, abscissa range: 400-4400 cm^{-1}, signal to noise ratio better than 0.1 % T peak-to-peak, beam size at focus 8mm, resolution: 1-64 cm^{-1},, scanning time: from 1sec at 4 cm^{-1}.

Scanning time is an important parameter in data collection. The more time allowed for the scan, the more data is collected and, thus, the better is the chance of obtaining reliable data. However, when the resolution is high, say 1 cm^{-1}, extended time would not necessarily be beneficial[67], especially considering that the pellet may absorb some moisture as a result of a longer exposure to air. As a compromise, the resolution was set at 1 cm^{-1} and 50 scans were carried out in about 5 minutes and their average taken

as the spectrum of a pellet. Note that there were 3 pellets for each sample.
Using the actual weights and ratios of the materials, it was possible to remove the matrix content of each pellet by subtraction of an appropriate factor of a pure matrix pellet from the sample. Spectra were saved in digital format as data files.

2.5.7 Data Processing

The matrix free data were transferred into a computer and smoothed by a factor of 4 (for data handling and to conserve disk space); this reduced the number of data-points per spectrum from 4000 to 1000. Again using the recorded weight of the sample, each pellet was normalised to 1 mg of MnO_nH_s per cm^2 of pellet. The three normalised spectra of each sample were averaged to give the final spectrum of the sample. This processing was carried out in Grams 32 V5 software (from Adept Sci.) and MS Excel spreadsheet.

2.6 FTIR at Low Temperature

2.6.1 The Low Temperature Cell

A variable temperature cell (VTC) operating in the range +250 to -196 °C was employed for the low temperature study (see Fig. 2.6). The coolant was liquid nitrogen as recommended by the manufacturer (Graseby Specac Ltd, Kent). The VTC was driven by an automatic temperature controller, with digital display of the actual and required temperatures, from the same company. A schematic representation of the VTC is reproduced here, from Issue 6 of the Operating Manual of the VTC[73]. The VTC worked as follows: the sample was mounted in a sample holder (20) which was fitted in the bottom of the refrigerant chamber (16) while located within the vacuum tight jacket (2). Suitable IR-transparent windows (NaCl in this work) were used to seal off the sample and obtain suitable vacuum by connecting the VTC to a vacuum pump (5). All connections were tightly secured and, when appropriate, vacuum grease used to ensure good and tight thermal conduction [e.g. the sample holder and the O ring (12)]. Thermocouple feedback to the Automatic Temperature Controller (ATC), provided through port (40), enabled the control and monitoring of the sample temperature while the windows were warmed through the socket 21 to avoid fogging and condensation. After evacuation, liquid nitrogen and accessories (7 and/or 42) were introduced in the refrigerant chamber, which was then closed with the bung (8).

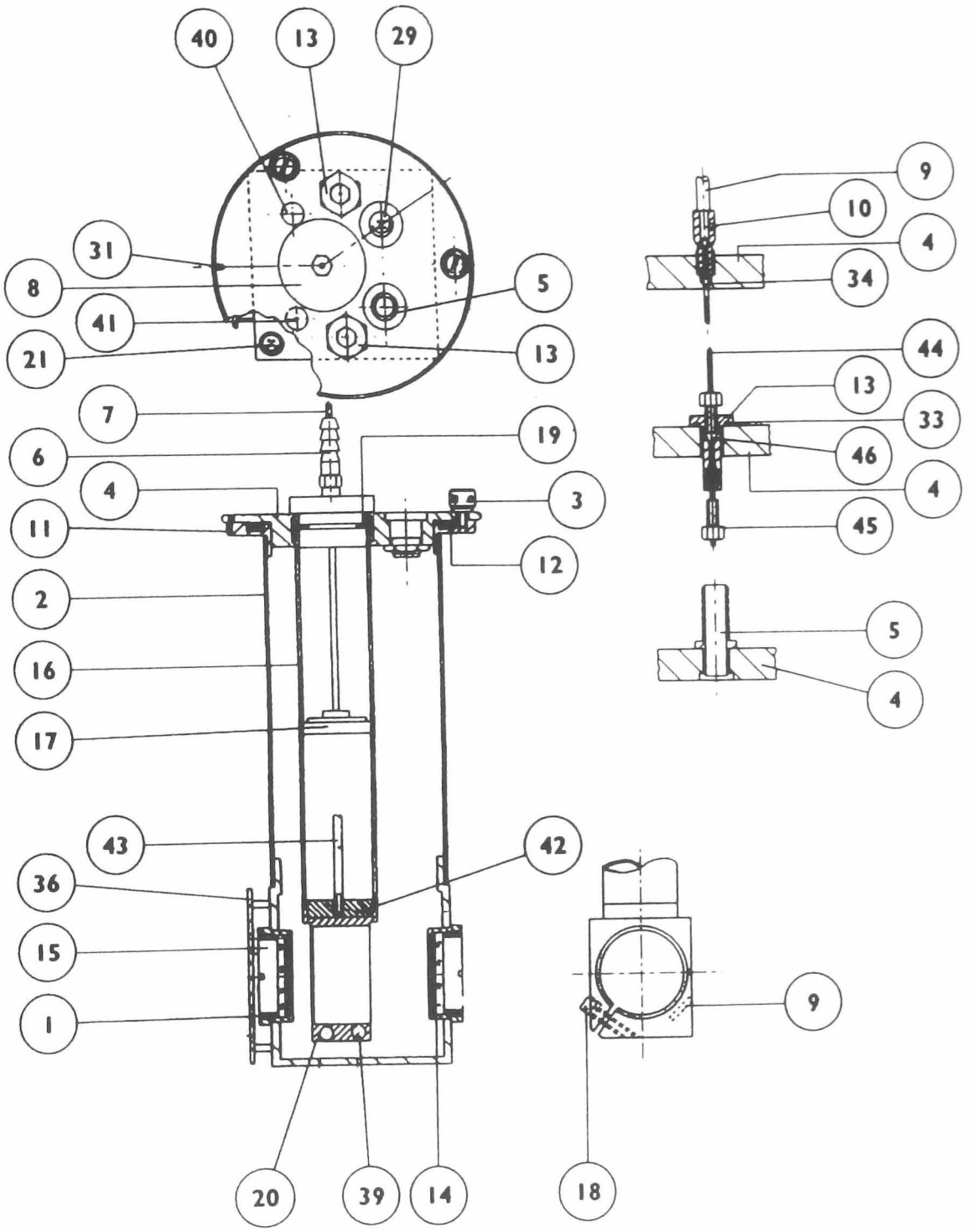

Fig. 2.6 Variable Temperature Cell (reproduced from "Variable Temperature CellOperating Manual,Issue 6, p.13", Graseby Specac Ltd, Kent, England). 1. Silicon Elastomer seal, 2. Vacuum tight jacket, 3. Thumb screws to hold top plate, 4. Top plate of cryostat unit, 5. Vacuum pump connection, 6. Metal venting bung, 7. "Mushroom" piston, 8. Refrigerent chamber bung, 9. Copper-Constantan thermocouple and thermocouple well, 10. Screw plug for thermocouple, 11. Locating pin for top plate, 12. 'O' ring retaining groove of top plate, 13. Flow through connector ports, 14. Jacket window, 15. Screw threaded retraining ring, 16. Refrigerent chamber, 17. Polyurethane foam layer of "mushroom", 18. Clamp screw of cell holder, 19. 'O' ring groove for bung, 20. Cell holder, 21. Latching sockets for windows, 29. Electrical leads socket for cell holder, 31. Pin locating slot on top plate, 33. 'O' ring for connector ports, 34. Silicon Elastomer seal for thermocouple, 36. 3" x 2" mounting plate, 39. Heaters for sample holder, 40. Thermocouple port for cell holder, 41. Extra access port, 42. Stailess steel 'drop disc', 43. Stailess steel threaded rod for 'drop dis', 44. Stailess steel rod for plugging flow through connector ports, 46. Ferrule seal.

Evaporated nitrogen escaped from venting tube (6) and was conducted away from the spectrometer via a rubber tube.

2.6.2 The Vacuum

Before cooling the cell, a high vacuum was necessary to isolate the windows (required to be above ambient temperature to avoid fogging) from the cell (temperature down to –196 °C). A vacuum of 0.067 mbar (or better) was recommended[73]. In this study, no pressure lower than ~ 0.4 mbar could be reached, with the available equipment and the ATC was set to the lowest limit, -250 °C to avoid any unwanted heating. However, the lowest temperature was only -180 °C instead of -196 °C, reachable with liquid nitrogen. Nevertheless, this temperature was sufficiently low to affect one of the materials studied here, R2 (Chapter 6).

2.6.3 Scanning

Upon refrigerating, the cell temperature decreased quite dramatically, especially at the beginning, down to -172 °C. Hereafter, the rate of decrease was much slower. This means that for the higher low temperatures only a few scans could be done before the temperature changed while more scans were possible at lower temperatures. To be consistent, the same number of scans, 5, has been applied to all samples. No significant difference was observed from a greater number of scans.

2.6.4 Samples

Selected pellets used for the room temperature study have been used for the low temperature too. Prior to scanning samples, the NaCl windows were scanned both at room and low temperatures to ensure that no fogging or other impurity contaminated them. This also showed that the accessible range of wavenumber, using NaCl windows, was approximately 800 to 4400 cm^{-1}; see Fig. 2.7.

The selected pellets included the starting materials, solvent affected samples (section 2.2.4), the most H-inserted samples, and a few other materials carefully selected to reflect the behaviour during all levels of H-insertion. This choice enabled observed changes to be linked to the appropriate circumstances. The results are reported in Chapter 6.

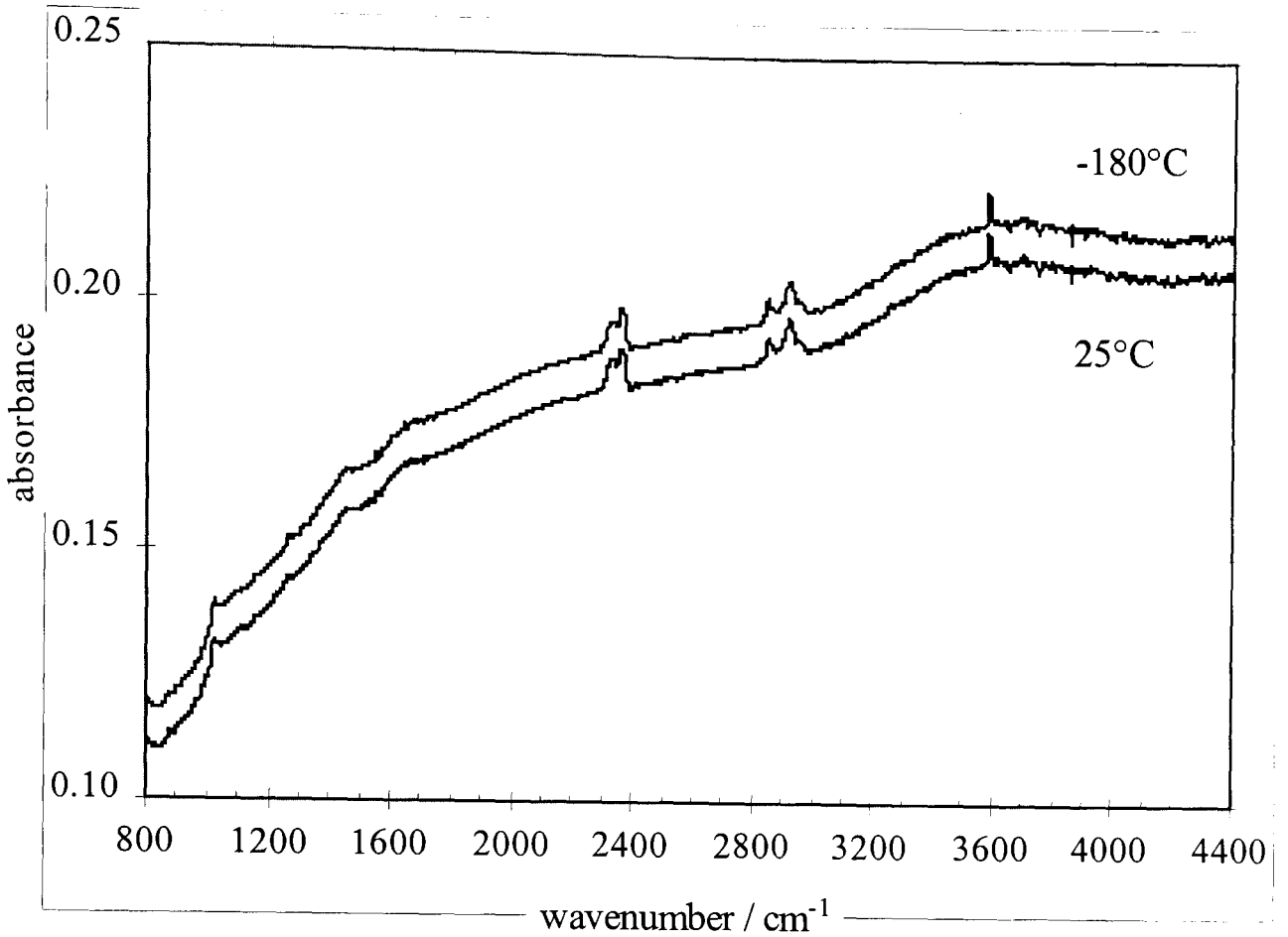

Fig. 2.7 FTIR spectra of NaCl windows used in the VTC at 25° and –180° C at enlarged scale.

2.7 Electrode Potential Measurement

The literature[39-41,43-47,74-77] shows extensive studies of the potential of manganese dioxide. Some difficulties in obtaining reproducible electrode potential of this material have been reported, particularly in alkaline electrolyte[43]. Although not all the literature gives full descriptions of the experimental details, some[e.g.39,43,76] of the arrangements for potential measurement of manganese dioxide consisted of a current collector (usually Pt) in contact with the manganese dioxide and a reference electrode immersed in the same electrolyte solution. This approach has the advantage of eliminating complications due to the reaction at the zinc electrode and possible local undesirable reactions if a battery were used. However, its main disadvantage is the continuous fluctuations rendering the potential measurement close to unreliable. MacLean[21], for instance, reported a "stabilisation time" of up to 2 hours to reach fluctuations of less than 0.1 mV in 5 minutes.

On the other hand, none has reported problems in measuring the potential of a battery.

Thus, if the undesirable reactions in a battery could be controlled, a measurement of open-circuit battery voltage could lead to a reliable estimate of manganese dioxide potential.

In this work, the potential of γ-manganese dioxide has been investigated in Leclanché battery environment throughout the H-insertion, range $0 \leq s \leq 0.9$ (s in MnO_nH_s), for the three materials studied. This choice meant that additional chemical entities (such as the electrolyte, the other electrode) must be considered. The overall reaction of the battery may be written as:[81-83]

$$2MnO_nH_{\alpha\,(ss)} + \beta Zn_{(s)} + 2\beta NH_4Cl_{(s)} \rightarrow 2MnO_nH_{\alpha+\beta(ss)} + \beta Zn(NH_3)_2Cl_{2(s)} \qquad (2.7)$$

where the subscripts s and ss stand for solid and solid solution respectively.

The potential is related to the Gibbs free energy change (ΔG) by:

$$\Delta G = -nFE \qquad (2.8)$$

where F is the Faraday, n the number of electron and E the potential.

Although (2.7) is the overall reaction in a Leclanché battery, it does not show readily the parameters to be considered for satisfactory measurement of the ΔG variations of the species. The half-cell reactions, however, reveal directly the variables involved. The half-cell reaction of the manganese dioxide electrode is looked at first:

$$(MnO_n)_{ss} + \alpha H^+ + \alpha e \rightarrow (MnO_nH_\alpha)_{ss} \qquad (2.9)$$

The Gibbs free energy change for reaction (2.9) is:

$$G^0_{(MnO_nH_\alpha)_{ss}} - G^0_{(MnO_n)_{ss}} + RT\ln\frac{a_{(MnO_nH_\alpha)_{ss}}}{a_{(MnO_n)_{ss}}} - RT\ln a_{H^+} \qquad (2.10)$$

G^0 is the standard Gibbs free energy of the subscripts and a the activity.

The Gibbs free energy change of reaction (2.9) is clearly dependent on the ratio of MnO_n to MnO_nH_α; i.e. the composition of the manganese oxyhydroxide solid solution as well as to the pH.

The half-cell reaction of the zinc electrode, in the Leclanché battery is:

$$Zn + 2NH_4Cl \rightarrow Zn(NH_3)_2Cl_2 + 2H^+ + 2e \quad (2.11)$$

The ΔG of reaction (2.11) could be simplified by saturating the electrolyte with both NH_4Cl and $Zn(NH_3)_2Cl_2$, in which case the ΔG (and the zinc potential) becomes only dependent on pH; i.e.

$$\Delta G = \text{Const.} + 2RT\ln a_{H+} \quad (2.12)$$

Const. is a constant term containing the ΔG^0 of the constituents of (2.11).

Thus, for satisfactory measurement of potential of reaction (2.7), which is the sum of (2.9) and (2.11), it is necessary to control the pH, the composition of the manganese dioxide phase and to keep the electrolyte saturated with NH_4Cl and $Zn(NH_3)_2Cl_2$. These were the conditions of potential measurement observed in this work and are detailed in the following section.

2.7.1 Condition of Potential Measurement

At a given insertion level, the manganese oxyhydroxide phase should presumably be constant. However, previous studies[39-41] showed that unless precautions are taken, a side reaction (2.13) altered the composition of the solid solution.

$$2MnOOH + 2H^+ \leftrightarrow MnO_2 + Mn^{2+} + 2H_2O \quad (2.13)$$

Reaction (2.13) means that an acidic medium will cause the Mn(III) to disproportionate into Mn(II) and Mn(IV). Hence maintaining the pH constant at a suitable value is an absolute necessity if reliable potential is sought.

An additional cause of composition change of the manganese dioxide solid solution phase is ion exchange as previously reported[80]. The ion exchange between water adsorbed on the MnO_2 and a cation M^{k+} can be written as:

$$kMnO_2 \bullet HOH + M^{k+} \leftrightarrow (MnO_2 \bullet HO^-)_k M^{k+} + kH^+ \quad (2.14)$$

Similarly to (2.13), reaction (2.14) can be controlled by keeping the pH at a

sufficiently high and constant value.

If reactions (2.13) and (2.14) decrease significantly the pH of the electrolyte, the zinc electrode may be attacked, which is a further error on the potential determination.

Thus, fixing the pH of the electrolyte is the main requirement for a fix manganese oxyhydroxide composition and is the key to successful potential determination of the manganese dioxide electrode [equation (2.10)].

As for the zinc electrode, saturation of the electrolyte with NH_4Cl and $Zn(NH_3)_2Cl_2$, in addition to the fix pH, is the main requirement for reliable potential.

2.7.2 The electrolyte

The electrolyte was a 1.8 molal solution of zinc chloride in which solid ammonium chloride was dissolved until saturation (solid NH_4Cl precipitated in the solution). The exact weight of ammonium chloride was recorded. This solution was then titrated by solid ZnO until the pH was fully buffered. Therefore, the electrolyte meets fully the requirements for satisfactory measurement of the zinc potential set out above, and partially fulfils the conditions for the manganese dioxide electrode through the buffered pH. Fig. 2.8 shows the evolution of pH with addition of solid ZnO. Both, the pH and the amount of ZnO added were noted.

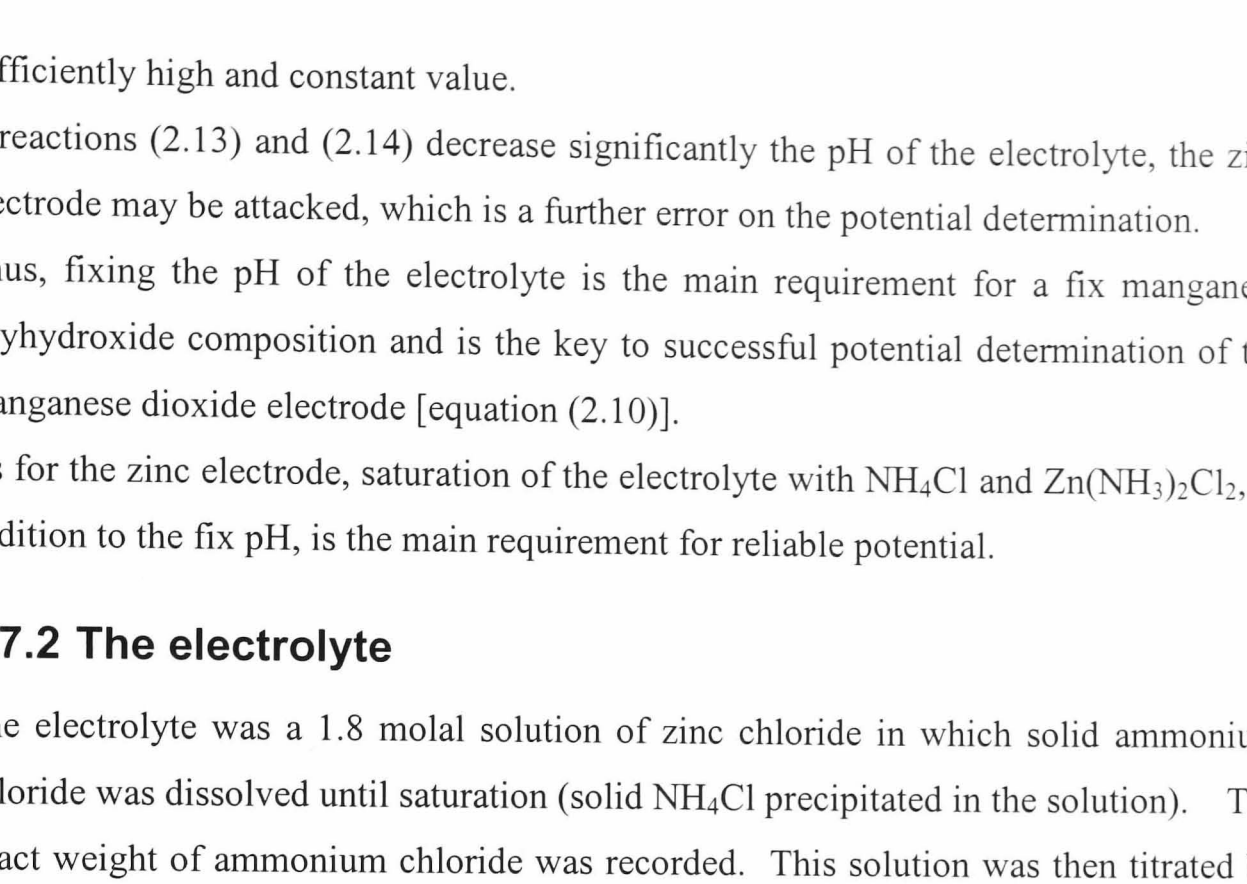

Fig. 2.8 pH buffering of the Leclanché electrolyte.

2.7.3 The Cathode Mix

The manganese dioxide electrode consisted of a mixture of manganese dioxide powder and other products designed to meet the precautions outlined in section 2.7.1. These were:

- **Carbon black:** The beneficial effect of carbon with regard to improving the electric conductivity of a manganese dioxide cathode mix has been known since Leclanché's first pile[2]. Caudle et al.[84] investigated interactions between carbon and manganese dioxide and their study has shown that the potential of MnO_2 decreases as the ratio C:MnO_2 increases. Therefore, a compromise must be reached whereby enough carbon is added to improve the electronic conductivity, but in small amount so as to reduce interaction with the manganese dioxide. Although the ratio C:MnO_2 was not investigated in this work, the value of 10% w/w C:MnO_2; has been chosen since it is close to the ratio used in the battery industry[77].
- **NH_4Cl & ZnO:** Both compounds are involved in the electrolyte and their lack (or low concentration) may alter the activity of Zn^{2+} or the pH which results in erroneous data. Presence of both compounds in solid form was required to meet the conditions of potential measurement. The ZnO would prevent pH from dropping within the cathode mix, thereby inhibiting reactions (2.13) and (2.14) and counteracting the effect of ion exchange. The ammonium chloride would help to maintain a saturated electrolyte. These conditions meant that no ion other than H^+ was able to exchange with the manganese dioxide surface as previously[40,41,76] recommended to obtain reliable data. The w/w ratios of these materials with respect to manganese dioxide were 10 and 4% for NH_4Cl and ZnO respectively.

This mix, called dry mix, was stored in a suitable sample bottle and allowed one week to settle in terms of ion exchange.

- **Electrolyte:** The dry mix was wetted by addition of a few drops of the electrolyte in a sample bottle of suitable size, and shaken until the mix became consistent. Minimising the amount of added electrolyte was a recommended precaution[39] to minimise (or avoid) self-decomposition of manganese dioxide by reaction (2.13). Note was taken of the amount of electrolyte added, and this was investigated on a few samples of the starting materials varying each time the amount of electrolyte added. The minimum ratio that gave reproducible potential data was chosen for each material.

The average composition of the cathode mix, for each set of samples, is given in Table 2.4

Table 2.4 Average composition of cathode mix in % w/w of MnOx

Material	$ZnCl_2$	NH_4Cl	ZnO	H_2O	C Black
SBP-A	7.7	22.6	5.0	31.5	9.9
Faradiser	12.4	30.6	5.9	50.5	10.0
R2	10.1	26.6	5.3	41.2	9.5

2.7.2 Mounting the Cell

The cathode mix was kept in a sealed sample bottle for at least 24 hours to ensure good ion exchange between the components and was then introduced into an R6-sized[77] zinc can with paper separator on its inner wall and a bottom washer. The mouth of the can was covered with a layer of cling film to avoid direct contact between the zinc and the cathode mix (short-circuit). The cathode mix was then pushed gently in the bottom of the can to ensure consistency before a carbon rod, held through a cylindrical piece of polystyrene (of the same diameter as the Zn can), was introduced. At the top of the zinc can, the cell was sealed with sealant provided by a battery company. Finally, the cell was covered by a plastic jacket and the tip of the carbon rod covered with a metallic cap (Fig. 2.9).

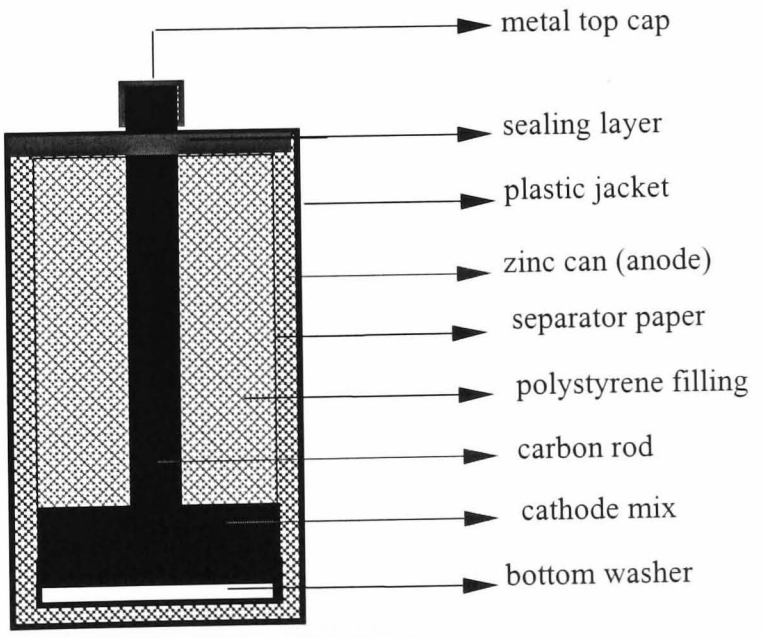

Fig. 2.9: Schematic representation of the R6 cell used for the potential measurement.

All cells were kept in paraffin oil in a water bath at 25 ± 0.1 °C and their OCVs

measured daily for at least 25 days. The polystyrene piece aimed to reduce the volume of oxygen incorporated in the cell whilst the sealing and the oil bath stopped any further oxygen ingress.

2.7.3 Monitoring The OCV

Observation of the OCVs of the cells revealed two types of behaviour: the starting and slightly H-inserted materials showed an increasing OCV over the first 7 days, and decreased thereafter (Fig 2.10). The higher H-inserted materials behaved similarly in the first week but tended to keep their OCVs constant at the value obtained after 7 days thereafter (Fig. 2.11). The increase of OCVs in the first week (part AB, Figs 2.10 & 2.11) was due to the consumption of oxygen incorporated in the cell. This oxygen would oxidise locally the zinc can making its potential higher, thus decreasing the OCV. As the oxygen was consumed, the Zn potential moved back to its initial value (less anodic) which resulted in increasing the OCV. By 7 days, all the available oxygen had been consumed and the zinc potential was expected to stabilise. It was then expected that the OCV would remain constant so long as the composition of the electrodes did not alter. This behaviour was shown by the higher H-inserted materials (BD of Fig. 2.11). However, the lower H-inserted samples behaved differently (BC of Fig. 2.10) and it is not clear why their OCVs decreased. Although this decrease was not more than 6 mV a day, it contrasted sharply with the OCVs of the higher H-inserted samples.

2.7.4 Correction for Zn Potential

The OCV is the potential difference between the two electrodes as described by eq. (2.7). To reach the MnO_x potential, the Zn potential must be subtracted. A similar assembly to that used by Larcin[82,83], was employed to measure the Zn potential under similar conditions to that present in the batteries. A zinc can of R20 size[77] (from the same supplier of the R6 can) was used for this experiment as the R6 can was too small. The assembly is shown in Fig. 2.12, and consisted of a zinc can (with separator and bottom washer) containing some electrolyte in which a Saturated Calomel Electrode (SCE) was immersed. Also immersed in the electrolyte was a tube through which nitrogen was bubbled in order to remove dissolved oxygen from the electrolyte. The test tube (containing the same solution as the zinc can) aimed to avoid loss of concentration of the electrolyte due to direct bubbling of nitrogen into the zinc can.

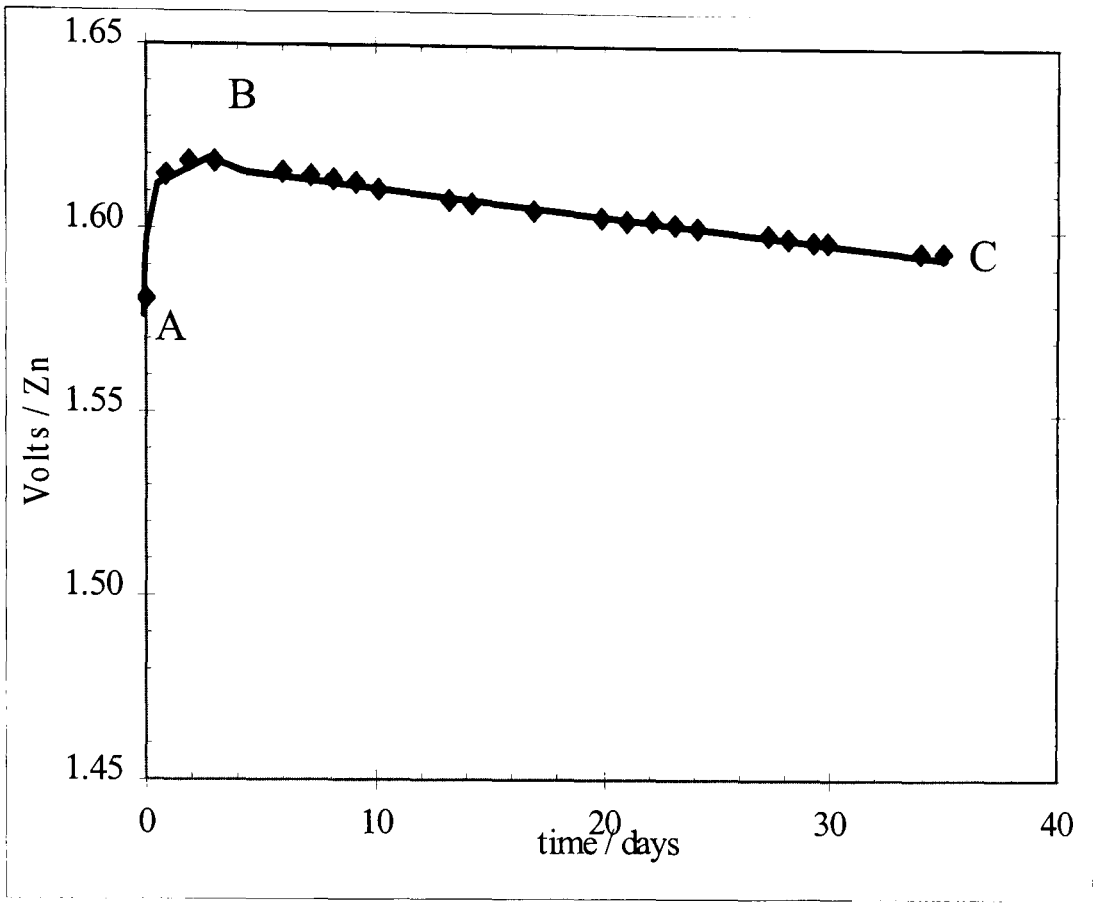

Fig. 2.10: Evolution of potential of Faradiser M starting material.

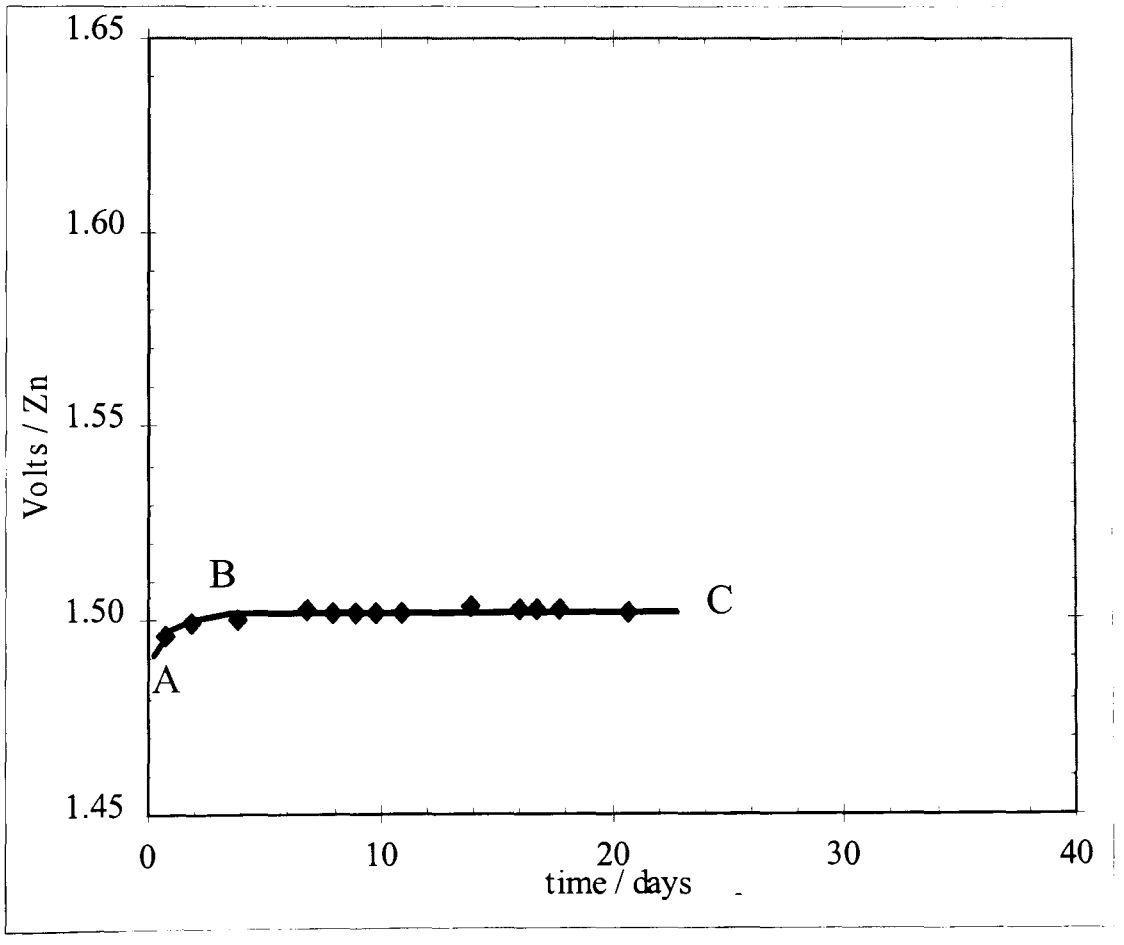

Fig. 2.11: Evolution of potential of a H-inserted Faradiser M sample, s = 0.757.

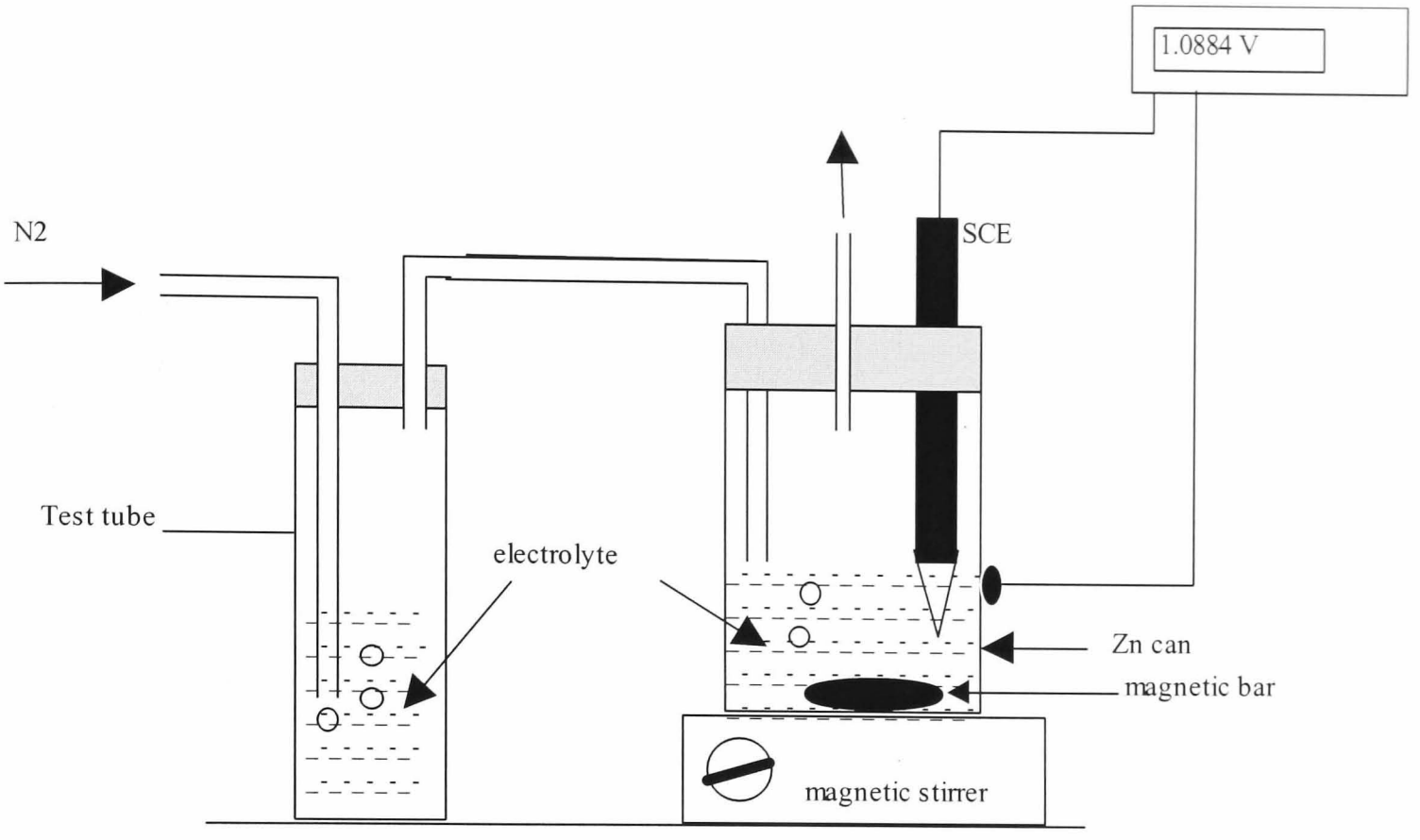

Fig. 2.12: The assembly used to determine Zn potential

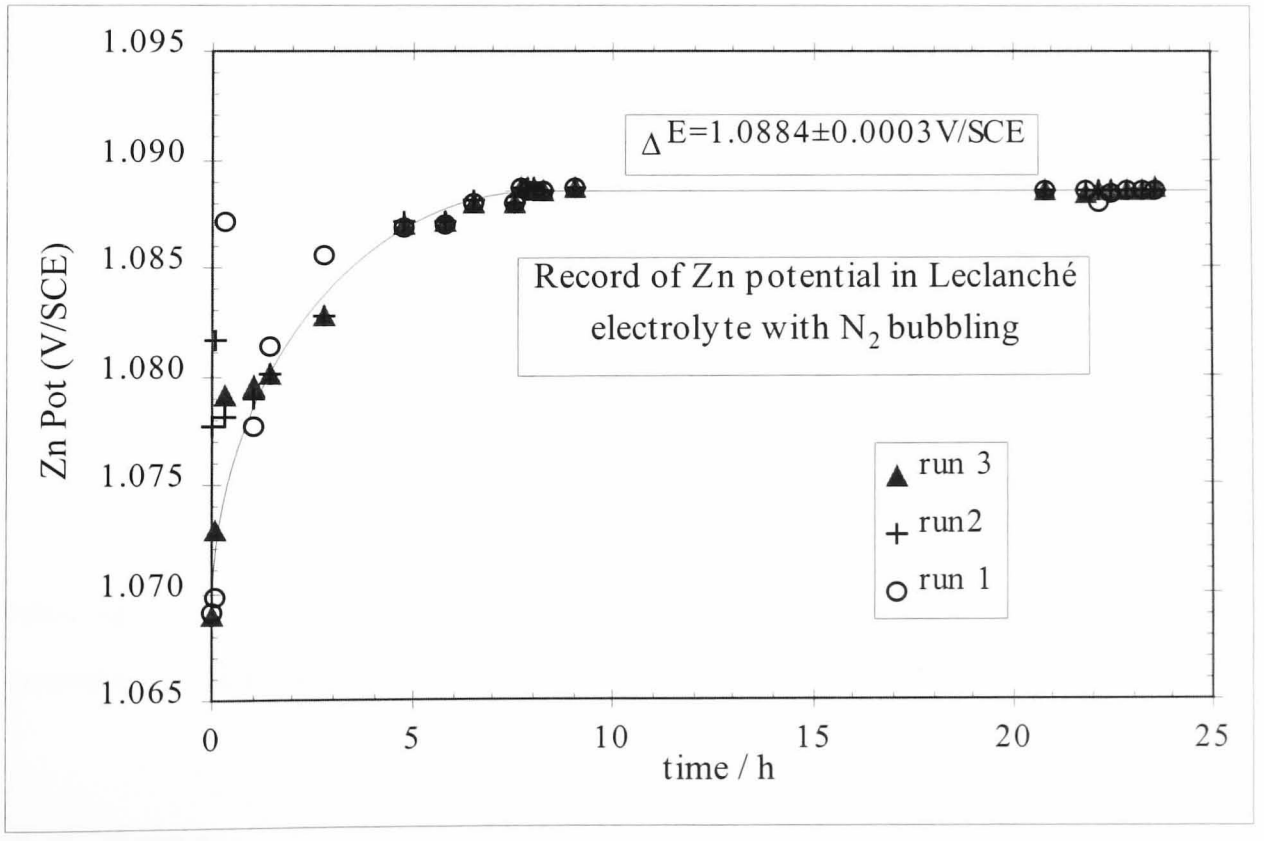

Fig. 2.13: Evolution of zinc potential against time.

After 15 minutes of bubbling through the test tube alone, the nitrogen was introduced to the zinc can. The potential of the zinc electrode was then measured against SCE as shown on Fig. 2.13.

This experiment was repeated three times and gave reproducible results. Omitting the first part of the curve due to the presence of oxygen (~ 7 hours), the Zn potential was very stable and the average value of the three runs carried out here gave 1.0884 Volts versus SCE.

2.7.5 Calculation of MnO_x Potential

Observation of the potential traces shown in Figs. 2.10 & 2.11 suggested that a more representative OCV could be obtained by extrapolation of the BC section of the trace back to zero time, assuming a linear regression. So, at the end of each measurement period of at least 25 days, the data of the first week was omitted and a regression line was fitted through the remaining data points. The value at zero time was then estimated. From this value, the potential of the manganese dioxide material was easily calculated by subtracting the Zn potential. Finally, the potential data was presented against the Standard Hydrogen Electrode (SHE). In summary, the procedure was as follows:

$$MnO_x - Zn = OCV \quad (2.15)$$

$$Zn - SCE = -1.0884\ V \quad (2.16)$$

$$SCE - SHE = 0.2458 + 0.0592pH \quad (2.17)$$

$$MnO_x - SHE = OCV - 0.8426 + 0.0592pH \quad (2.18)$$

or,

$$\mathbf{MnO_x - SHE = OCV - 0.51108} \quad \mathbf{(2.19)}$$

with pH of 5.6 (Fig. 2.8). This formula was used to convert the OCV to MnO_x potential vs. SHE for all samples.

2.8 SEM

Occasionally, an SEM study was carried out to investigate the morphology of selected samples when further information was sought. The equipment used was a

Stereoscan 240 (Cambridge Scientific Instruments Ltd.) scanning electron microscope.

The instrument was also equipped with an AM 1085 Energy Dispersive X-ray Spectrometer (EDX) for elemental analysis

2.8.1 Sample Preparation

Thin layer of carbon cement was spread on the surface of an SEM aluminium stub (Agar Scientific) to collect a sample of manganese dioxide that had been spread on a flat glass slide. The stub, when dried, was coated with a thin layer of gold by vacuum evaporation[78]. This coating was necessary for specimens which were poor electronic conductors, such as manganese dioxide. The gold layer aimed to conduct away the excess charge of the incident beam through the stub, giving better visualisation of the morphology of the samples. However, the gold layer was very thin so as not to mask the morphology of the specimen; a typical thickness of this layer was 10 nm. The low pressure reached for the vacuum evaporation was of the order of 0.1 torr and the evaporation lasted for a few seconds. Pumping down to such a low pressure took 8-10 minutes.

The specimen was then mounted into the specimen chamber of the SEM and fixed carefully to ensure appropriate electron conductance for good SEM images.

2.8.2 Images

The instrument was set at 30 kV for the acceleration voltage of the tungsten filament. Mechanical controls enabling the adjustment of sample position, magnification, resolution and working distance (WD)* were used to investigate the morphology of specimens. First, magnification was set low to see the whole specimen; then gradually increased for closer examination. Representative images of appropriate areas were then taken as black and white photos on an A52 Polaroid film (KJP Ltd.).

2.8.3 EDX

"Whenever electrons with several kilovolts of energy strike a solid specimen, X-rays characteristic of the atoms present in the specimen are produced"[79]. As the

* Working Distance is the distance between the surface of the specimen and the last lens of the incident beam, and is expressed in mm.

accelerating voltage was set at 30 kV, it was possible to use the AM 1085 Energy Dispersive X-ray Spectrometer (EDX) facility for elemental analysis.

The output of this technique was a spectrum of peaks whose heights (and areas) are proportional to the concentration of elements they represent, provided that the X-ray lines are of the same series (K, L, ...) as the required energy to excite each series is different. In this study, since the only element expected to be detectable in the working conditions was Mn, the EDX was used rather as an occasional tool to prove that no unwanted elements were present in the SEM pictures.

3 XRD & FTIR Study of SBP-A

3.1 Introduction

The low microtwinning and predominance of Mn atoms belonging to ramsdellite blocks (74%)[37] make SBP-A a γ-MnO_2 relatively close to the ramsdellite limit (see section 1.2). The remaining fraction of manganese atoms are part of the pyrolusite structure. Based on the ramsdellite structure, MacLean and Tye[37] developed recently a two-parameter approach, which enabled them to explain changes in both XRD patterns and FTIR spectra of this material during H-insertion. Furthermore, the approach may be extended to other γ-manganese dioxide varieties. Their hypothesis is outlined below and is then applied in the interpretation of the data collected in this work. This development was possible due to the multiple XRD lines, which were relatively sharp available from SBP-A in contrast with the few broad lines typical of EMD. The pyrolusite part is thought to undergo changes to match the ramsdellite part; particularly in the *a* direction. Changes in the pyrolusite part are discussed further in chapter 4.

3.1.1 The Expansion-Rotation Hypothesis

This hypothesis can easily be understood from Fig. 3.1 and Fig. 3.3. Fig. 3.1 shows a superposition of the ramsdellite and groutite structures in the *ab* plane, centred on a corner connection. It can be seen that the two structures exhibit different rotations about the common origin and have different octahedral size. Fig. 3.3 aligns the two octahedra along their apical lines (see Fig. 3.2 for identification of apical lines) and shows immediately that the octahedra in groutite are larger (expanded) compared with those in ramsdellite.

The angles and distances of the ramsdellite and groutite structures are given in Table 3.1. As the H-insertion (reaction 2.1) transforms ramsdellite blocks into groutite, the fully H-inserted product must have undergone some rotation and expansion to turn into the groutite structure.

From Table 3.1, Fig. 3.1 and Fig. 3.3, the major changes which occur to ramsdellite structure are an expansion of 18.7% in the apical distance (i.e. FC) and a decrease of its angle with the *b* axis of about 19°. Hence, the expansion-rotation hypothesis refers essentially to the apical line. The H-insertion consists of capturing electrons by the Mn

atoms in the centres of the octahedra and inserting the associated protons in the tunnels. The capture of electrons results in an increase in the radius of the manganese cations which require an expansion of the octahedra to accommodate the Mn^{3+}'s.

Table 3.1 distances and angles of ramsdellite and groutite as drawn in Figs. 3.1 and 3.3 and derived from ref.'s 19 & 37. Lattice parameters are also included.

RAMSDELLITE				**GROUTITE**				
Distances / Å		angles / ° in Fig. 3.1		distances / Å		angles / ° in		
							Fig. 3.1	Fig. 3.3
FD	2.3106	OFD	13.847	FD	2.6056	OFD	0.682	17.725
FC	3.7727	OFC	40.817	FC	4.4769	OFC	23.774	40.817
FH	2.3134	OFH	78.442	FH	2.6509	OFH	59.325	76.368
lattice parameters / Å								
A	4.533			*a*	4.560			
B	9.270			*b*	10.70			
C	2.870			*c*	2.850			

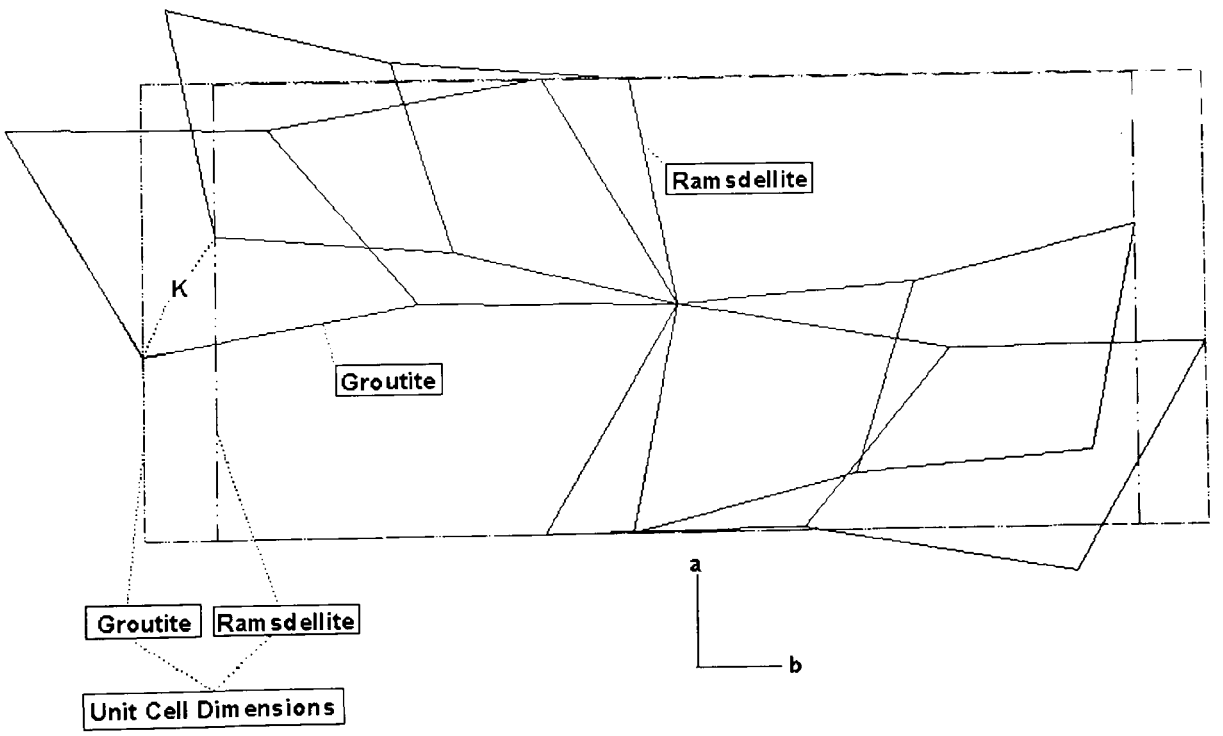

Fig. 3.1 Comparison of groutite and manganite projection on the ab plane (Fig. 12 of ref. 37)

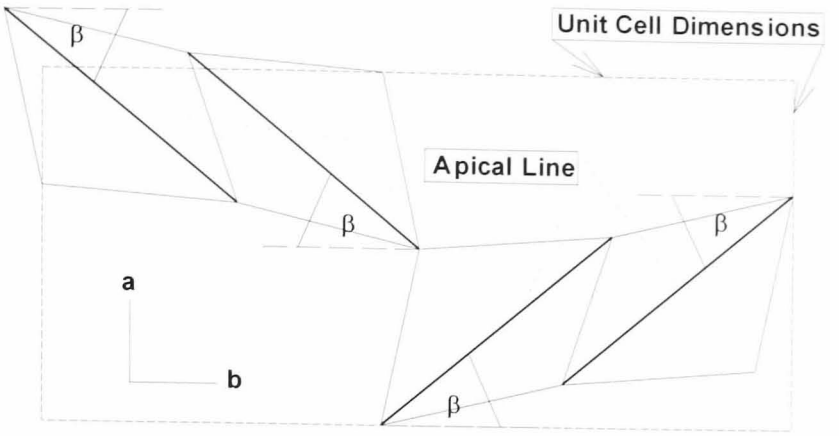

Fig. 3.2 Identification of apical line and rotation angle β. (Fig. 1 of ref. 38)

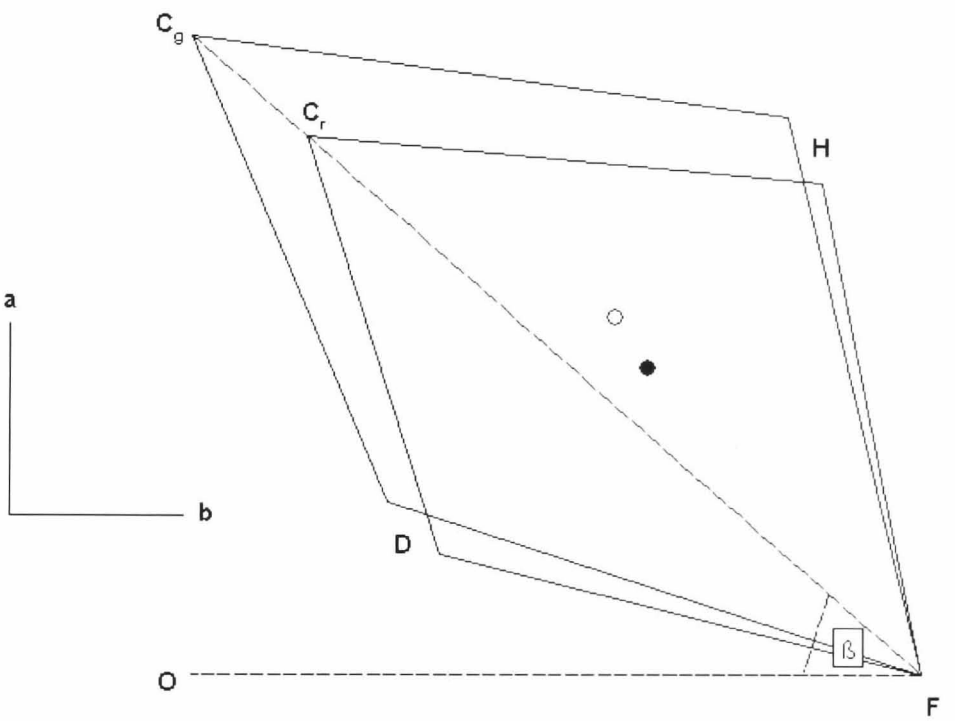

Fig. 3.3 Groutite and ramsdellite octahedra aligned on their apical lines. (fig. 13 of ref. 37)

Also, the new electron configuration of d^4 of the Mn^{3+} would engender a moderate Jahn-Teller distortion producing a more stable d_z^2 orbital[91]; which is oriented in the direction of the apical oxygens. This is a further good reason to concentrate the study of the expansion of the octahedra to the apical expansion.

Consideration of Fig. 3.1 reveals that the rotation of the ramsdellite-like blocks occurs in opposite directions. So if a block rotates clockwise, the four adjacent corner-connected blocks rotate anticlockwise and so on throughout the structure. The axes of rotation connect the corners of the blocks and run parallel to the *c* axis. This

movement was described as hinging[37] around these axes. Quantitatively, the rotation is measured by the angle β (hinging angle) that the apical line makes with the *b* axis (Fig. 3.2).

The structure of each H-inserted sample, thus, could be characterised by its percentage of apical expansion above the apical distance in ramsdellite, z, and a rotation angle, β. Starting from ramsdellite values of z and β, MacLean and Tye[37] developed a structural map linking these two parameters to the unit cell dimensions of each sample.

3.1.2 Structural Map

Due to the fact that the rotation is around the *c* axis, the apical expansion is perpandicular to the *c* axis and also that the *c* dimension changes only slightly between ramsdellite and groutite (see Table 3.1), the structural changes accompanying the H-insertion can be studied in the *ab* plane. This reduces the problem to two dimensions. The hinging angle in fully H-inserted groutite is 23.774° vs. 40.817° in ramsdellite while z is 18.67% larger in groutite than the z for ramsdellite (Table 3.1). By considering Fig. 3.3 (or Fig. 3.1), it can be seen that if the co-ordinates of points C, H, D and K are known, then so are the angles CFO, HFO, DFO and KFO. By increasing the length FC of the ramsdellite part by increments of 2% and working out the corresponding lengths of FD, FH,...using linear interpolation, it was possible to construct a grid showing the effects of z and the hinging angle β on the lattice parameters *a* and *b*[37]. This grid is reproduced here with increments of 1% and 1° in z and β respectively (see Fig. 3.4). Putting the *a* and *b* lattice parameters of SBP-A (and other MnO_x) samples on the structural map reveals directly their z and β values and considerably aids interpretation of H-insertion.

3.2 Results of the XRD Study of SBP-A

Thirty-four samples of SBP-A material were H-inserted as described in section 2.2. The H-insertion range covered zero to 0.851 in s in $MnO_{1.971}H_s$ i.e. about 90% of the full theoretical fill*. The XRD study outlined in section 2.4 was carried out for all the samples and the results of selected samples are presented in Fig. 3.5.

---

* The theoretical fill is $s_{max} = 1 - 2(2 - 1.971) = 0.942$

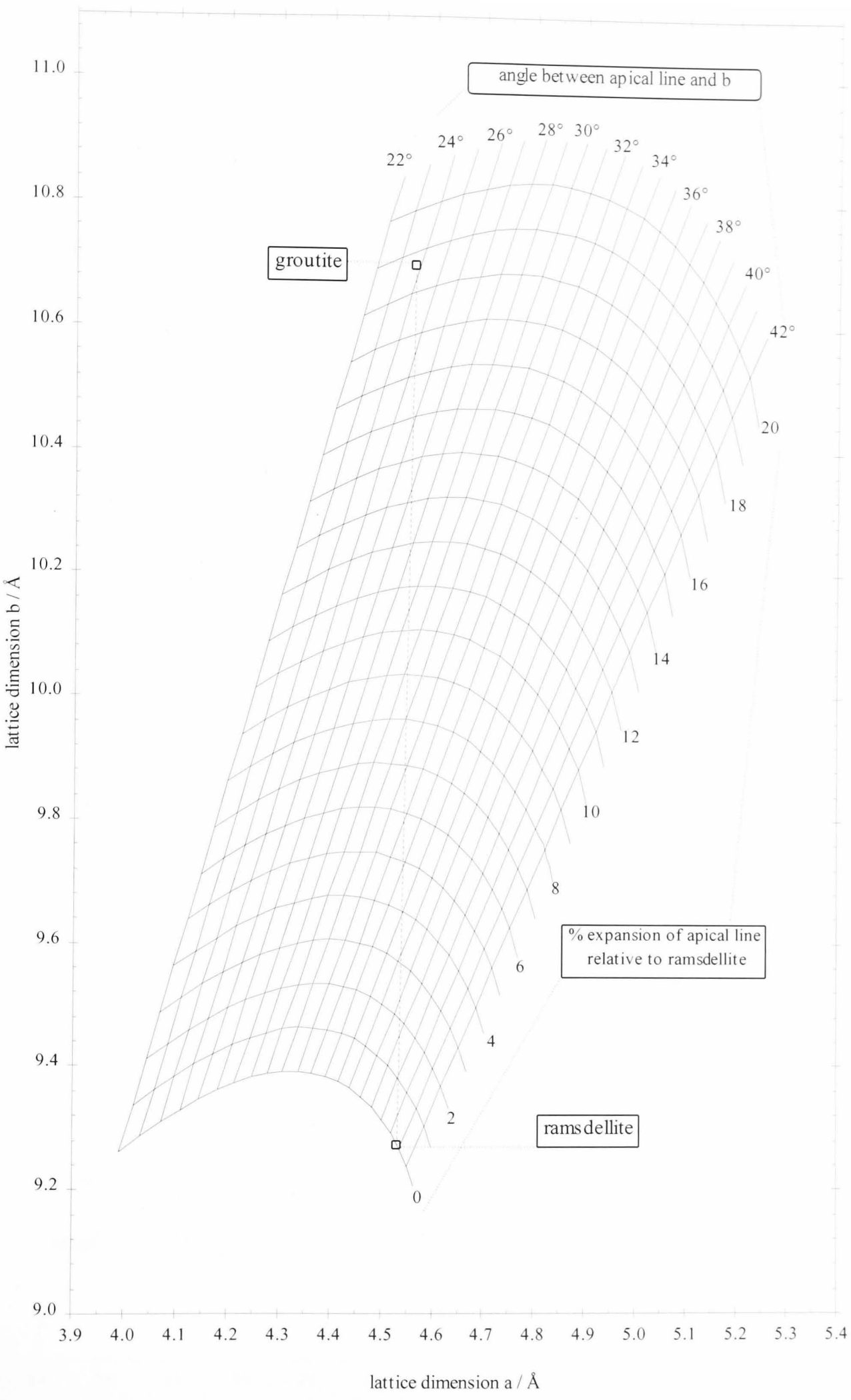

Fig. 3.4 Structural map showing the relationship between apical expansion (z), hinging angle (β) and the *a* and *b* lattice parameters of ramsdellite and groutite (from ref. 19).

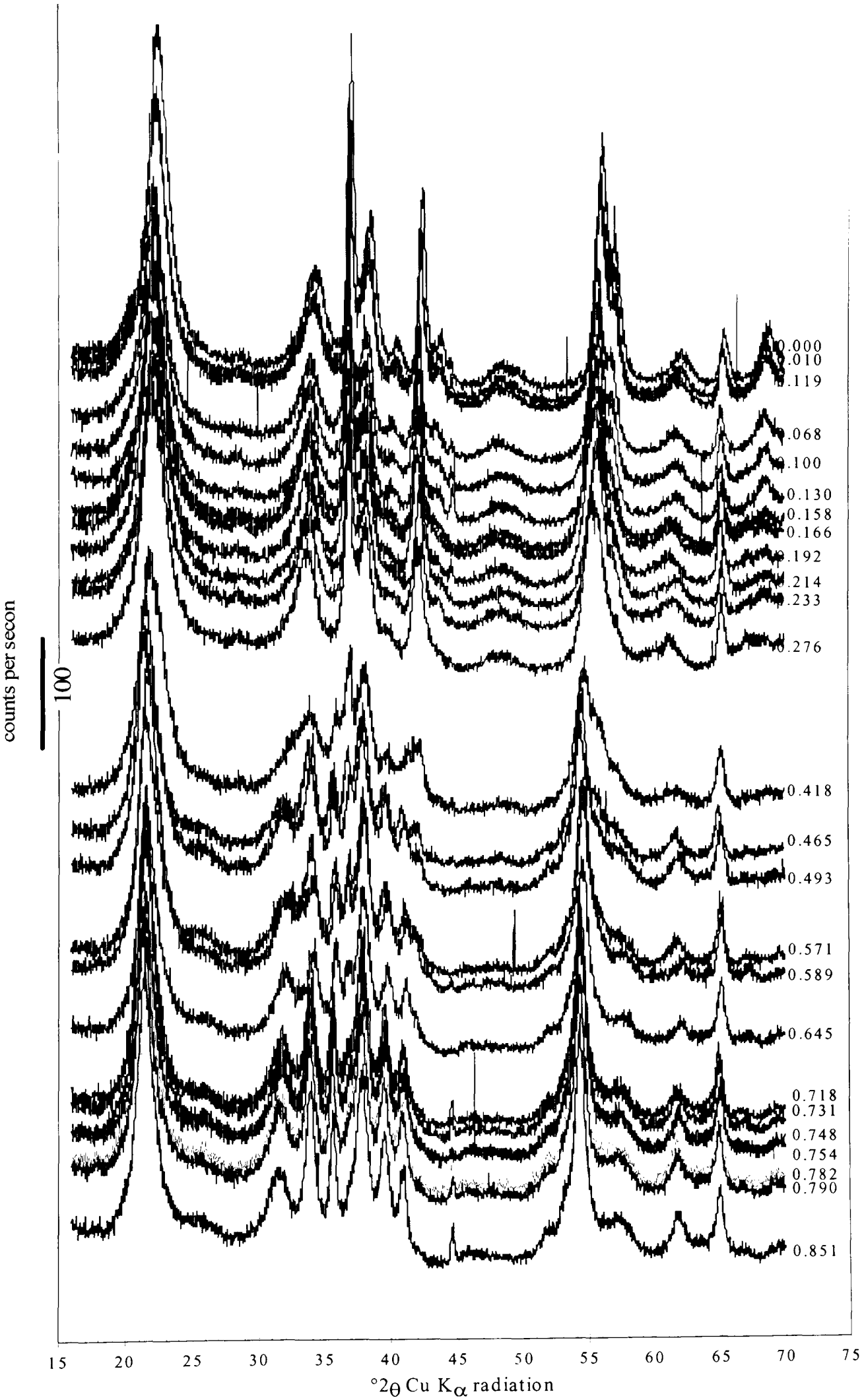

Fig. 3.5 XRD patterns of selected H-inserted SBP-A samples stepped down the page in proportion to the H-insertion level s in $MnO_{1.971}H_s$. hkℓ lines are omitted but shown in Figs 3.9, 3.15 and 3.17. The insertion level is shown on the right of each XRD spectrum.

Inspection of the overall figure (Fig. 3.5) shows three sets of XRD patterns. The first set is similar to the diffractogram of the starting material, essentially with some lines shifted towards lower angles. This set extends over the range $0 < s < 0.3$. It was assigned to H-insertion in a homogeneous phase. The next set of XRD patterns ($0.3 < s < 0.7$) shows practically no line shift with emergence of new lines side by side with the initial lines from the first set.

This set, thought to take over from the homogeneous phase, was assigned to H-insertion in a heterogeneous phase.

The third set of XRD patterns covers the last stretch of the H-insertion from $s = 0.68$, and seems consistent with a homogeneous insertion towards the final product of the H-insertion. The similarity in features of the XRD above 0.7 in s and the slight shift towards lower angles as s increases support the above suggestion.

The delineation of the three phases of the H-insertion was clearly shown by plotting the deconvoluted peak positions of suitable neighbouring $hk\ell$ lines from both ramsdellite- and groutite-like structures against the insertion level. If a ramsdellite-like line *r* of the starting material appears at an angle θ_r, and a groutite-like line *g* of the end product appears at a nearby angle θ_g then the relative positions of θ_r and θ_g would shape the transition curve from *r* to *g*. If $\theta_r < \theta_g$, upon H-insertion the line *r* would first shift to lower angles reflecting the expansion in the homogeneous phase[31]. At the onset of the heterogeneous phase, *g* is formed and a mixture of *r* and *g* is present. The groutite-like line is at a high angle θ_g and the ramsdellite-like line at a low angle θ_r, hence the transition from *r* to *g* would consist of a shift to higher angles. Therefore, a sharp slope change results delineating these two phases. By the end of the heterogeneous phase, the final product was fully formed and further H-insertion led to homogeneous expansion of the structure to the end product. As a result, θ_g is now expected to move to lower angles drawing thereby the dividing line between the heterogeneous and the second homogeneous phases.

Two sets of this type of lines were available (130_r and 040_g) and (151_r and 061_g). The positions of these lines as a function of the H-insertion level are plotted in Fig's 3.6 and 3.7 respectively.

The case where $\theta_r > \theta_g$ can be deduced through similar reasoning; and an example is provided by the relative positions of 200_r and the doublet $(200\&140)_g$. The movement

of these lines with the H-insertion is shown on Fig. 3.8. Here, the heterogeneous transition occurs at the same position since both the reactant and the product overlap. These three phases are discussed in the next sections and will be referred to in the interpretation of the H-insertion into Faradiser M and R2 in the next chapters.

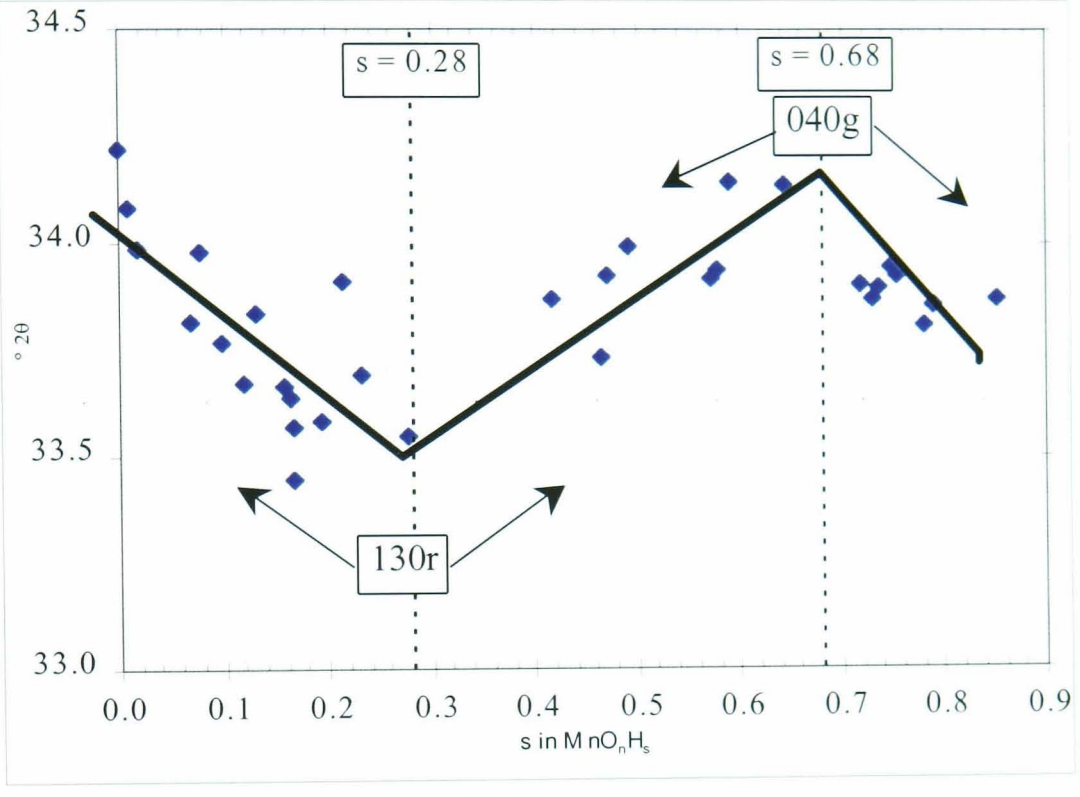

Fig. 3.6 Position of the 130_r and 040_g lines vs. H-insertion levels in SBP-A showing the three regions of the H-insertion.

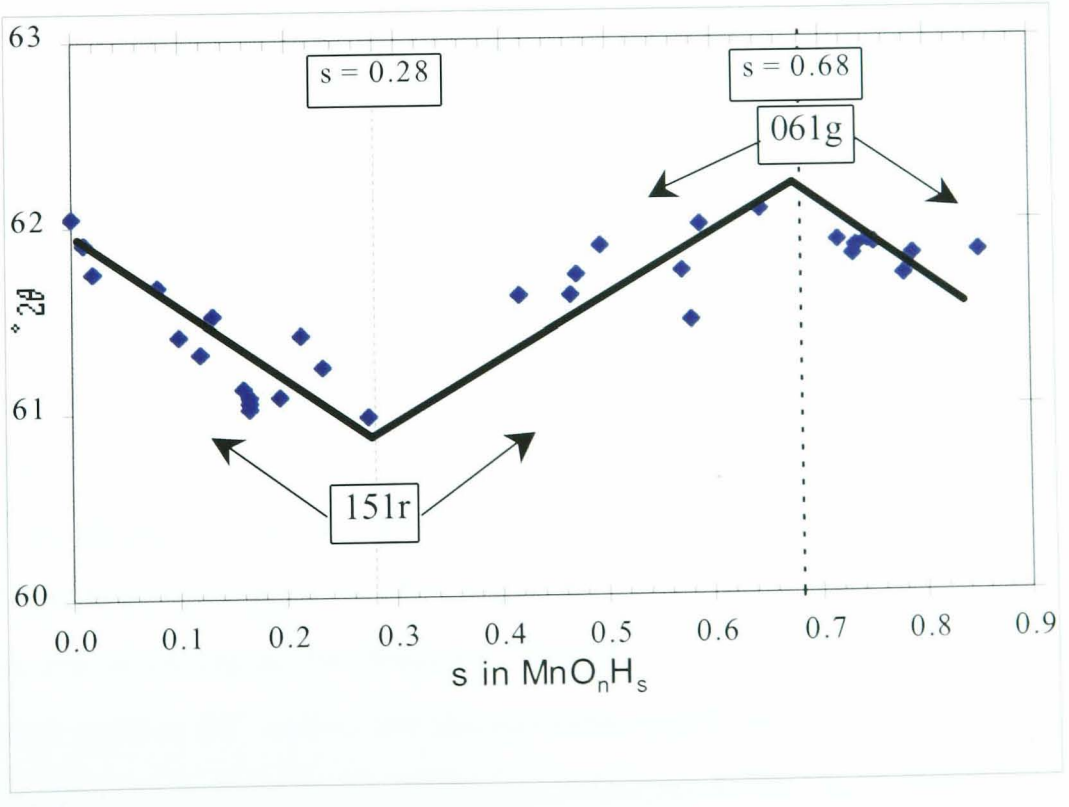

Fig. 3.7 Position of the 151_r and 061_g lines vs. H-insertion levels in SBP-A showing the three regions of the H-insertion.

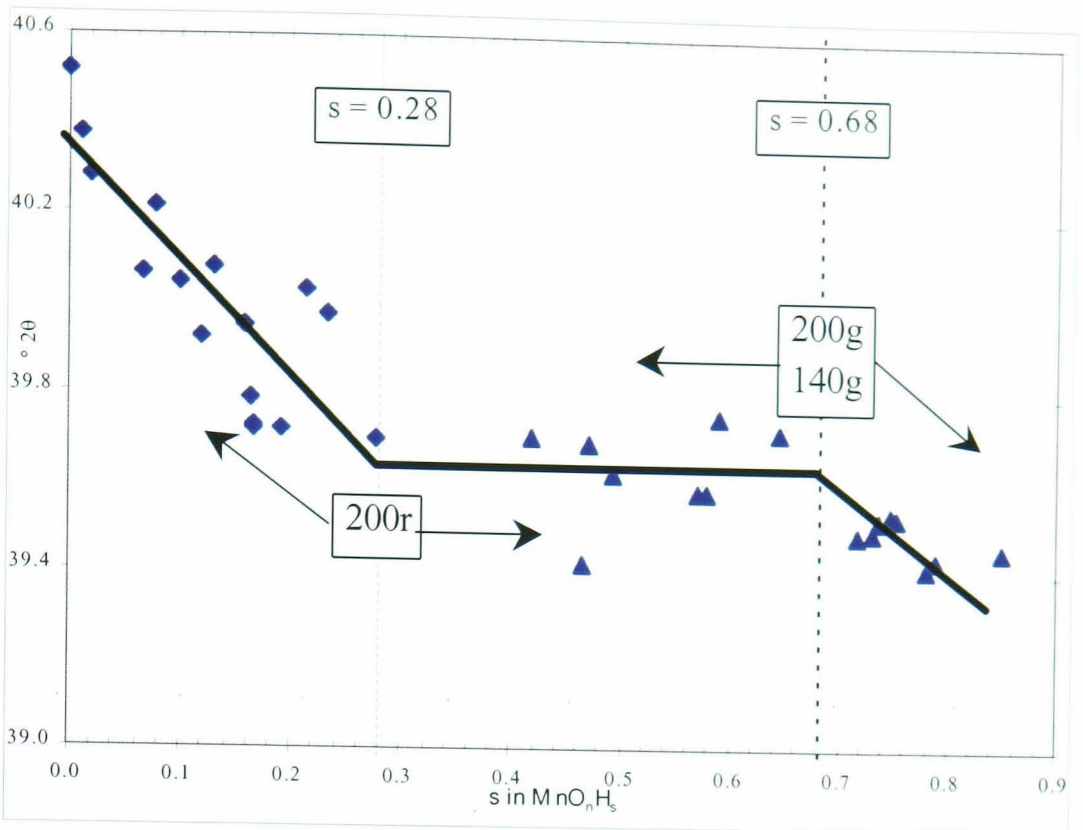

Fig. 3.8 Position of the 200_r and $200\&140_g$ lines vs. H-insertion levels in SBP-A showing the three regions of the H-insertion.

It must be mentioned that the above arguments leading to Figs. 3.6 - 3.8 are only valid if the amount of microtwinning remains unchanged. Variation of microtwinning causes XRD lines to shift as it is shown in Table 1.2. The lines shown in Figs. 3.6 – 3.8 do not consistently shift in either the direction predicted by microtwinning or in the opposite direction. This means that the line movements presented in Figs. 3.6 – 3.8 are not due to microtwinning or demicrotwinning; they reflect the stages of the H-insertion into SBP-A. The low amount of microtwinning in SBP-A is a possible justification to obtain such figures.

3.2.1 Homogeneous H-insertion into the Initial Structure

"Homogeneous H-insertion" means that the H-inserted manganese dioxide coexists with the starting material as a single phase; they form a solid solution, as first suggested by Brenet[31]. From a study of slightly H-inserted materials, Tye[85] was the first to show that coexistence of Mn^{4+} and Mn^{3+} arose simply because of the mobility of protons and electrons in the structure. Further studies[13,44-46,86,87] suggested that the two inserted entities (H^+ and e) are thermodynamically independent species. In fact, the thermodynamic species in the oxyhydroxymanganese are Mn^{3+}, Mn^{4+}, O^{2-} and OH^-. Electrons interchange the cations while protons do the same to the anions; hence, only mobility of the couple H^+/e is required to switch from the unreduced to the reduced

form of manganese dioxide. The mobility of these two entities has been shown[86,87] to be independent from each other in the homogeneous stage of the H-insertion. This independence allowed ideal mixing thermodynamics to be applied, as was shown earlier by Tye[86,101] and enabled the change of electrode potential of a commercial EMD with H-insertion to be explained.

In this work, the XRD patterns for selected samples of SBP-A H-inserted up to 0.28 in s are shown in Fig. 3.9. The homogeneous behaviour is shown through the similarity of the XRD patterns of all samples involved; indicating the same phase. The main difference exhibited by these patterns is a shift (with s) towards slightly lower angles due to expansion of the lattice as a result of the accommodation of H (see Chapter 1). Examples of this shift are provided by the movement of the selected hk*l* lines shown above in Fig's 3.6 through 3.8.

Careful inspection of Fig. 3.9 shows that the 200 line, which is based solely on the *a* lattice dimension of the ramsdellite block, had almost vanished by s = 0.2. This was because the 200 plane moved rapidly since it is not constrained to any restriction on the *b* and *c* axis and overlapped with the neighbouring doublet (111 & 040). This fact is also shown on Fig. 3.8 that monitored the movement of the deconvoluted 200_r. Planes which cut additional axis moved slower than 200 depending on the steepness of the angles at which these planes cut the three axis, particularly the *a*. For example, the 221 and 240 moved faster than 121 as can be seen from observing Fig. 3.9 and easily from Fig's 3.10 through 3.12.

The 021r line, which is parallel to the *a* axis, hardly moved in the first homogeneous stage. All these facts indicate that the expansion must have taken place in the *a* dimension.

Another plane parallel to the *a* axis, but one that was considerably shifted during this stage is the 061r, Fig. 3.13. However, the movement of this XRD line is presumably due a slight increase in the *b* dimension that was magnified by the high k index of this line*. Fig. 3.14 shows the effect of the rotation (or hinging) angle on the position of the set of ramsdellite lines encountered in the XRD patterns of EMD. This figure

---

* The 2θ position of the (0k1) family of ramsdellite planes is given approximately in terms of k and the slight increase in the b_r dimension of ramsdellite noted ε, by: $2\theta(k) = 2\arcsin[0.770(k^2/(b_r+\varepsilon)^2+0.123)^{1/2}]$. As ε is negligible, the position 2θ depends largely on k.

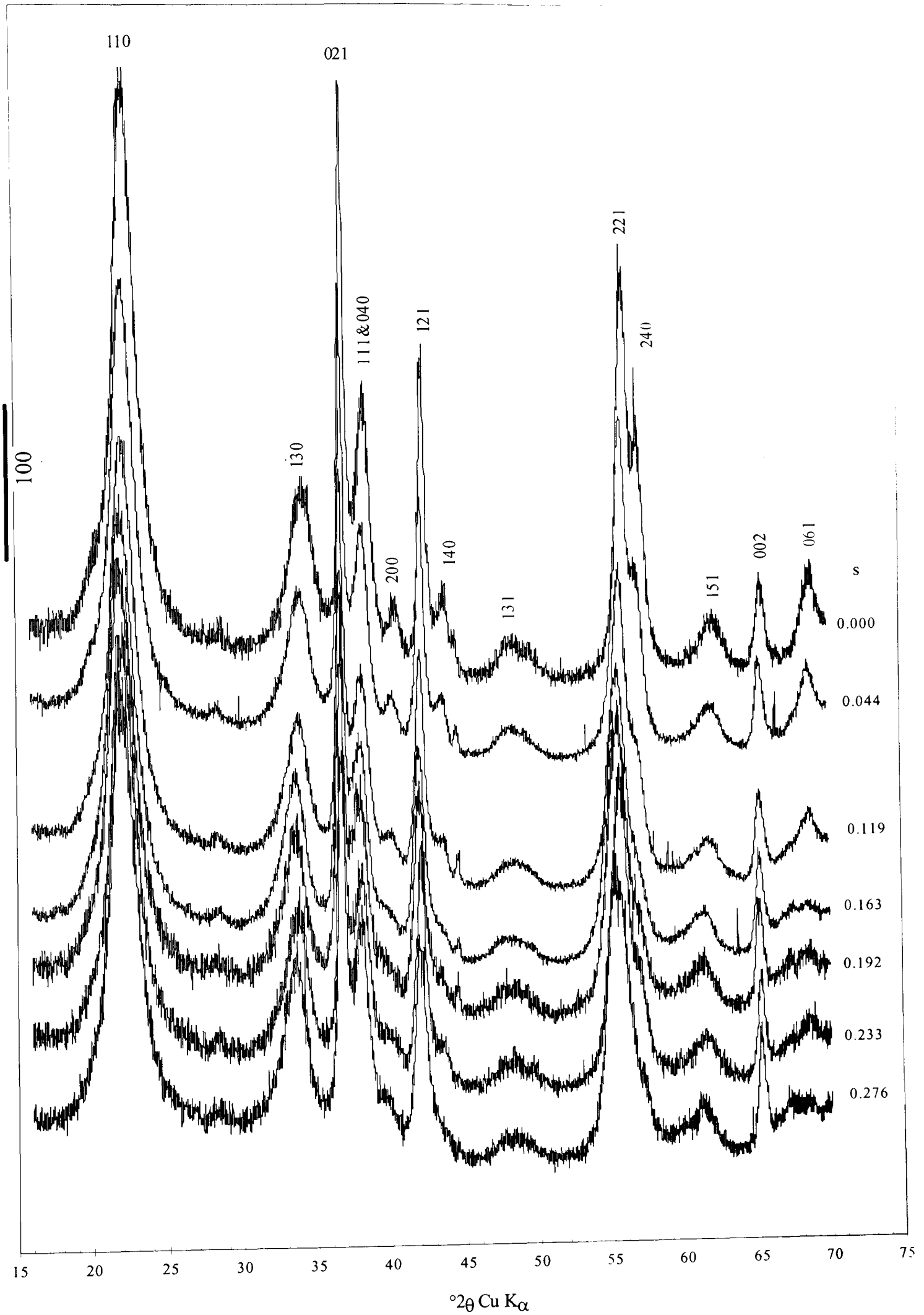

Fig. 3.9 XRD patterns of some H-inserted SBP-A samples in the first homogeneous region. The hkℓ indices refer to ramsdellite structure.

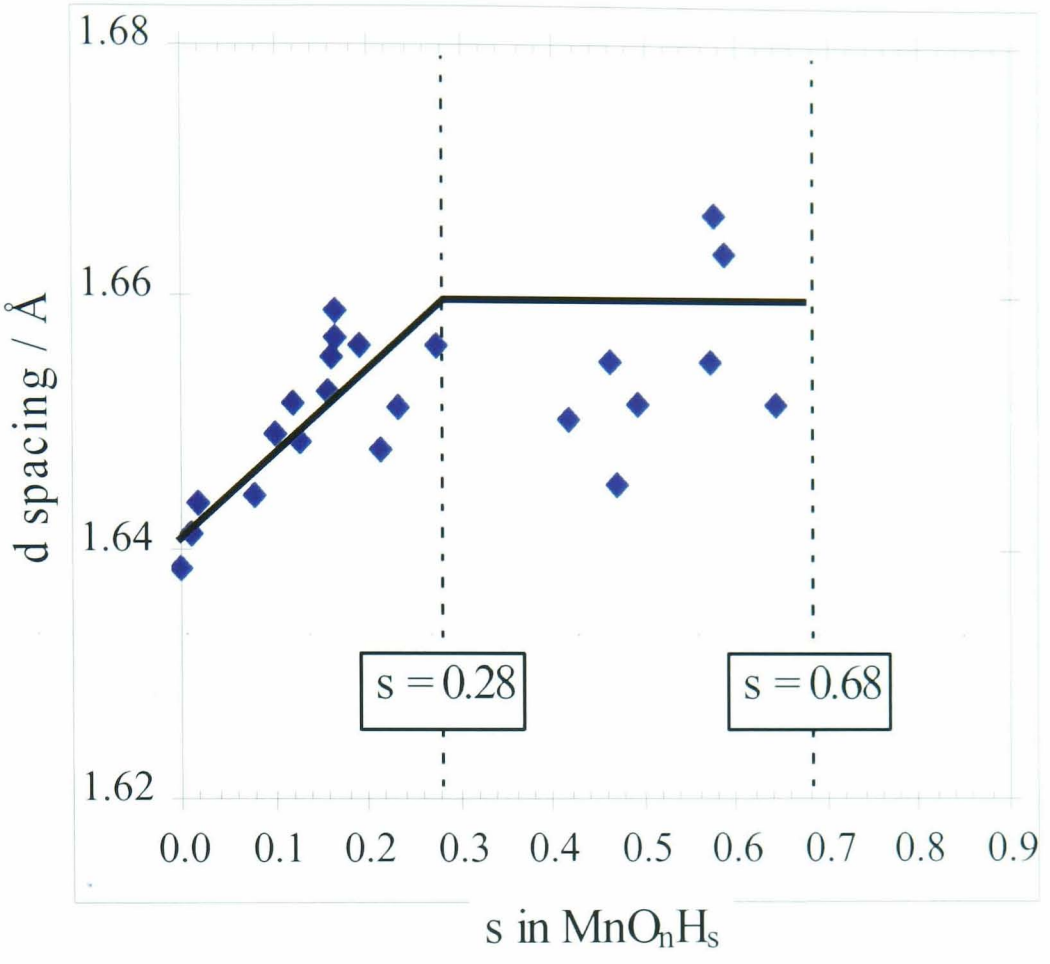

Fig. 3.10 Movement of the 221r line vs. the H-insertion level.

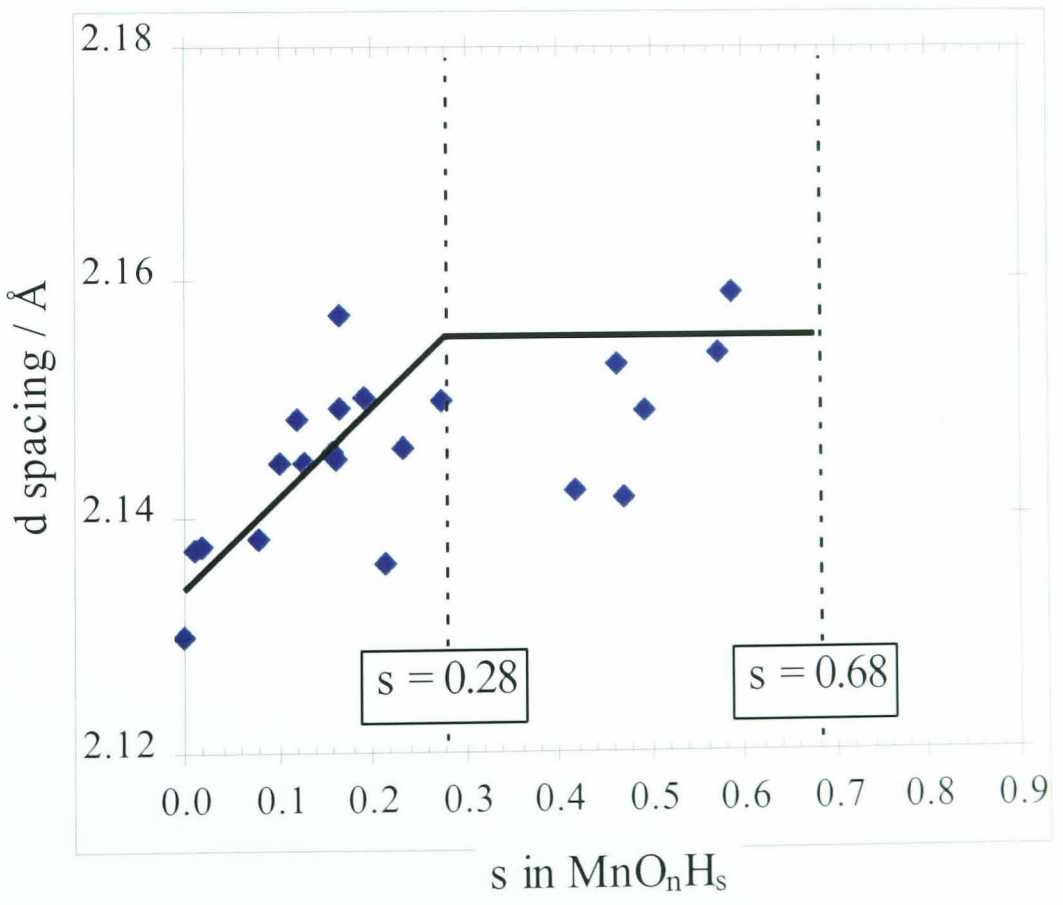

Fig. 3.11 Movement of the 121r line vs. the H-insertion level.

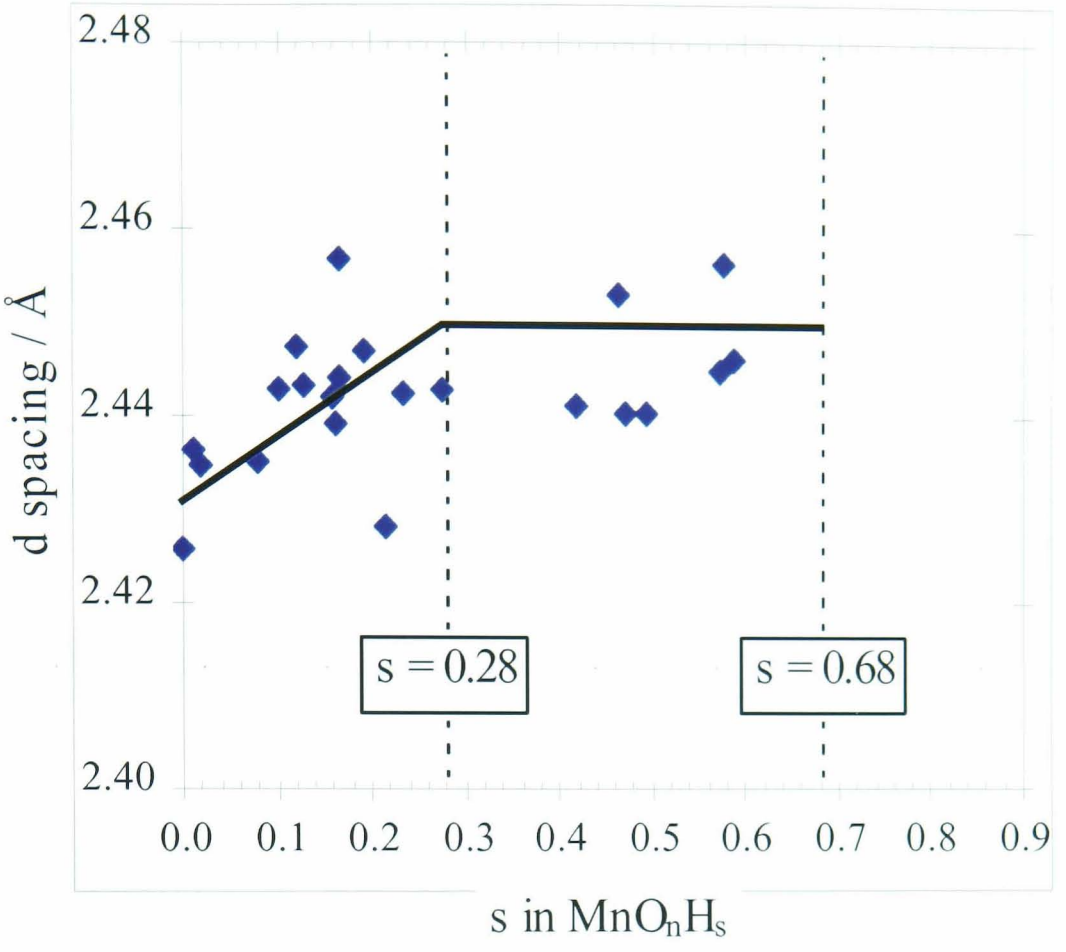

Fig. 3.12 Movement of the 021r line vs. the H-insertion level.

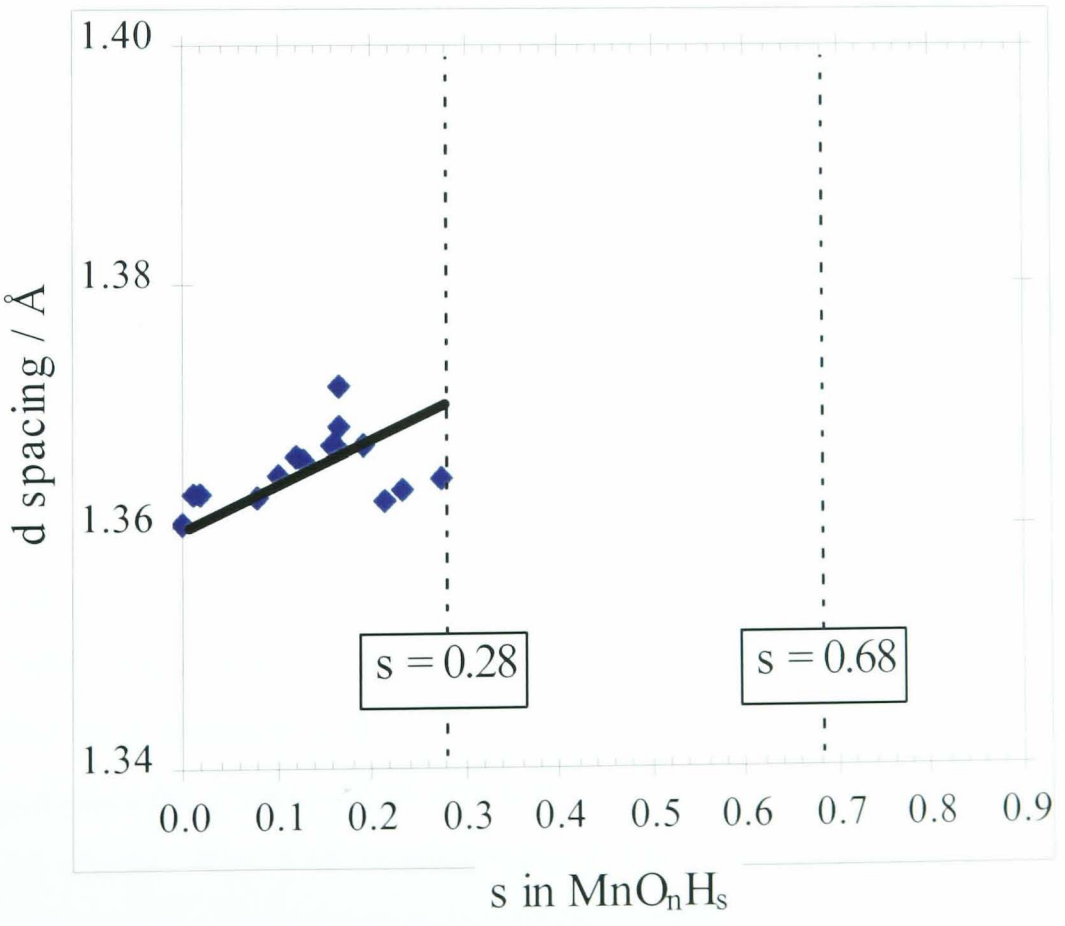

Fig. 3.13 Movement of the 061r line vs. the H-insertion level.

shows particularly how 061 moves faster to lower angles than 021, a fact that can only be due to the difference in steepness on the *b* axis; in other words the k index.

The same figure (Fig. 3.14) also shows how the 200 line moves rapidly to lower angles when the structure rotates as a result of H-insertion. Lines with the same steepness on the *a* axis but different steepnesses on the *b* axis such as the 221 and 240 would be expected to shift keeping the same distance apart as the rotation proceeds (Fig. 3.14). In practice, however, this is not the case. Fig. 3.9 shows that the 240r and 221r move closer together; this is because there is some expansion in the *b* dimension which is magnified by the high k index (4) of the 240r.

3.2.2 Heterogeneous H-insertion

Fig. 3.15 (reproduced from Fig. 3.5), displays the XRD patterns of H-inserted SBP-A samples, between 28 and 44 °2θ, in the interval of 0.42 to 0.65 in s. The range of diffraction angles was chosen because it is where the sharpest changes of the XRD patterns took place. This set of patterns interestingly has features from both the reactant and the product of the solid state H-insertion reaction. Thus, there are clearly two phases present side by side in this set of samples; hence heterogeneous H-insertion. The lines of the end product are indexed in a groutite structure and are shown with a g subscript to distinguish them from the lines of the reactant that are marked with a r subscript (after ramsdellite). This is the first time the clear coexistence of the reactant and product of H-insertion has been reported.

Heterogeneous behaviour of H-insertion into γ-manganese dioxide has been always concluded from data analysis but no such obvious evidence was presented previously. A further new finding was that the heterogeneous H-insertion did not proceed in the classical way whereby a new constant phase grows from an initial constant phase at a fixed Gibbs free energy change (ΔG). Here, the new phase grew at the expense of the initial phase but the XRD of both phases kept shifting. It is thus suggested that the two phases affect each other, hence the ΔG of this transition could shift progressively. Possibility of a structural link across the *ac* plane between the two phases may be envisaged since the *a*'s and *c*'s of both structures are of the same order of magnitude as Fig. 3.16 shows. Fig. 3.16 compares the *a* and *c* lattice dimensions derived from ramsdellite (a_r and c_r) with those derived from groutite (a_g and c_g) in the heterogeneous region and shows that these dimensions are very similar, and support the above

suggestion. Individual values of the lattice dimensions of each SBP-A sample are available in Appendix 3.

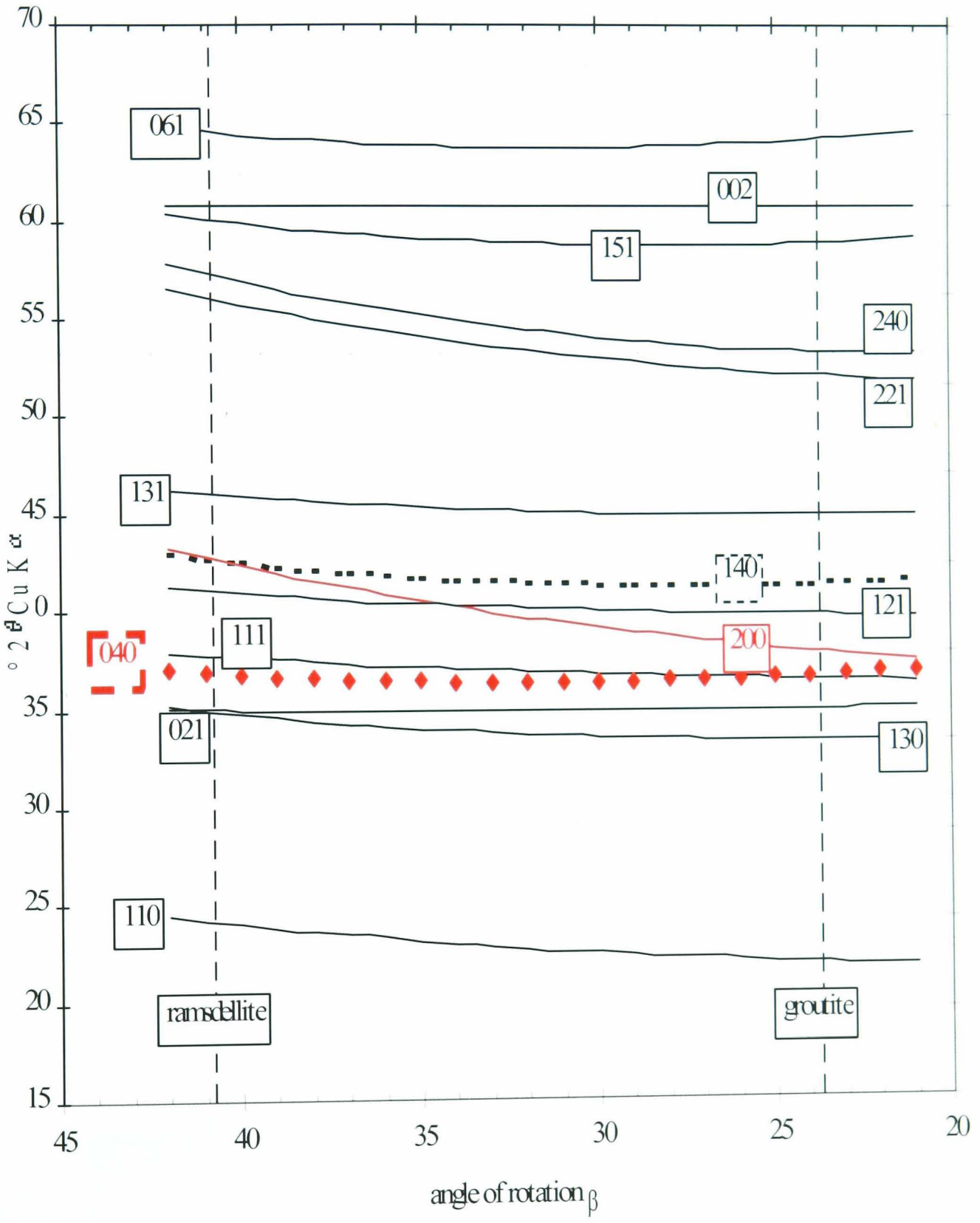

Fig. 3.14 Shift of some ramsdellite XRD lines as a function of the rotation angle β. Note that lines 121 and 040, 240 and 221 also 200 and 140 do not overlap.

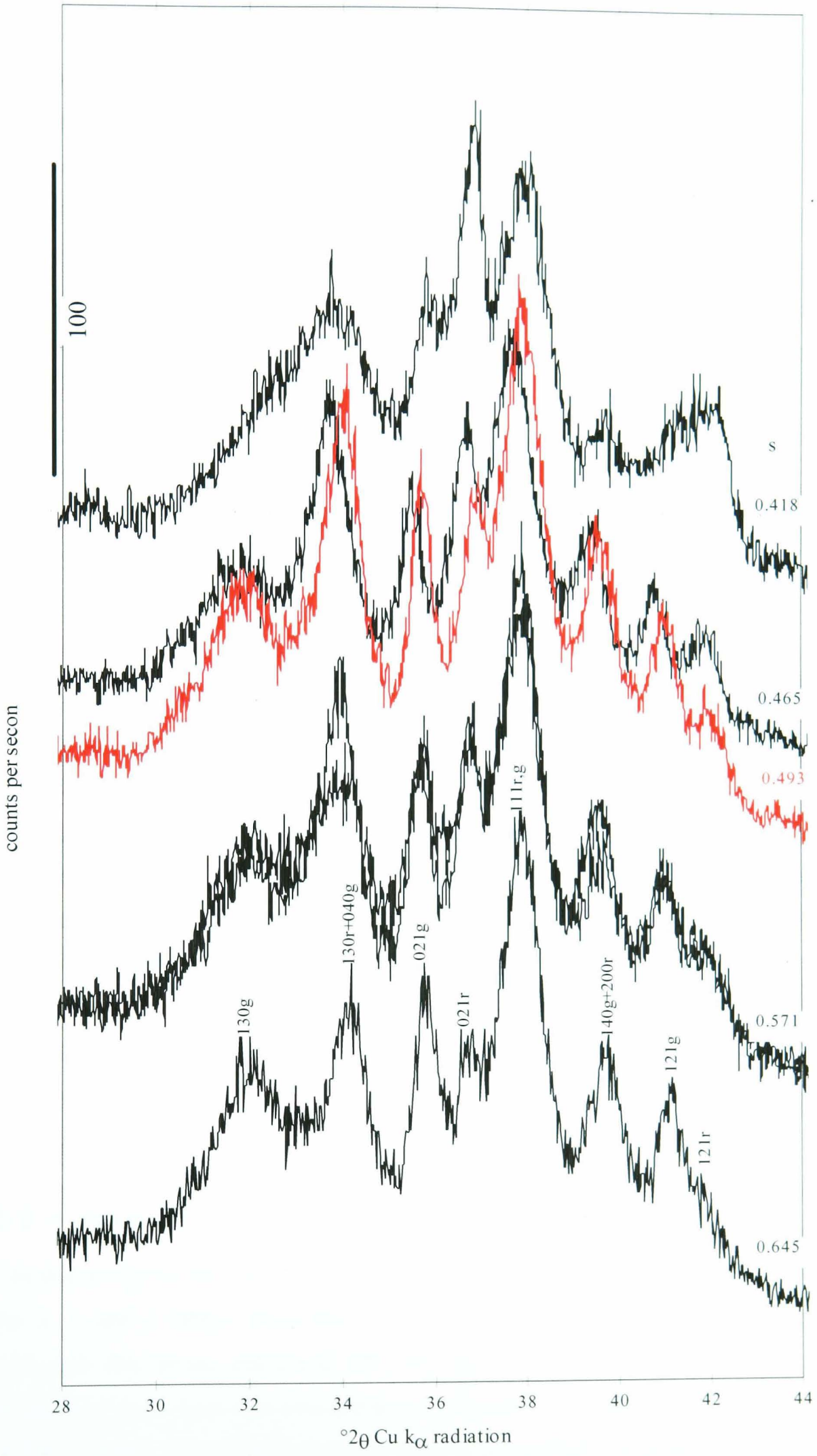

Fig. 3.15 Selected XRD patterns of H-inserted SBP-A samples in the heterogeneous region. The hkℓ indices from ramsdellite and groutite structure are labelled with subscript r and g respectively.

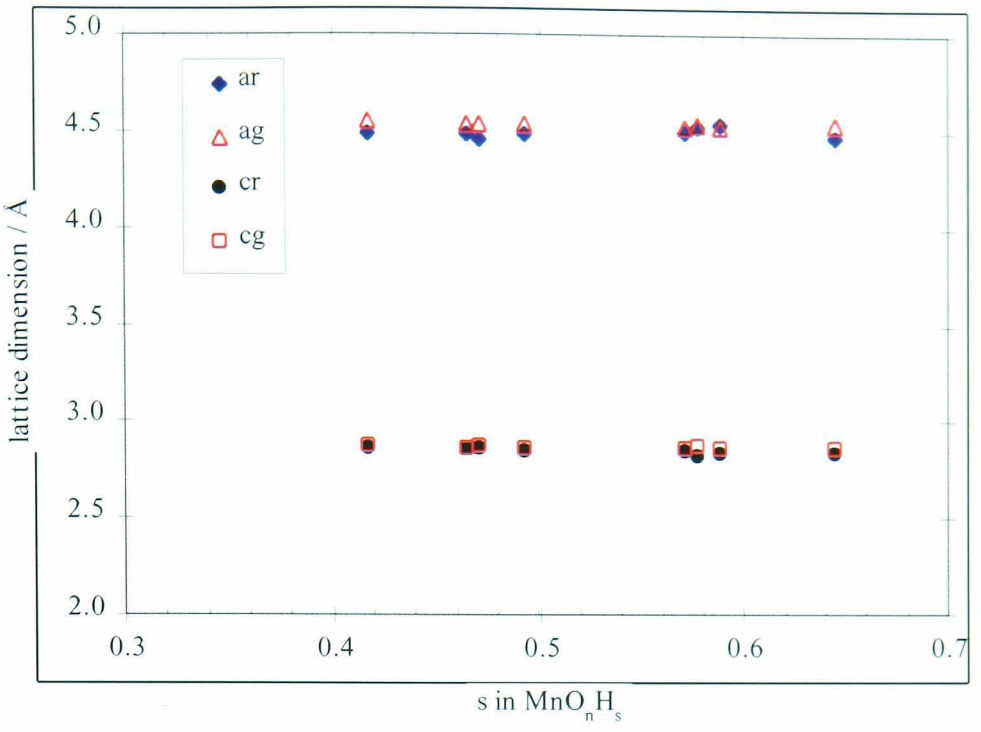

Fig. 3.16 Comparison between the *a* and *c* lattice dimensions derived from ramsdellite (*a*r and *c*r) and groutite (*a*g and *c*g) in the heterogeneous region of H-insertion into SBP-A.

3.2.3 Homogeneous H-insertion Into The Final Structure

By s = 0.68, the final structure of H-insertion had been formed and further H-insertion simply maintained the features of the XRD pattern. At this stage, the XRD lines also shifted slightly to lower angles as is visible in Figs. 3.6, 3.7 and 3.8. Thus, above 0.7 in s, the H-insertion proceeded homogeneously in the final product in the same way it occurred in the starting material. Fig. 3.17 shows the XRD patterns of the samples available in this region. The similarity of the patterns in Fig. 3.17 confirms the homogeneous behaviour. The shift towards lower angles observed in Figs. 3.6 – 3.8, which confirms some dilation of the structure, is however less obvious in Fig. 3.17. The limited shift reflects the restricted H-insertion range of available samples ($0.72 \leq s \leq 0.85$).

3.2.4 Structural Map of SBP-A

The deconvoluted ramsdellite lines 021r, 121r, 221r, 061r and 002r were used to obtain the *a*, *b* and *c* lattice parameters (section 2.4.8) of the first homogeneous phase. Although this phase continued into the region of heterogeneous H-insertion, the position of these lines was considered insufficiently reliable for determination of unit cell parameters. Thus, no further information is available in the heterogeneous region on the structure of the reactant phase. The *a*, *b* and *c* parameters of the product phase of heterogeneous insertion and of final homogeneous phase were determined from the

deconvoluted positions of the 021g, 121g, 221g, 061g and 002g lines of groutite. Thus, up to s = 0.28 the lattice parameters *a*, *b* and *c* refer to ramsdellite structure and above this level to groutite structure. Lattice dimensions of all samples, as well as the parameters z and β, are given in Appendix 3.

The *a* and *b* unit cell dimensions are put on the structural map in Fig. 3.18.

Fig. 3.18 shows that the samples in the first homogeneous region possess a structure close to that of ramsdellite. SBP-A starting material falls below the *a* and *b* dimensions of ramsdellite. This fall has been suggested to be due to the restricted choice of XRD lines available for lattice parameters refinment[37].

The set of 15 samples covering the first homogeneous phase is squashed between 4.440 and 4.507 Å in the *a* direction (Fig. 3.18) at a practically constant *b*. That is a maximum expansion of 1.5 % in the *a* dimensions compared with the starting material. This represents a maximum apical expansion of about 1 % and an increase in the rotation angle β of approximately 2° to produce a constant *b* dimension. The low amount of microtwinning, which is across the 021 and 061 planes[18], restricted the expansion in *b* and *c* directions but not in the *a* direction. An additional support is provided by a previous publication[33] that concluded that anisotropic expansion predominantly in the *b* direction changed the angle between the microtwinning planes and the *b* (and *c*) axis. It is this change that "generates forces which cause splitting along the planes of weakness, in other words demicrotwinning"[33]. Hence, since only a negligible increase in the *b* dimension occurred, no demicrotwinning would be expected to take place.

A consequence of the limited expansion of the structure was an increase of density of the mobile proton/electron in the host material. This would encourage hydrogen location at an earlier insertion level compared with a structure where more (apical) expansion is permissible. This must be due largely to the mild H-insertion conditions used in the present work in comparison with previous similar work[37] carried out on the same material (see section 3.2.6).

By s = 0.42, a fraction of the initial structure had demicrotwinned and turned into a predominantly groutite-like structure as a result of dramatic expansion of the *b* dimension accompanied by a sharp hinging of the angle β. This phase transition proceeded heterogeneously as already shown. Thus, the heterogeneous H-insertion affected essentially the *b* axis only.

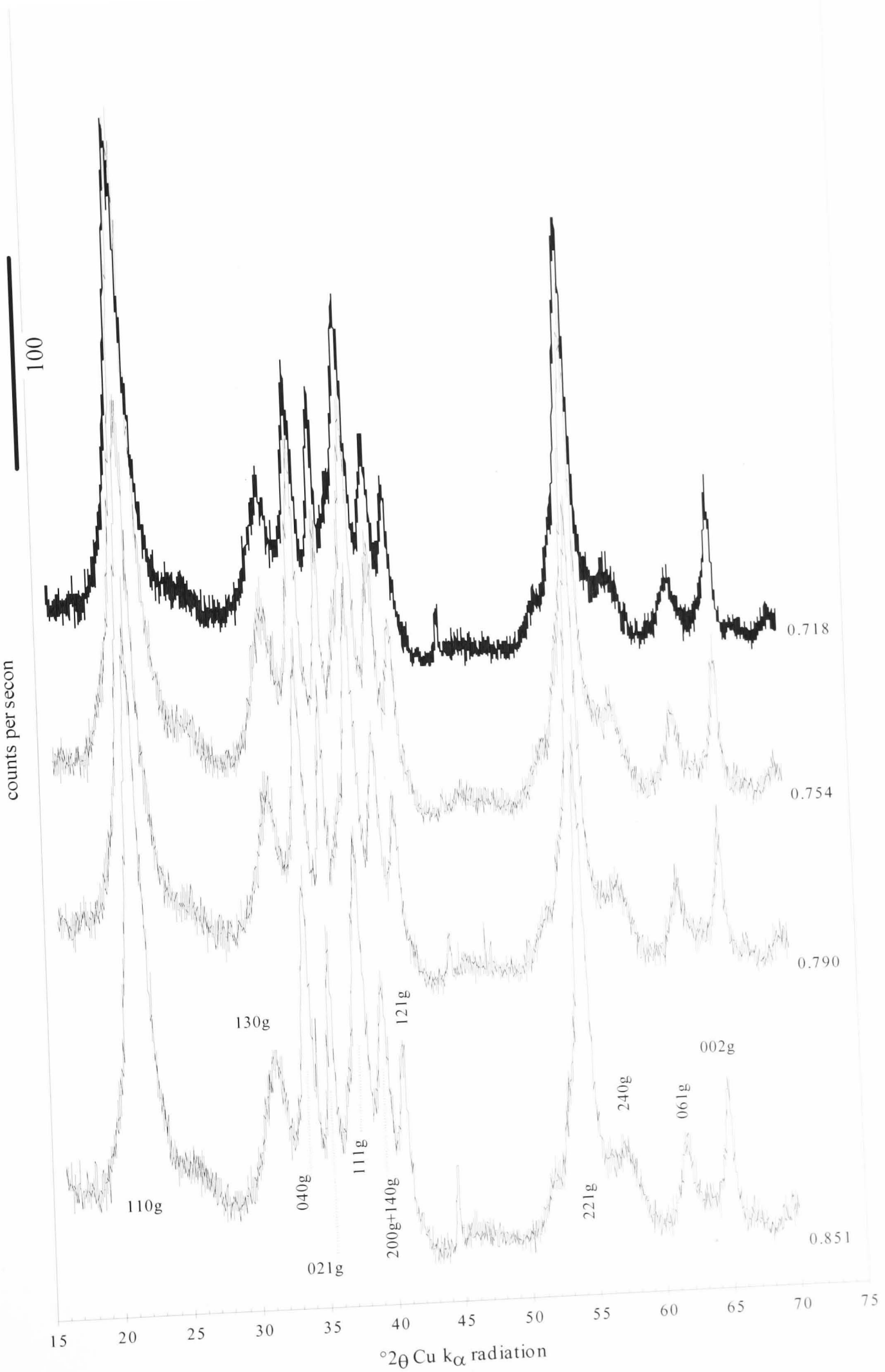

Fig. 3.17 Selected XRD patterns of H-inserted SBP-A in the second homogeneous region. The hkℓ indices refer to groutite structure.

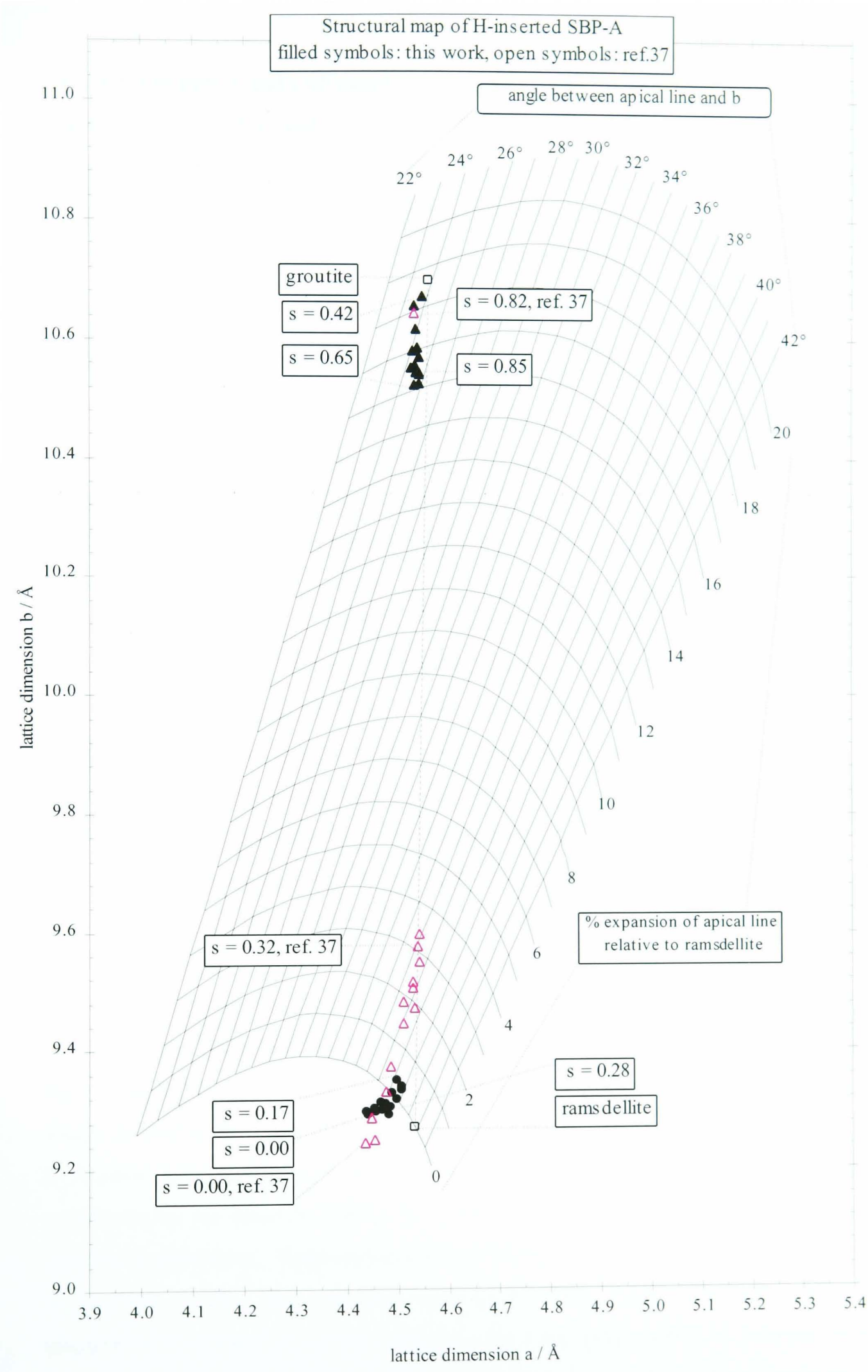

Fig. 3.18 Structural map of SBP-A material and its H-inserted modifications. Results of MacLean and Tye[37] are also shown along with the lattice dimensions of ramsdellite and groutite taken after Byström[19].

Lattice parameters *a* and *c* of samples of insertion levels above 0.68 fall between 4.537 and 4.543 Å and 2.866 and 2.868 Å respectively. The b dimension however ranged between 10.526 and 10.571 Å. Therefore, the possibility of linked structures throughout the heterogeneous phase remains possible.

From s = 0.72, the structure approached the stable groutite structure and so there was little scope for parameter change.

3.2.5 Comparison with Previous XRD Study

Fig. 3.18 also displays the *a* and *b* parameters of H-inserted SBP-A, using either contact with acetone at room temperature or reflux in propanol, as carried out by MacLean and Tye[37]. Thus, the H-insertion method was different from that followed in this work (section 2.2). H-insertion in the cited paper proceeded into two stages: homogeneously up to s = 0.34 and heterogeneously above this level[37]. Another main difference with the present work is that the homogeneous expansion of the structure occurred predominantly in the *b* direction as can be seen in Fig. 3.18.

The starting material was the same for both works and gave the same XRD patterns as shown on Fig. 3.19. Up to s = 0.28, the H-insertion was homogeneous in both works. However, comparison of the lattice dimension (shown on the structural map, Fig. 3.18), reveals a large difference in the *b* dimension. Therefore, this difference is expected to show through the XRD patterns from both works. Fig. 3.20 compares the XRD patterns of the two works at two insertion levels within the common homogeneous phase. At s = 0.17, the pattern from this work is slightly shifted to lower values of 2θ and exhibits generally broader peaks in comparison with the published pattern[37] at the same insertion level as shown in Fig. 3.20A. Two lines are exceptions: the 002 peak which is not shifted at all (solely on the *c* axis) and the 240/221 peak which is shifted the most due to the k index of the 240 (see section 3.2.1). The difference between the two patterns is thought to be due to the slight rotation undergone by the structure during the homogeneous phase of this work to maintain constant *b* dimension. Rotation has been shown to cause many lines to shift to lower angles (Fig. 3.14). The structural map, in the other hand, demonstrates that the samples of the paper[37] are more dilated (in the *b* direction) and their patterns should thus appear at lower angles. The suggestion is that the inter-planar spacing d_{hkl} is

perhaps more sensitive to alteration of the hinging angle β at a constant *b* than to change in *b* at constant β.

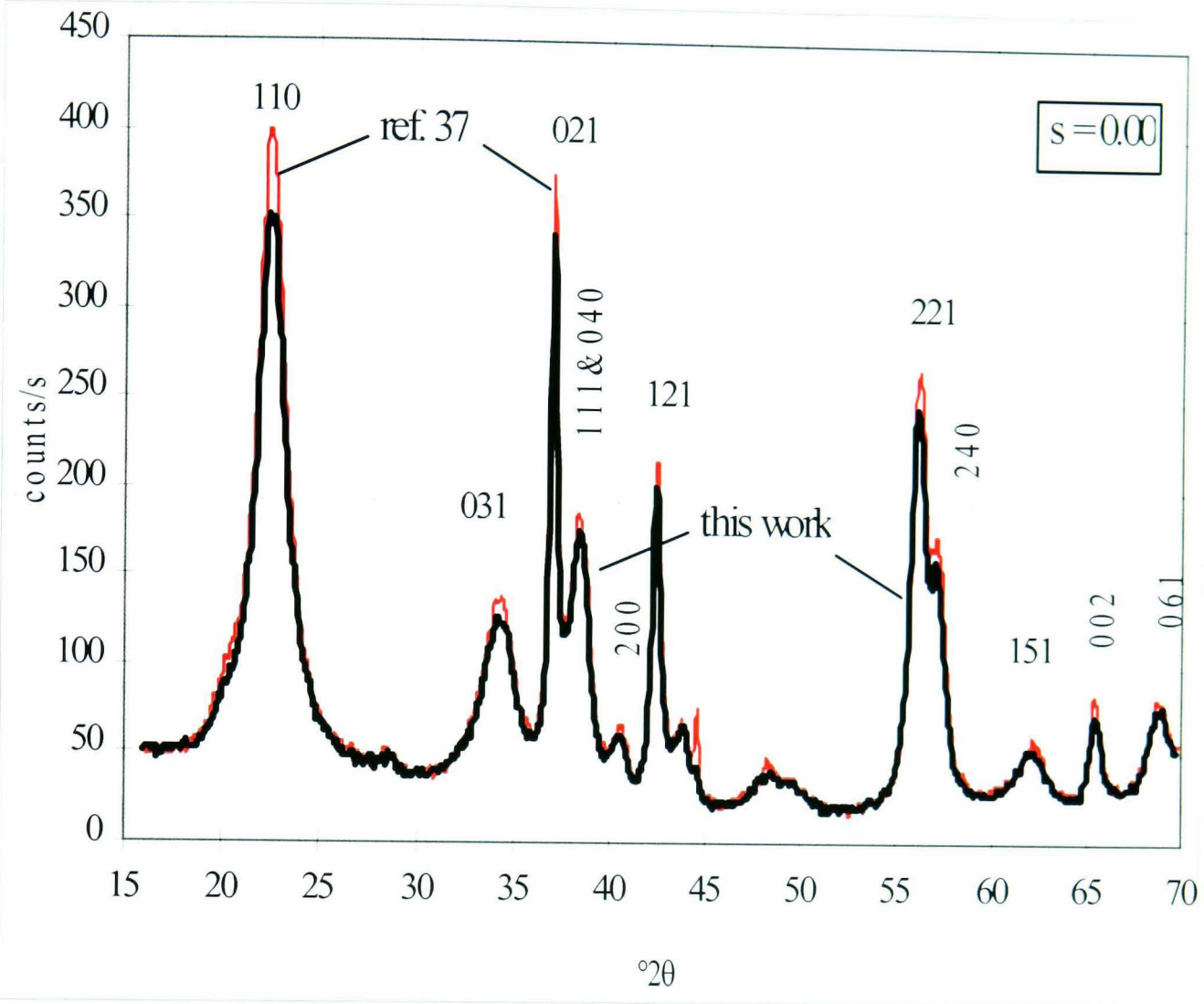

Fig. 3.19 Comparison between the XRD patterns of SBP-A starting material in this work and in ref. 37. The hkℓ indices refer to ramsdellite structure.

The discussion above applies to insertion level as high as s = 0.28. Fig. 3.20B shows the fingerprint area of the XRD patterns of H-inserted samples at s = 0.28 from both works. At this level, the broadening of the peaks of this work's pattern is obvious and the structure prepares to engage into heterogeneous insertion.

Since the heterogeneous phase in the compared work[37] starts at s = 0.34, comparison between the patterns from both works in the range $0.28 < s < 0.34$ would have added some information about the insertion reaction. Unfortunately, no sample with an insertion level in that range was available from this work. Between 0.34 and 0.68 in s, the two sets of XRD patterns are representing heterogeneous behaviour. Figs. 3.21 and 3.22 compare selected XRD patterns of close H-insertion levels from both works.

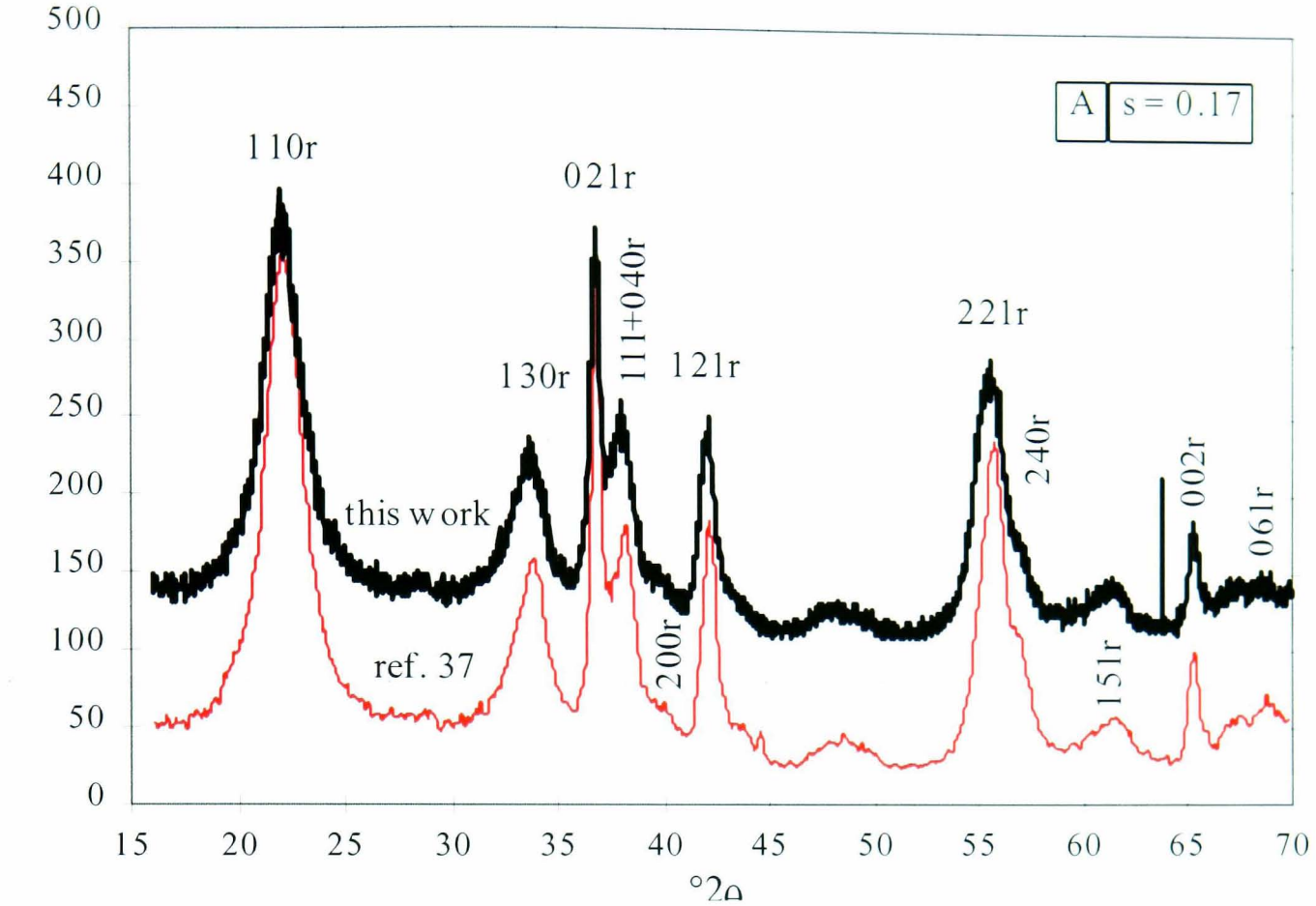

Fig. 3.20 Comparison between the XRD patterns of H-inserted SBP-A in the homogeneous stage, in this work and in ref. 37 at two insertion levels: A s = 0.12 & B s = 0.28.

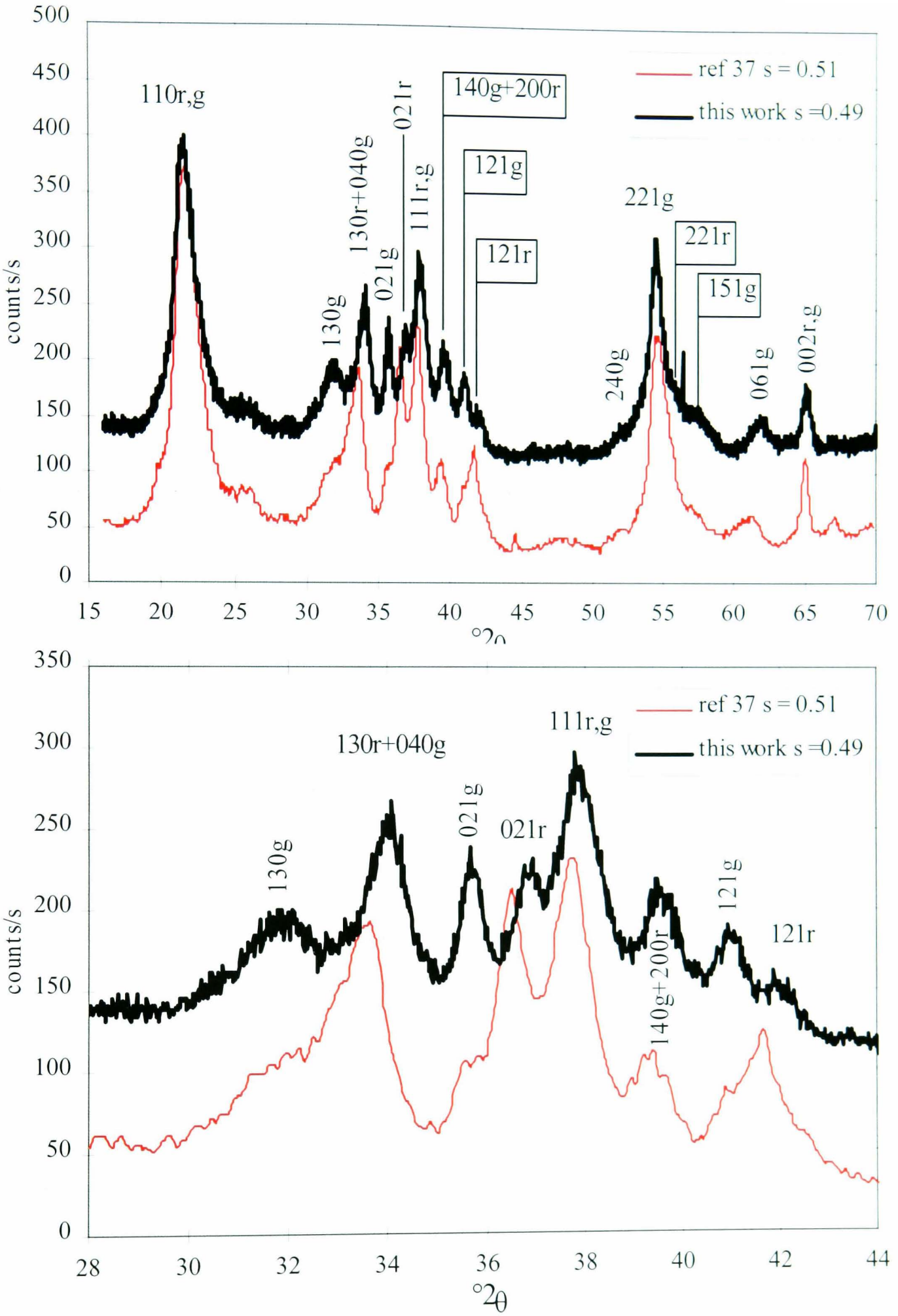

Fig. 3.21 Comparison between the XRD patterns of H-inserted SBP-A in the heterogeneous stage, in this work and in ref. 37 at s ≈ 0.5. Top: the full diffractograms, Bottom: the fingerprint are. Note that hkl's from both ramsdellite ($_r$) and groutite (g) are present simultaneously in the patterns of this work.

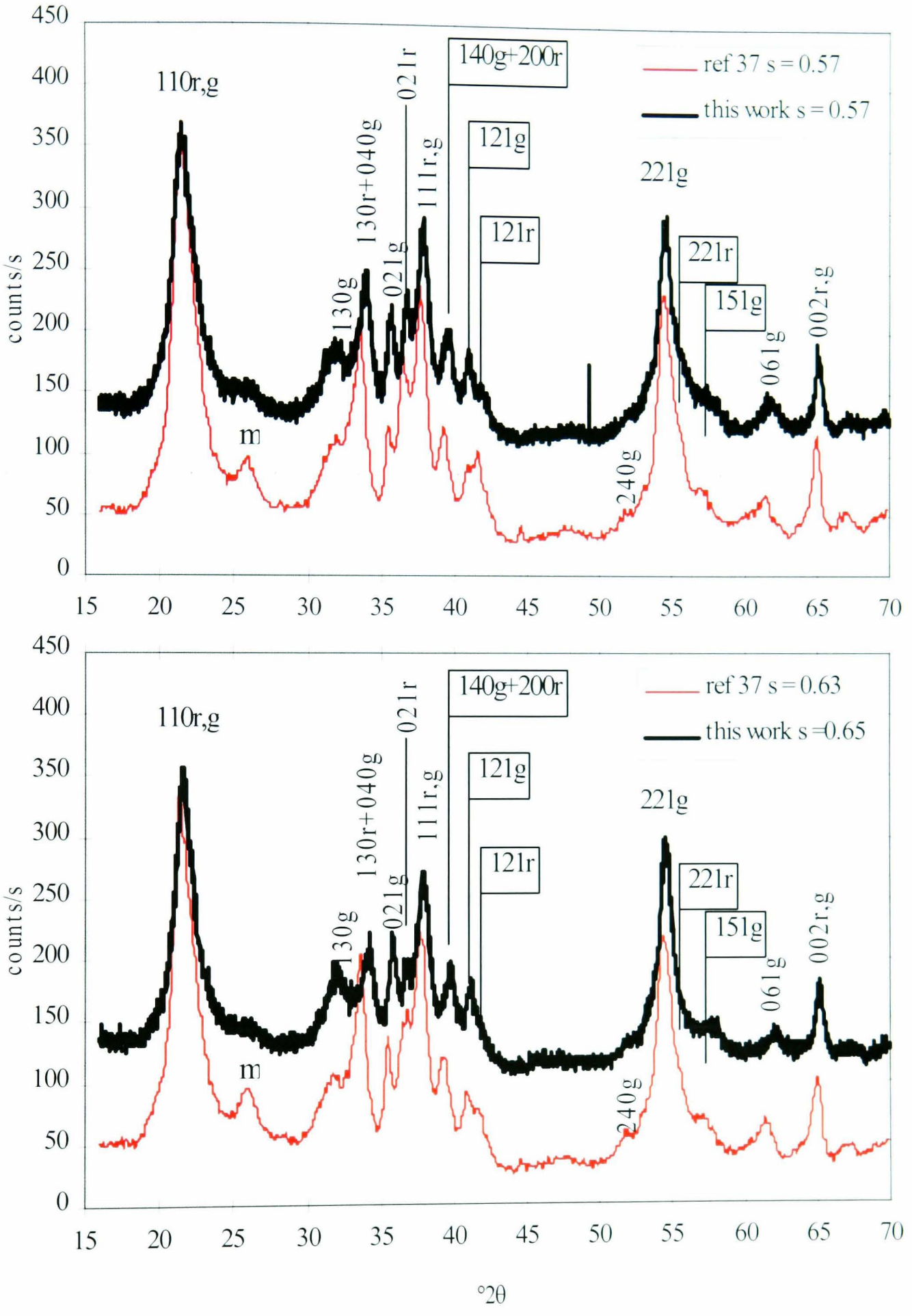

Fig. 3.22 Comparison between the XRD patterns of H-inserted SBP-A in the heterogeneous stage, in this work and in ref. 37 at two advanced H-insertion levels: Top: s = 0.57 and Bottom: s = 0.64. Note that the patterns of this work still have more r & g lines while manganite impurity (marked m) merged in the ref.'s samples.

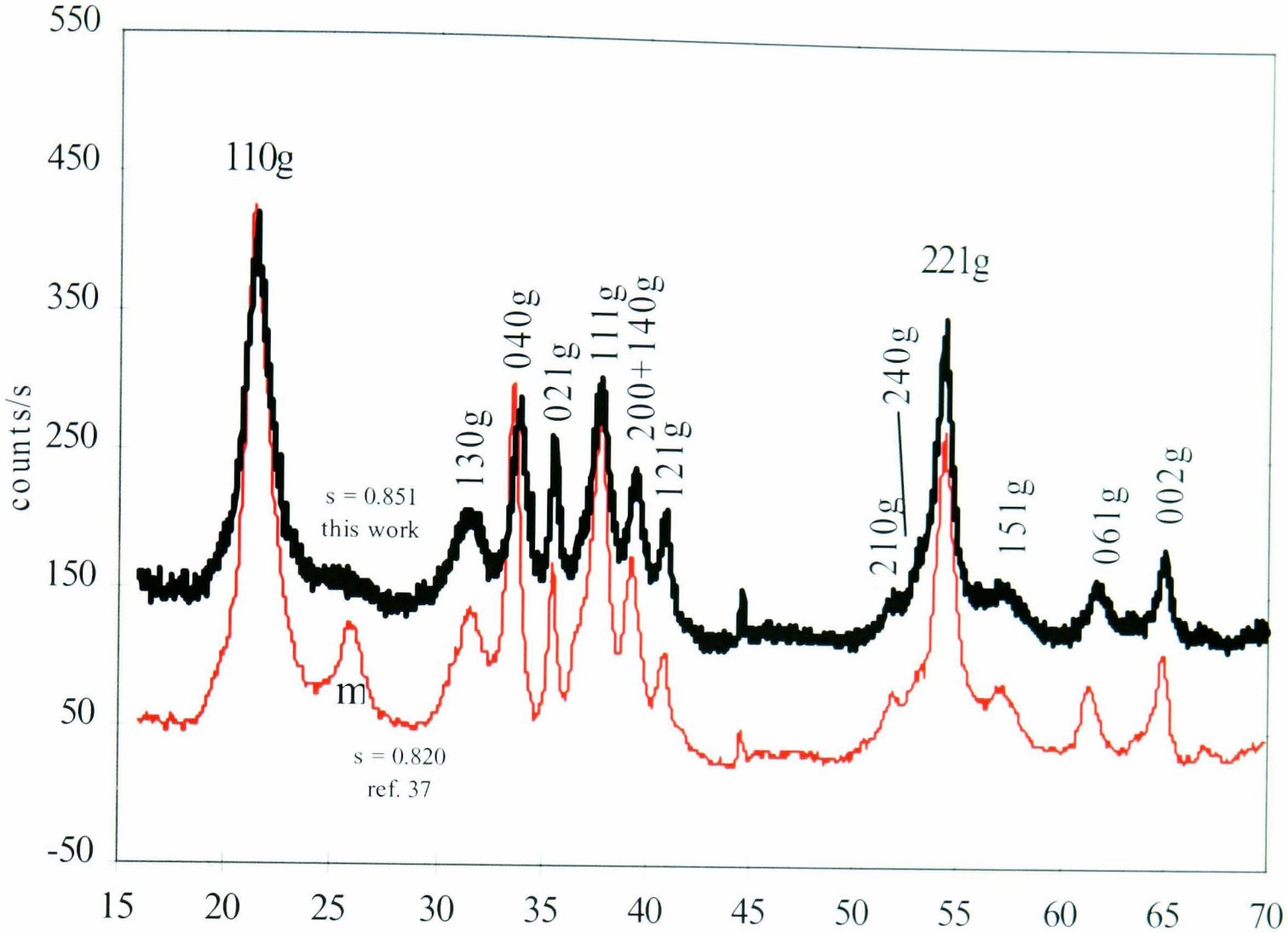

Fig. 3.23 Comparison between the XRD patterns of most H-inserted SBP-A in this work and in ref. 37. The patterns are similar except that there is considerable amount of precipitated manganite (marked m) in the paper's sample.

There are undoubtedly more (resolved) lines in the patterns of this work confirming the co-existence of both the initial and the end phases- see the hkℓ indices. In the paper[37], the patterns of this region have fewer lines that are resolved. The H-insertion conditions must be the cause of these differences. While the gentle conditions (controlled amount of reagent at low temperature) allow more time for the product to grow and all its lines to manifest themselves, high temperature and excess of reagent did not provide such an opportunity. The former case applies to the patterns of this work, which have been prepared by regulated addition of hydrazine hydrate at a temperature not exceeding 1° C. The latter case describes the prolonged reflux in propanol used to H-insert the samples of SBP-A (above s = 0.12) studied in the paper[37].

When the features of the end product of the H-insertion were reached, the two sets of patterns meet again and the differences are reduced to the presence of precipitated manganite in the authors' work[37] as shown in Fig.3.23.

3.3 Results of the FTIR Study of SBP-A

3.3.1 Introduction

Infrared spectroscopy is increasingly used as a characterisation technique in the manganese dioxide H-insertion field of study[10,13,16,37,38]. Fourier Transform Infrared (FTIR) spectra of all SBP-A samples were collected and processed as described in Chapter 2. This study aimed to monitor H location through inspection for OH bond vibrations. Qualitatively, the H-insertion products identified were compared with published spectra of groutite and manganite[10]. Comparison with previous work[37] has also been carried out. It is noteworthy that FTIR spectroscopy has been found more sensitive than XRD for qualitative analysis.

The infrared spectra of manganese dioxide have been divide into two regions: the low frequency side was assigned to the [MnO_6] octahedra vibrations while OH bond vibrations took place in the rest of the frequency range. Potter and Rossman[10] suggested that the boundary between these two regions was 1400 cm^{-1}, a claim denied by Fitzpatrick et al.[13] who gave an alternative value of 800 cm^{-1}. A third boundary of 700 cm^{-1} has also been suggested by Kohler et al.[16]. In this work, selected spectra of samples covering the whole H-insertion range are shown in Fig. 3.24. The "valley" separating the features due to the ionic framework (the octahedra) vibrations and the rest of the spectra is located around 788 cm^{-1}. Therefore, the 800 cm^{-1} choice seems more reasonable. Although both domains of vibrations provided information on the H-insertion, this study focused mainly on the OH bonding frequencies.

A common feature of the FTIR spectra (Fig. 3.24) is the rising tails at higher wavenumbers (> 3200 cm^{-1}). This is likely to be due to scattering from large particles since the initial sizes range between 45-90 μm for the most H-inserted and the starting materials respectively. Although grinding of up to 30 minutes was tried (section 2.5.2), the particles were still far larger than the ideal size, which should be less than the shortest wavelength investigated (i.e. below 2.3 μm), for quality IR spectra[102]. Before proceeding to the discussion of the spectra, it is noted that the signals situated

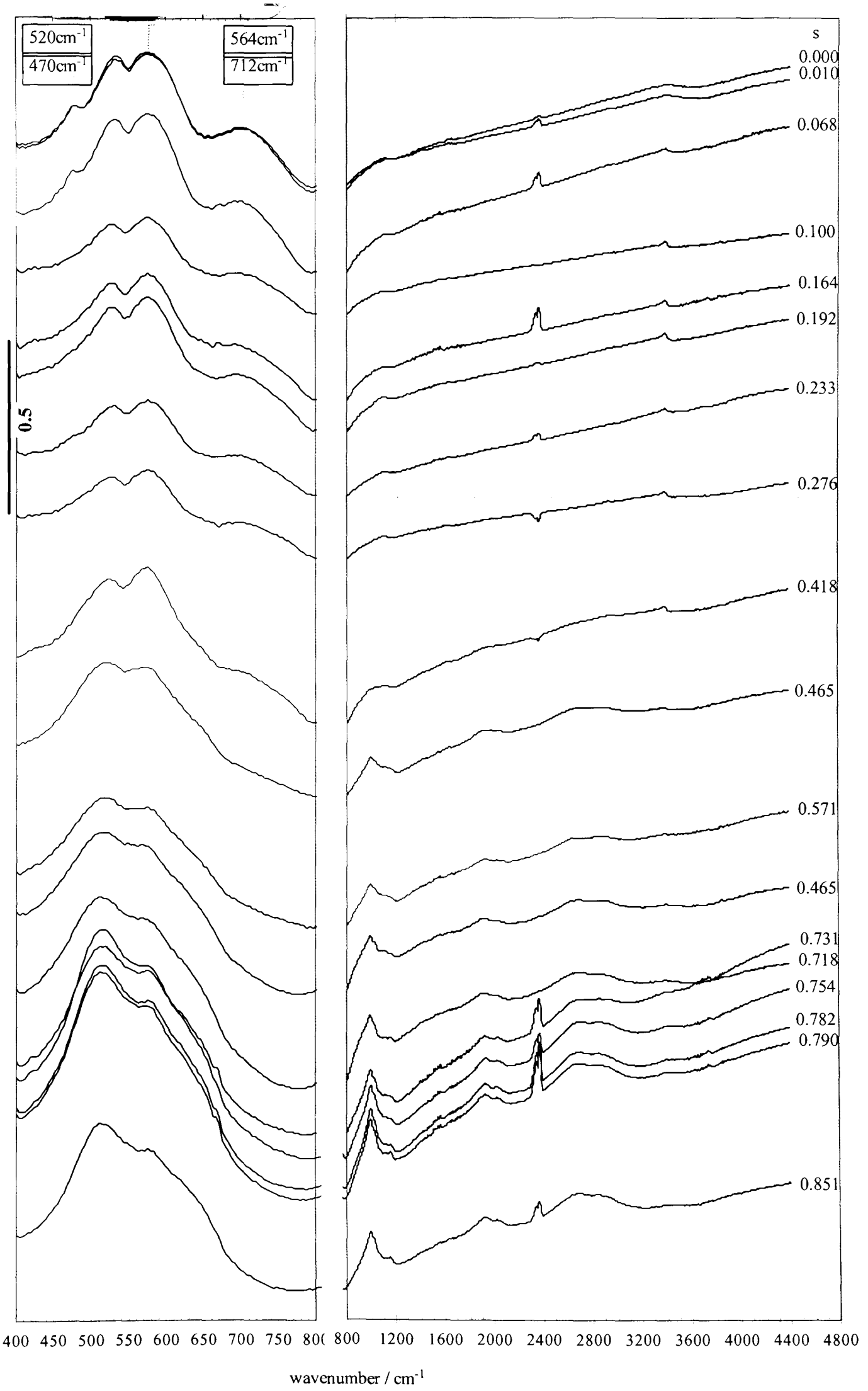

Fig. 3.24 Selected FTIR spectra of SBP-A stepped down the page in proportion to the insertion level. Left octahedral vibrations, Right OH vibrations.

between around 2240 and 2380 cm^{-1} are due to minor errors in the background correction. They appear positive or negative, high or low according to the local CO_2 level at the time of spectra measurement.

3.3.2 Mobile H

Careful examination of Fig. 3.24 reveals that the spectra of samples with $s \leq 0.28$ kept the features of the spectrum of the starting material. This is evidence that the initial structure has not changed. However, the shoulders of the main doublet (520 & 564 cm^{-1}) in the starting spectrum, seemed to shift as the H-insertion proceeded. This was also the case for the shoulder at ~ 470 cm^{-1} which died away as early as 0.16 in s. Another shoulder at ~ 712 cm^{-1} persisted over a wider range of s but become completely absent in the spectra of higher H-insertion levels. All of these peaks and shoulders moved to lower wavenumbers (lower energies). This is an indication of some change in the local environment of the octahedra which may be due to the limited structural rotation already concluded from the XRD data.

Table 3.2 Assignment of FTIR bands to O-H vibration modes from ref. 13.

band range / cm^{-1}	O-H vibration	band code
2248-3200	O-H stretching + adsorbed OHX*	ar1
1752-2152	O-H stretching	ar2
1300-1672	overtones of octahedral bending frequencies	ar3
856-1224	in-plane & out of plane OH bending	ar4

*OHX refers to hydrous compounds physically or chemically adsorbed on the MnO_x surface.

As for the spectra above 800 cm^{-1}, no changes at all occurred up to and inclusive of 0.28 in s; indicating that there was no O-H bonding in this region. Thus, while the H inserted in the range $0 \leq s \leq 0.28$ altered the octahedral vibration, due to change in charge on central Mn ion, no OH bonding was detected. The H inserted must have been mobile in the structure. Absence of O-H bonds in the homogeneous region is further illustrated in Figs. 3.25-3.27 displaying the net peak area of three fundamental O-H vibrations. These peaks have been assigned[13] to specific O-H vibrations (as indicated in Table 3.2) based on the work of Verdonk et al.[94] on goethite (α-FeOOH) as both goethite and groutite belong to the same diaspore structure (α-AlOOH)[95].

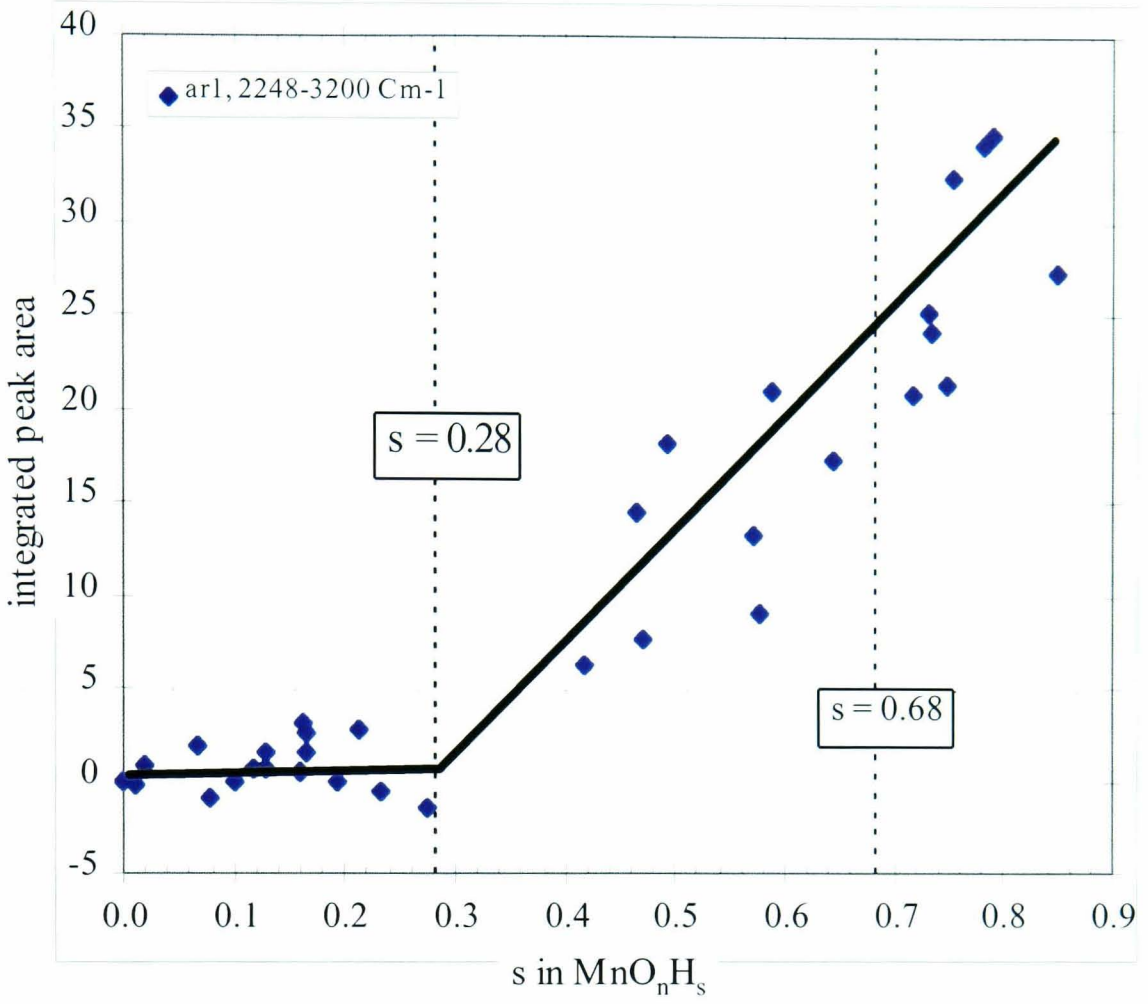

Fig.3.25 Peak area of band Ar1 vs. insertion level s. OH stretching + adsorbed OHX

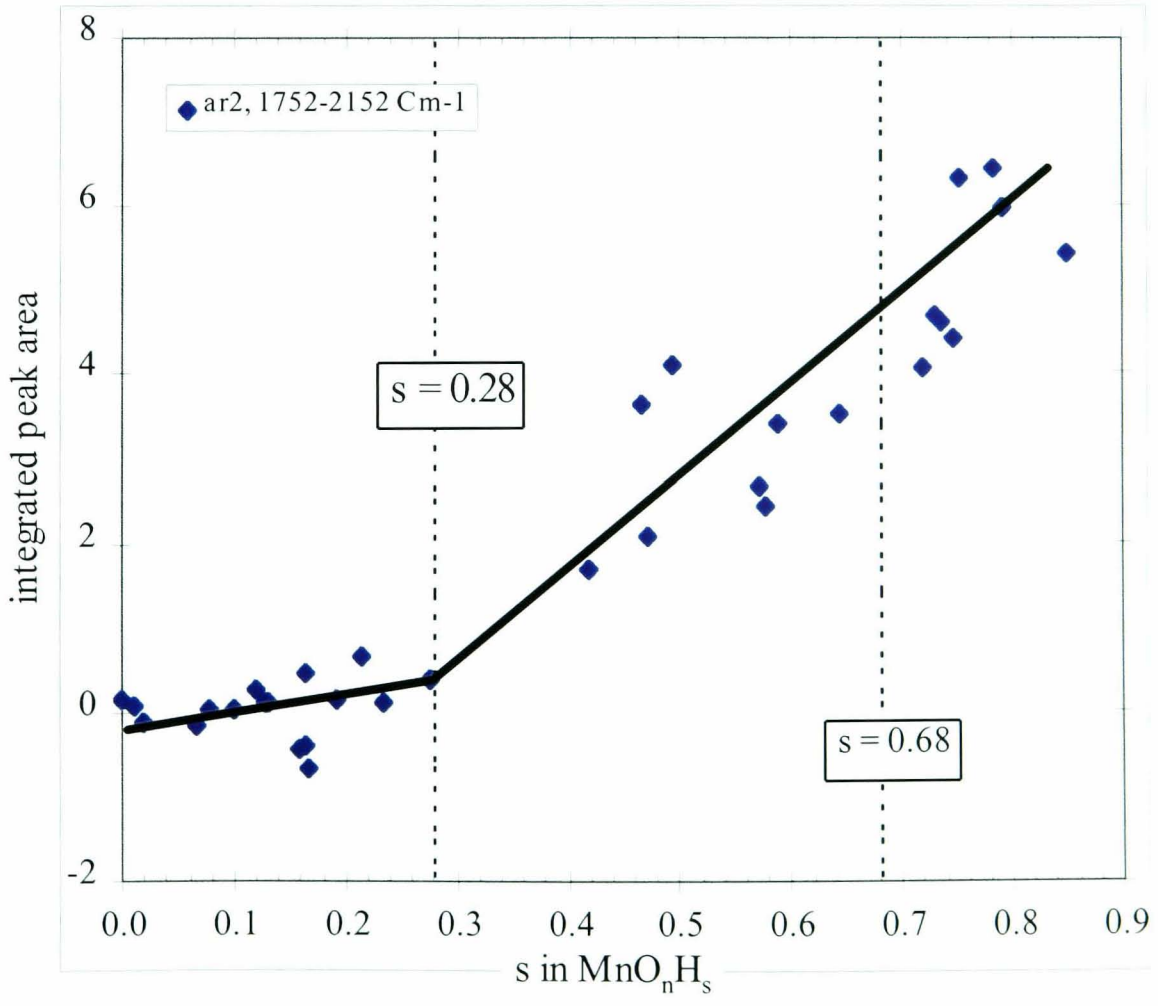

Fig.3.26 Peak area of band Ar2 vs. insertion level s. OH stretching mode.

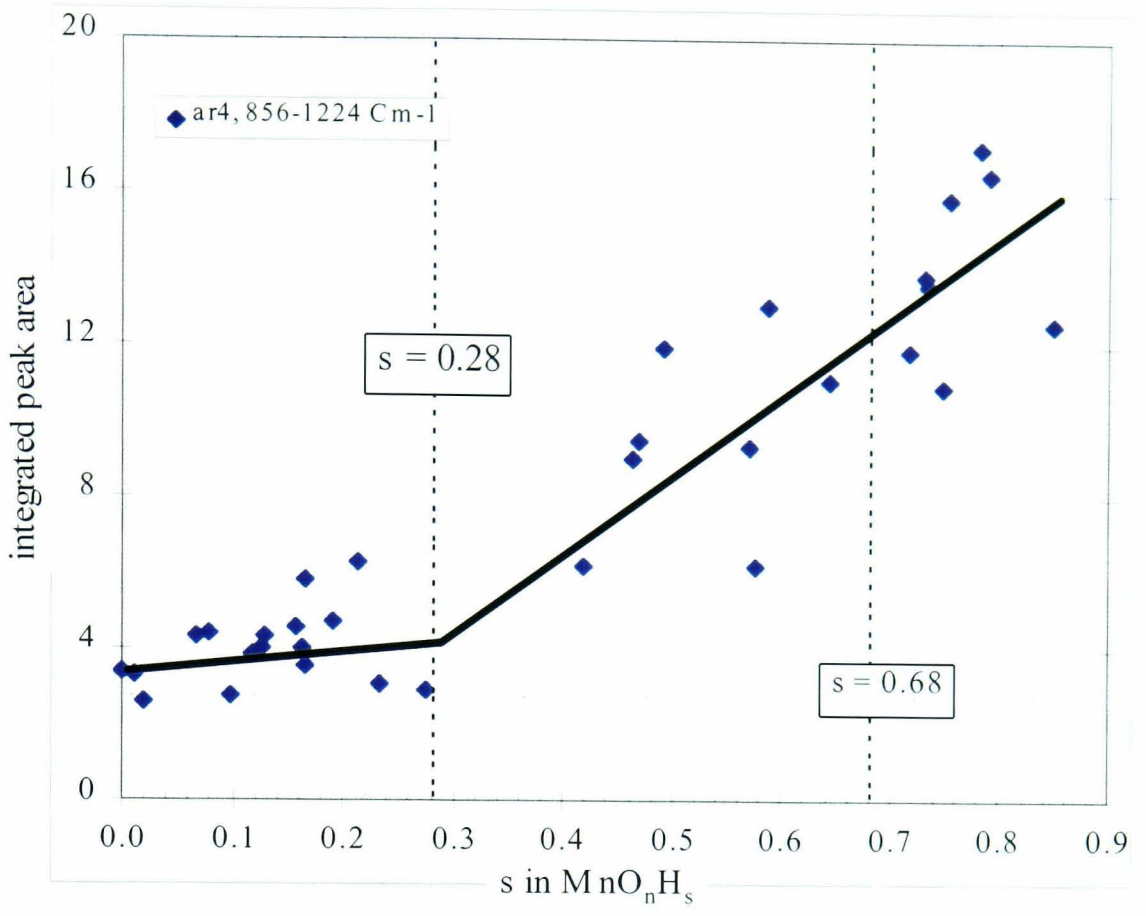

Fig.3.27 Peak area of band Ar4 vs. insertion level s. in-plane & out of plane OH bending modes.

3.3.3 Located H

Above 0.28 in s, the octahedral vibrations changed and the intensity of the two peaks in the main doublet changed so that the weaker peak (initially at 520 cm^{-1}) became stronger at about 500 cm^{-1} and the strong peak became a shoulder at ~ 550cm^{-1}. This is an indication of structural change. Thus, different changes in octahedral vibrations are apparent in the first two regions of H-insertion. The third region ($s > 0.7$) where the H-insertion proceeded homogeneously to the end product is not expected to be detected by FTIR since it did not incur significant changes in the octahedral structure. Hence, only two regions could be delineated from the FTIR spectra.

The main characteristic of the spectra above $s = 0.28$ is, however, the presence of O-H bond vibrations in contrast to their absence in the first homogeneous region. The areas of the O-H vibration bands were integrated and the background, which was evaluated by a straight line connecting the band boundaries, was subtracted. Hence, the net areas coded ar1-ar4 (Table 3.2) were obtained, as previously[13,37]. Plotting these areas against the H-insertion level is expected to reveal when OH bonds were formed, i.e. when H located. Three out of the four areas commenced with a flat section of

practically nil area showing that no OH bonding was detected; the bands areas are independent of H-insertion level. As from s = 0.28, OH bonds were clearly formed and enhanced steadily upon H-insertion. The fourth band between 1300 and 1672 cm^{-1} has been assigned previously[13,37,38] to overtones of octahedral bending frequencies particularly at 1415 and 1548cm^{-1}. This assignment was justified by the fact that two small peaks appeared at those frequencies in the early homogeneous region and persisted throughout the full H-insertion range, at about the same intensity. These peaks did not appear in the spectra of SBP-A, in this work (Fig. 3.24), and are now thought to be due to an organic substance from the reaction media since organic reagents were employed in all those studies[13,37,38]. This claim is supported by the spectra of H-inserted Faradiser M (Fig. 4.16) and that of R2 (Fig. 5.17) where these peaks are also absent.

3.3.4 Preferential H-Insertion Sites

The second homogeneous insertion into SBP-A provides an opportunity to examine for preferential H location sites. Since by this stage H was already located, further H-insertion (between s = 0.72 and 0.85 in this work) simply enhanced the OH band in the FTIR spectra. Thus, monitoring the OH bond vibrations in the spectra of the samples could reveal whether groutite or manganite vibrations were enhanced. Fig. 3.28 compares the spectra of selected H-inserted SBP-A in this region with the spectra of groutite and manganite[10]. The position of peaks characteristic of both manganite and groutite are shown by dotted lines. Inspection of the most H-inserted SBP-A material indicates clearly that, in addition to the obvious groutite bands, there is a small amount of manganite in the intergrowth as evidenced by the shoulders at 1088 and 1152 cm^{-1}. These manganite shoulders appeared simultaneously with the groutite bands, see Fig. 3.28. Fig. 28 shows clearly that H-insertion occurred in both the groutite and manganite blocks in the product of the heterogeneous insertion. Furthermore, the ratio between the peaks of the two blocks did not significantly change throughout the second homogeneous stage. Therefore, there were no preferred octahedral sites for the inserted hydrogen.

The light bump around 3390 cm^{-1}, which coincides with a manganite broad band, could not be assigned to manganite absorption simply because it appeared in the starting material and to s = 0.57 but weakened thereafter. However, the decrease appeared to coincide with a decrease in the octahedral vibration at 564 cm^{-1} so it is

suggested that this bump is an overtone of the 564 cm^{-1} band. The additional information yielded here is that the 564 cm^{-1} band may belong to pyrolusite.

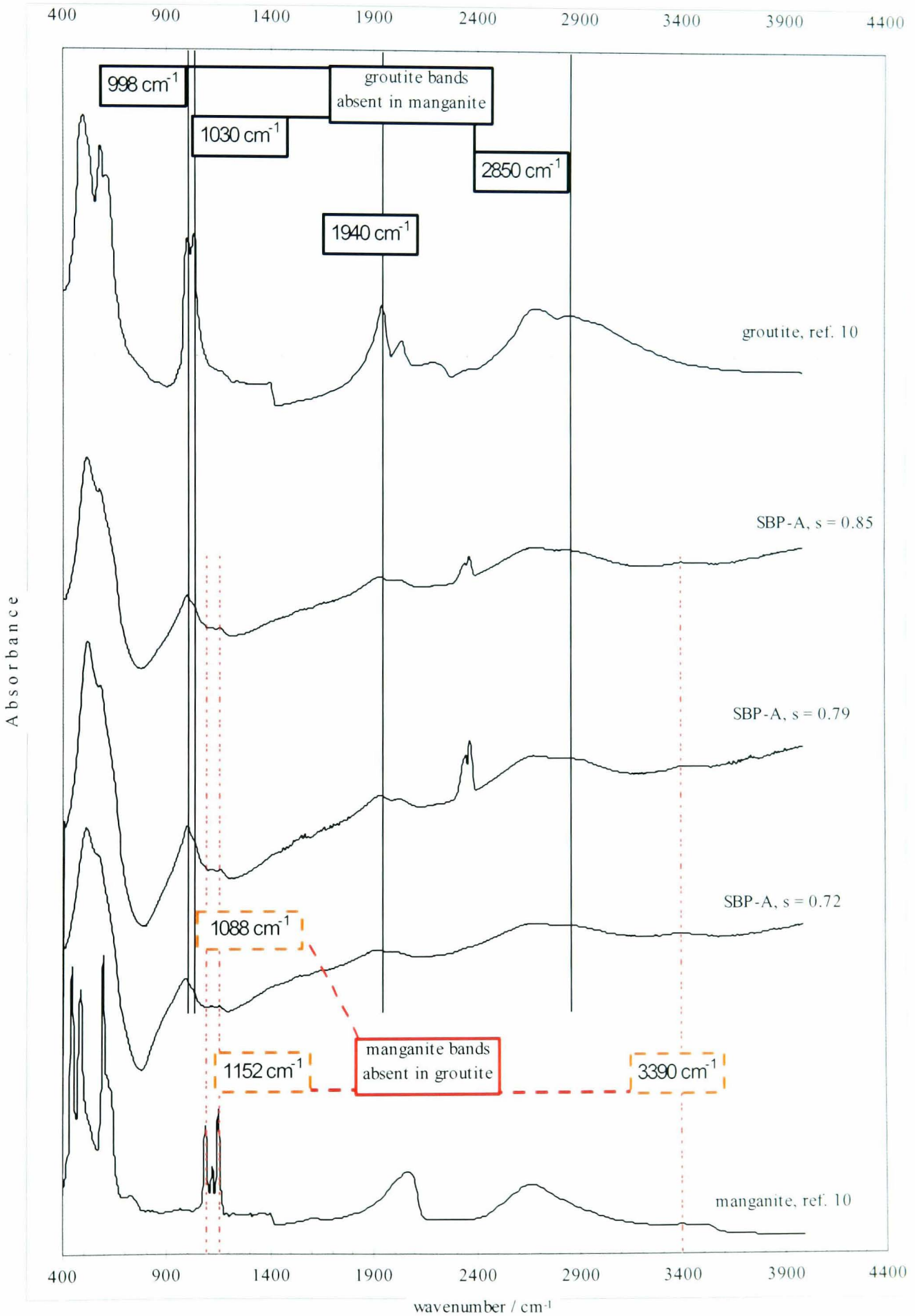

Fig. 3.28 FTIR spectra of selected H-inserted SBP-A samples in the last homogeneous stage, compared with published spectra of manganite and groutite (from ref. 10).

3.3.5 Comparison with Previous FTIR Study

The FTIR spectra of SBP-A samples were compared with the spectra of the same material as studied by MacLean and Tye[37]. Selected compared spectra are shown in Figs. 3.29-3.32. The spectra of this work was multiplied by a factor ranging from 1.4 to 3, in order to match the octahedral vibrations of the two sets for easy comparison.

The huge difference in intensity between the two sets is probably due to the different pellet preparation techniques. The procedure quoted in the reference paper[37] consisted of mixing ~3 mg sample with ~450 mg CsI and grinding this mixture, then taking approximately 200 mg to make the pellet. This procedure might have introduced sampling error altering the sample to matrix ratio in favour of manganese dioxide, the densest constituent; hence the higher absorbance. The experimental procedure followed in this work is detailed in section 2.5.

Again, this comparison shows that there is substantially more manganite in the authors' samples, particularly at high insertion levels, as already was concluded from the XRD study.

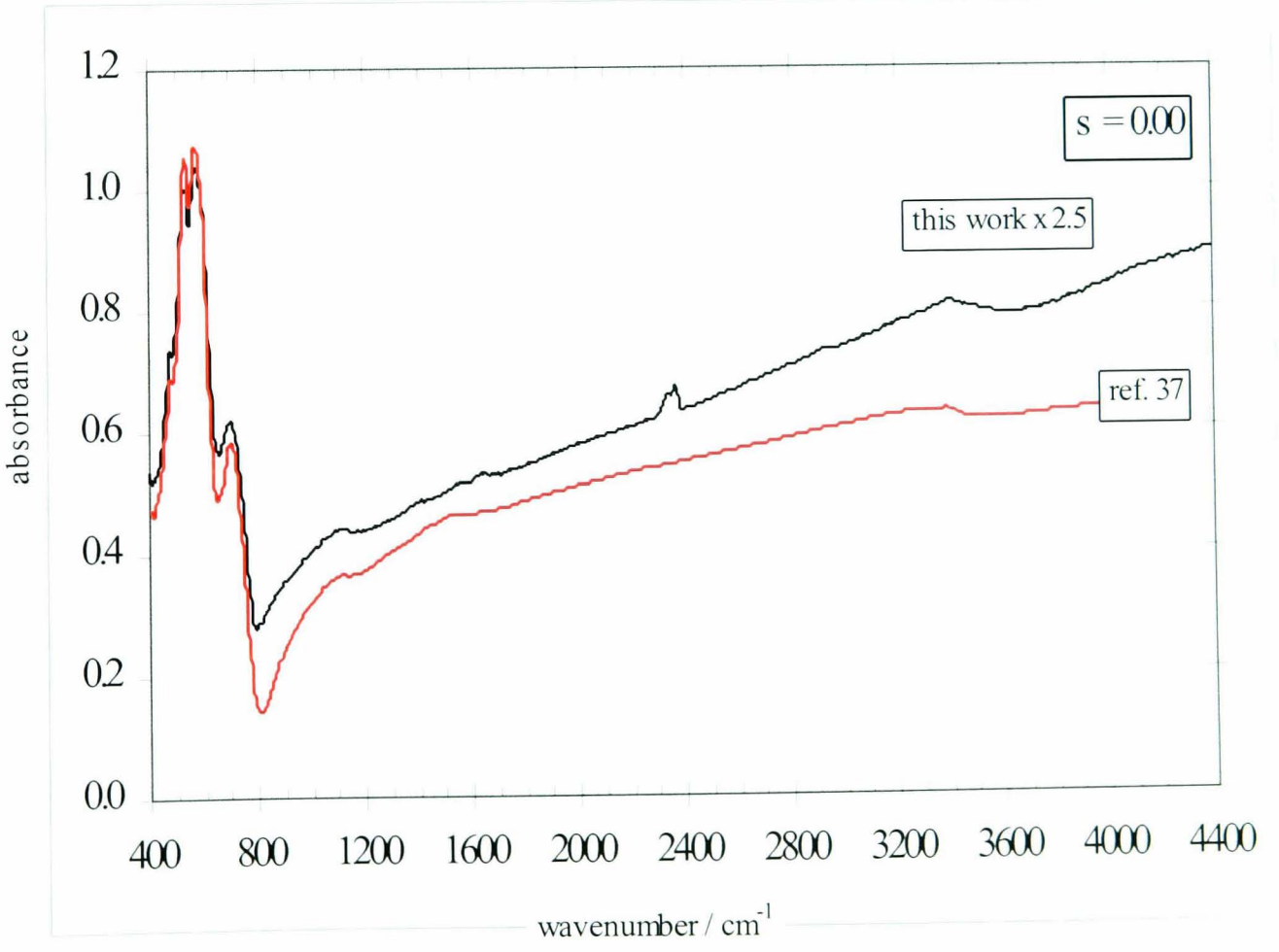

Fig. 3.29 Comparison of FTIR spectrum of SBP-A in this work and in ref. 37.

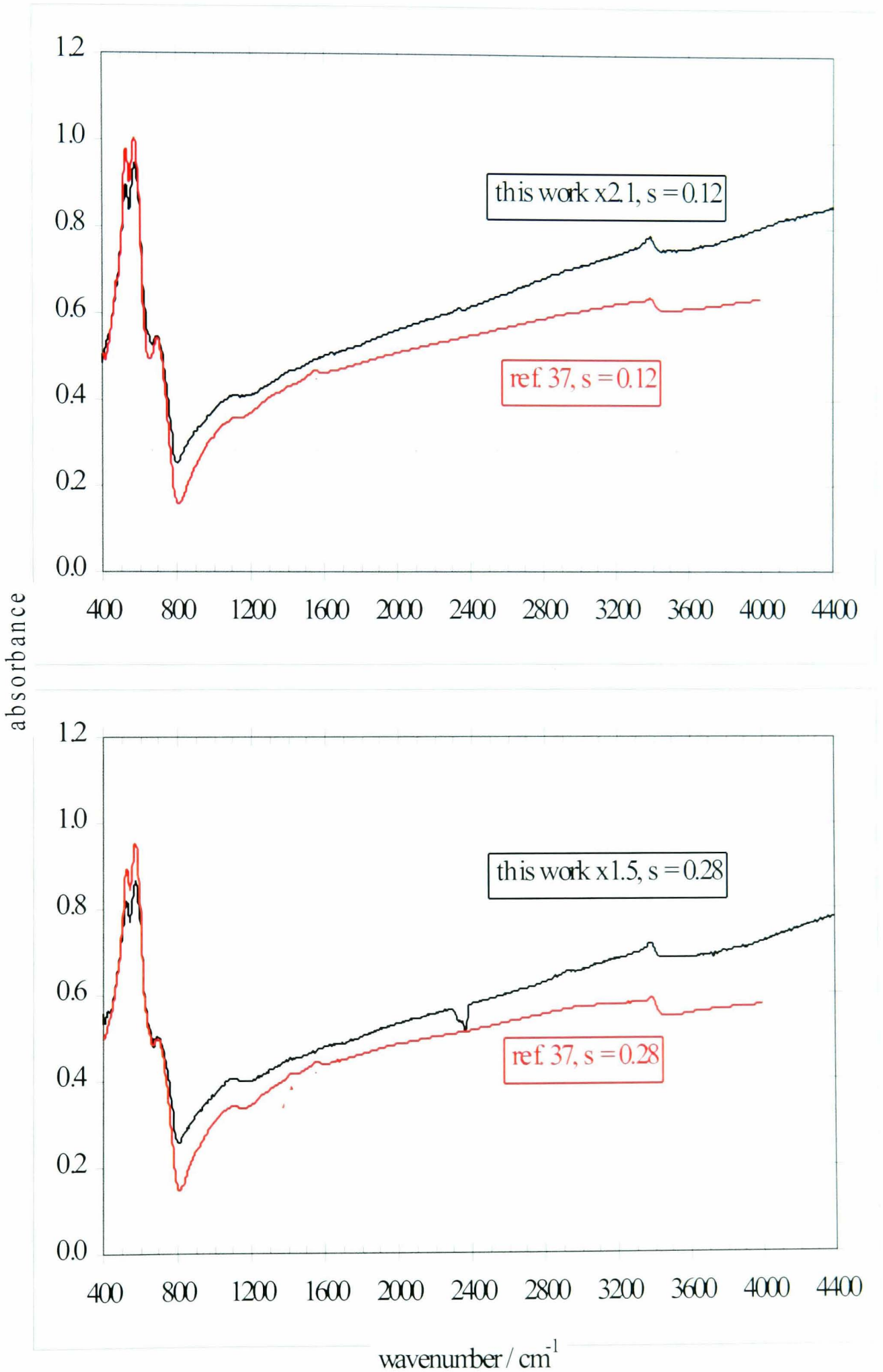

Fig. 3.30 Comparison of the FTIR spectra of H-inserted SBP-A, in this work and ref. 37, at the early (s = 0.12) and late (s = 0.28) homogeneous stage.

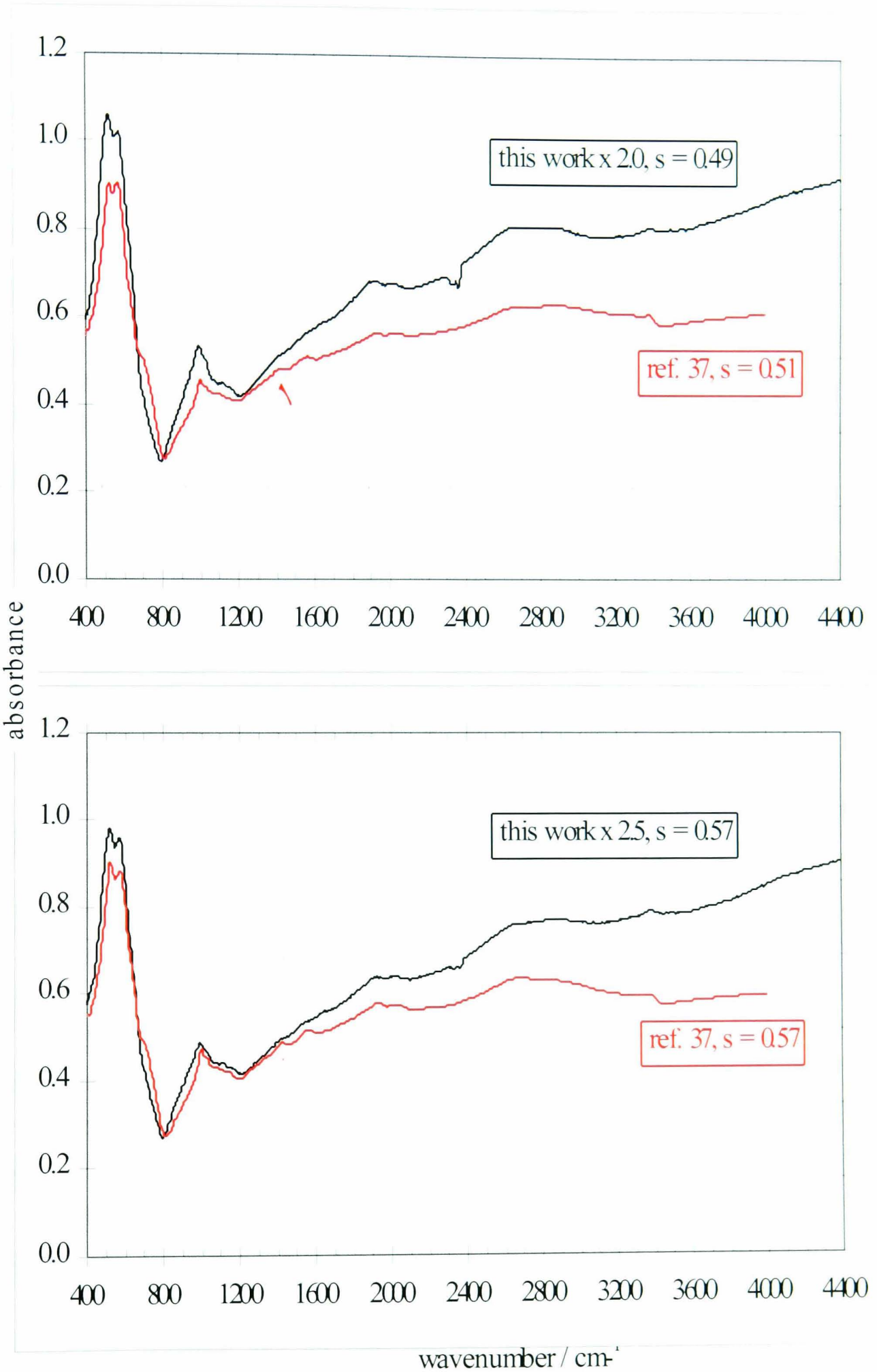

Fig. 3.31 Comparison of the FTIR spectra of H-inserted SBP-A, in this work and ref. 37, at two H-insertion levels (s ~ 0.5 and s ~ 0.6) in heterogeneous stage.

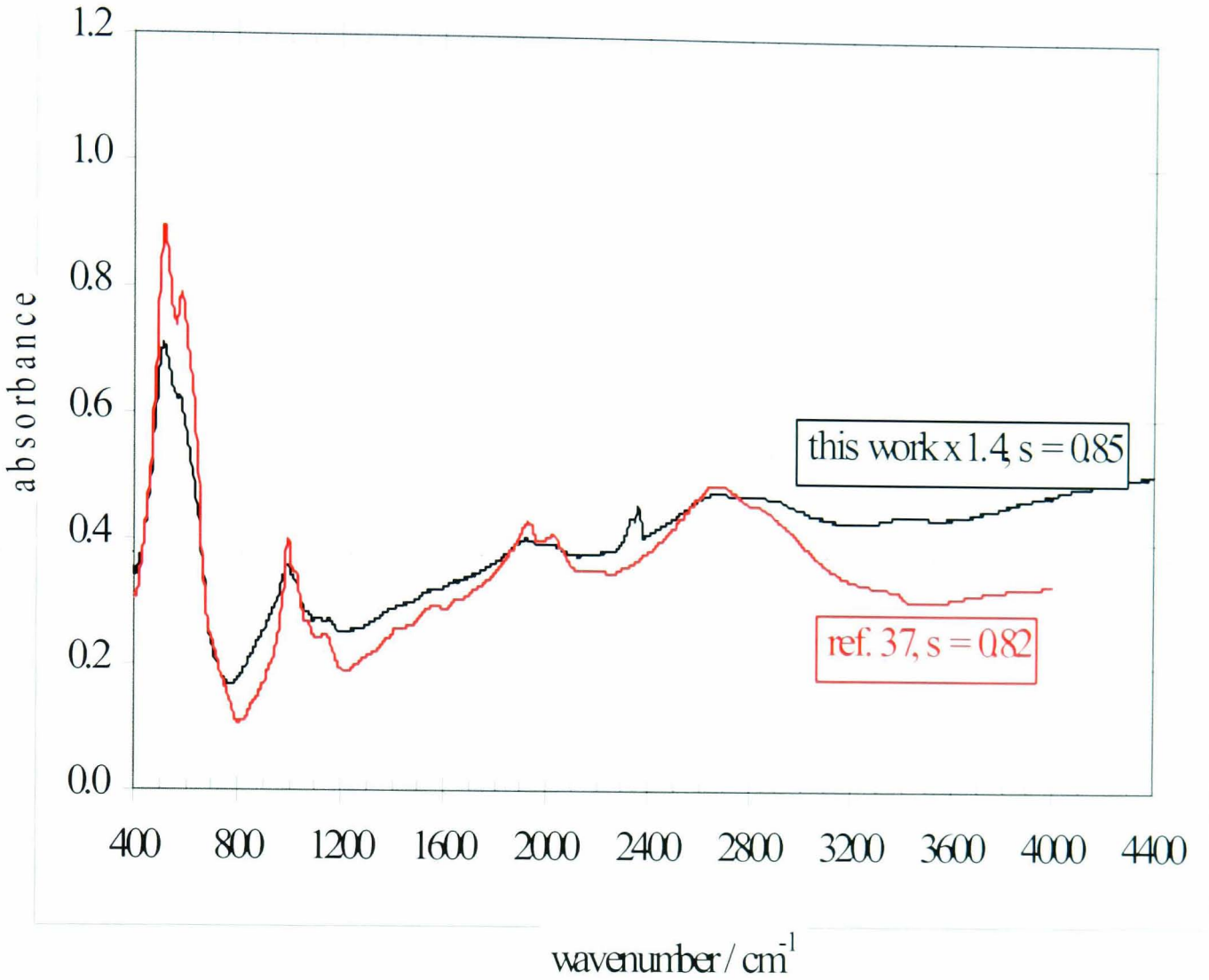

Fig. 3.32 Comparison of the FTIR spectra of the most H-inserted SBP-A, in this work and ref. 37.

3.4 Discussion of The H-Insertion into SBP-A

The XRD study of mild chemically H-inserted SBP-A samples has revealed that the insertion proceeded in three stages: homogeneously in the range $0 \leq s \leq 0.28$, heterogeneously between 0.28 and 0.68 and homogeneously thereafter. A major advantage of the XRD patterns, as compared with previous works, is that they are free from precipitated manganite. This is thought to be due to the gentle H-insertion conditions developed in this work. Precipitated manganite was an inevitable side product of previous studies of manganese dioxide H-insertion. It is hoped that the elimination of this impurity makes the results of this work more reliable and closer to the "true" product of the H-insertion.

The first homogeneous stage took place in the initial structure of predominantly ramsdellite blocks. As Brenet[31] has shown earlier, the structure dilated as a result of

the insertion. However, unlike the previous work on the same material[37], the homogeneous expansion did not occur either along the line connecting the apical oxygens of the octahedra or in the *b* direction as predicted by many earlier papers[13,18,31,33,37,38]. Instead, a limited expansion along the *a* axis at practically constant *b* was revealed by both observation of lines movement and lattice parameter evaluation; see Figs. 3.8, 3.10 – 3.13 and 3.18.

Fig. 3.18 shows a limited rotation of the structure of SBP-A occurred in the homogeneous H-insertion. This limited rotation resulted in a slight increase of the *a* lattice parameter while the *b* and *c* remained unchanged. The reason for unchanged *b* and *c* dimensions is likely to be that the microtwinning, though in low amount, across the 021 and 061 lines is restraining the structure in these directions. The gentle H-insertion conditions are insufficient to remove the microtwinning at this stage. This behaviour is a new finding.

The FTIR spectra during this stage have no sign of OH vibrations, ruling out the possibility of OH bonding and leaving the only option of mobile H in the structure.

Another important finding was that at the onset of the heterogeneous reaction (s > 0.28) the lattice parameter *b* expanded considerably from a value close to the *b* dimension of ramsdellite to a new value close to that of groutite. This transformation occurred between s = 0.28 and s = 0.68. In comparison with the work of MacLean and Tye[37] presented on the same figure (Fig. 3.18), this huge expansion in *b* must mean that the initial restraint, which inhibited expansion during the homogeneous insertion, was now removed; i.e. the structure must have demicrotwinned. Evidence of H location in the heterogeneous phase is provided by the FTIR spectra discussed in section 3.3. The shape of OH absorption bands, particularly the main band at about 2800 cm^{-1} (Fig. 3.24), indicates that hydrogen bond vibration is included in addition to the proper OH bond vibration. The evidence is the broadness and shift towards the low frequency side of the band[124].

Therefore, the heterogeneous insertion proceeded from a microtwinned ramsdellite-like structure with mobile H to a demicrotwinned groutite-like structure where the H is located. Hydrogen location in groutite tunnels while mobile in ramsdellite tunnels strongly indicates that the driving force to the H location is the rotation of the initial structure (compare tunnel shapes apparent from Fig. 3.1 and the angles in Table 3.1). In fact, the rotation brings the O2 and O1 oxygens (section 1.2.2) closer together and facilitates the formation of a H bond. The absorption bands are due to covalent H-O2

bond and hydrogen bond with O1; i.e. O2-H···O1. This point is reviewed with further details in Chapter 6.

The demicrotwinning, leading to expansion in *b* dimension, must break up the initial structure. This is in line with scanning electron microscope (SEM) pictures. The SEM images show two main facts: the particles are of the same size throughout the first homogeneous phase and occasional slight cracking can be seen at higher magnifications. This cracking may be due to high local H-insertion. At this stage particles of as large size as 140 μm can immediately be seen, see Figs. 3.33 through 3.35. However, in the heterogeneous stage, the fraction of the larger particles has substantially reduced and the cracks persist and increase, see Figs. 3.36 to 3.38.

In conclusion, demicrotwinning seems central to the heterogeneous phase H-insertion leading to four simultaneous facts: large expansion of the *b* dimension, H location, emergence of new XRD lines and (limited) particle break up.

In the last homogeneous stage, the insertion proceeded in the structure of the final product which is an intergrowth of groutite and manganite layers reflecting the original de Wolff disorder in the starting material[92]. An important result drawn from the FTIR spectra in the last homogeneous stage was that the inserted H located simultaneously into both the groutite and manganite blocks of the intergrowth as is shown in Fig. 3.28.

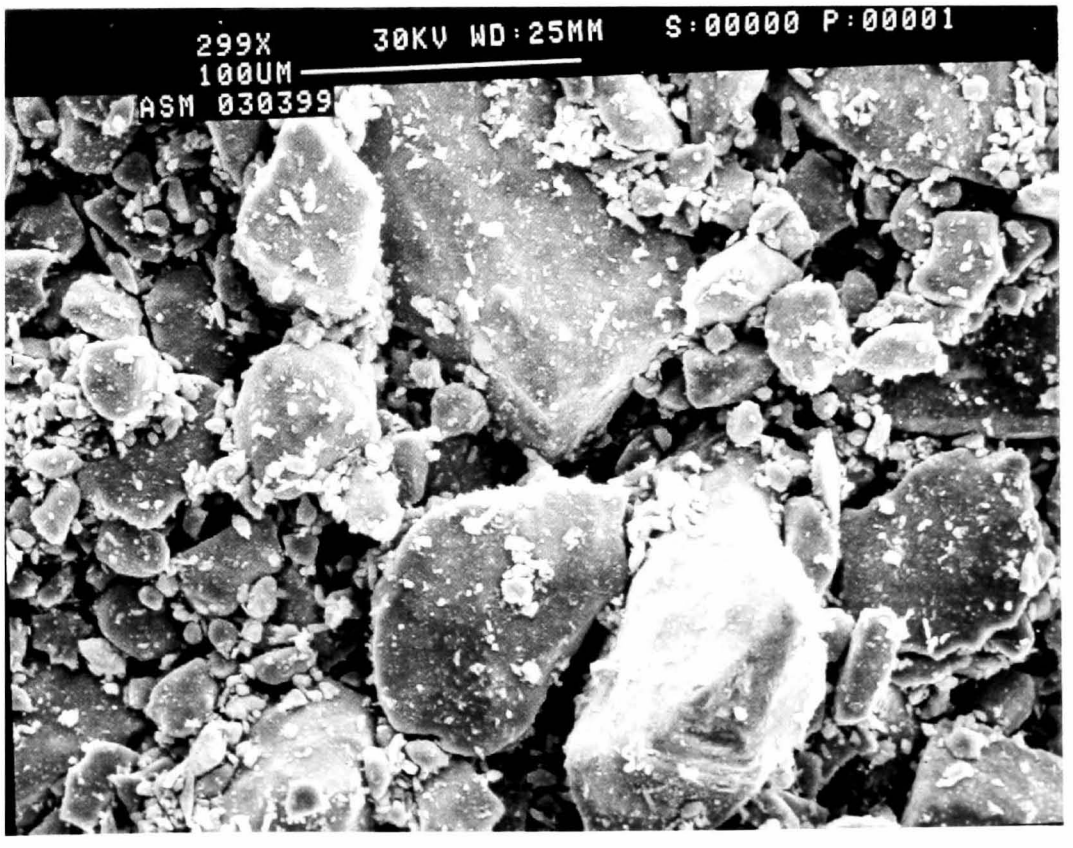

Fig. 3.33 SEM picture of SBP-A starting material at low magnification. Note the large size of the particles.

Fig. 3.34 SEM picture of H-inserted SBP-A in the homogeneous region (s = 0.143) at medium magnification. Note the limited cracking of the particles.

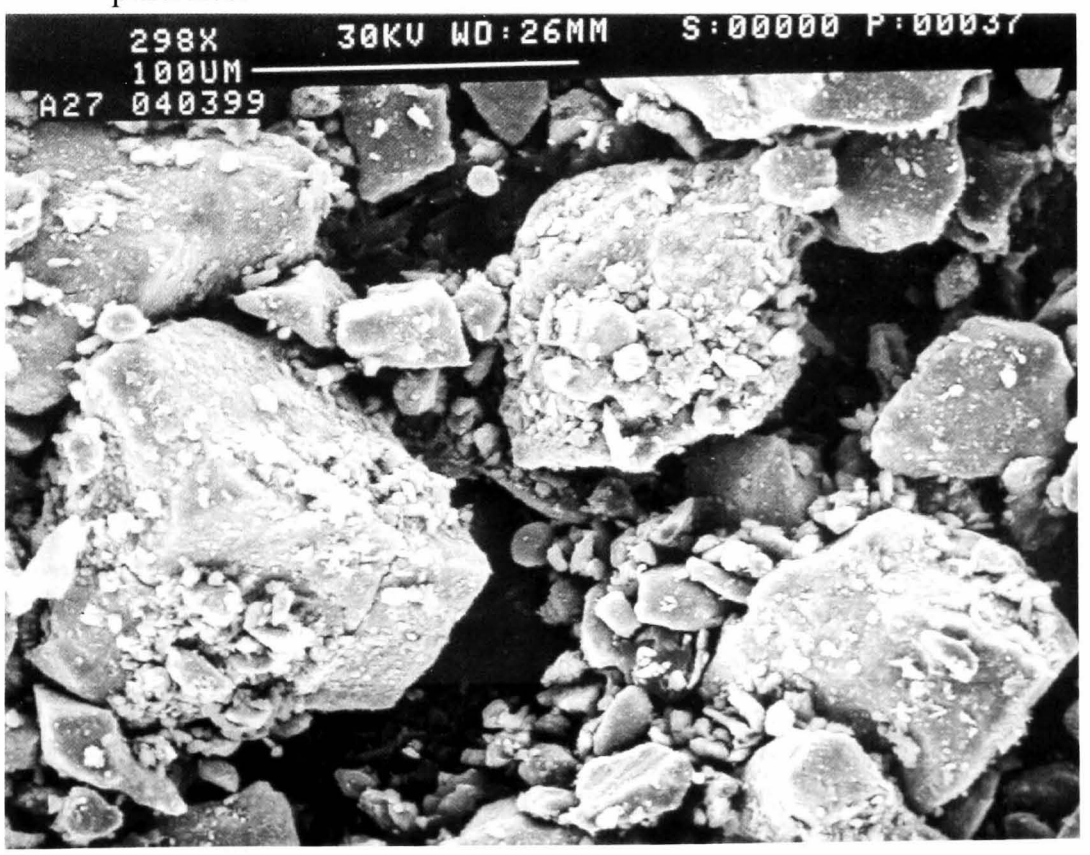

Fig. 3.35 SEM picture of H-inserted SBP-A in the homogeneous region (s = 0.276) at low magnification. Note that the particles size is still large.

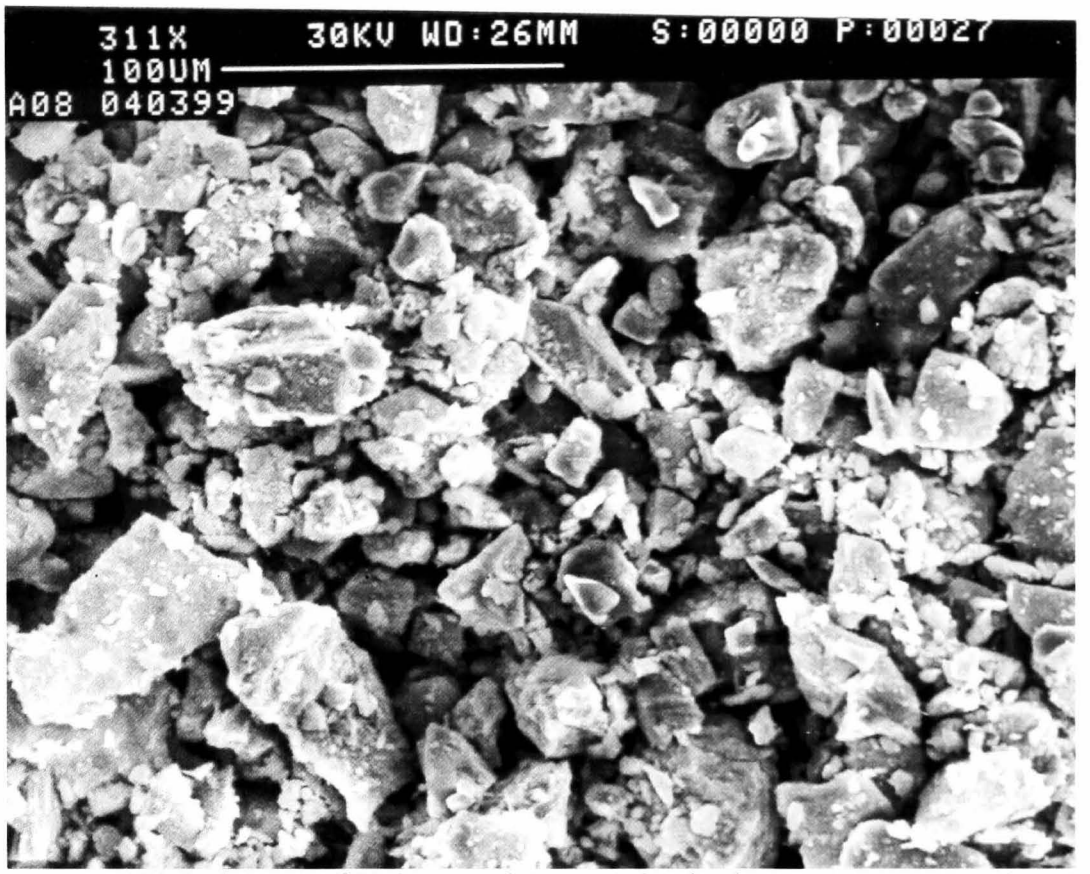

Fig. 3.36 SEM picture of H-inserted SBP-A in the heterogeneous region (s = 0.589) at low magnification. Note that the particles size has reduced significantly.

Fig. 3.37 SEM picture of H-inserted SBP-A in the heterogeneous region (s = 0.645) at low magnification. Further H-insertion led to further reduction of particles size.

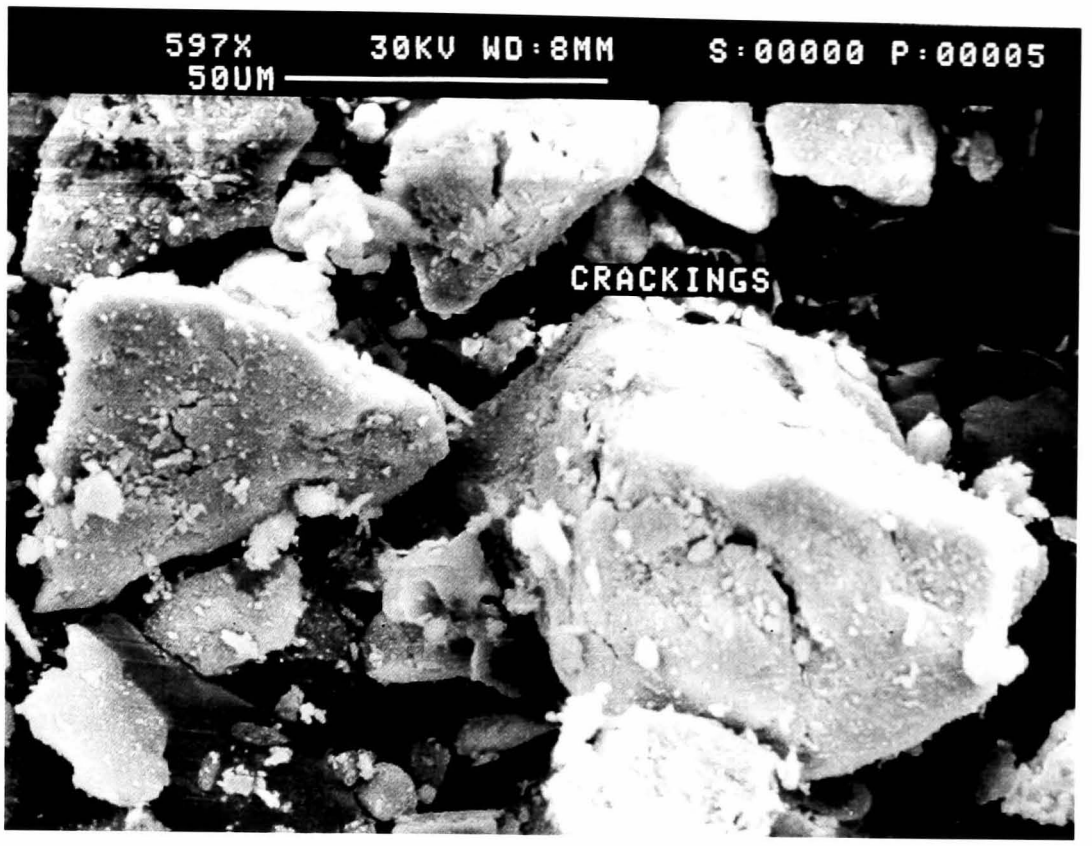

Fig. 3.38 SEM picture of H-inserted SBP-A in the second homogeneous region (s = 0.782) at low magnification. Note the severe particles cracking.

The conclusion conflicts rather sharply with a mechanism suggested by Pannetier[18,25-29] and co-workers[88,89] which states that the Mn atoms in ramsdellite part of the intergrowth are reduced first and the pyrolusite part is reduced in a later stage; i.e. the H-insertion occurs preferentially into the ramsdellite blocks.

3.5 Conclusions

- XRD study has shown that H-insertion into material SBP-A proceeded in three different and distinguishable stages. In the first, a homogeneous single phase was formed between the H-inserted and the host materials, as H was mobile. The second stage was a heterogeneous reaction in which, for the first time, the initial and final phases were present side by side. The heterogeneous reaction transformed steadily the initial homogeneous phase into the final product structure. The boundary between these two stages was found to be close to 0.28 in s. The third stage was a homogeneous growth of the final H-insertion product. This conclusion is evidenced by the movements of the orthorhombic lattice parameters *a* and *b* of ramsdellite as well as the vibrations of the [MnO6] octahedra and OH bond formation.

- The main effect the first homogeneous stage was a limited rotation of the structure. resulting in an increase of the *a* dimension of the unit cell at a constant *b*. This rotation was evidenced by the evaluated lattice parameters as shown in the structural map. This behaviour is a new finding. The FTIR data added two main characteristics to the homogeneous stage: bands due to the octahedral vibrations moved to lower energy and those due to OH vibrations were completely absent.
- The heterogeneous stage was featured by the appearance of new XRD peaks, belonging to the structure of the final product, and OH bond formation in the FTIR spectra indicating location of initially mobile H.
- The H-insertion occurred in both ramsdellite and pyrolusite slabs simultaneously and without preference of either site.

4 XRD & FTIR Study of Faradiser M

4.1 Introduction

Faradiser M is a CMD produced by SEDEMA[36] (Belgium) for the primary battery industry. It has been characterised as having approximately 70 % de Wolff disorder and a low amount of microtwinning[18] (section 2.1). This means that 7 out of 13 Mn atoms belong to the pyrolusite part of the intergrowth and the remaining 6 atoms to the ramsdellite part. The first question, hence, was in which structure should the few broad XRD lines of Faradiser M be indexed.

As the H-insertion caused the structure of the host material to expand and hinge (section 3.1.1), indexing the XRD lines of the starting material in pyrolusite was not convenient since the hinging would change the tetragonal symmetry into orthorhombic. In this case, further refinement and indexing of the orthorhombic lines would be necessary for the H-inserted samples. This is not attainable from the poor XRD lines of these materials (see below). Additional reasons for not assigning the XRD lines of this material to the pyrolusite structure derive from the results of two different computer simulations[18,21]. MacLean[21] and Pannetier[18] simulated the XRD of γ-MnO_2 starting from the ramsdellite[103] and pyrolusite[104] data cards. By increasing gradually the pyrolusite portion from zero (pure ramsdellite) to 1 (pure pyrolusite), both authors have shown that the main pyrolusite peak at about 28.7° 2θ Cu Kα did not appear before 0.9 pyrolusite. On the other hand, the main ramsdellite peak at 22.2° 2θ Cu Kα persisted (although shifted) until 0.7 pyrolusite. Thus, the XRD lines of Faradised M were assigned to the ramsdellite/groutite structure.

The limited number of XRD lines (in the starting material) and their poor quality is obvious from Fig. 4.1. This fact makes it difficult to assign them precisely to their counterparts in ramsdellite. If the broad bump below 30° was omitted, the "best" three lines situated at about 37, 43 and 57° still exhibit some asymmetry and breadth; both symptoms of hidden lines.

In addition, the small peak around 65° is poor and weak, also indicating overlap with other lines. It was therefore necessary to deconvolute these peaks and refine the originals. This was carried out as described in section 2.4.7, and the refined peaks at about 37, 43, 57, 65 and 69° were assigned to the 021, 121, 221, 002 and 061 of

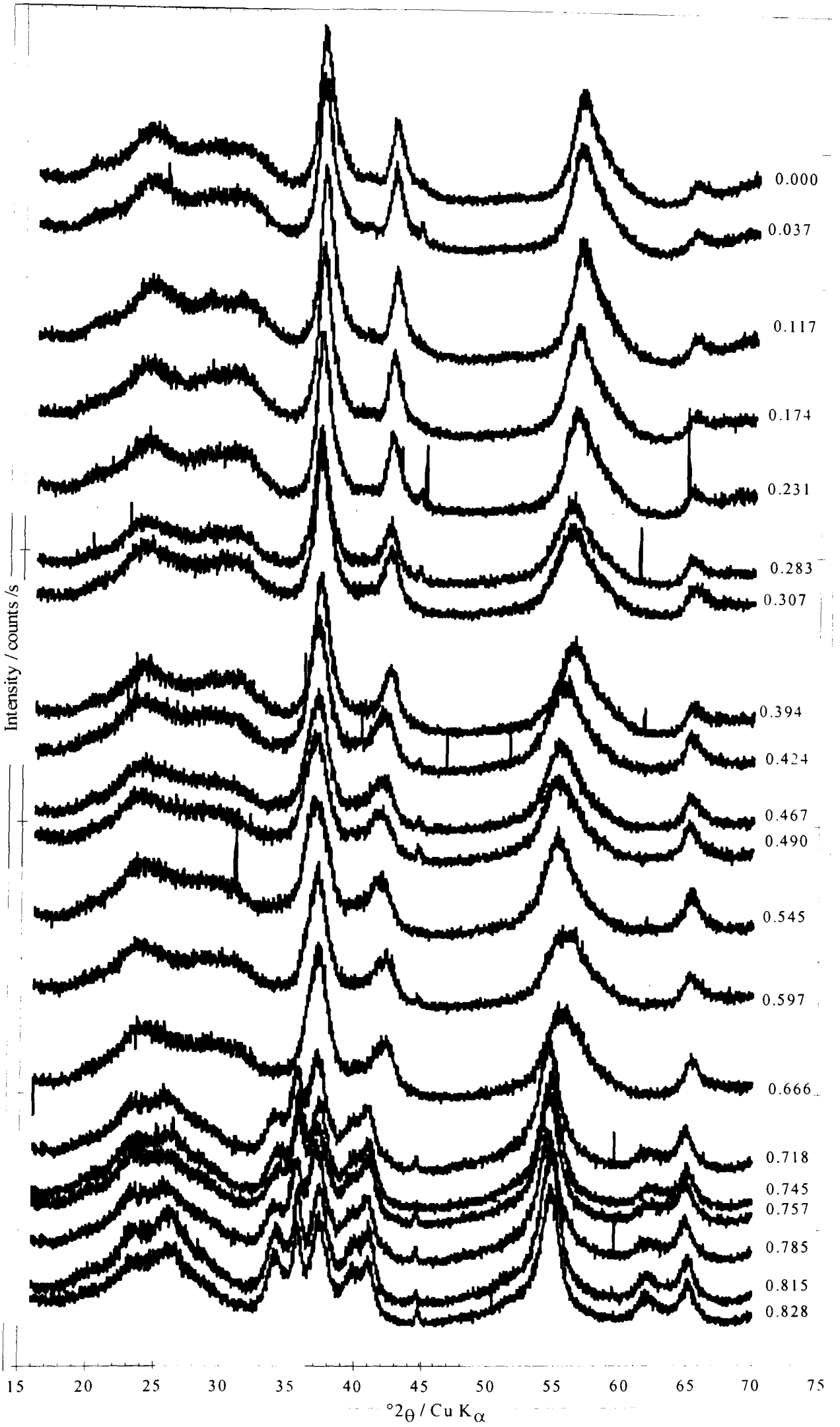

Fig. 4.1 Selected XRD patterns of H-inserted Faradiser M stepped down the page in proportion to the H-insertion level s (shown). hkℓ indices are omitted for clarity but shown in Figs. 4.2 and 4.7.

ramsdellite respectively.

The assignment of the XRD lines of Faradiser M to the ramsdellite/groutite structure follows the precedent set in a recent publication[38], studying the same material, to which reference is made here for both interpretation and comparison of the results.

A similar reporting procedure to that used in Chapter 3, is followed with this material; i.e. determination of the stages of the H-insertion, establishment of structural map, inspection for preferential H-insertion sites and comparison with previous work.

4.2 Results of the XRD Study of Faradiser M

Thirty samples of Faradiser M were H-inserted as described in section 2.2.6. The range of H-insertion covered $0 \leq s \leq 0.83$ for s in $MnO_{1.952}H_s$. These samples were subjected to the XRD study outlined in section 2.4. A selection of 23 samples has been chosen to investigate the behaviour of this material and is presented in Fig. 4.1. The new finding here was the sudden change in the XRD patterns between s = 0.67 and 0.72 which must reflect a sudden change in structure as discussed below. Fig. 4.1 shows two sets of diffractograms completely distinct from each other, reflecting two distinct phases. They are assigned to two homogeneous H-insertion stages.

4.2.1 First Homogeneous H-insertion

The first set of diffractograms that are all similar to the starting material's are shown in Fig. 4.2. All the patterns have the same features (same phase) in the range 0 to 0.67 in s in MnO_nH_s. The only difference is a steady shift towards lower angles (higher d-spacings) as s increases. There is, thus, one single phase whose unit cell dimensions vary with the insertion level. The starting material and the inserted hydrogen formed a single homogeneous phase up to 0.67 in s.

Demonstration of the homogeneous behaviour may also be seen by the shift of the deconvoluted lines over this insertion range. The same lines chosen for SBP-A material (section 3.2.1), to investigate the homogeneous/heterogeneous behaviour, have been selected for Faradiser M in Figs. 4.3-4.6.

The inter-planar spacing d_{hkl} of all four peaks increased steadily with insertion level up to 0.67 in s. This is an indication of the expansion of the structure.

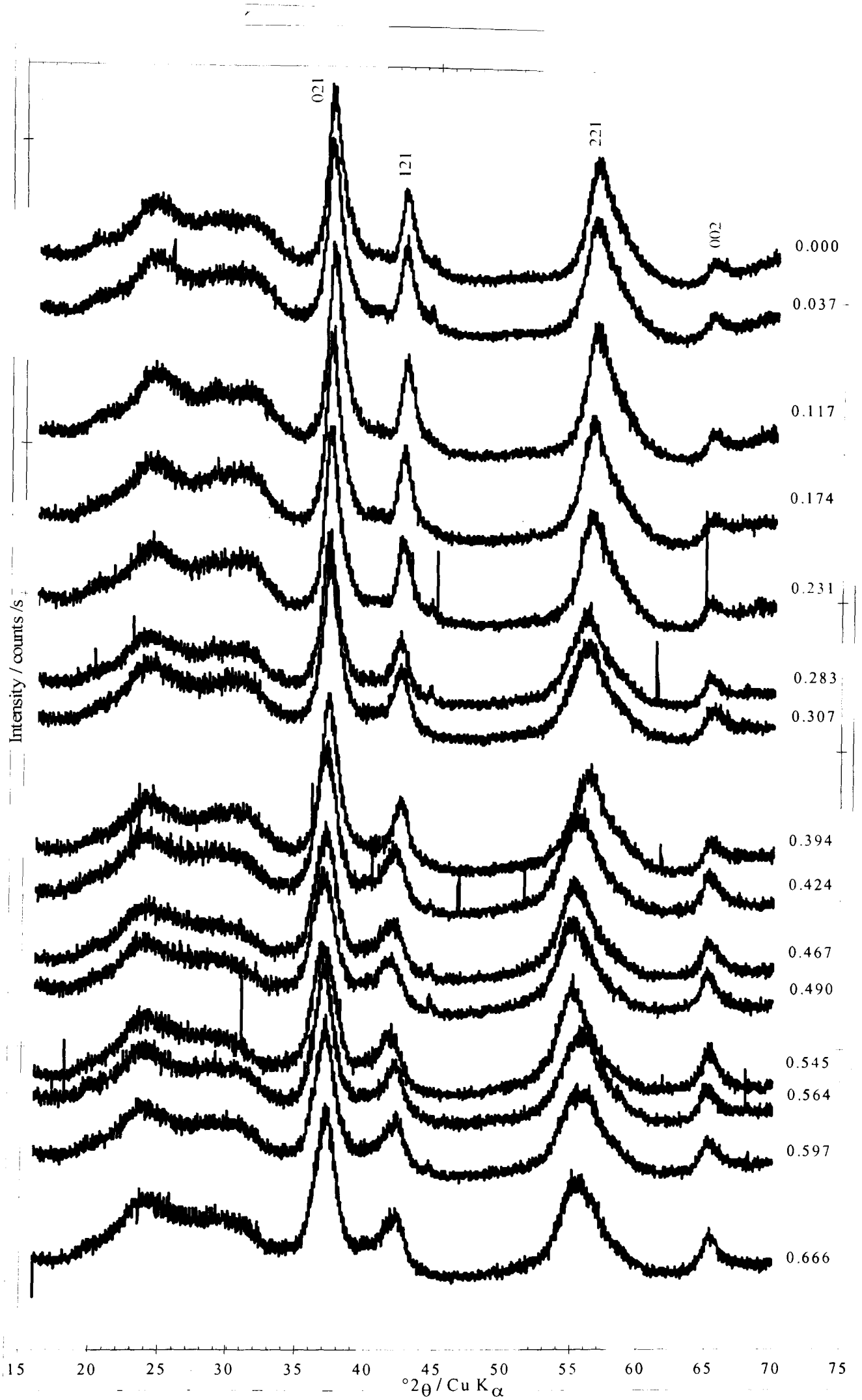

Fig. 4.2 Selected XRD patterns of H-inserted Faradiser M in the first homogeneous region stepped down the page in proportion to insertion level s (shown). The hkl indices shown refer to ramsdellite structure.

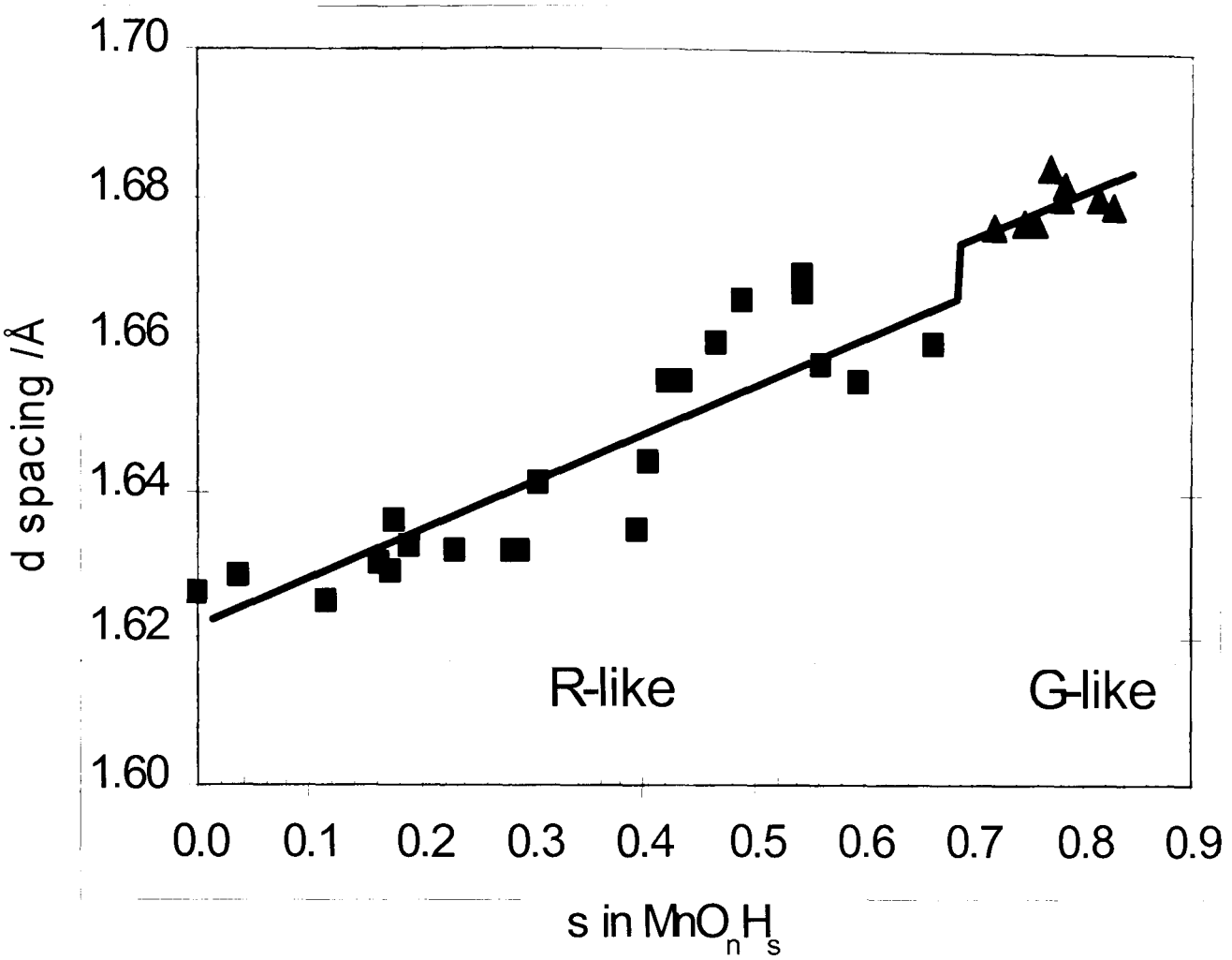

Fig. 4.3 Inter-planar spacing vs. H-insertion level of the deconvoluted 221 line of the ramsdellite (R-like) and groutite (G-like) parts.

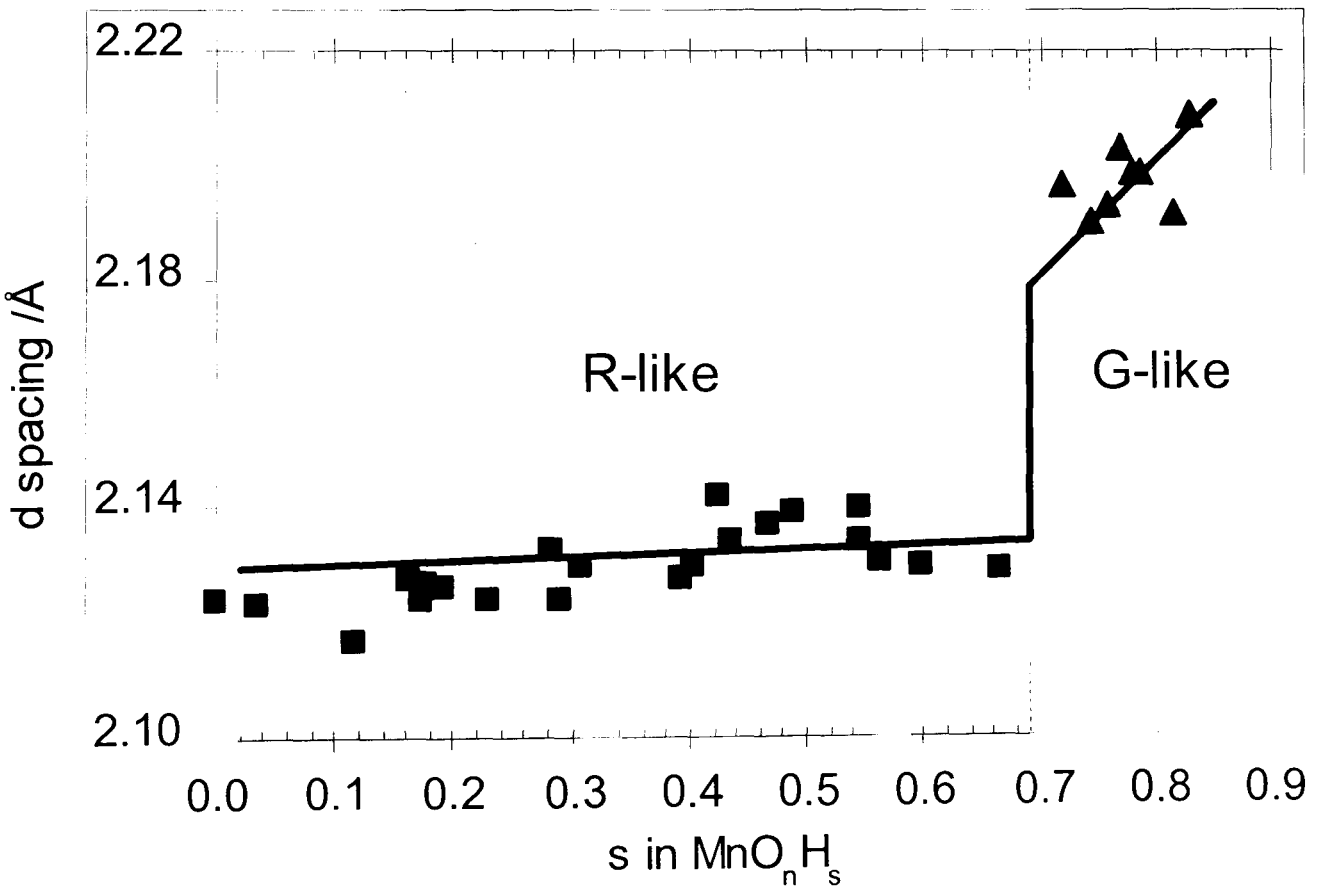

Fig. 4.4 Inter-planar spacing vs. H-insertion level of the deconvoluted 121 line of the ramsdellite (R-like) and groutite (G-like) parts.

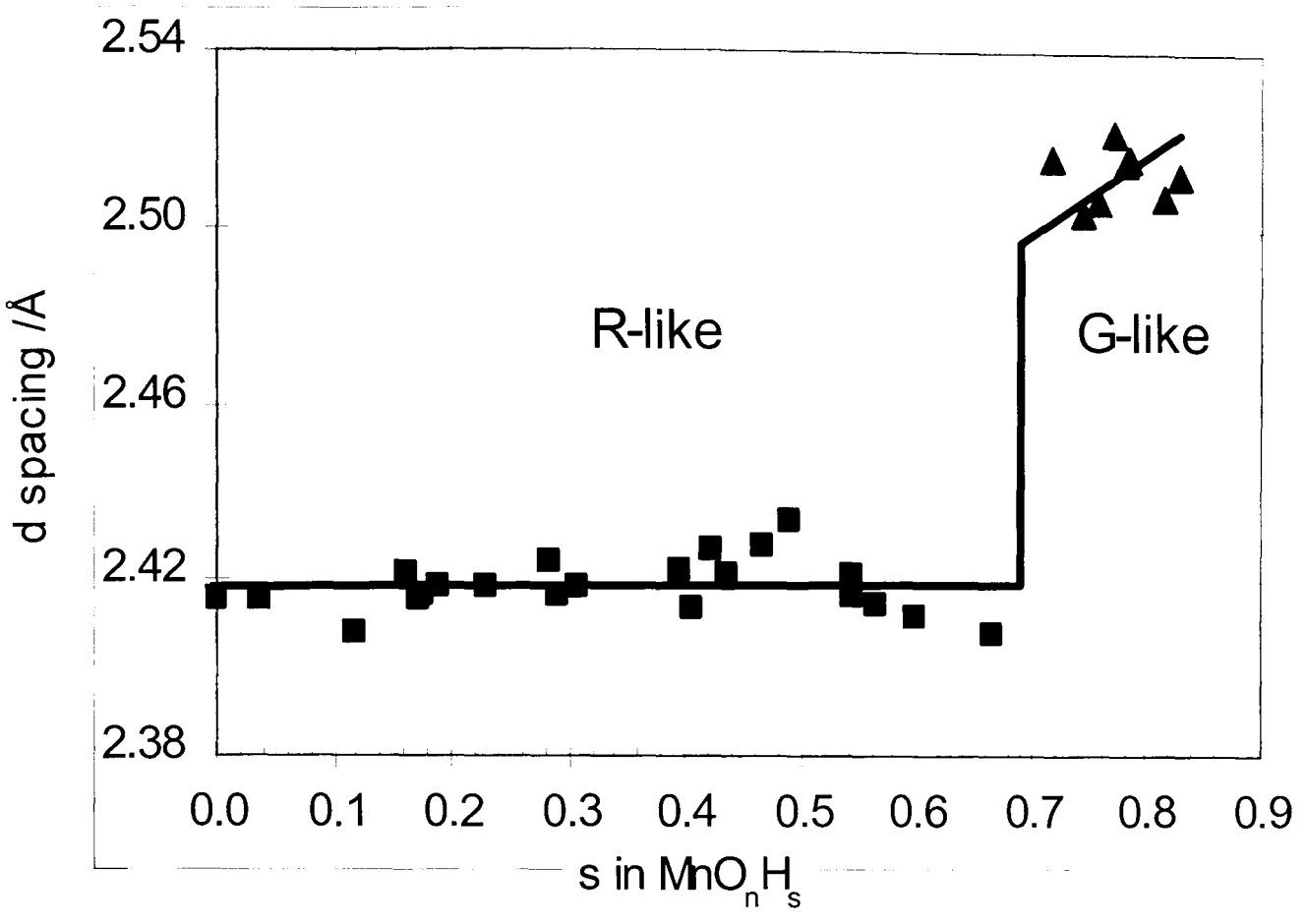

Fig. 4.5 Inter-planar spacing vs. H-insertion level of the deconvoluted 021 line of the ramsdellite (R-like) and groutite (G-like) parts.

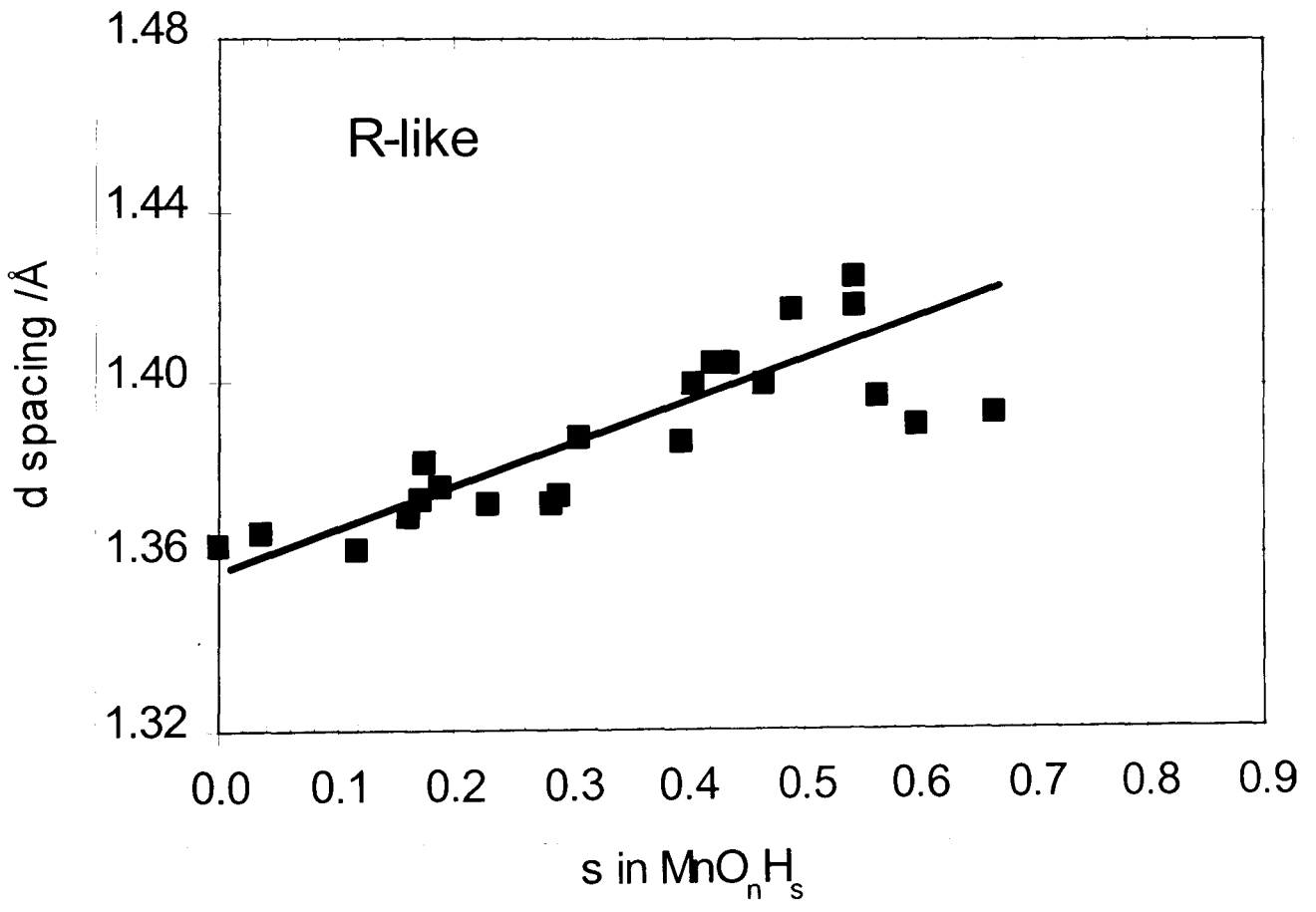

Fig. 4.6 Inter-planar spacing vs. H-insertion level of the deconvoluted 061 line of the ramsdellite. The 061 groutite was unreliable.

The broken lines drawn of Figs. 4.3-4.6 suggest that the first homogeneous stage of the H-insertion ended at s = 0.69, where the second homogeneous stage commenced after a phase transition.

4.2.2 Second Homogeneous H-insertion

The subset of XRD patterns in Fig. 4.1 with s above 0.67 is reproduced in Fig. 4.7 at a larger scale. All of the patterns in Fig. 4.7 have the same features and are shifted (slightly) to lower angles indicating a homogeneous expansion as in 4.2.1. The limited shift is partly due to the restricted H-insertion range of this stage ($0.72 \leq s \leq 0.83$). The patterns in this subset are clearly different from those in the first homogeneous stage. New lines appeared at about 62, 39, 36 and 34°; these were assigned to the 061, 140, 021 and 040 of groutite. Other lines such as 121 and 221 of the initial ramsdellite structure were shifted to near their position in groutite. Hence, a significant phase transition took place whereby the ramsdellite-like starting structure turned suddenly at a particular s value into the groutite-like final structure, hence the jump. This transition occurred between s = 0.666 and s = 0.718 and the midpoint of 0.692 is suggested as the transition point.

At this stage the final product essentially developed homogeneously from about s = 0.7 to the theoretical limit of $s_{max} = 0.9$. The inter-planar spacing of the deconvoluted hkℓ groutite lines supports strongly this homogeneous behaviour as can be seen on Fig. 4.3-4.5 and 4.8.

The inter-planar spacing of 221, 121, 021 and 040 lines of the groutite structure increased steadily from s = 0.72 to 0.83 indicating a homogeneous expansion of the structure.

This is the first time that H-insertion has been found to occur in two sequential and different homogeneous phases.

4.2.3 Structural Map of Faradiser M

A structural map similar to that in Fig. 3.17 has been constructed for Faradiser M and is shown in Fig. 4.9. Fig. 4.9 demonstrates that the main feature in the first homogeneous stage was an expansion in the *b* direction. This expansion occurred immediately even at very low insertion levels confirming that there was no restriction/inhibition such as microtwinning to oppose the expansion of the *b* dimension. This must mean that Faradiser M is not microtwinned. However, the *a*

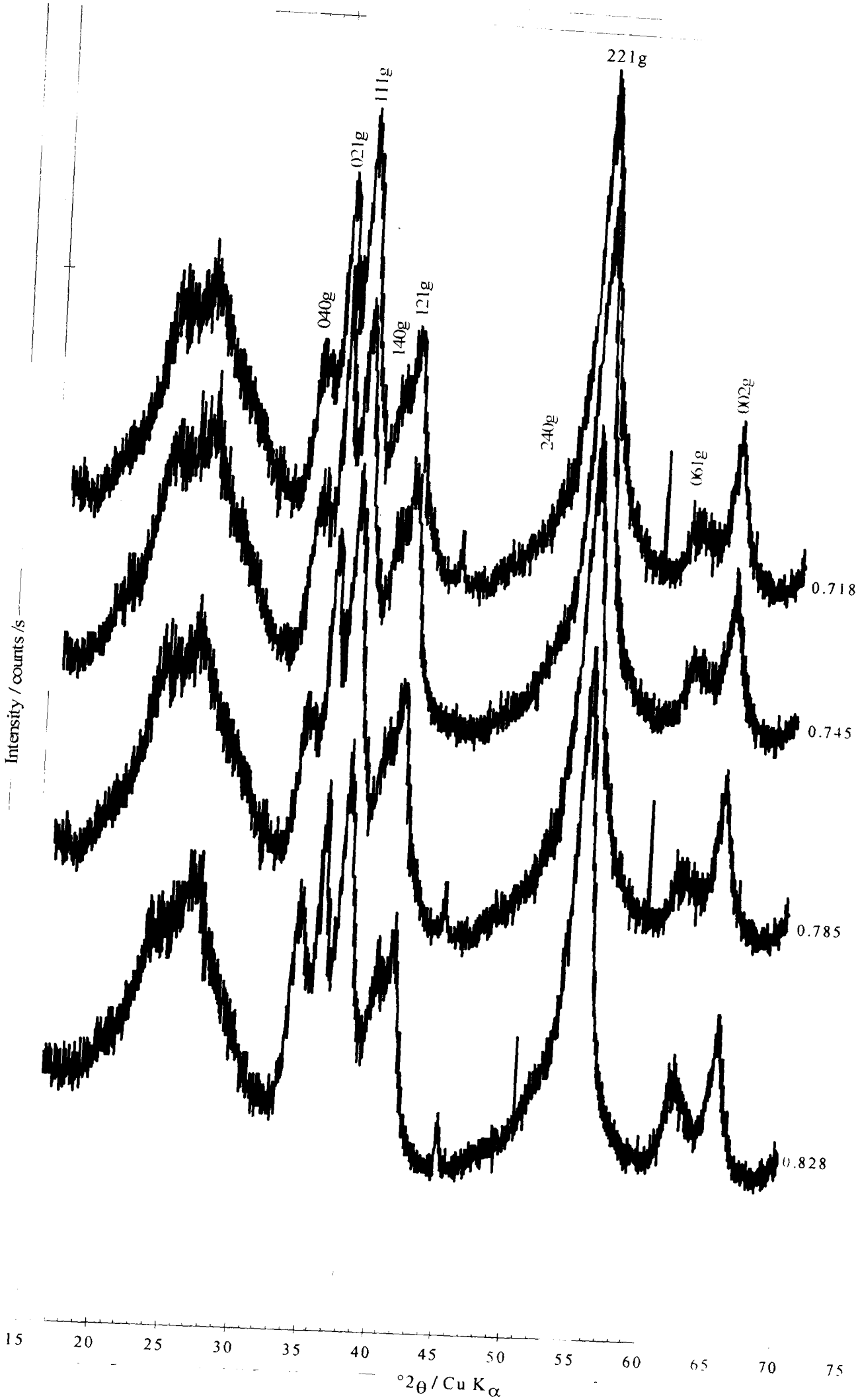

Fig. 4.7 Selected XRD patterns of H-inserted Faradiser M in the second homogeneous region stepped down the page in proportion to insertion level s (shown). The subscript g in the hkℓ indices refers to groutite structure.

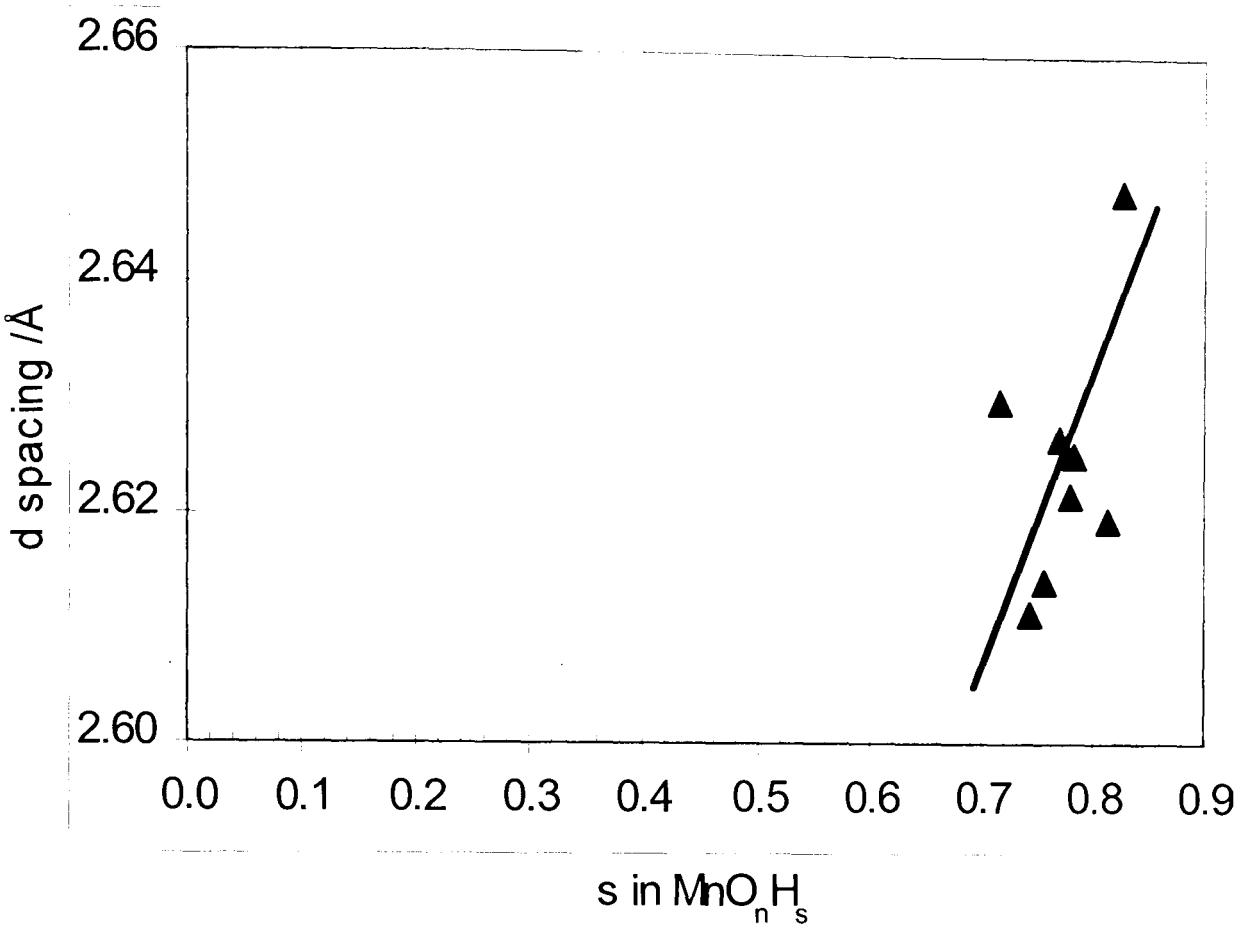

Fig. 4.8 Inter-planar spacing vs. H-insertion level of the deconvoluted 040 line of groutite.

axis remained practically constant at this stage. The β angle as well as the apical expansion *z* were altered by the expansion of *b* to compensate for the almost constant *a* since these parameters are inter-related. All these changes (Fig. 4.9) were moving the structure towards that of the final product. By the end of the first homogeneous phase the parameters *a*, *b*, *z* and β were all closer to their value in the end product. These parameters are listed in Appendix 4.

The *a* dimension increased in the first homogeneous stage from 4.398 Å to 4.411 Å. At the onset of the second homogeneous phase, the same lattice parameter was 4.495 Å, which is close to the maximum value of the *a* dimension in a hinged pyrolusite 4.497 Å[38].

This remark suggests that the pyrolusite part of the intergrowth must have hinged as the second homogeneous phase began. This hinging increased the *b* dimension to a value closer to that of groutite and further insertion essentially increased the *a* dimension to reach the dimensions of the final product.

H-insertion above 0.69 led to a homogeneous increase of the *a* dimension towards the *a* dimension of the end product. This conclusion is based on the calculated values of *a* and *b* at different insertion levels, displayed in Fig. 4.10 and 4.11.

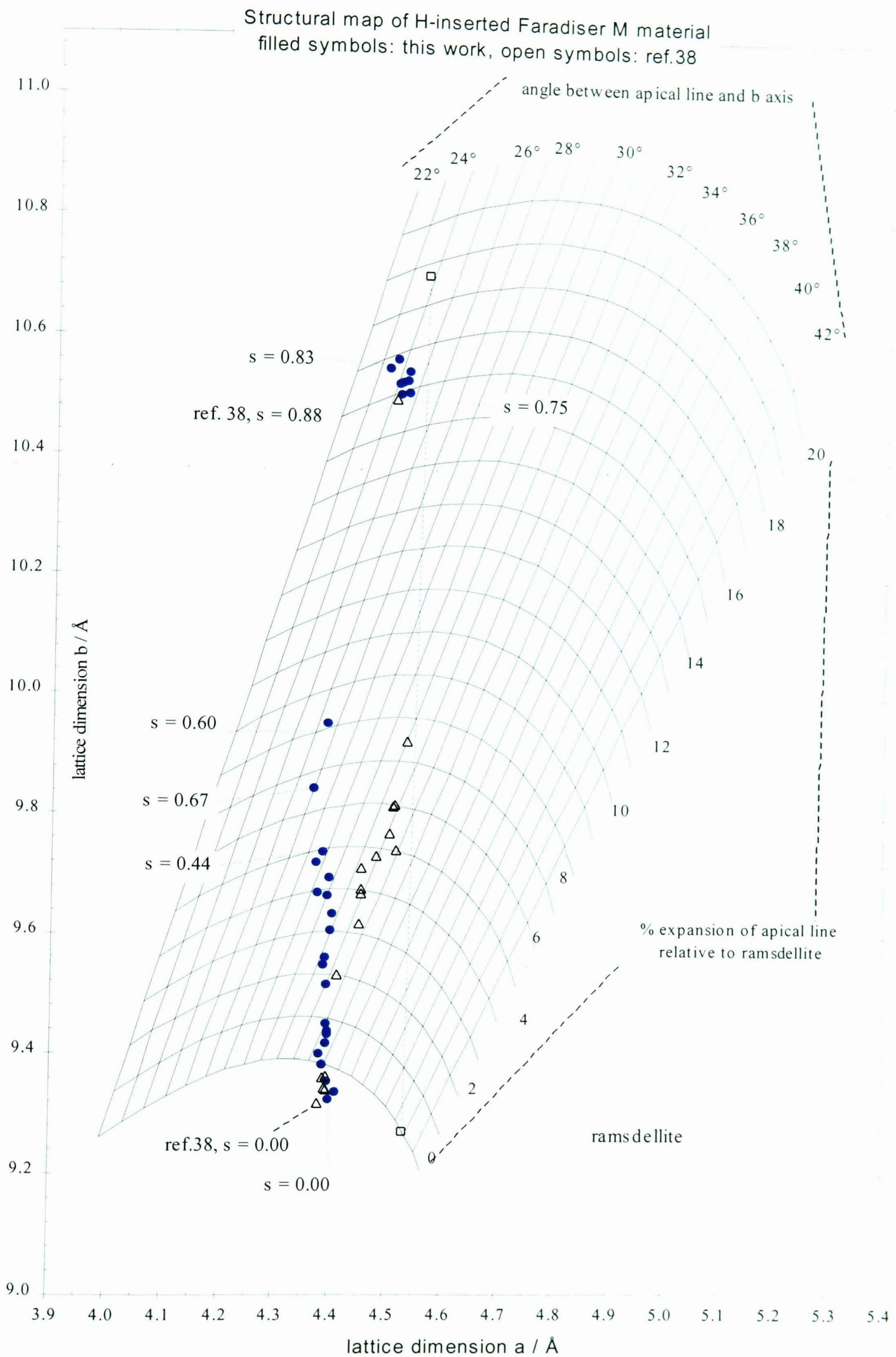

Fig. 4.9 Structural map of Faradiser M showing the *a* and *b* lattice dimensions. Results of MacLean and Tye[38] on the same material are also shown.

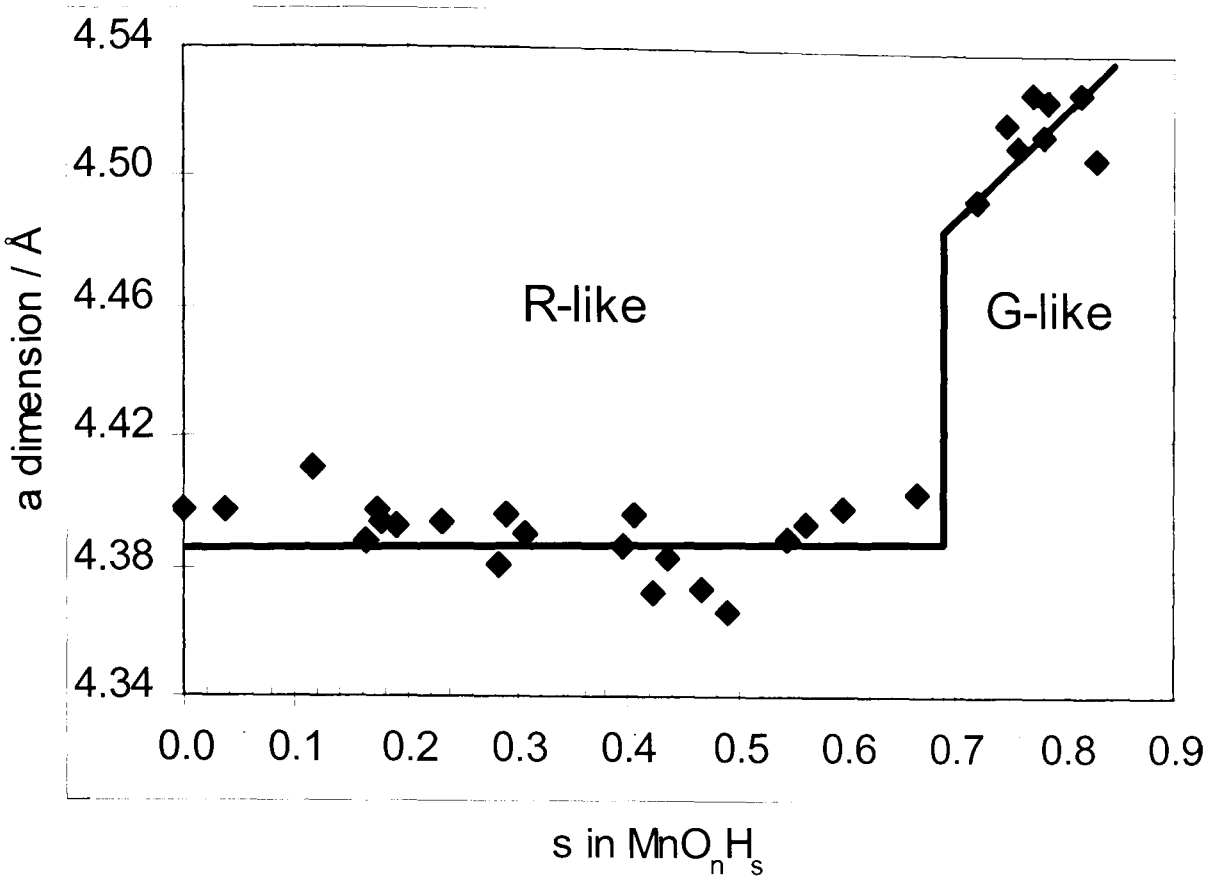

Fig. 4.10 Calculated values of the *a* dimension of ramsdellite and groutite structure at various insertion levels. Ramsdellite (R-like) structure evaluated from the 021, 121, 221, 002 and 061 lines. Groutite (G-like) structure evaluated from the 021, 121, 221, 002 and 040 lines.

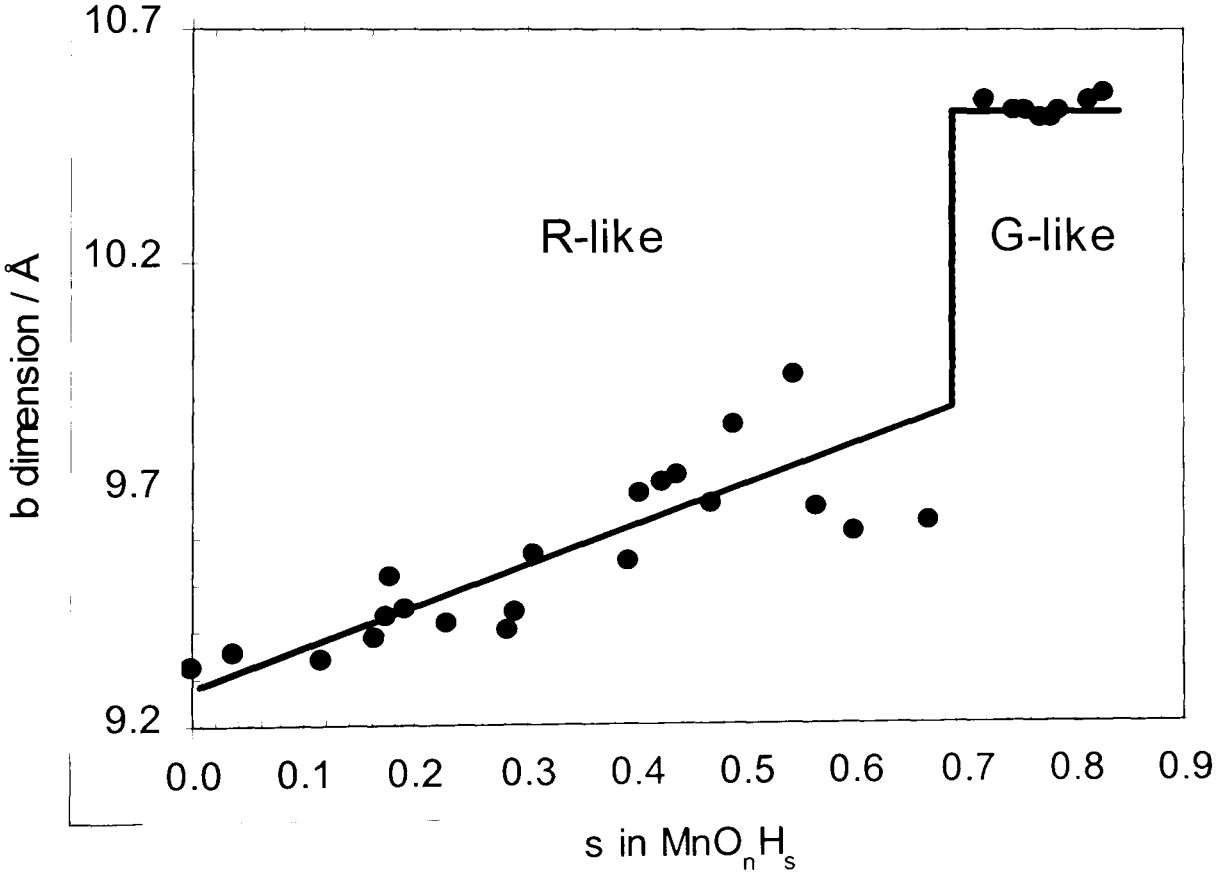

Fig. 4.11 Calculated values of the *b* dimension of ramsdellite and groutite structure at various insertion levels. Ramsdellite (R-like) structure evaluated from the 021, 121, 221, 002 and 061 lines. Groutite (G-like) structure evaluated from the 021, 121, 221, 002 and 040 lines.

4.2.4 Comparison with Previous XRD Work

The recent publication[38] reporting on H-insertion into Faradiser M is now considered for results comparison. Firstly, the experimental conditions and reagents were different from the controlled additions of hydrazine hydrate at low temperature method outlined in section 2.2.6. The authors[38] employed short contact with acetone at 20° C for low H-insertion levels ($0 \leq s \leq 0.24$). For higher H-inserted materials, they used propan-1-ol at temperatures ranging between 20 and 97° C for periods of up to 8 days. Although the experimental conditions were different in both works, the H-insertion still proceeded initially in a homogeneous phase. The second stage of the insertion was a heterogeneous phase in the published work, in contrary to the second homogeneous phase in the present work. The boundary between the two stages of the insertion was $s = 0.69$ in this work against $s = 0.56$ in the publication cited[38].

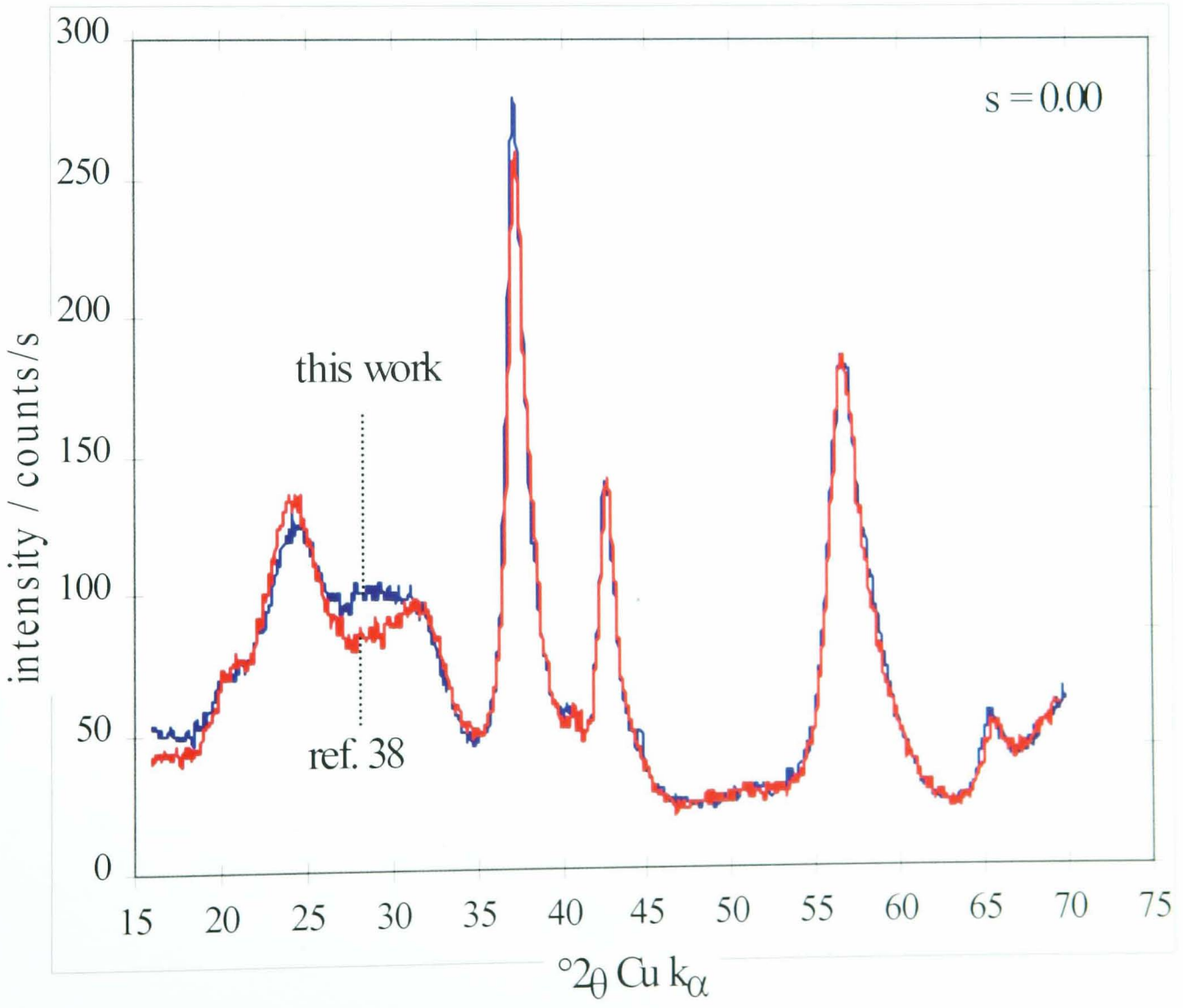

Fig. 4.12 Comparison of the XRD patterns of Faradiser M starting material in this work and in MacLean and Tye paper (ref. 38).

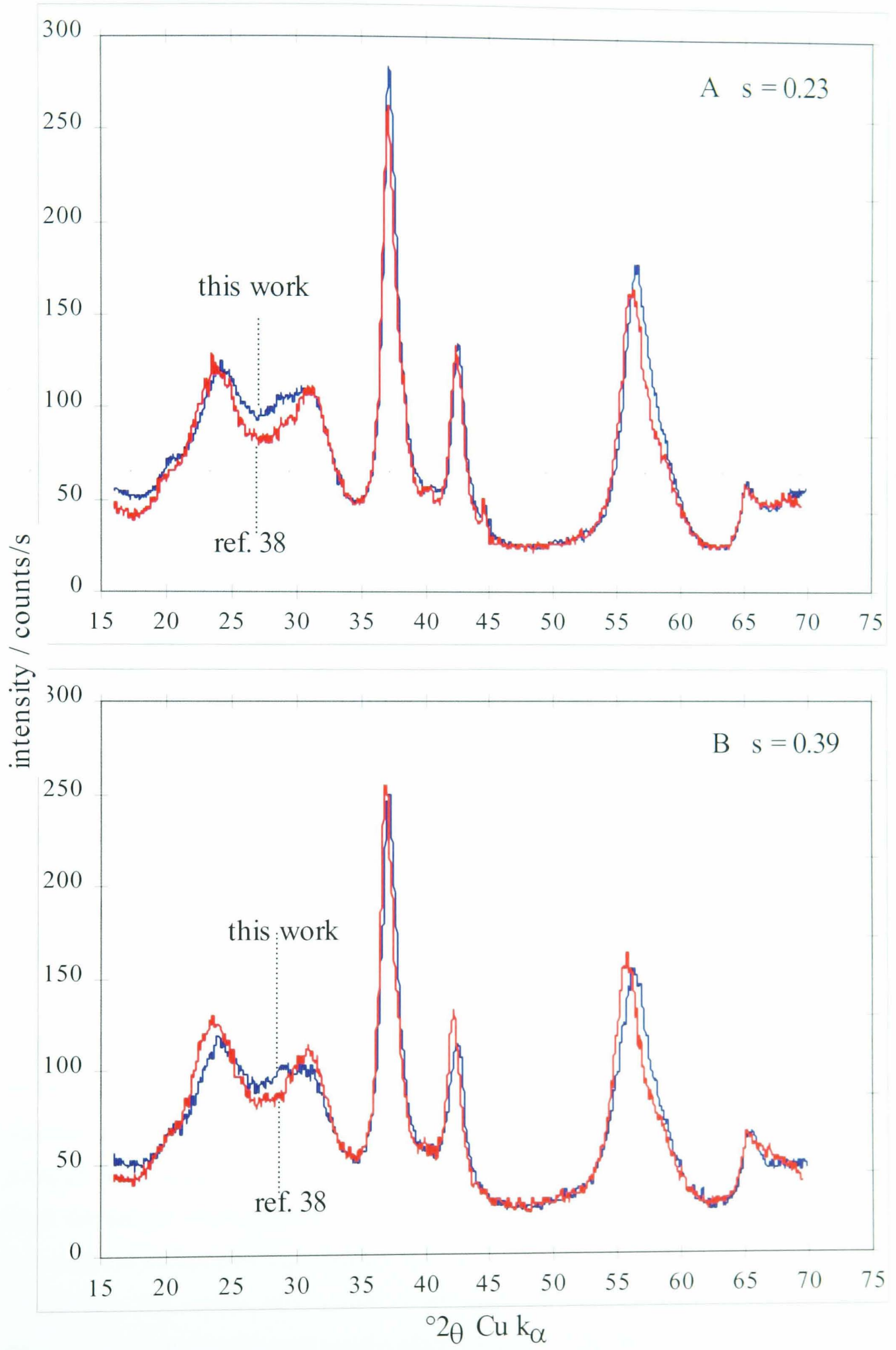

Fig. 4.13 Comparison of the XRD patterns of H-inserted Faradiser M in the common homogeneous stage, in this work and in MacLean and Tye

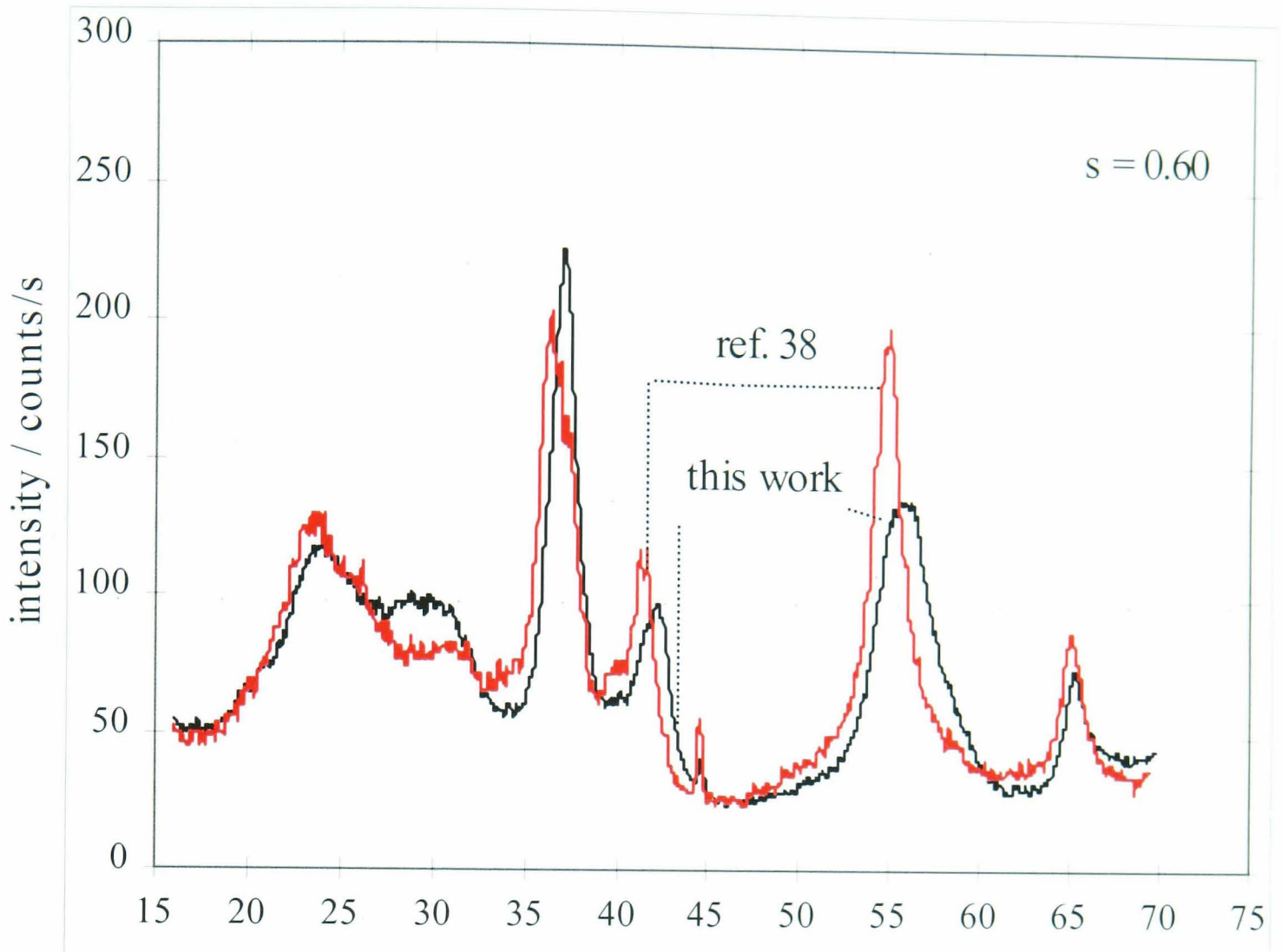

Fig. 4.14 Comparison of the XRD patterns of H-inserted Faradiser M at s = 0.60, in this work and in MacLean and Tye paper (ref. 38).

Thus, below 0.56 in s, the two works are expected to be more or less similar since they refer to similar phases. This is confirmed by Figs. 4.12 and 4.13* that compare the starting materials and two H-inserted levels within the common homogeneous range. Between 0.56 and 0.69 in s, the two sets of results are expected to differ since in this work the H-inserted structure was still in the first homogeneous stage while the materials in the cited work had crossed to the heterogeneous phase. Fig. 4.14 compares two materials at s = 0.6 and confirms the above statement. Note that in this work the sample retained the structure of the starting material while in the cited work new peaks at shifted positions indicate the onset of a new structure.

In addition, the sample at s = 0.60 in the cited work was shifted to lower angles compared to a similar inserted sample from this work. This shift is rather a sign of the hinging of the initial structure leading to the final product.

---

* The XRD patterns published in the paper[38] covered only between 33° and 44° 2θ Cu Kα. The author is thankful to have access to the full data.

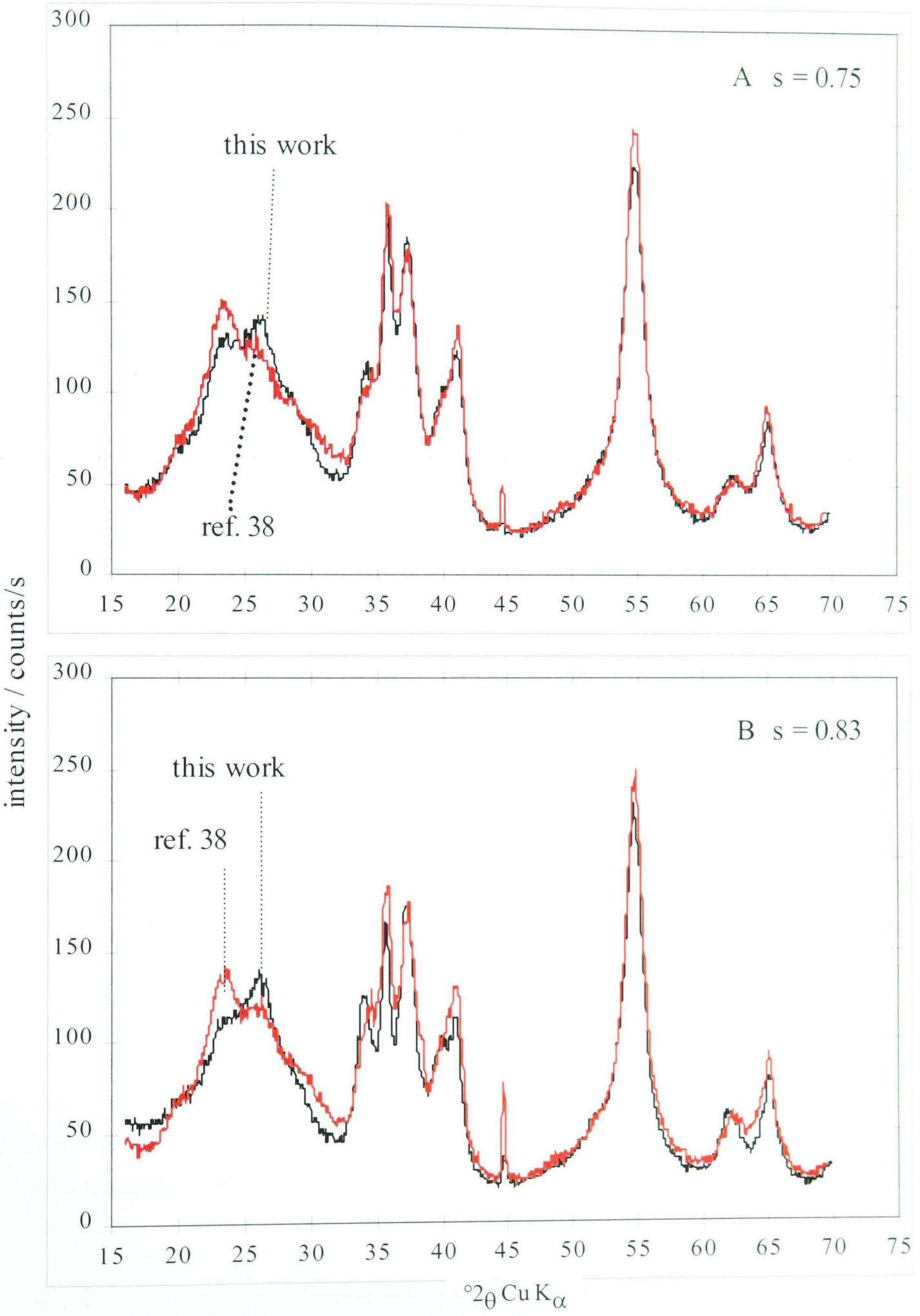

Fig. 4.15 Comparison of the XRD patterns of highly H-inserted Faradiser M samples in this work and in MacLean and Tye paper (ref. 38).

Above s = 0.69, XRD patterns from the two works are expected to coincide again if the same final materials were produced. Fig. 4.15 shows two different insertion levels at which the XRD patterns originating from both works are similar overall.

A main difference between the two sets of XRD patterns can be observed on the hump below 30°. This hump consisted initially of two broad peaks at about 24.4 and 31.7°. Both "peaks" shifted to lower angles at higher insertion levels (s > 0.7) in both works. At the onset of the second homogeneous stage the higher angle peak at about 26.5° enhanced in this work while the other peak weakened significantly; the reverse occurred in the reference paper[38] leading to a peak around 23.8°. As this hump could not be deconvoluted successfully, definite peaks assignment was not possible. Nevertheless, the main manganite[93] peak at 26.1° and the main groutite[90] peak at 21.1 can be suggested for satisfactory deconvolution or peak refinement.

Apart from the difference in the hump, the XRD study did not reveal other differences between the patterns of samples of both works. As will be shown however, the FTIR study did reveal differences.

4.3 Results of the FTIR Study of Faradiser M

4.3.1 Introduction

FTIR spectra of H-inserted Faradiser M samples were measured and manipulated in the same way as the SBP-A samples (section 3.3.1), and selected samples covering the whole insertion range are presented in Fig. 4.16. Although the particle size of Faradiser M is significantly smaller (25 - 35 μm) than that of SBP-A, it was still big enough to produce high scattering at high frequencies (Fig. 4.16). There are also fluctuating signals between 2240 and 2380 cm^{-1} which are due to the local CO_2, at the time of measurement, affecting the background correction. Like SBP-A, the spectra of this material were divided into two ranges on either sides of 800 cm^{-1}. The low range was assigned to the Mn[O6] octahedral vibrations and the range above to OH vibrations.

4.3.2 First Homogeneous phase: Mobile H

The FTIR spectra in the initial homogeneous H-insertion, which has been shown by the XRD study to extend over the range $0 \leq s \leq 0.69$, are distinguished from the spectra above s = 0.67. Fig. 4.17, reproduced from Fig. 4.16, displays a selection of the

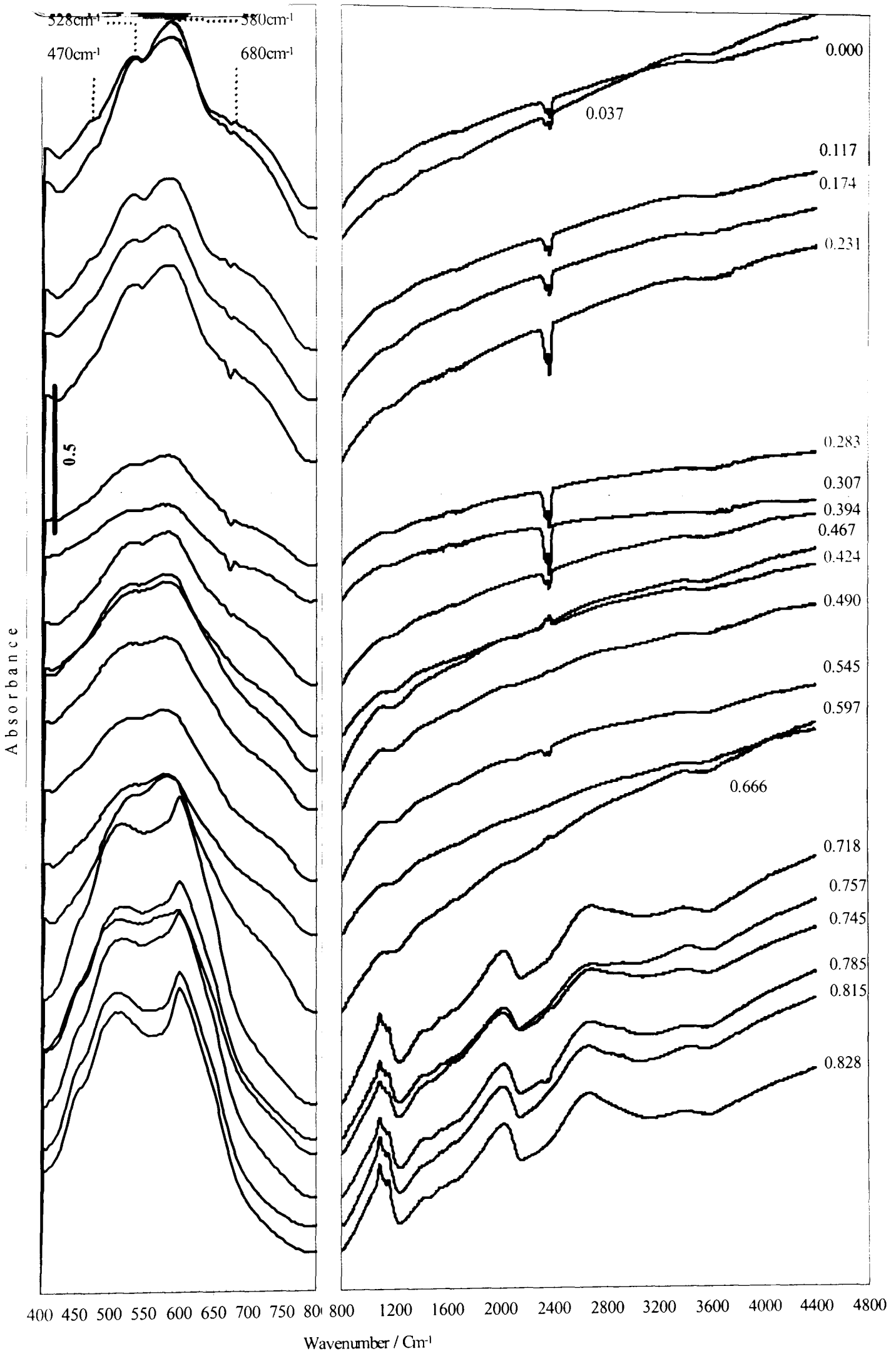

Fig. 4.16 FTIR spectra of selected H-inserted Faradiser M samples in the range $0.00 \leq s \leq 0.83$ stepped down the page in proportion to s. Left: octahedral framework vibrations, Right: OH vibrations.

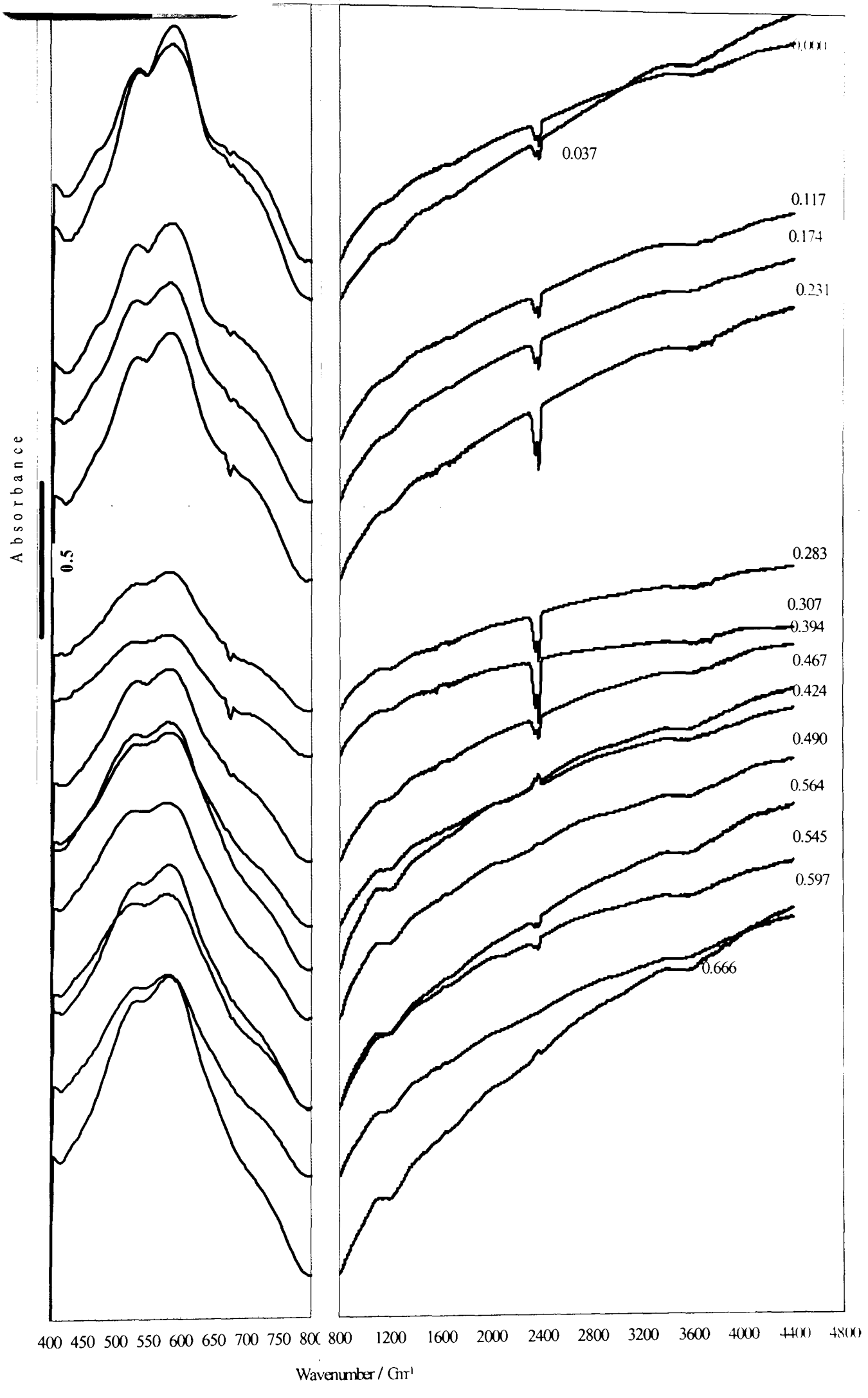

Fig. 4.17 FTIR spectra of H-inserted Faradiser M samples in the first homogeneous region. Left: octahedral framework vibrations, Right: OH vibrations.

spectra of H-inserted Faradiser M samples up to s = 0.67. All the spectra keep similar shape as the spectrum of the starting material, indicating that limited changes occurred to the local environment. Careful inspection of the spectra below 800 cm^{-1}, reveals that the shoulders at 470 and 680 cm^{-1} of the [MnO6] octahedra, continued to shift to lower wavenumbers (lower energies), and so did the main doublet initially present at about 580 cm^{-1}. The OH vibrations side of the spectra does not show any sign of band formation indicating that protons are mobile at this stage.

4.3.3 Second Homogeneous phase: Located H

Fig. 4.18 presents the FTIR spectra of the samples of insertion levels above 0.7. Here, the spectra are different from that in Fig. 4.17 and support the phase transition already suggested from the XRD study. Both the octahedral and the OH vibrations provide evidence of a new behaviour. The [MnO6] octahedral vibrations sharpened and the doublet at 500 and 600 cm^{-1} become more resolved, indicating a serious change within the environment of the octahedra, a new structure. This new structure developed homogeneously from s = 0.72 to the most H-inserted sample at s = 0.83. As the octahedra of the end product developed, the minimum between the doublet at about 500 and 600 cm^{-1} deepened.

The OH vibrations side of the spectra provides clear evidence of H location. Figs. 4.19 – 4.21 display the net peak areas of three different O-H vibrations as described in Table 3.2. All three figures demonstrate that no OH bond was formed in the first homogeneous region (s < 0.69), but that substantial bands appeared at the onset of the second homogeneous region indicating that all H inserted must have located. The growth of the OH band is represented in Figs. 4.19 – 4.21 by a straight line. The absence of OH bond below s = 0.69 is indicated by the solid horizontal line and the broken line suggests the shape of the curve if the mobile H had been located.

Immediately above s = 0.69, the net peak areas are slightly below the trend (Figs. 4.19 – 4.21). This is because of the peak boundaries were chosen for the final product in a heterogeneous reaction[13] and do not account for the shift observed in this homogeneous phase. When moving from the most H-inserted sample to lower insertion levels, keeping the same boundaries, fractions of the peak area will be missed out, hence the fall below the trend. Only the peak areas of the most H-inserted sample are fully represented. To account for the homogeneous shift, each sample should have its own peak boundaries. However, since the shift was limited due to restricted

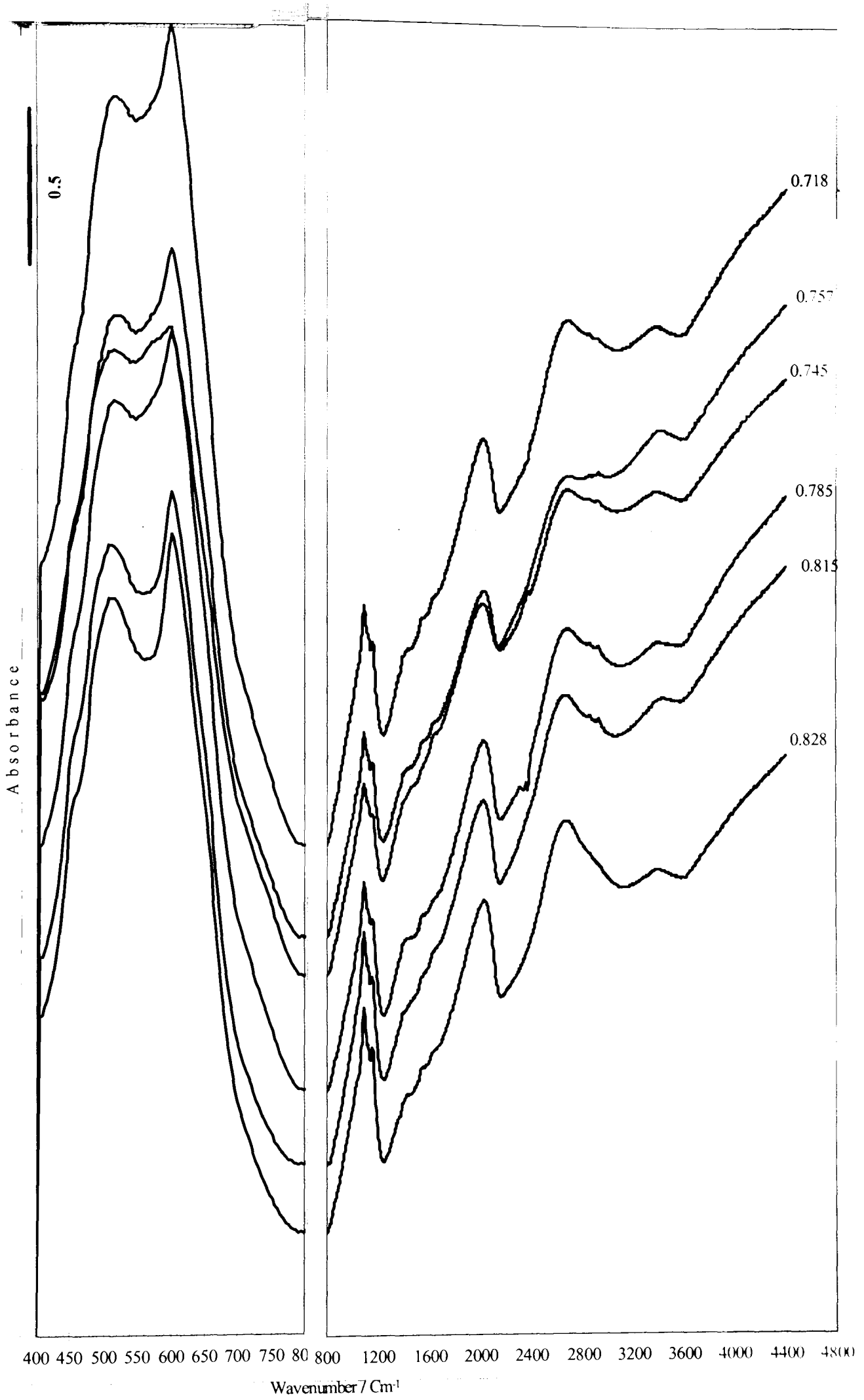

Fig. 4.18 FTIR spectra of H-inserted Faradiser M samples in the second homogeneous region. Left: octahedral framework vibrations, Right: OH vibrations.

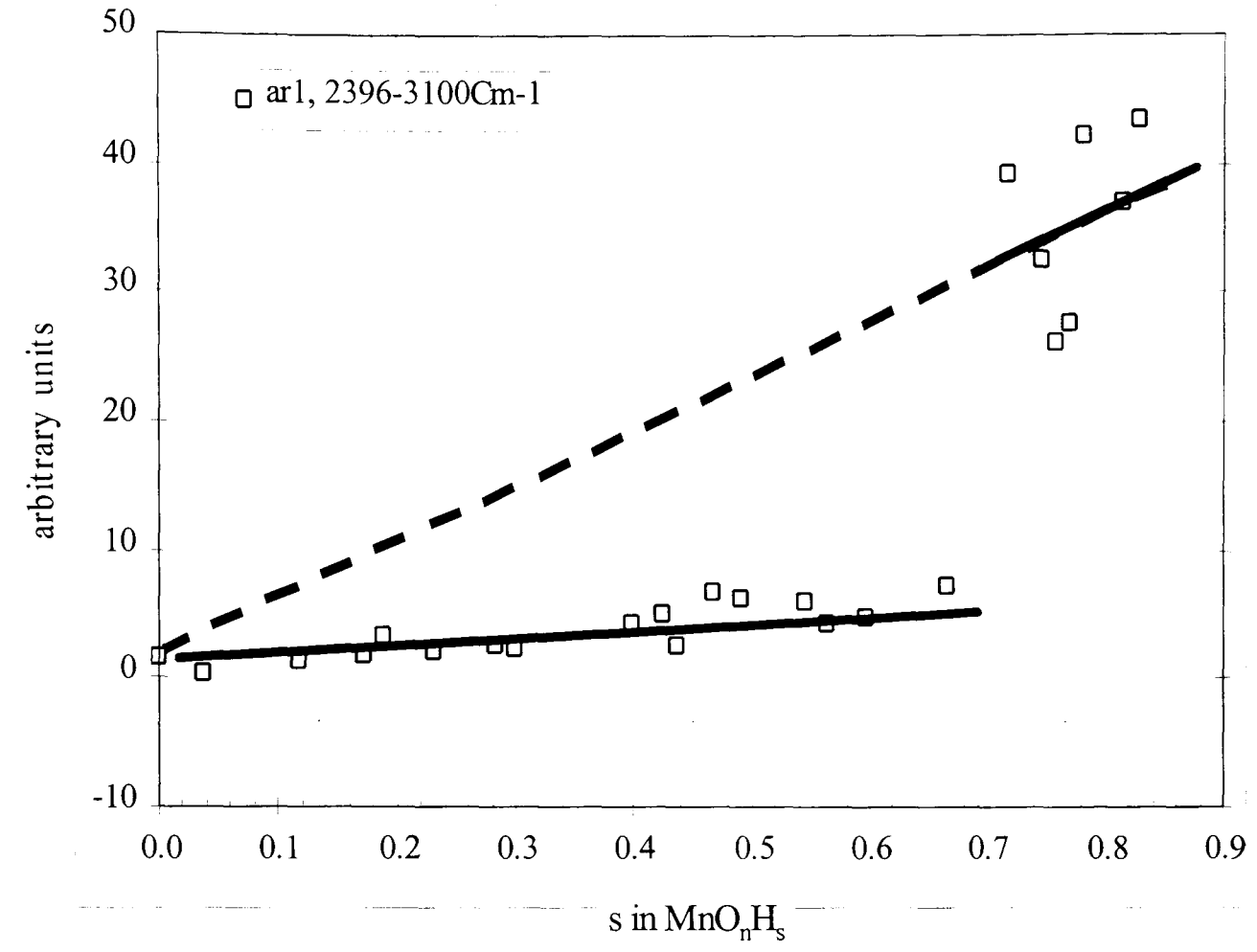

Fig. 4.19 Net peak area of the band between 2248 – 3200 cm^{-1} of O-H stretching + adsorbed OHX (Table 3.2). H located in the second homogeneous region ($s \geq 0.69$).

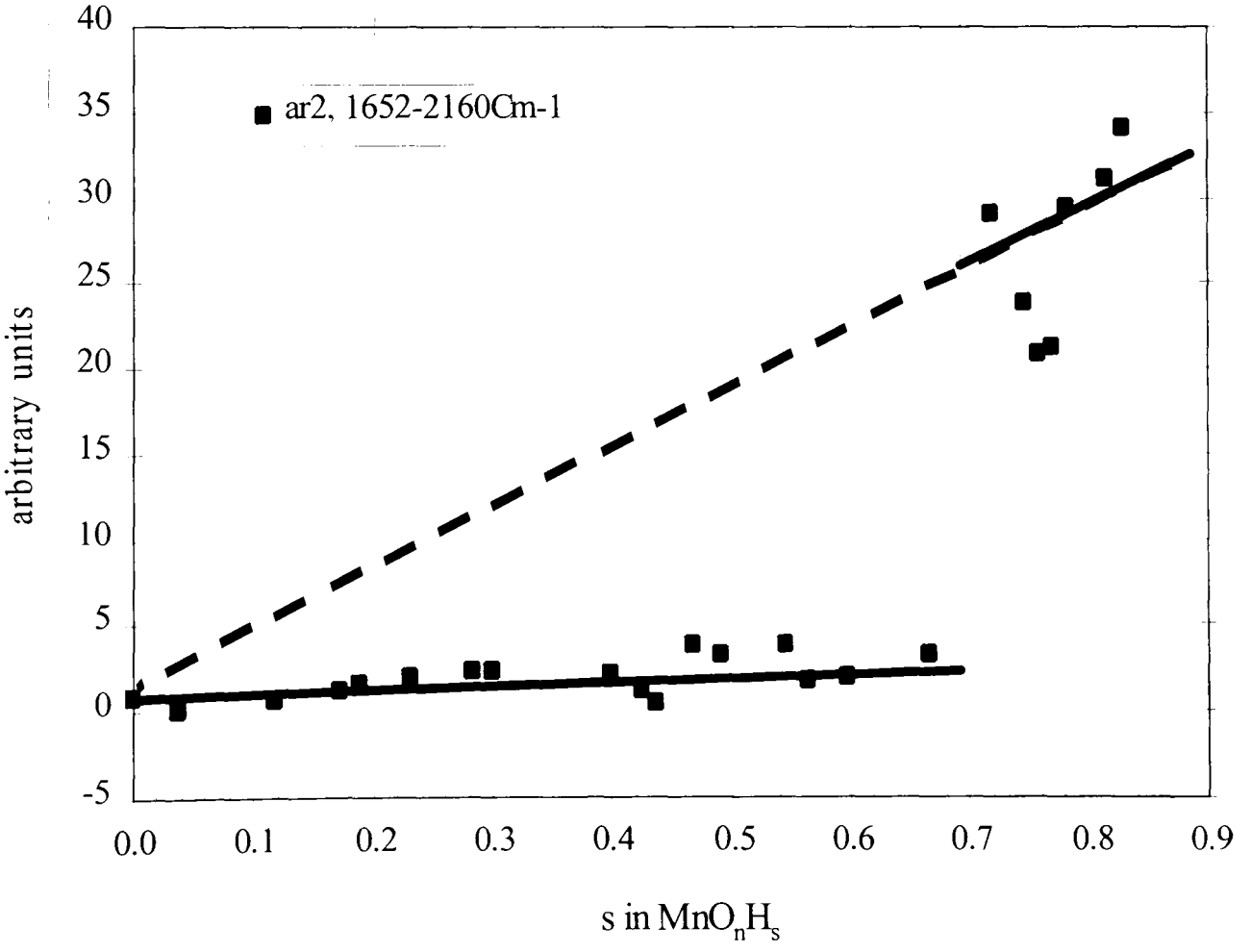

Fig. 4.20 Net peak area of the band between 1752 – 2152 cm^{-1} of O-H stretching. H located in the second homogeneous region ($s \geq 0.69$).

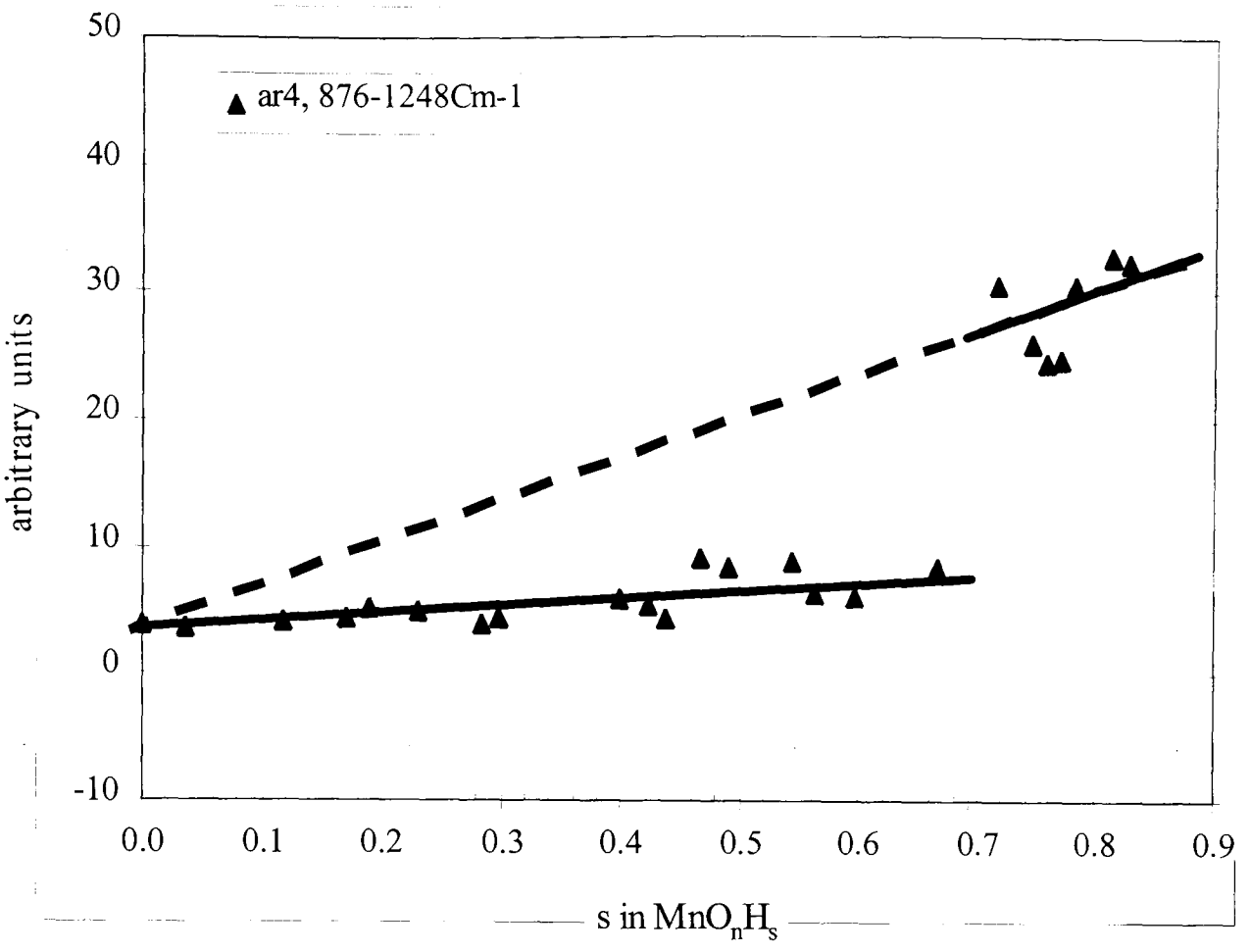

Fig. 4.21 Net peak area of the band between 856 – 1224 cm^{-1} of in-plane & out of plane O-H bending. H located in the second homogeneous region ($s \geq 0.69$).

insertion range, keeping the same peak boundaries throughout seemed a reasonable choice.

4.3.4 Preferential H-insertion Sites

As with the SBP-A material, the second homogeneous phase of the H-insertion into Faradiser M, provides an opportunity to examine the FTIR spectra for preferential H location into the groutite and/or manganite part of the intergrowth. Fig. 4.22 compares the spectra of the second homogeneous phase, at three insertion levels, with those of groutite and manganite[10]. Manganite peaks at about 1088 and 1152 cm^{-1} are clearly present in the H-inserted Faradiser M samples indicating H location in the 1x1 tunnels. Groutite peaks at 998 and 1030 cm^{-1} are, however, less resolved and simply broadened the lower frequency end of the broad band. Two factors are thought to be behind this observation: the high pyrolusite content of Faradiser M and the relative shape and position of the doublets in both groutite and manganite. The manganite doublet in Fig. 3.22 is sharper and more resolved than the groutite one. Since the two doublets are close to each other, a suitable combination of them can produce a trace close to that of the highly H-inserted Faradiser M samples shown in Fig. 4.22. Similar reasoning

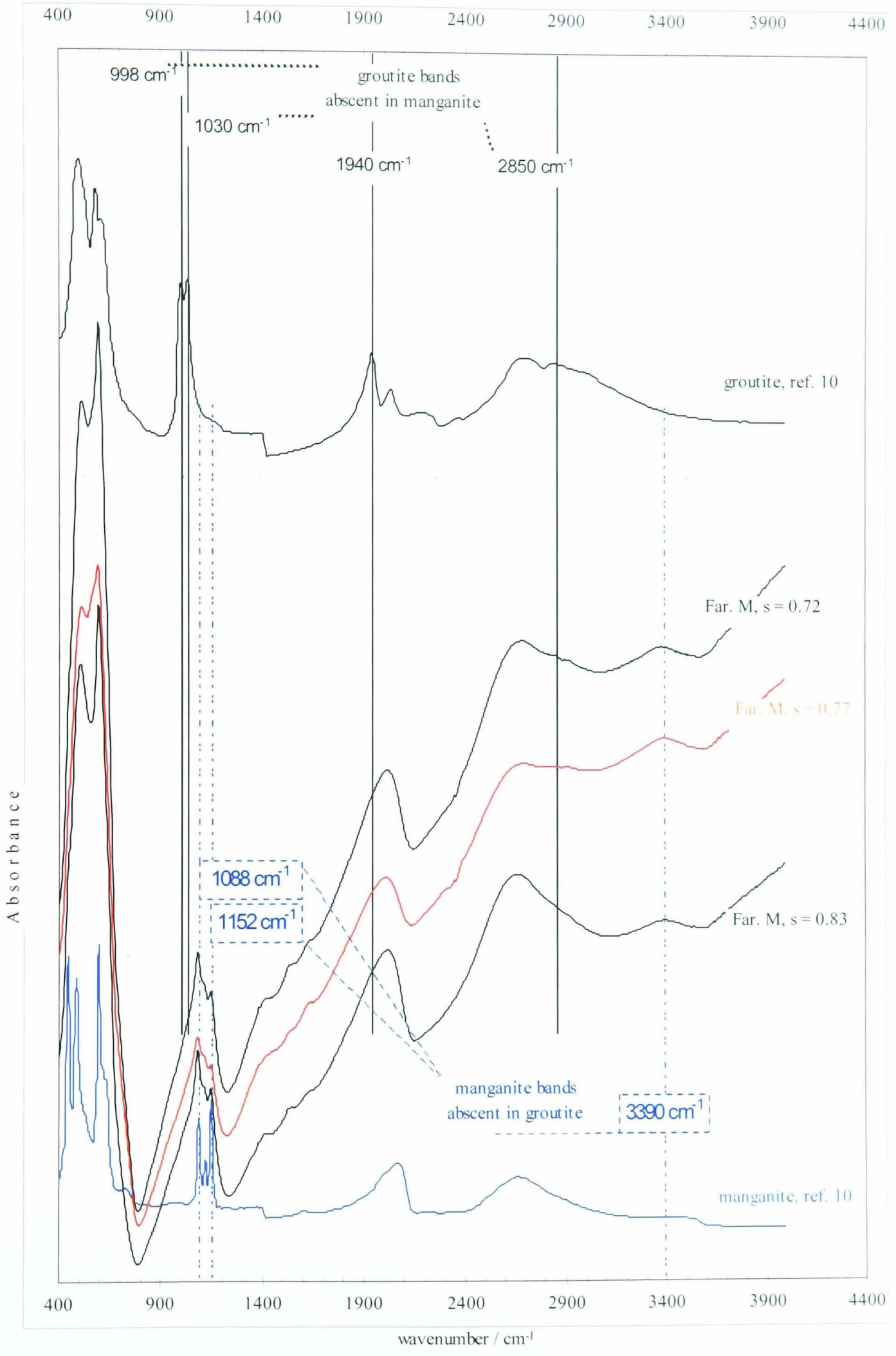

Fig. 4.22 Comparison of selected spectra of H-inserted Faradiser M in the second homogeneous phase with the spectra of groutite and manganite[10].

applies to the groutite bands at 1940 and 2850 cm^{-1}. Hence, the H must have located into the 2x1 tunnels of groutite and the 1x1 manganite tunnels simultaneously.

Comparison between Fig. 4.22 and Fig. 3.27 shows that groutite bands are stronger in the intergrowth of the most H-inserted SBP-A material while the manganite bands are stronger in the intergrowth of the most H-inserted Faradiser M. This reflects the initial intergrowth structure (de Wolff faults) of these materials, 41% and 70% respectively. However, by inspection of the spectra, it seemed that the relative size of the manganite/groutite bands did not confirm the ratio of the de Wolff faults. Hence, the Pr parameter of both materials may need to be recalculated. This point is discussed further in Chapter 7.

4.3.5 Comparison with Previous FTIR Work

Faradiser M has been the subject of a recent similar study[38] by MacLean and Tye as already mentioned (section 4.1.4). The FTIR spectra published* in that paper are now considered for comparison with the results of this work. For the reason given in section 3.3.5, the spectra of this work had lower absorbance and was multiplied by a factor ranging from 1 to 2.3, to aid comparison.

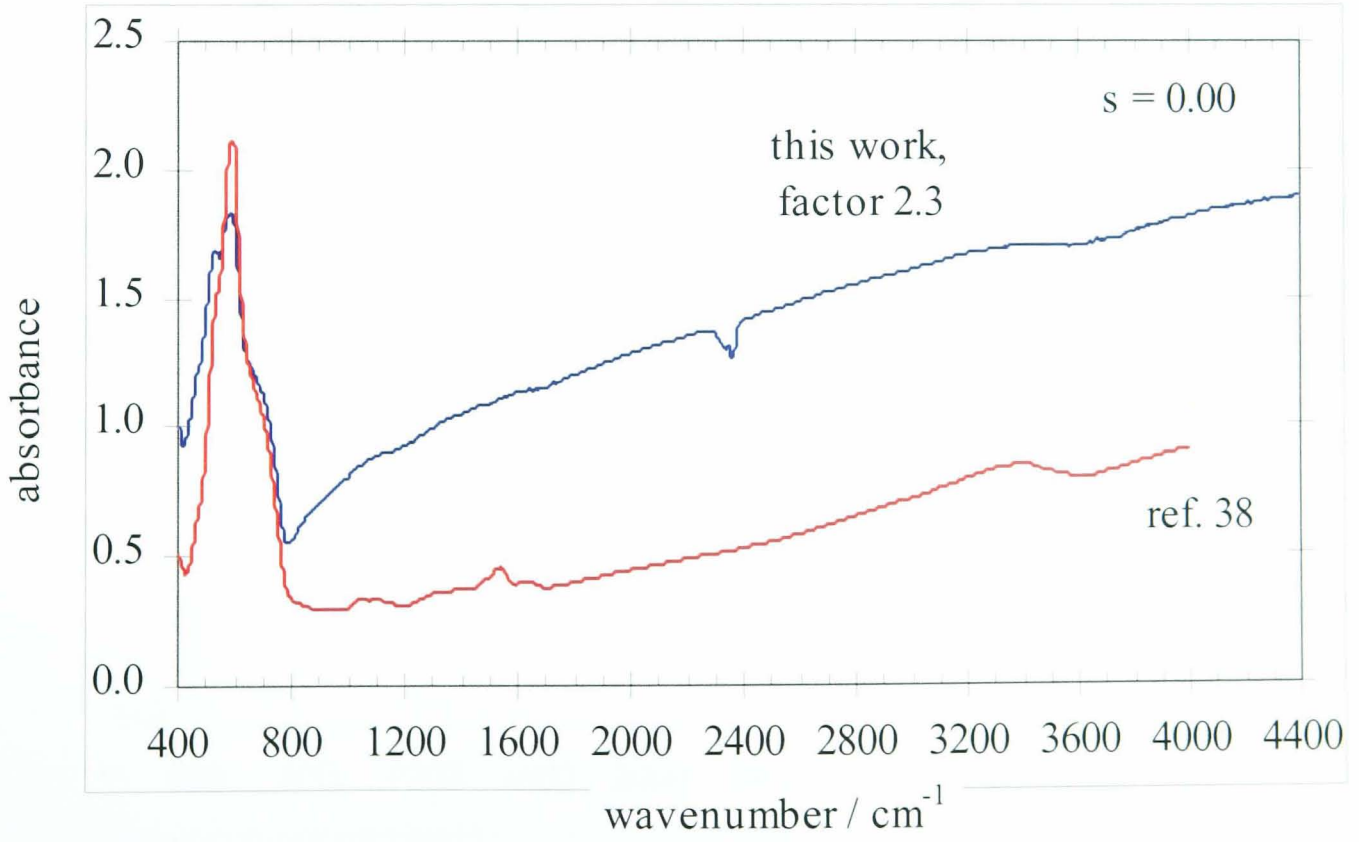

Fig. 4.23 Comparison between the spectrum of Faradiser M starting material in this work and in ref. 38.

* The spectra published covered only 800 to 4000 cm^{-1}. The author is thankful to have access to the full range.

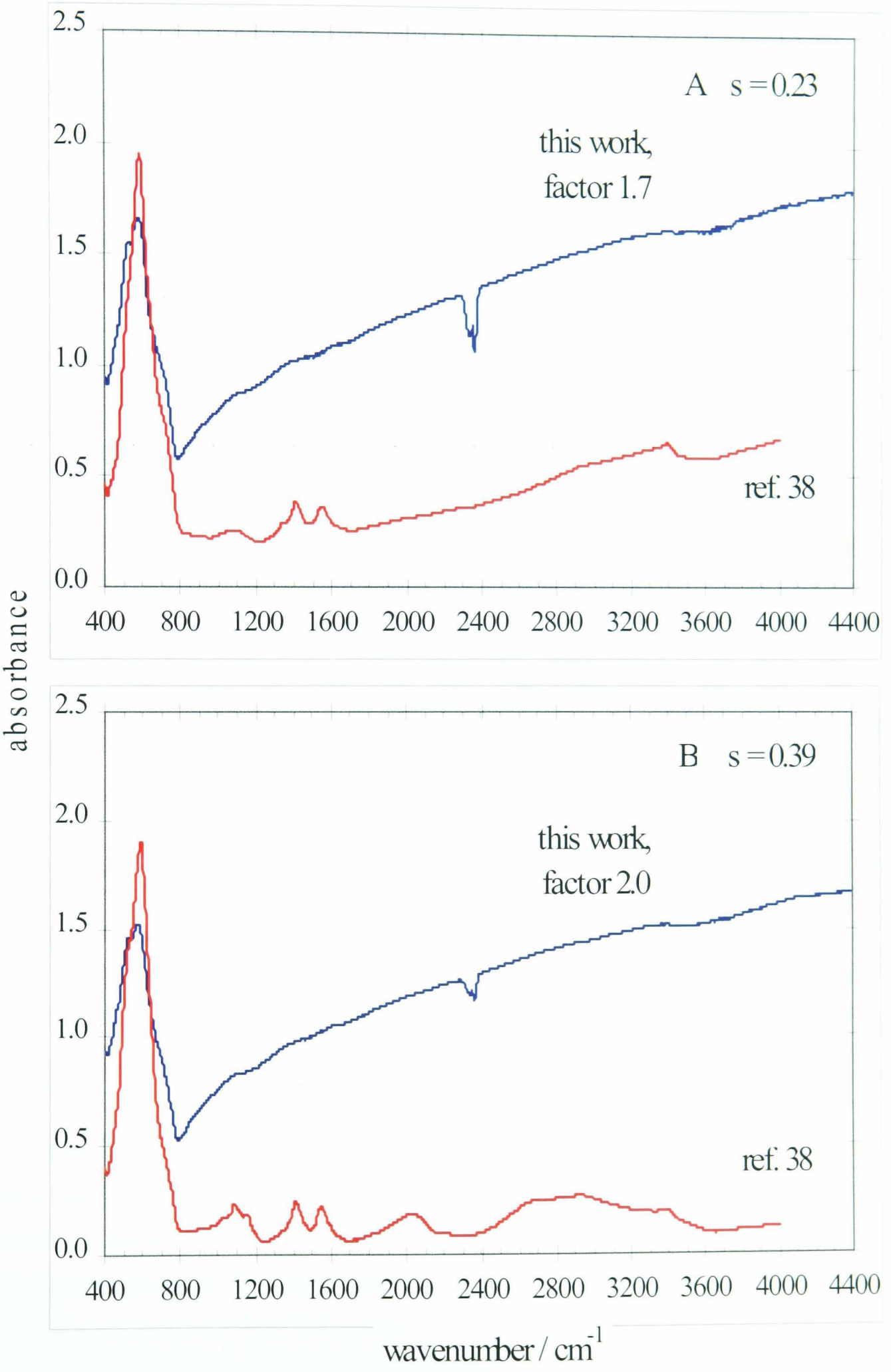

Fig. 4.24 Comparison between the spectra of H-inserted Faradiser M in this work and in ref. 38. (A) before and (B) after H location in ref. 38.

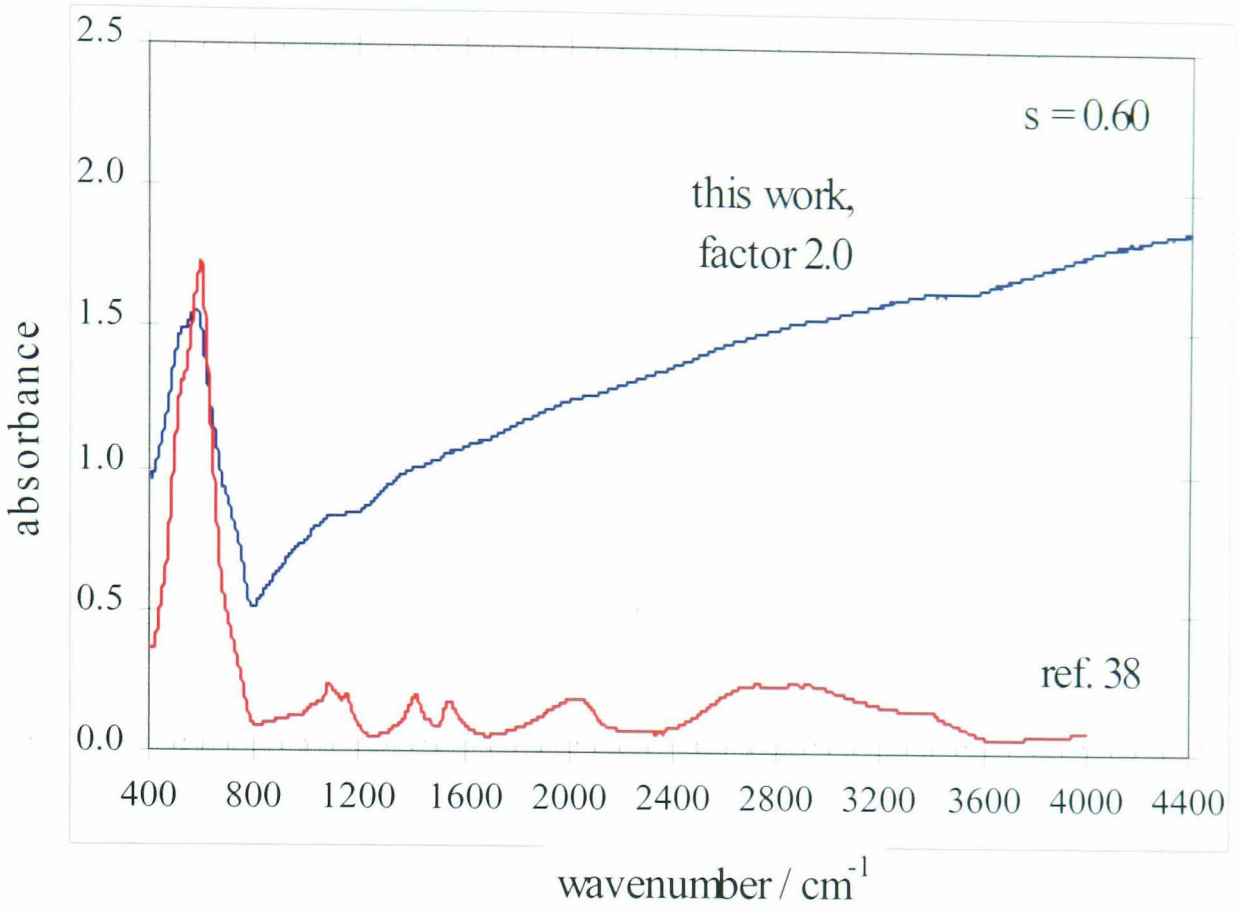

Fig. 4.25 Comparison between the spectra of H-inserted Faradiser M in this work and in ref. 38 at s = 0.60. This work: homogeneous insertion, no H location. Ref. 38: heterogeneous insertion with H location.

Spectra were compared at six insertion levels covering the similarities and differences in features of both works.

While the spectrum of the starting material is similar in the two works (Fig. 4.23), differences arise throughout the insertion range. One persistent difference is the presence of a doublet at about 1415 and 1548 cm^{-1} in the spectra of the authors[38]. This doublet has been assigned previously to overtones of octahedral vibrations[13], but is now thought to be due some organic substance (section 3.3.5). In the common homogeneous stage, and before H location in either work, the difference is limited to this doublet as in Fig. 4.24A, s = 0.23. After H location within the homogeneous (Fig. 4.24B) or heterogeneous (Fig. 4.25) stages of the cited work[38] and before H location in this work, the presence of OH bands in the cited work and their absence in this work are an additional difference between the two works. A similarity however, was that all previously mobile H located in one step.

At higher insertion levels, when H has located in both works, the difference is only the doublet at 1415 and 1548 cm^{-1}, Fig. 4.26.

The rising tails of the spectra at higher frequencies as well as the odd features around 2240 2380 cm^{-1} are due to scattering from larger particles and to the local CO_2 level at the time of scanning the spectra, as already mentioned in section 3.3.1.

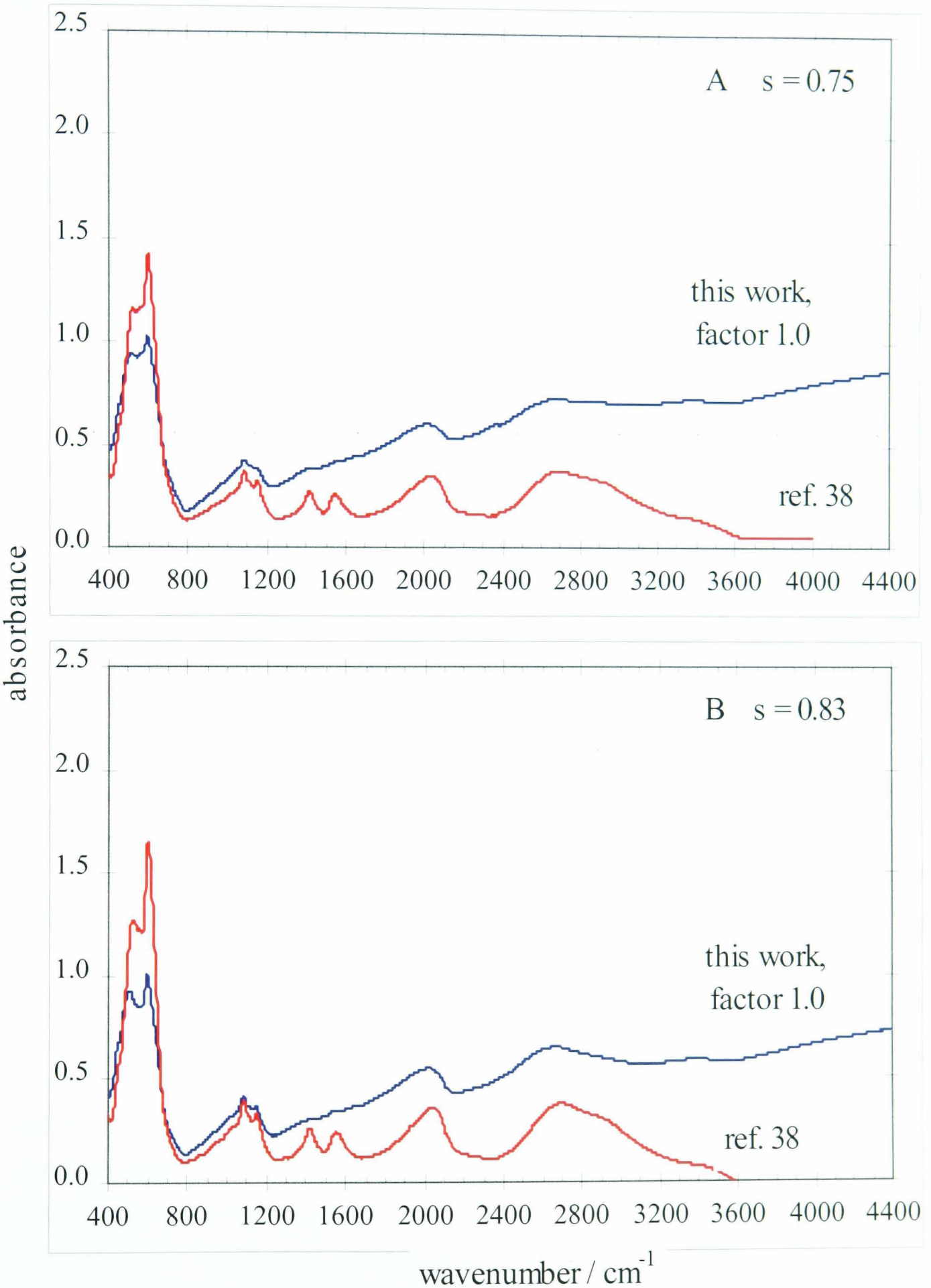

Fig. 4.26 Comparison between the spectra of H-inserted Faradiser M in this work and in ref. 38 at high insertion levels. This work: homogeneous insertion with H location. Ref. 38: heterogeneous insertion with H location.

4.4 Discussion of The H-insertion into Faradiser M

The XRD patterns and the structural map show that H-insertion into Faradiser M, as carried out in this work, proceeded through two homogeneous phases. In the first phase, the H-insertion caused a homogeneous expansion of the structure anistropically in the *b* direction. The structure was similar to that of the starting material which has been indexed in the ramsdellite structure. Thus, at this stage the octahedra are of ramsdellite type and the tunnels (see Fig. 3.1) are almost rectangular. This stage lasted from the starting material to an insertion level of s = 0.67.

By about s = 0.69, a sudden phase transition occurred when the structure hinged causing the tunnels to change shape and made the octahedra groutite-like. This transition from ramsdellite-like to groutite-like structure was accompanied by a decrease of the hinging angle β and a further increase in the apical expansion. The new structure has the *b* value of the end product but shorter *a*.

FTIR spectra have shown clearly that inserted H was mobile in the first homogeneous phase and located all at the onset of the second homogeneous phase. This is revealed by the size of the absorption bands of the OH vibrations. The sudden location of all previously mobile H must mean that all the tunnels became suitable for H bonding; in other words, a *total* structural change as the XRD has shown.

An interesting finding was that the H-insertion led to an expansion of the *b* dimension at constant *a*, which is the reverse of the behaviour that occurred with SBP-A. This finding puts a question mark on the amount of microtwinning associated with Faradiser M, since microtwinning inhibits the expansion in the *b* dimension as was concluded from the previous chapter. The conclusion here is that Faradiser M is not microtwinned.

The expansion along the *b* axis was also accompanied by substantial particle cracking and break up, just as occurred when SBP-A demicrotwinned (section 3.4). However, in this material the cracking and break up started immediately with the H-insertion and proceeded in the first homogeneous phase. Figs. 4.27 – 4.30 show SEM pictures of four H-inserted Faradiser M samples within the first homogeneous phase. The particles, initially round and smooth with peas-like appearance at the starting material, cracked and broke up upon insertion and became smaller and angular.

The particle break up seems now to be associated with an increase in the *b* dimension, or more generally anisotropic expansion, rather than demicrotwinning as Faradiser M

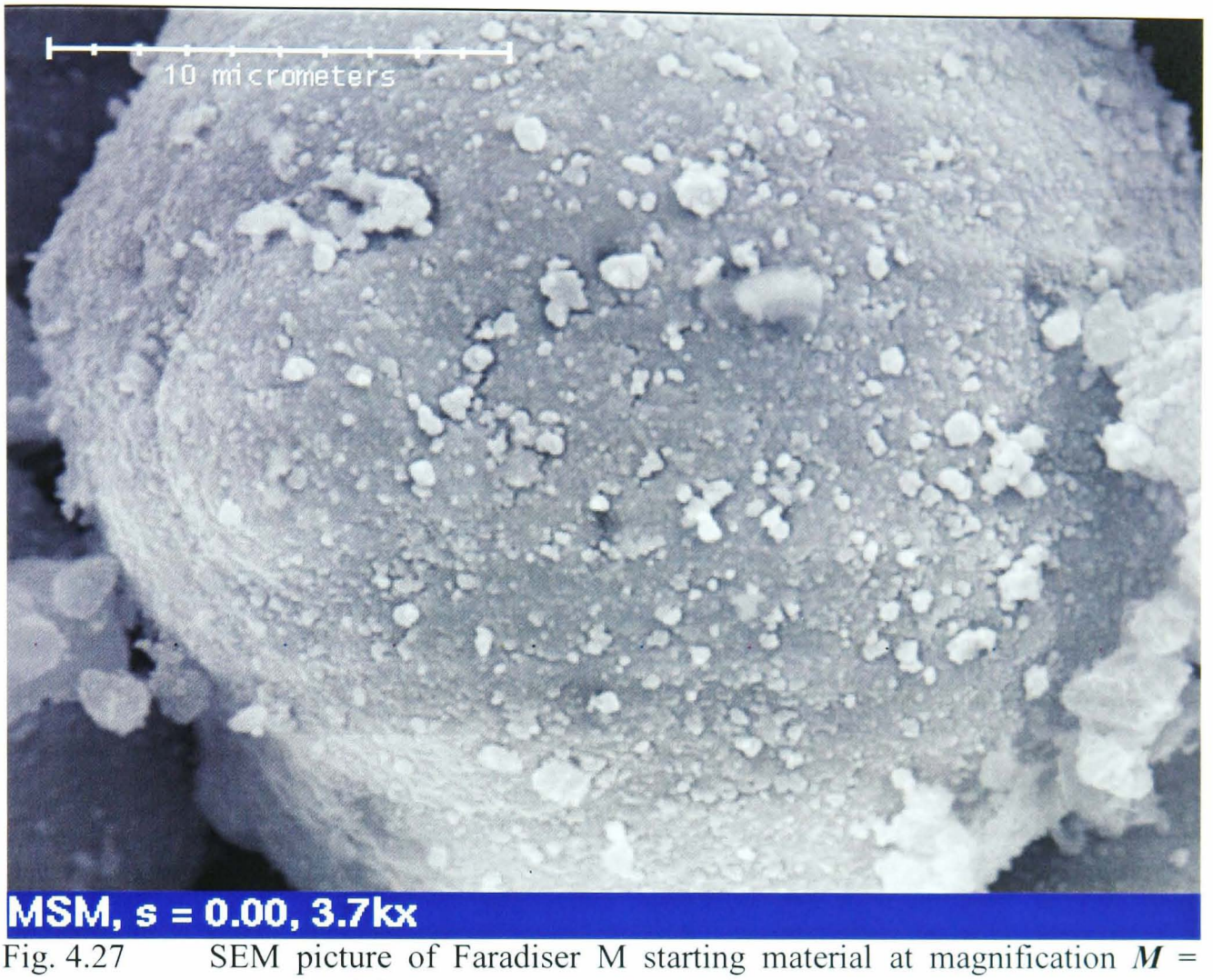

Fig. 4.27 SEM picture of Faradiser M starting material at magnification ***M*** = **3.7k**. Particles are smooth and unbroken.

Fig. 4.28 SEM picture of slightly H-inserted Faradiser M (s = 0.117) at about ½***M***. Particles are cracked and broken.

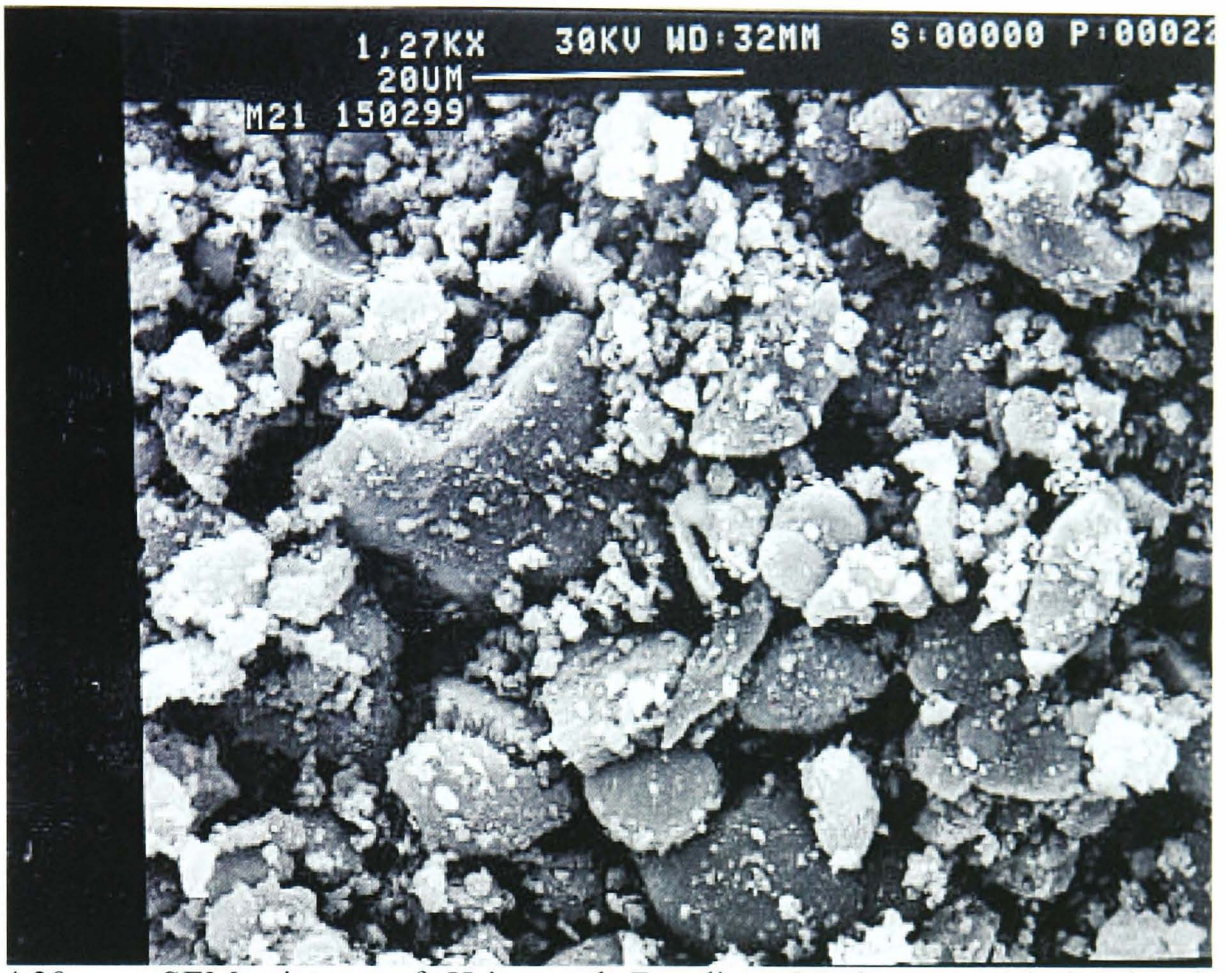

Fig. 4.29 SEM picture of H-inserted Faradiser M (s = 0.564) in the first homogeneous phase at about ½***M***. Particles are further cracked and broken.

Fig. 4.30 SEM picture of the last H-inserted Faradiser M (s = 0.666) in the first homogeneous phase at about ½***M***. Particles are further cracked and broken.

is only slightly[18] (if at all) microtwinned.

4.5 Conclusions

- XRD study provided evidences that H-insertion into Faradiser M proceeded in a single homogeneous phase with the structure of the starting material, from s = 0 to s = 0.69. During this phase, the FTIR spectra had shown that protons were mobile in the host structure. The main feature in this stage was a substantial anisotropic expansion of the *b* dimension which started immediately with the H-insertion and caused the particles of the materials to break up.
- The immediate expansion of the *b* axis at very low insertion level suggests that there is no restriction in the *b* direction; in particular, there is no microtwinning. (compare with SBP-A, Chapter 3).
- Above s = 0.69, the insertion proceeded also in a homogeneous phase but with the changed structure of the product. Hydrogen was located in the tunnels of the structure. Hydrogen location was evidenced by OH bond vibrations in the FTIR spectra. In this stage, limited anisotropic expansion occurred in the *a* direction at a constant *b* value for the unit cell.
- The difference in the values of the rotation angle β between the two phases strongly suggested that a sharp and sudden rotation must have taken place, at an insertion level between s = 0.67 and s = 0.72, leading to the structure of the end product. The value of s = 0.69 has been proposed as the insertion level at which the rotation occurred.
- The FTIR spectra of the most H-inserted samples have shown that the H-insertion occurred simultaneously into both groutite and manganite blocks of the intergrowth without preference. Furthermore, the ratio of the manganite and groutite peaks (in the FTIR spectra) of Faradiser M compared with SBP-A, suggested a link with the de Wolff fault in the starting materials.

5 XRD & FTIR Study of R2

5.1 Results of the XRD Study

5.1.1 Introduction

EMD R2 has been the subject of many studies[6,13,18,21,33,40-47,125]. It is probably the most studied manganese dioxide compound. However, a proper structural study is rather difficult to apply to this battery active material. The reason is essentially the extensive microtwinning of this γ-MnO_2 variety which causes all the XRD lines (except the 200) to either shift or broaden[18] (Table 1.2). In the previous materials, estimation of lattice parameters was possible from the lines with (½k + ℓ) even, on the ground of limited amount of microtwinning. The reader is reminded that (½k + ℓ) even lines are not affected by de Wolff disorder. The poor XRD patterns of R2 led Pannetier[18] to index them in a hexagonal system (as an alternative to the orthorhombic) with a = 2.785 and c = 4.432 Å. The hexagonal symmetry has been suggested to be only *apparent*[29] while the proper symmetry is orthorhombic. The extensive microtwinning of R2 has been estimated[18,33] as 100 % while the de Wolff faults were given the values of 0.42[18] and 0.43[33]. The fully H-inserted R2, however, can be readily indexed in the groutite-like orthorhombic structure and the set of lattice parameters a = 4.514, b = 10.490 and c = 2.867 Å was given[33] to a sample of s = 0.900 prepared by Fitzpatrick and Tye[42]. The pyrolusite fraction of 0.42 or 0.43 is close to that of SBP-A and application of the same argument (see section 3.1) leads to indexing R2 in a ramsdellite-like structure. Hence, the R2 starting material and its fully H-inserted modification can be looked upon as iso-structural, belonging to the ramsdellite/groutite structure but the extensive microtwinning in the starting material renders estimation of lattice parameters unreliable. Unlike the previous materials (SBP-A and Faradiser M), the peak deconvolution and lattice parameters estimation exercise has not been applied to R2 since the peak are shifted from their true position. The changes undergone by the starting material upon H-insertion through the most H-inserted samples were essentially derived from the peaks shape and movement. Conclusions on H-insertion into R2 were drawn with the aid of the structural changes in SBP-A and Faradiser M exposed in the previous chapters.

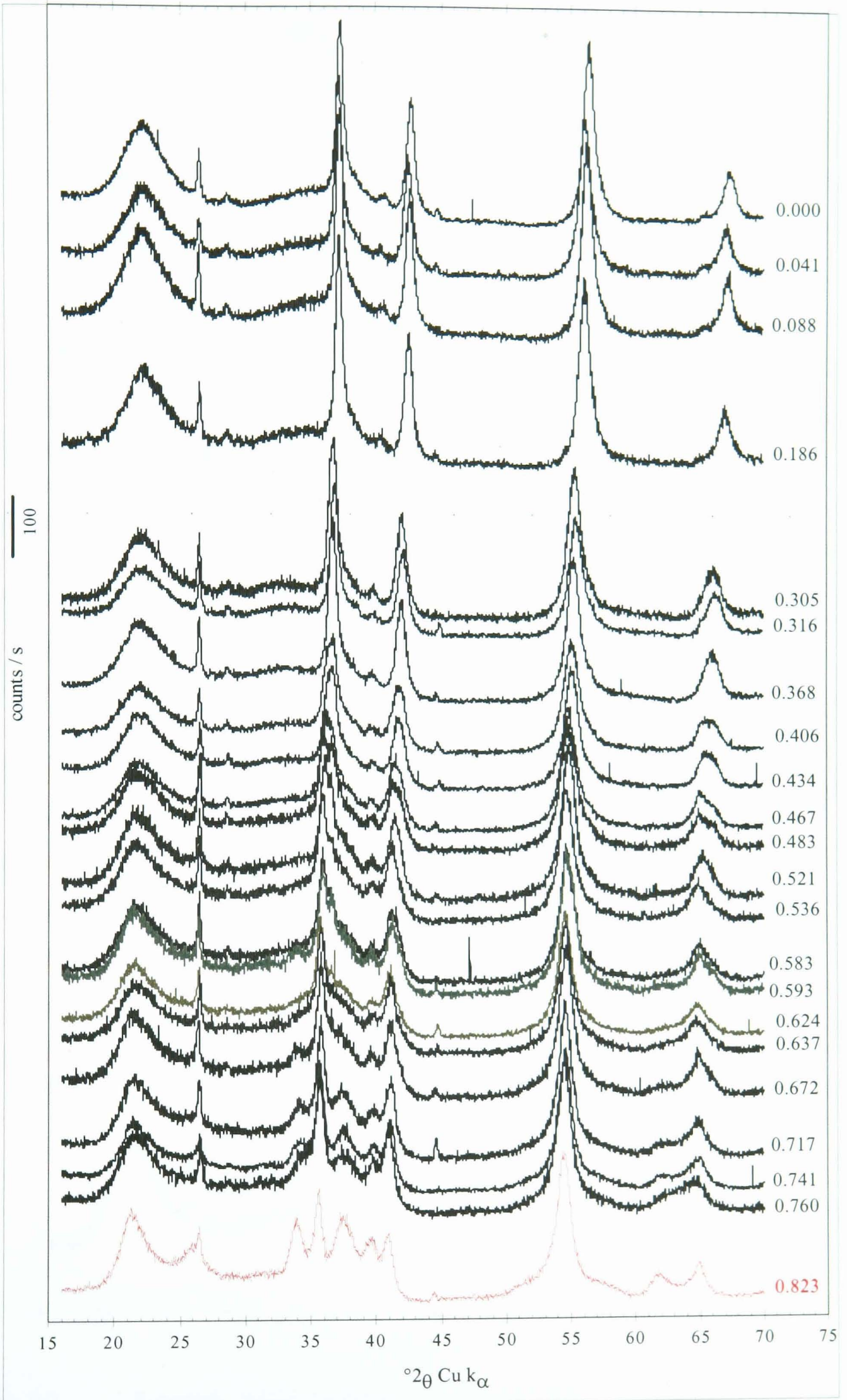

Fig. 5.1 Selected XRD patterns of R2 material stepped down the page in proportion with the insertion levels. H-insertion ranges from s = 0 to s = 0.823. hkℓ indices are omitted for clarity but shown in Figs. 5.2, 5.7 and 5.8.

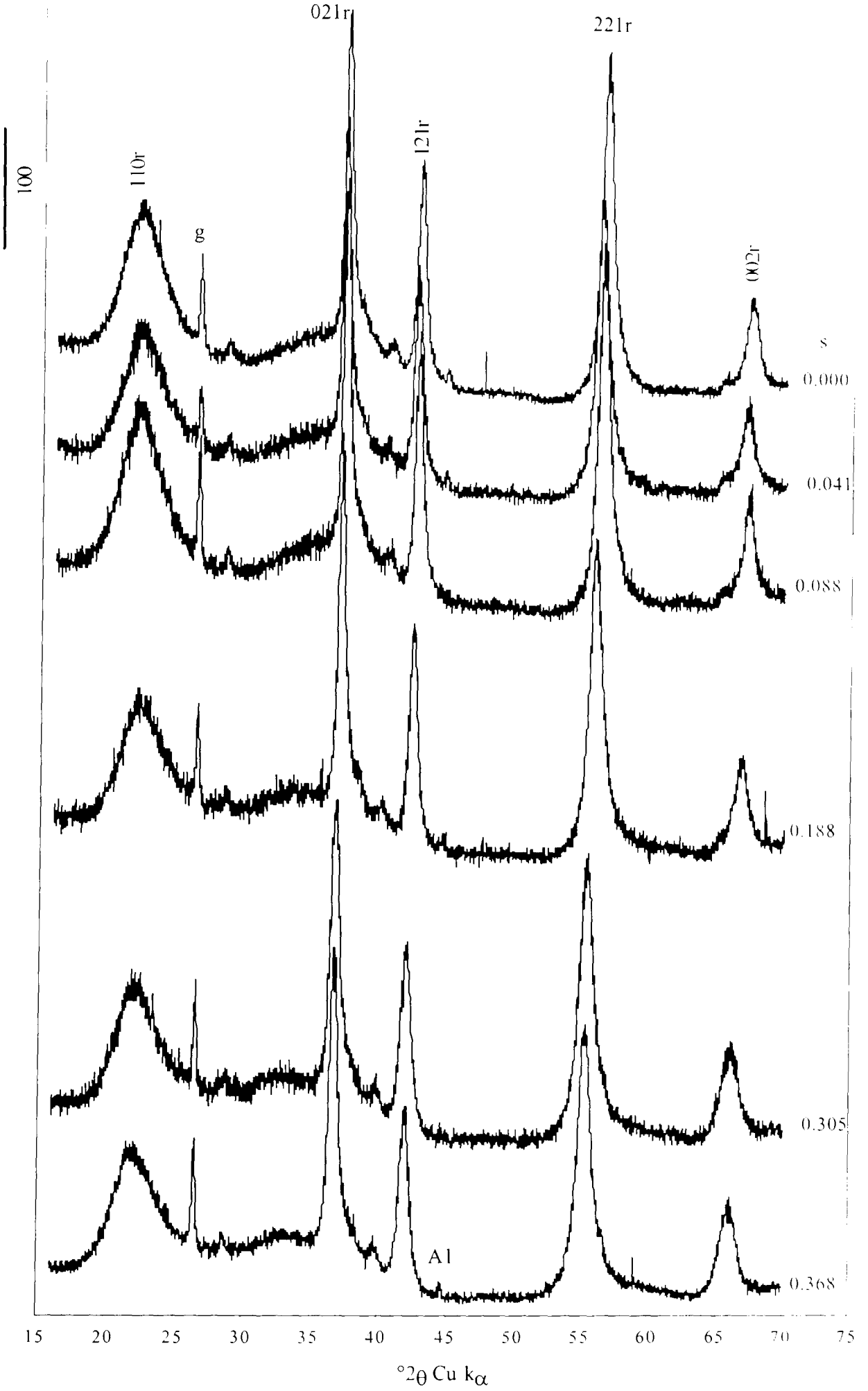

Fig. 5.2 Selected XRD patterns of R2 H-inserted patterns in the first homogeneous phase stepped down the page in proportion with the insertion levels. The $hk\ell_r$ indices refer to the most probably contributing lines of the ramsdellite structure. g stands for a graphite impurity from manufacture.

Therefore, peak assignment/indexing was made in comparison with the patterns of SBP-A and Faradiser M; and the most probable hkℓ lines are shown in the relevant figures

The XRD patterns of 22 (out the 30 R2 samples prepared, Appendix 5) covering the insertion range $0 \leq s \leq 0.82$ are shown in Fig. 5.1. Inspection of the patterns reveals three distinct regions of H-insertion, namely from s = 0 to s = 0.368 inclusive, from s = 0.406 to s = 0.624 inclusive and above s = 0.637.

These three regions will be shown below to be a homogeneous insertion region followed by two heterogeneous insertion regions.

5.1.2 Homogeneous H-Insertion

A subset of the XRD patterns of R2 ranging from s = 0.00 to s = 0.37 is shown in Fig. 5.2. The patterns have kept the same features indicating that they all belong to the same structure. The peaks did not change shape or intensity apart from minor increase/decrease of intensity reflecting slight changes in background. The change undergone by the patterns, however, was a steady shift towards lower angles. Peak position against insertion level demonstrates this behaviour as shown in Fig. 5.3 to 5.6.

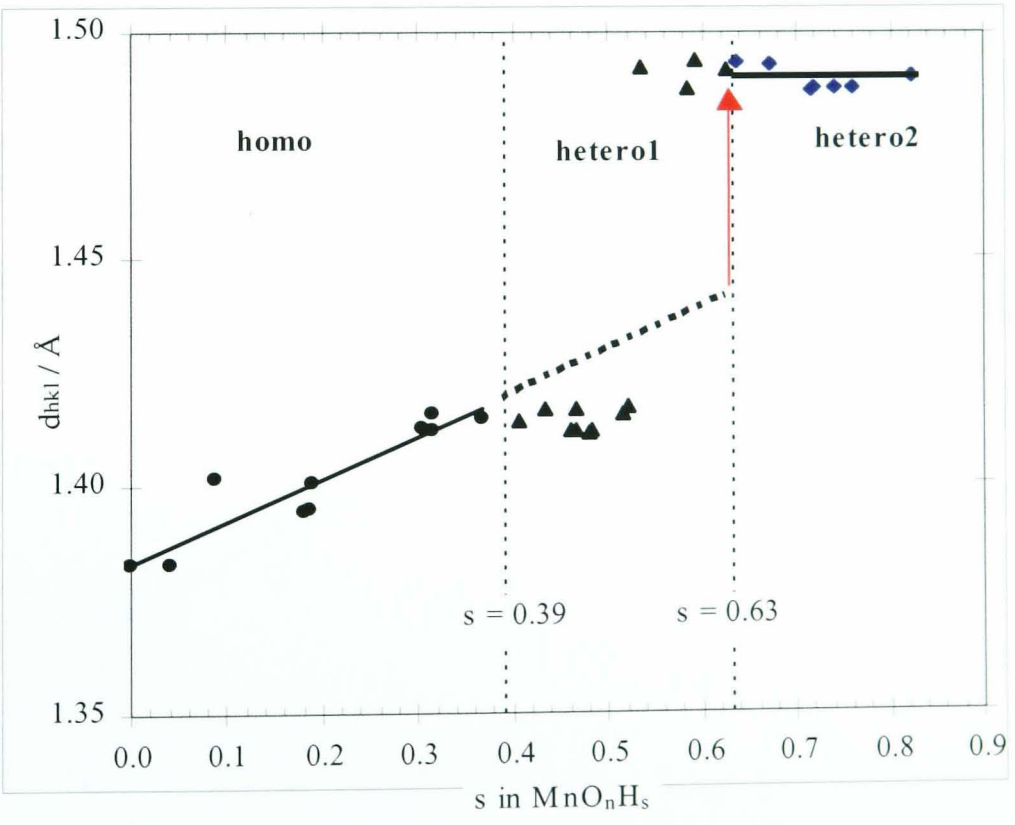

Fig. 5.3 Movement of the 002 line with insertion level into R2. The domains of the H-insertion regions are shown and the arrow marks the direction and amount of line shift in the final heterogeneous region.

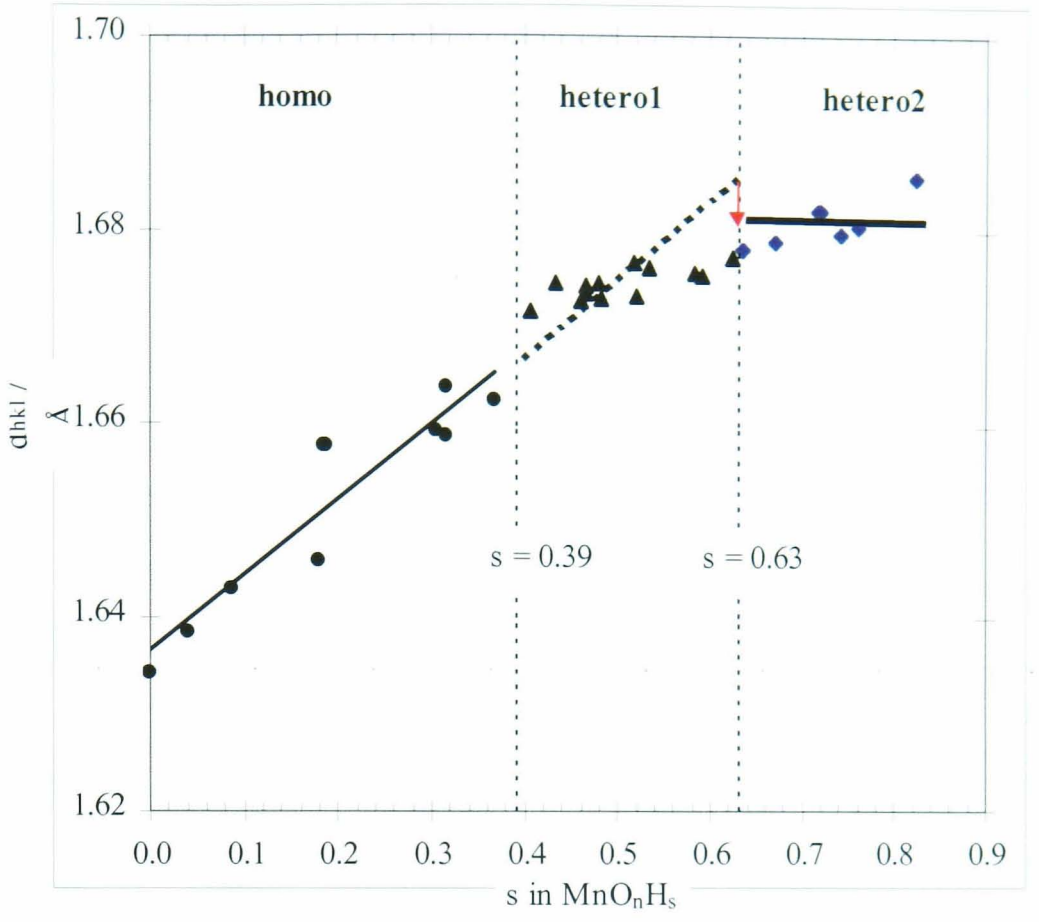

Fig. 5.4 Movement of the 221 line with insertion level into R2. The domains of the H-insertion regions are shown and the arrow marks the direction and amount of line shift in the final heterogeneous region.

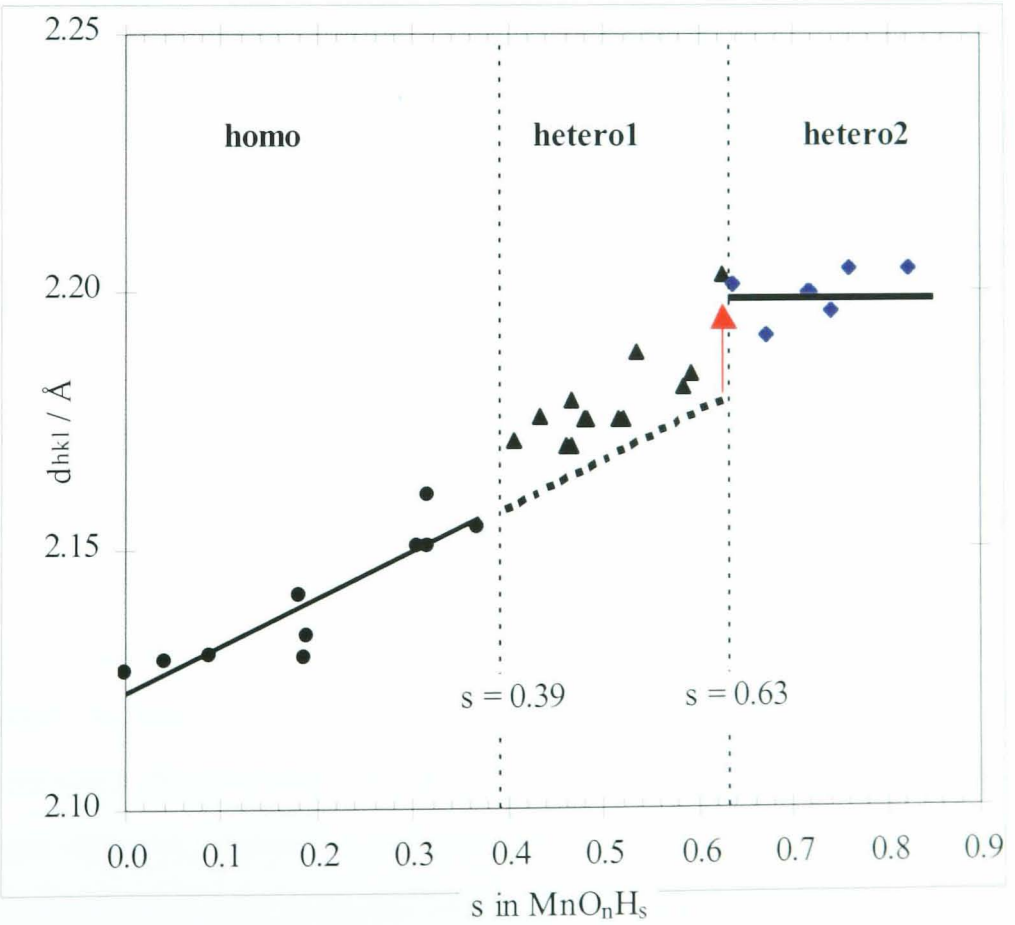

Fig. 5.5 Movement of the 121 line with insertion level into R2. The domains of the H-insertion regions are shown and the arrow marks the direction and amount of line shift in the final heterogeneous region.

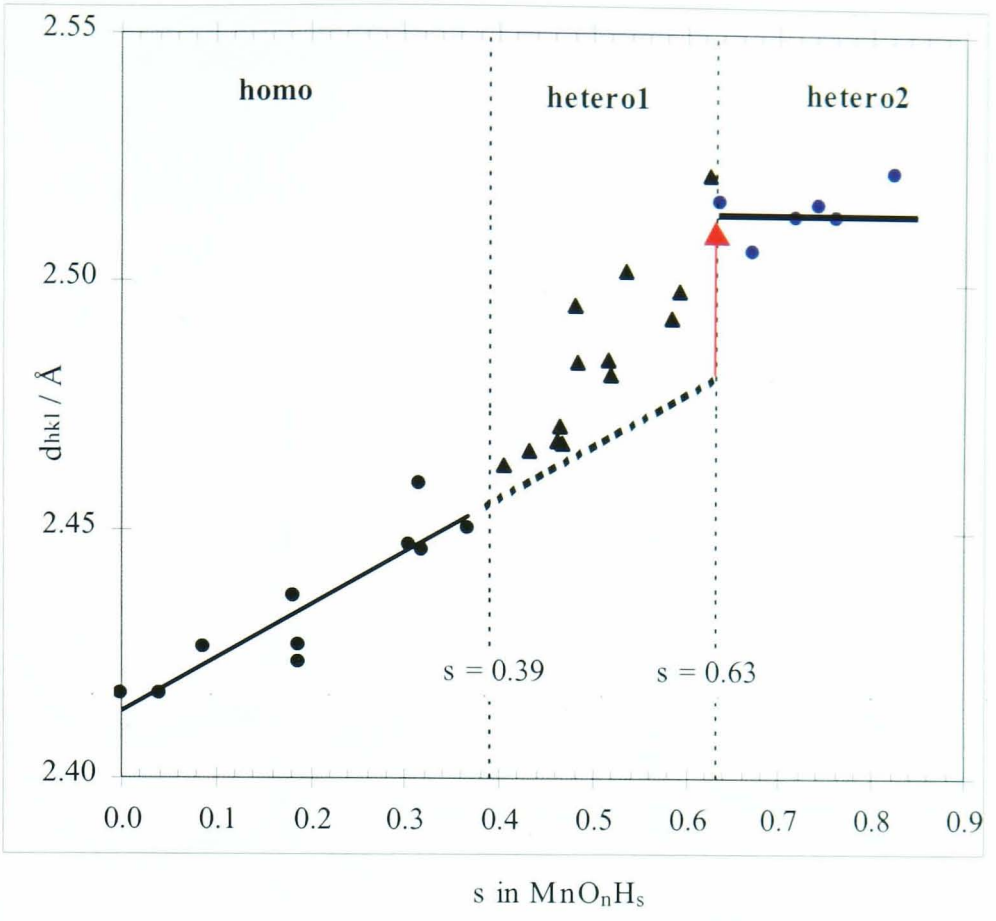

Fig. 5.6 Movement of the 021 line with insertion level into R2. The domains of the H-insertion regions are shown and the arrow marks the direction and amount of line shift in the final heterogeneous region.

Slight microtwinning has been suggested to restrict the expansion of the *b* dimension in SBP-A when only a limited anisotropic expansion in the *a* dimension occurred. Absence of microtwinning resulted in an immediate expansion of the *b* dimension in Faradiser M, as the insertion proceeded. Heavy microtwinning, however, seems to persist by allowing the whole structure to expand perhaps isotropically as it was suggested earlier[42]. This point will be returned to in section 5.3.

5.1.3 First Heterogeneous H-Insertion

From s = 0.406, early signs of structural change became evident from the XRD patterns, as shown in Fig. 5.7. At s = 0.406, the tip of the 002, 121 and 021 ramsdellite lines broadened suggesting a tendency to split into two lines. The diffractogram at s = 0.368 is shown in Fig. 5.7 to aid visualising this broadening. In addition, the background between the 021 and 121 lines has risen suggesting that new peaks may develop. These changes, which are evidence of heterogeneous phase, enhanced as the insertion proceeded up to and inclusive of s = 0.624. The obvious line broadening of 021r and 002r at s = 0.406 and s = 0.434 (Fig. 5.7) led to two shoulders on these peaks at subsequent insertion levels.

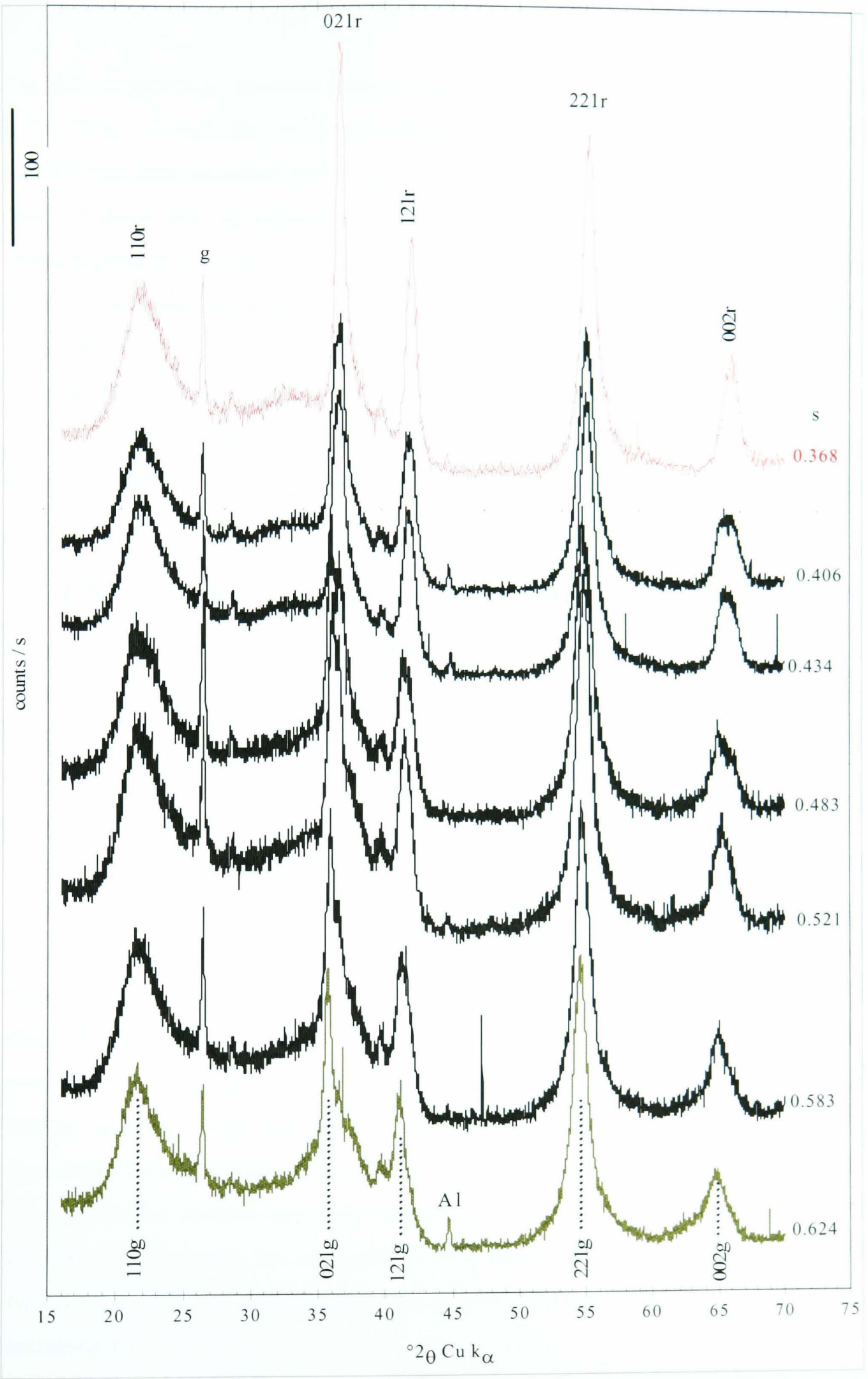

Fig. 5.7 Selected XRD patterns of H-inserted R2 samples in the heterogeneous phase stepped down the page in proportion with the insertion levels. The diffractogram at s = 0.368 is shown for comparison (not part of the set). g and r subscripts refer to groutite and ramsdellite hkℓ lines.

Fig. 5.3, in particular, provides further evidence of heterogeneous H-insertion between s = 0.39 an s = 0.63: the two sets of interplanar spacing at about 1.41 and 1.49 Å for the 002 line from the initial and the final structures respectively.

Fig. 5.7 shows that, in addition to the growing shoulder at about 63 and 37 °2θ, the diffractogram at s = 0.624 is shifted to lower angles compared with that at s = 0.368. This shift to lower angles does not fall on the lines extrapolated from the homogeneous region between s = 0.000 and s = 0.368 as shown by Figs. 5.3 to 5.6. Thus, this shift must be due to a different phenomenon from the lattice dilation.

Delineation of the extent of this stage on the insertion scale has been estimated in the same way applied to SBP-A and Faradiser M, and the boundaries are shown on Figs. 5.3 – 5.6 as s = 0.39 and s = 0.63.

5.1.4 Second Heterogeneous H-Insertion

Above s = 0.63, new lines emerged shaping the XRD patterns to the final product of the H-insertion, as shown in Fig. 5.8. All lines ceased to shift and the new lines strengthened in intensity while those of the reactant material (s = 0.637) weakened. These are obvious indications of heterogeneity. Examples of development of the new peaks characteristic of the final H-insertion product are demonstrated in Figs. 5.9 – 5.11. These figures plot the height of three peaks from the structure of the final H-inserted product. Figs. 5.9 – 5.11 also delineate the extent of the homogeneous phase at s = 0.39 and show the dividing line between the two heterogeneous phases at s = 0.63. These plots are discussed in turn.

Fig. 5.9 displays the counts at 34 °2θ against the insertion level. This spot is the position of the (040) groutite line (Fig. 5.8). In the homogeneous region, no peak was located near this angle and the counts reflected the background, with some slight fluctuation due to the shift of the adjacent peak, hence the light slope. From s = 0.39 to s = 0.63, the broadening of the adjacent peak (021r, see Fig. 5.7) caused further increase in the counts, but remained slightly above the order of magnitude of the background. Above s = 0.63, the (040) groutite line started to grow and the counts increased accordingly.

Fig. 5.10 monitors the counts at 37.78 °2θ, the location of the (111) groutite line in the final H-insertion product. Since the vertical at this angle is in the high angle side of peak 021r in the starting material, the counts decreased in the homogeneous phase as

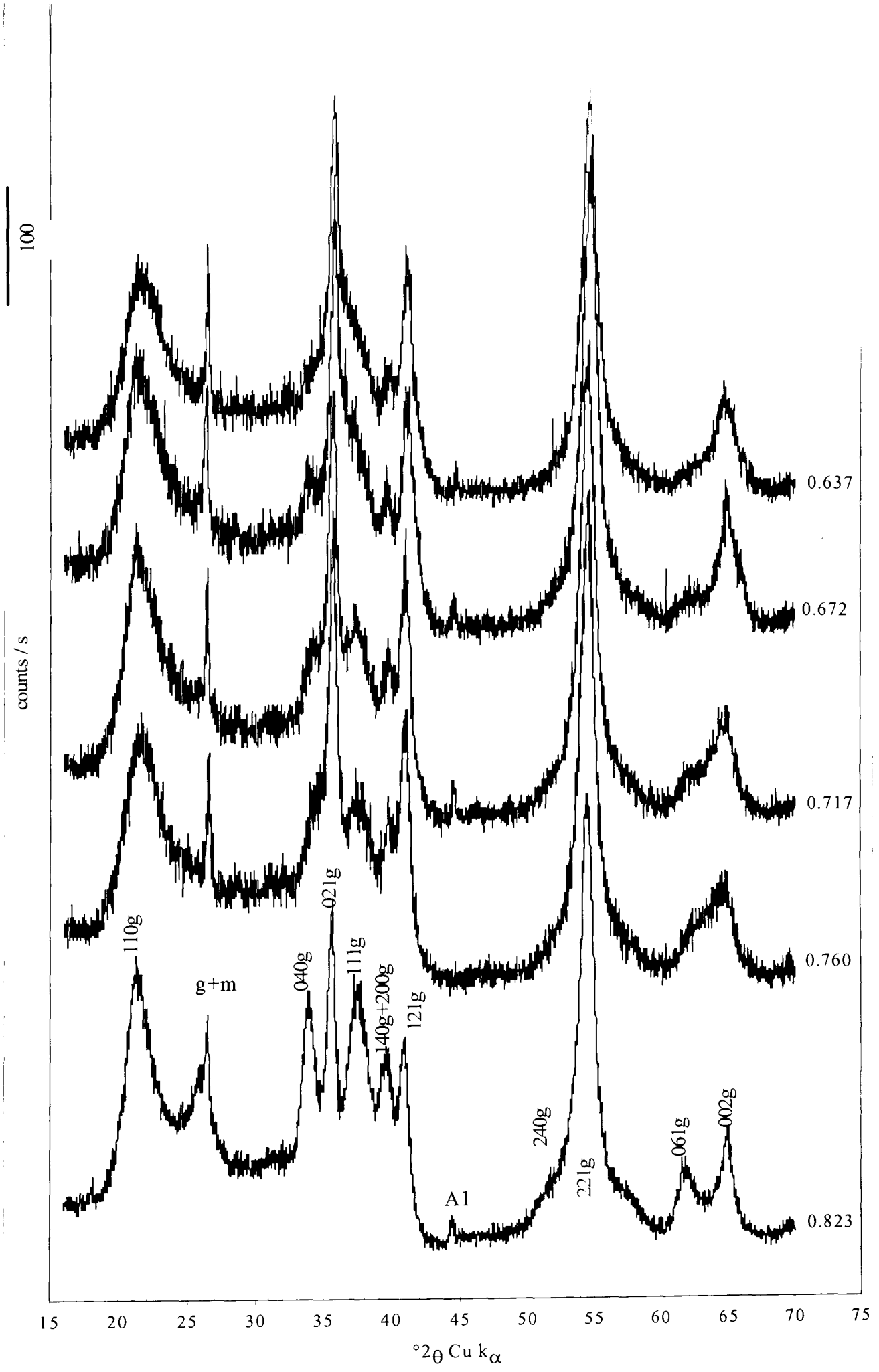

Fig. 5.8 Selected XRD patterns of H-inserted R2 samples in the second heterogeneous phase. The hkℓ labels refer to groutite structure. Manganite impurity is marked m, g and Al stand for graphite and aluminium impurities from manufacture and XRD the sample holder respectively.

the 021r line shifted towards lower angles. At the onset of the first heterogeneous h phase, the 021r line broadened and gave a shoulder extending to the right, hence the counts increased. In the second heterogeneous phase, this broad shoulder developed as a separate peak, the 111g in the final product; hence the counts increased further.

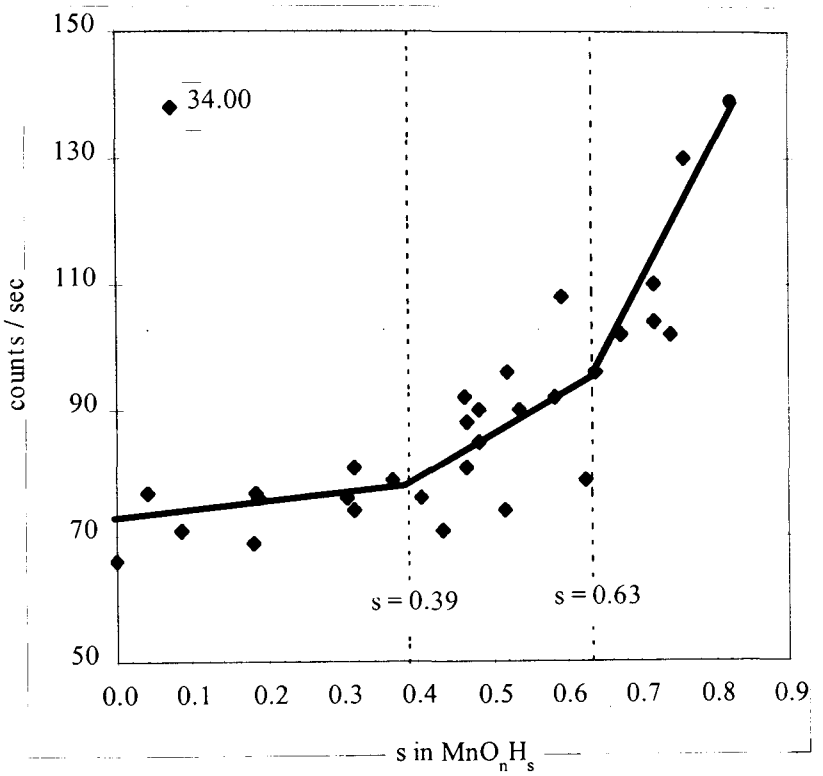

Fig. 5.9 Counts against insertion level at 34 °2θ showing the development of the 040g peak in the second heterogeneous phase.

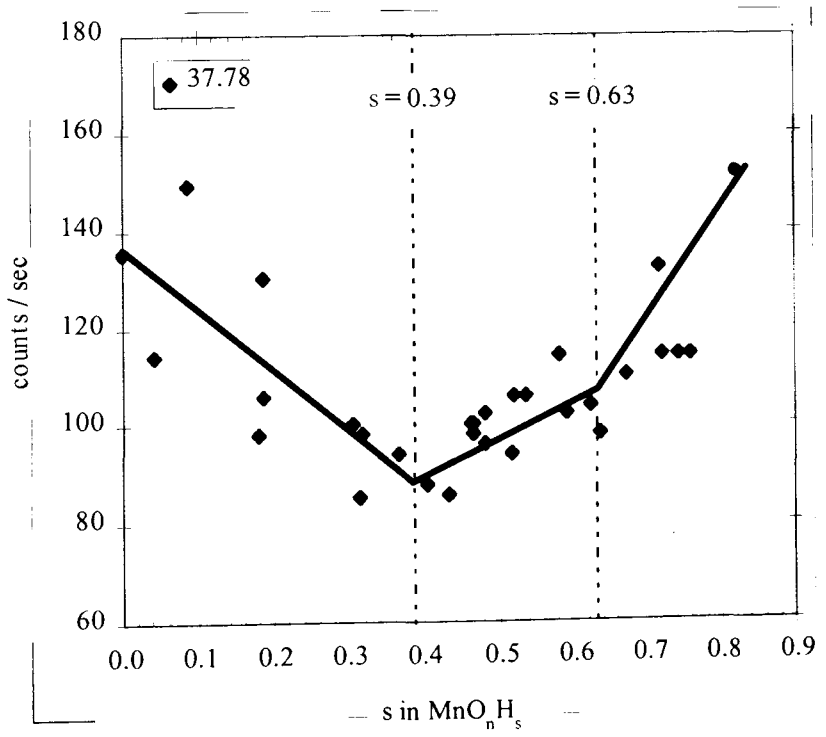

Fig. 5.10 Counts against insertion level at 37.78 °2θ showing the development of the 111g peak in the second heterogeneous phase.

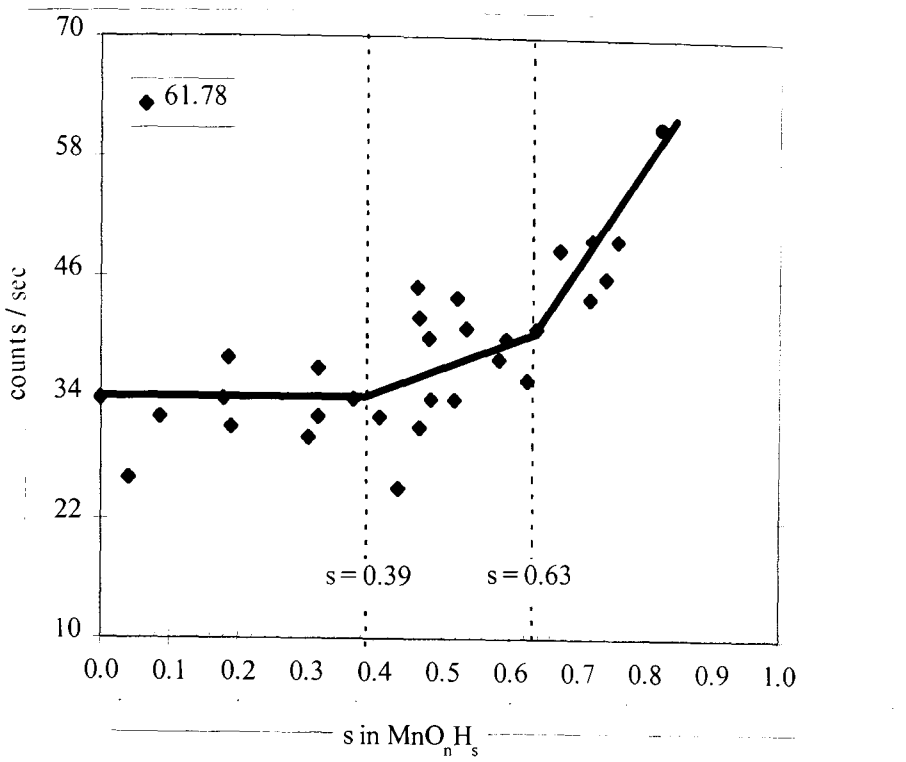

Fig. 5.11 Counts against insertion level at 61.78 °2θ showing the development of the 061g peak in the second heterogeneous phase.

The behaviour of Fig. 5.11 is similar to that in Fig. 5.9. The difference is that the background fluctuation in the first heterogeneous phase, was overall lower at 61.78 than at 34 °. This is because of this angle (61.78 °) is far enough from the tail of the 002r line. However, clear breaks at s = 0.39 and s = 0.63, when the 061g started to ```develop, were detected, as in the case of Fig.' 5.9 and 5.10.

It is noteworthy that the most H-inserted sample (s = 0.823 on Figs. 5.1 and 5.8) is, strictly speaking, not a part of the R2 - H-inserted compounds series due the manganite impurity peak, signalled "m", overlapped with the graphite peak. This manganite (pure phase) precipitated, at high H-insertion level by a side reaction, as an energetically easier product. That is to say, that precipitating a stable phase such as manganite would be more favourable than continuing to form highly distorted intergrowth structure, particularly near the end of the insertion.

A consequence of the manganite impurity precipitated on the surface of the insertion product, is an apparent improvement of the quality of the XRD patterns. Fig. 5.8 demonstrates that the quality of the patterns did not improve significantly from s = 0.717 to s = 0.760, i.e. over a stretch of 0.043 in s. For an additional 0.063 in s, when manganite was precipitated, the lines become sharper and more resolved as at s = 0.823. Here, the measured XRD patterns were rather for a *manganite-coated* H-inserted sample.

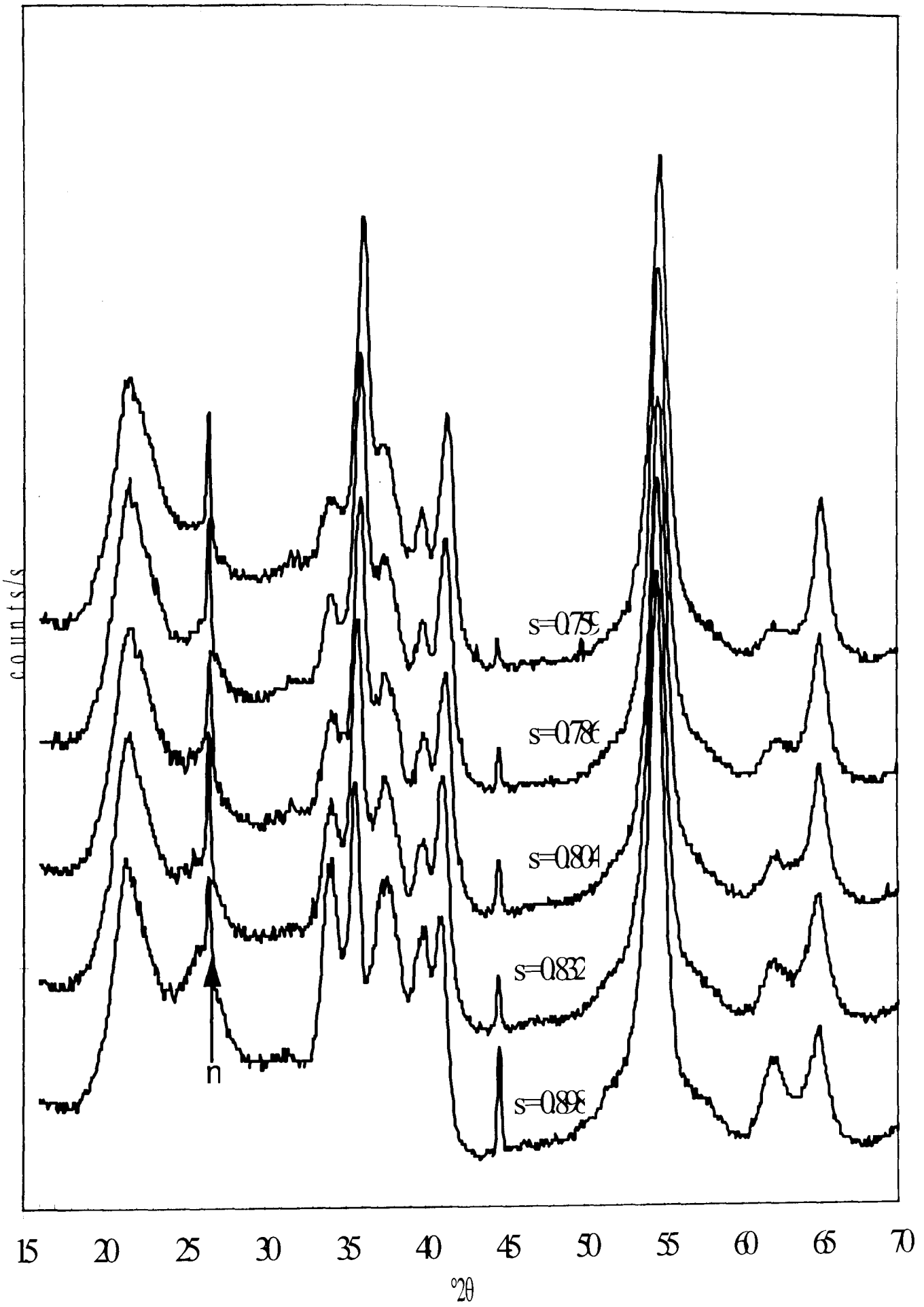

Fig. 5.12 XRD patterns of highly H-inserted R2 samples by J. Fitzpatrick. Note that the quality of the lines improved simultaneously with the amount of manganite impurity marked m and indicated with the arrow.

This conclusion is supported by observing the XRD patterns H-inserted R2 samples prepared under milder conditions, with much less precipitated manganite. by Fitzpatrick and Tye[42]. Fig. 5.12 displays the XRD patterns* of samples with insertion level above s = 0.7 (these patterns are not published in ref. 42). Inspection of the figure reveals that the quality of the XRD lines improved simultaneously with the amount of precipitated manganite.

If this manganite content was omitted, the remaining lines of this sample could presumably be considered a continuation from the previous sample (s = 0.760). MacLean and Tye[33] concluded that manganite impurity does not effect the XRD lines position from the comparison of two XRD patterns of Faradiser WSZ of virtually the same insertion level with and without manganite. However, this conclusion can also be predicted from the fact that most manganite lines are close to those of fully H-inserted manganese dioxide (see Chapter 7). Observation of that figure (Fig. 6 of ref. 33) reveals that the lines of the manganite-free patters are weaker and broader than the patterns from samples having manganite impurity.

An additional possible consequence of the manganite impurity is a misleading insertion level s. The pure manganite phase would tend to increase s. So, the insertion levels of manganite contaminated samples are only apparent and the true values are lower.

To account for the difference between manganite free and contaminated H-inserted samples, lines and counts derived from the contaminated sample of this work (s = 0.823) have been distinguished on the relevant figures.

5.1.5 Comparison with Previous XRD Work

Previous XRD studies of R2 have been carried at this Centre[42,50,51] and elsewhere[92]. However, only the work of Fitzpatrick and Tye[42] is available in digital format for comparison with this present work.

An earlier XRD study by Maskell et al.[92] reduced R2 material both electrochemically and chemically using a variety of methods including addition of drops of hydrazine hydrate. This paper[92] concluded that the H-insertion proceeded homogeneously throughout the full range on the basis that the new XRD lines emerging in the course

* The R2 H-inserted samples were prepared as described in ref. 42. The XRD patterns however were a re-examination of the same samples by L. MacLean[21].

of the H-insertion were assigned to precipitated manganite. In the light of more recent works[e.g.42,43,50,21,51] particularly this present work, which is manganite-free and bears similar new XRD lines, the above assignement seems in need of further consideration. Maskell et al.[92] were not alone to suggest that H-insertion into γ-manganese dioxide proceeds in a sngle phase, Giovanoli et al.[130] also suggested the one phase reduction with slight manganite precipitation from midpoint of the H-insertion.Comparison is now considered between the above XRD patterns and those published* by Fitzpatrick and Tye[42] for the same material. The authors employed acetone, cinnamyl alcohol and xylene individually and combined for the H-insertion. The H-insertion was conducted by prolonged storage of the R2 samples into excess of reagent in air-tight bottles at room temperature. Periods of up to 9 months were required for high insertion levels.

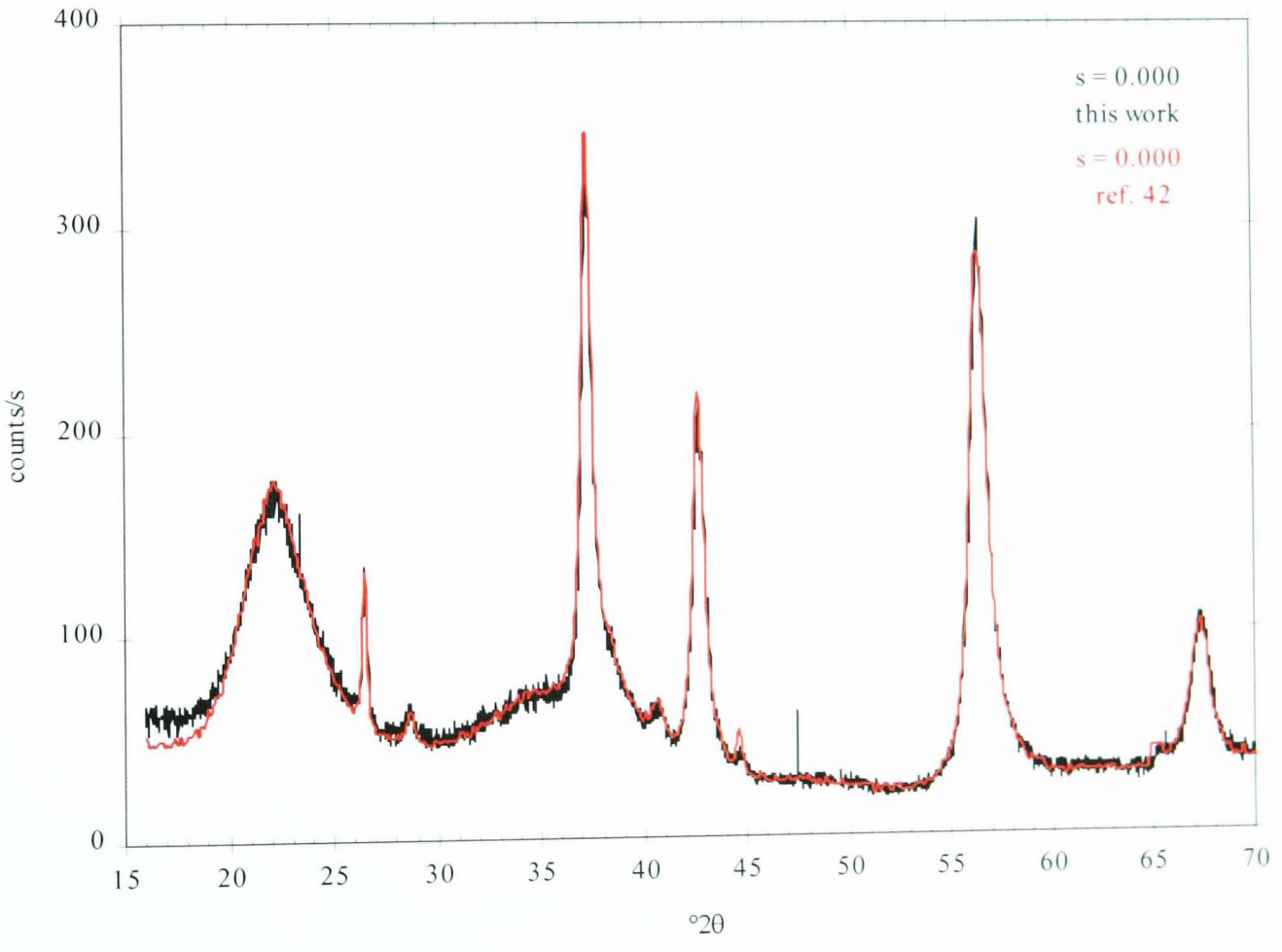

Fig. 5.13 Comparison of the XRD of R2 starting material in this work with that of Fitzpatrick and Tye[42]. The patterns are identical.

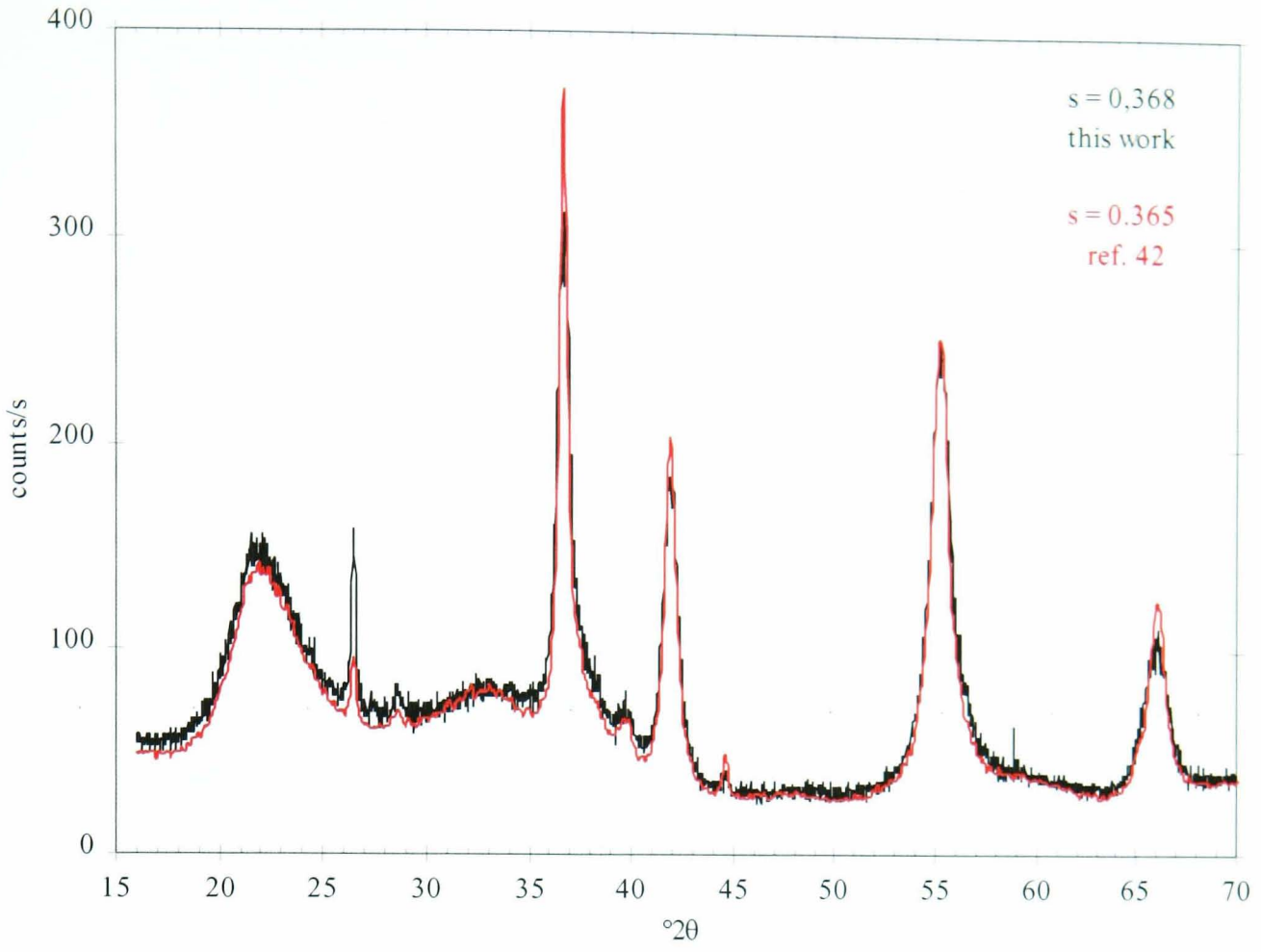

Fig. 5.14 Comparison of the XRD of H-inserted R2 in the common homogeneous region (s ≈ 0.37) in this work with that of Fitzpatrick and Tye[42]. The patterns are very similar.

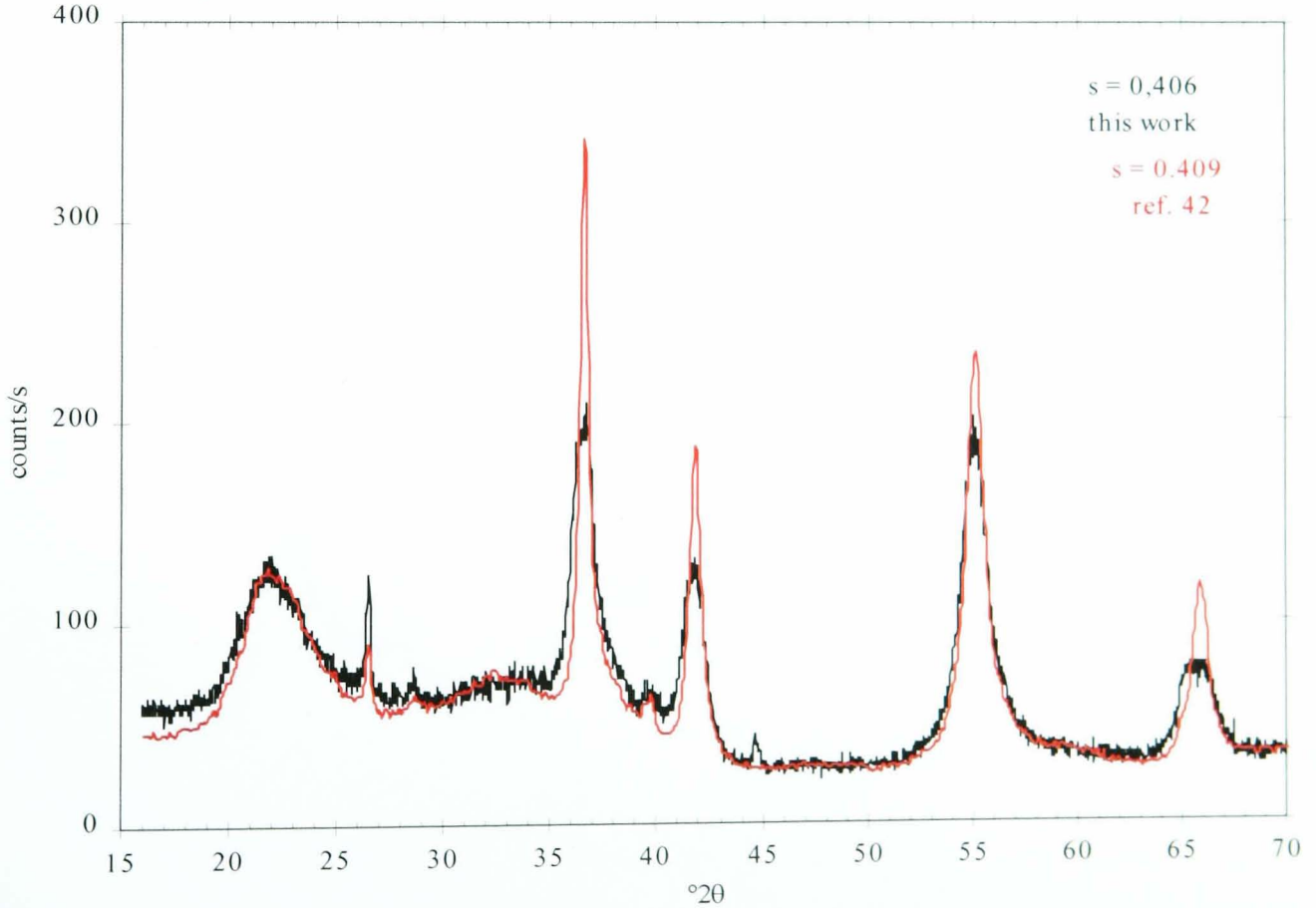

Fig. 5.15 Comparison of the XRD of H-inserted R2 (s ≈ 0.41) in this work with that of Fitzpatrick and Tye[42]. The patterns are different: this work heterogeneous.

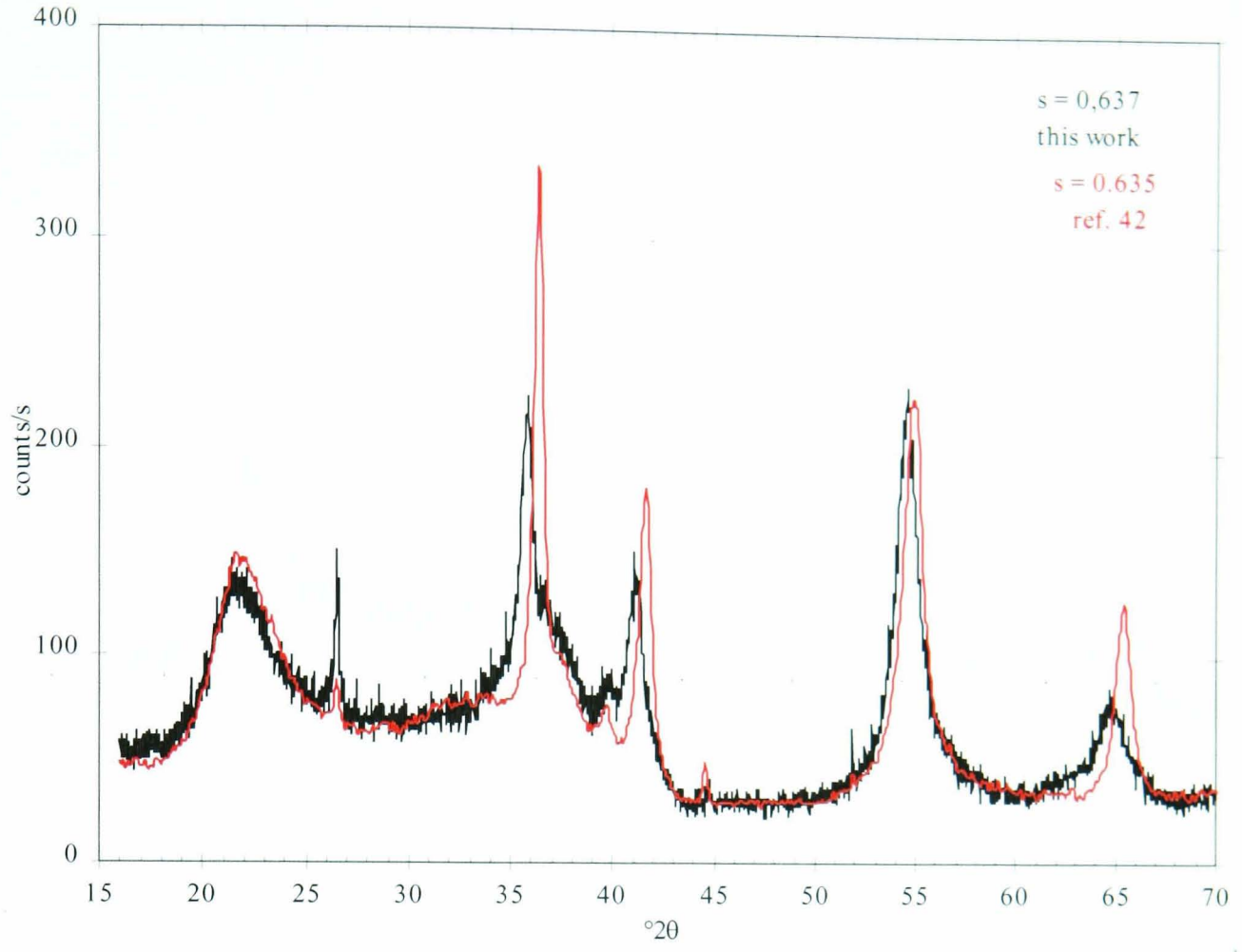

Fig. 5.16 Comparison of the XRD of H-inserted R2 (s ≈ 0.64) in this work with that of Fitzpatrick and Tye[42]. The patterns are different: both works in homogeneous region but different structures.

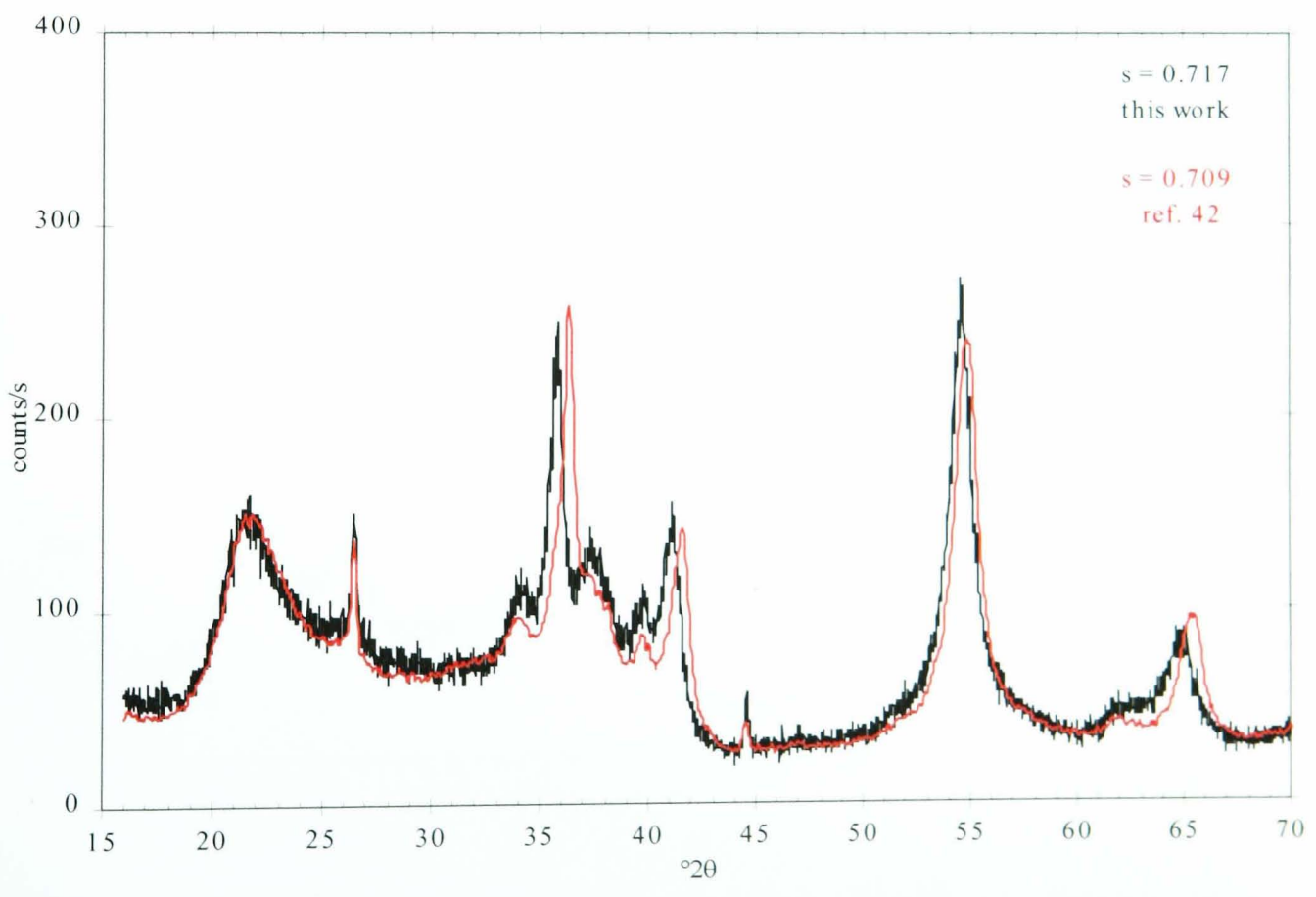

Fig. 5.17 Comparison of the XRD of H-inserted R2 (s ≈ 0.7) in this work with that of Fitzpatrick and Tye[42]. The patterns are different: ref. 42 heterogeneous, this work homogeneous.

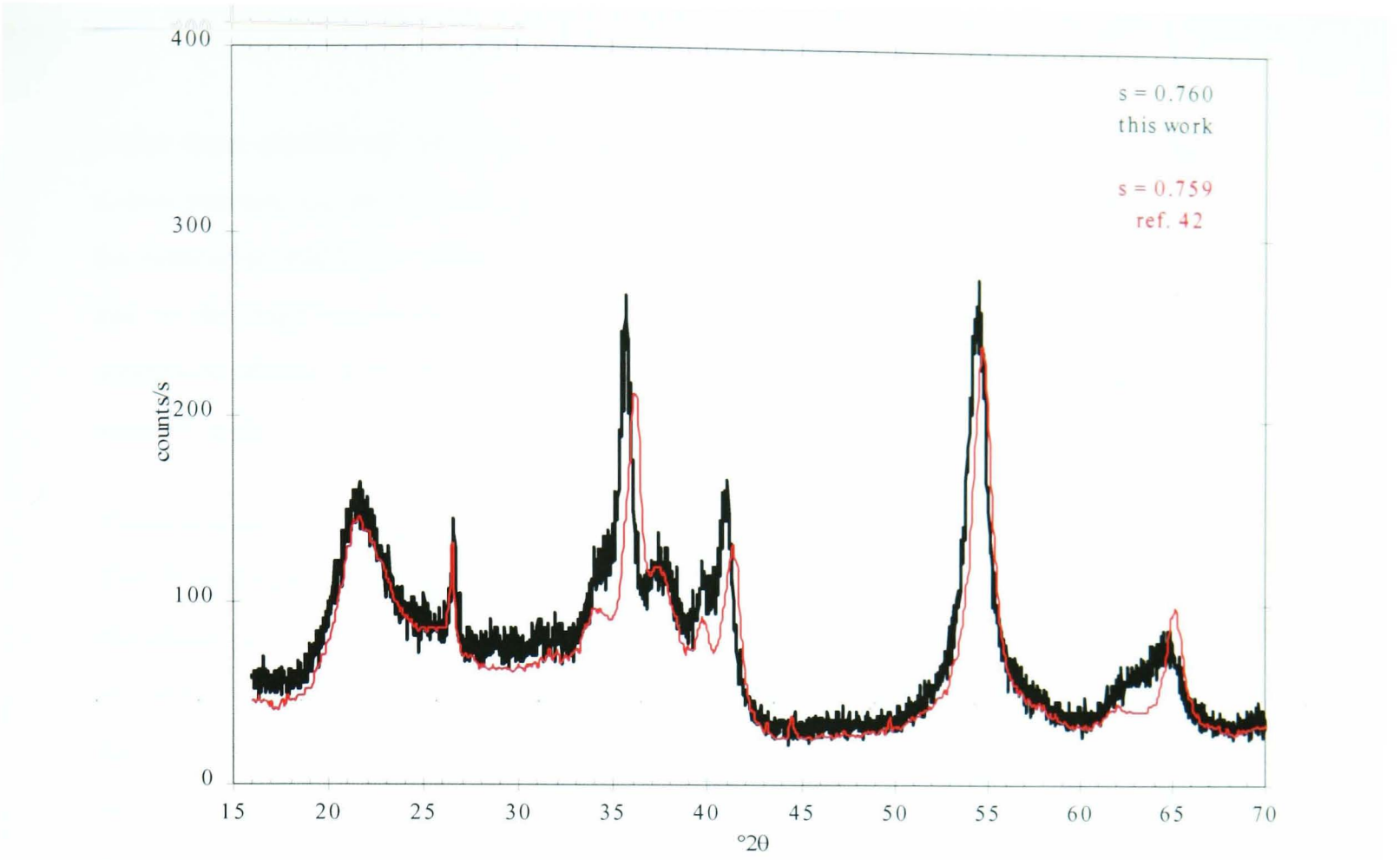

Fig. 5.18 Comparison of the XRD of H-inserted R2 (s ≈ 0.76) in this work with that of Fitzpatrick and Tye[42]. The patterns are different: ref. 42 heterogeneous, this work homogeneous.

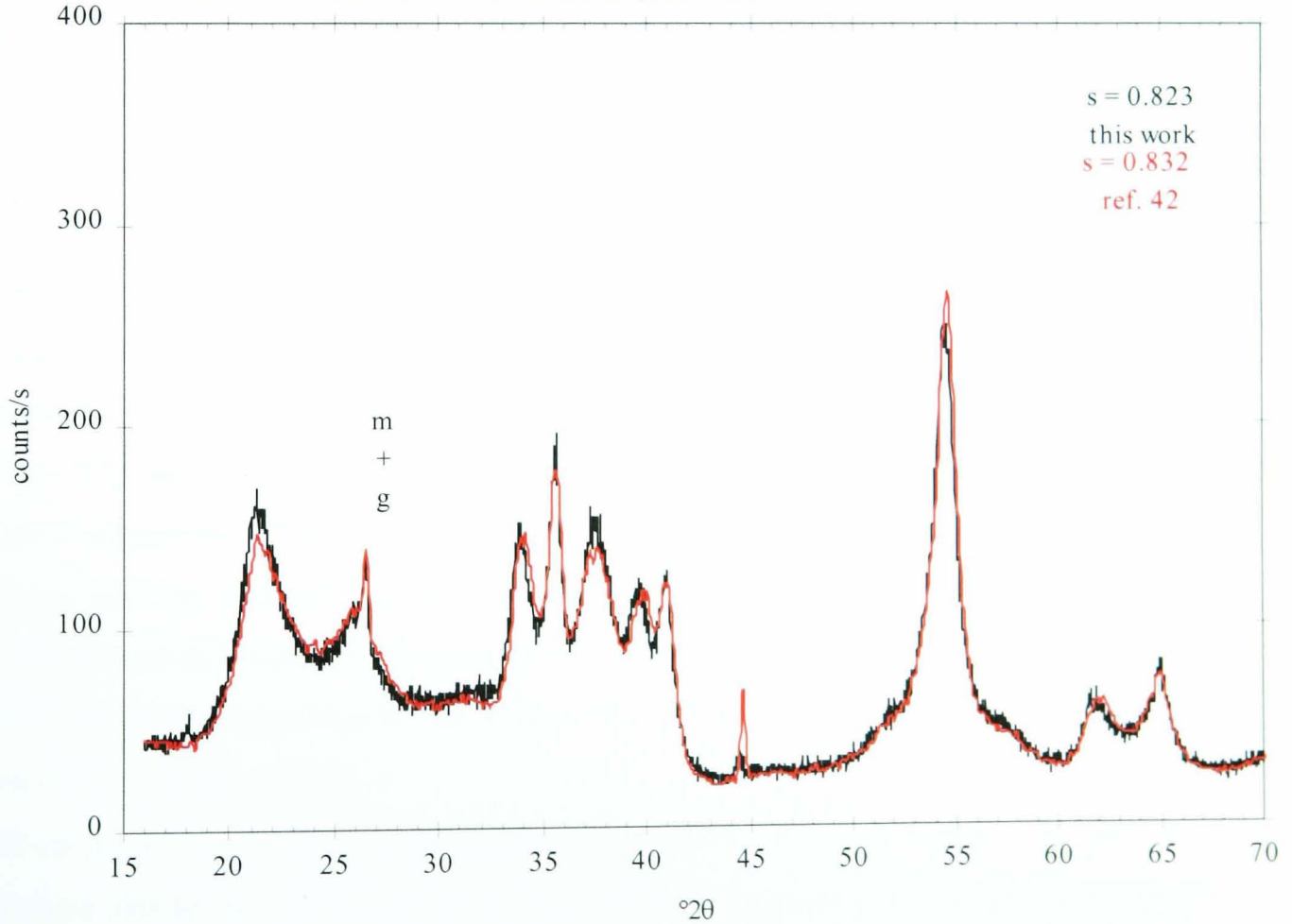

Fig. 5.19 Comparison of the XRD of the most H-inserted R2 (s ≈ 0.82) in this work with that of Fitzpatrick and Tye[42]. This work homogeneous, ref. 42 heterogeneous, but the precipitated manganite makes the patterns similar.

Under these conditions, the organic reagents were stable and extraction of H would be a slow process, i.e. the H-insertion was very gentle. The H-insertion was milder than the controlled additions of hydrazine hydrate at low temperature followed in this work, due to the high reactivity of hydrazine hydrate. The difference in the H-insertion conditions shows through the XRD patterns suggesting two different mechanisms in the two works.

There is good agreement on the XRD of unreduced R2 as shown in Fig. 5.13.
The H-insertion proceeded in a single homogeneous phase, in both works, reflecting the expected dilation of the crystal structure[31]. The extent of the homogeneous phase is, however, different. In the paper[42], the homogeneous phase extended from the starting material to an insertion level of s = 0.70, far ahead of the s = 0.39 limit in this work. This difference is likely to be due to the insertion conditions. In this work, the highly reactive hydrazine hydrate released spontaneously protons at the surface of the manganese dioxide. This easy release may generate a concentration gradient between the bulk and the surface causing the surface layer to enter a heterogeneous phase prematurely. In stable organic compounds, such as those employed by Fitzpatrick and Tye[42], pulling out protons is rather difficult and the material had time to assimilate the slowly released protons, hence the extended homogeneous stage.
Therefore, the two sets of patterns are expected to be similar where their homogeneous phases overlap (i.e. up to s = 0.39) and different above this level and below s = 0.70, when heterogeneous H-insertion overlaps in both works. Fig. 5.14 – 5.16 confirm this conclusion.
Figs. 5.15 and 5.16 highlight the difference between the two works and confirm the above statements. For an overall insertion level of s = 0.41, for example, Fig. 5.15 shows that the authors[42] sample still maintains the structure of the starting material, while this work's sample must have developed another phase. The same conclusion is dictated by the comparison of the shape of the XRD patterns shown on Fig. 5.16 for an insertion level of s = 0.64.
When the structure of the final product was reached, the patterns from the two works became similar again confirming that the same final product was formed although the routes were different (heterogeneous in this work and homogeneous in ref. 42).
Figs. 5.17 to 5.19 compare the patterns of three high insertion levels at which the H-insertion proceeded heterogeneously in both works. All the three figures show that the

patterns are very similar, and the slight shift could be due to correction of line position or slow development of the product phase in the compared work.

In the previous work[42], the slow kinetics of H-insertion permitted a longer region of homogeneous H-insertion thereby reducing the stages of the H-insertion to two.

5.2 Results of the FTIR Study

5.2.1 Introduction

All of the R2 samples were subjected to the FTIR study detailed in section 2.5. A selection of spectra covering the whole insertion range is presented in Fig. 5.20. As for the XRD data, the FTIR can be divided into three distinct sets of spectra reflecting the three stages of the H-insertion. Spectral changes were less noticeable before H location in the final stage. The [MnO6] octahedral vibrations particularly did not change significantly before the H-location stage. This new finding must mean that the local environment of the octahedra of heavily twinned manganese dioxide remained unchanged, i.e. no *net change* of dipole moment was induced[105]. Partial explanation of this inactivity is suggested in the next section.

The three stages are discussed in the following sections before comparing the results to a previous similar work[13].

5.2.2 Mobile H

A set of FTIR with insertion levels below s = 0.39 is shown on Fig. 5.21. The spectra are all alike and similar to the spectrum of the starting material indicating that the structure remained unchanged. The octahedral vibrations are practically identical throughout this stage confirming that the local environment was not altered. Around s = 0.3, a slight curvature was observed near 1050 cm^{-1} giving the spectra the shape found in the first heterogeneous phase. This is probably due to a minute local over-insertion that was not detected by the XRD. During this stage, no OH bond was formed (Figs. 5.23 –5.25) and the H was mobile in the structure.

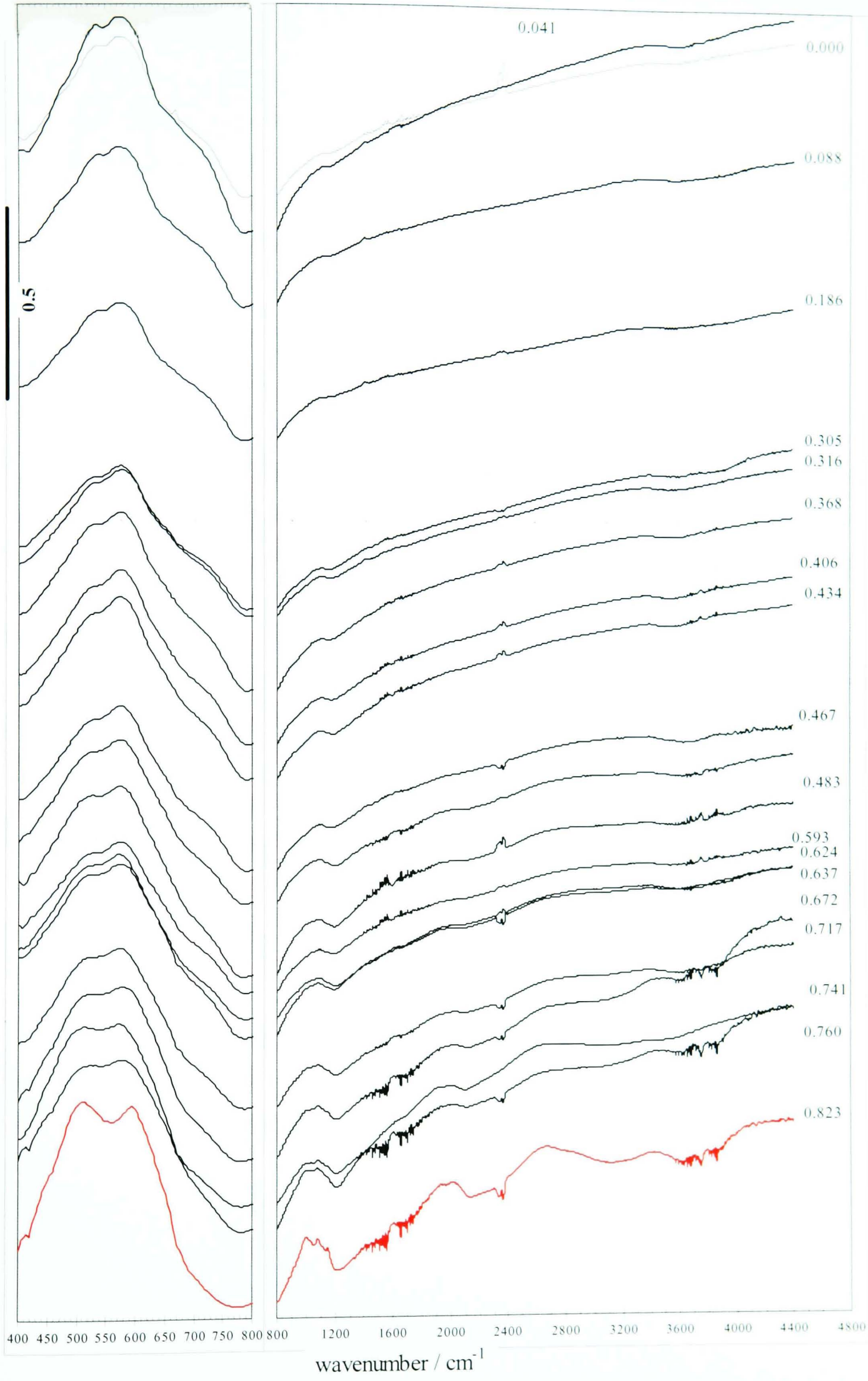

Fig. 5.20 Selected FTIR spectra of R2 material covering the insertion range $0 \leq s \leq 0.823$ stepped down the page in proportion with the insertion levels. Left: octahedral vibrations, Right: OH vibrations

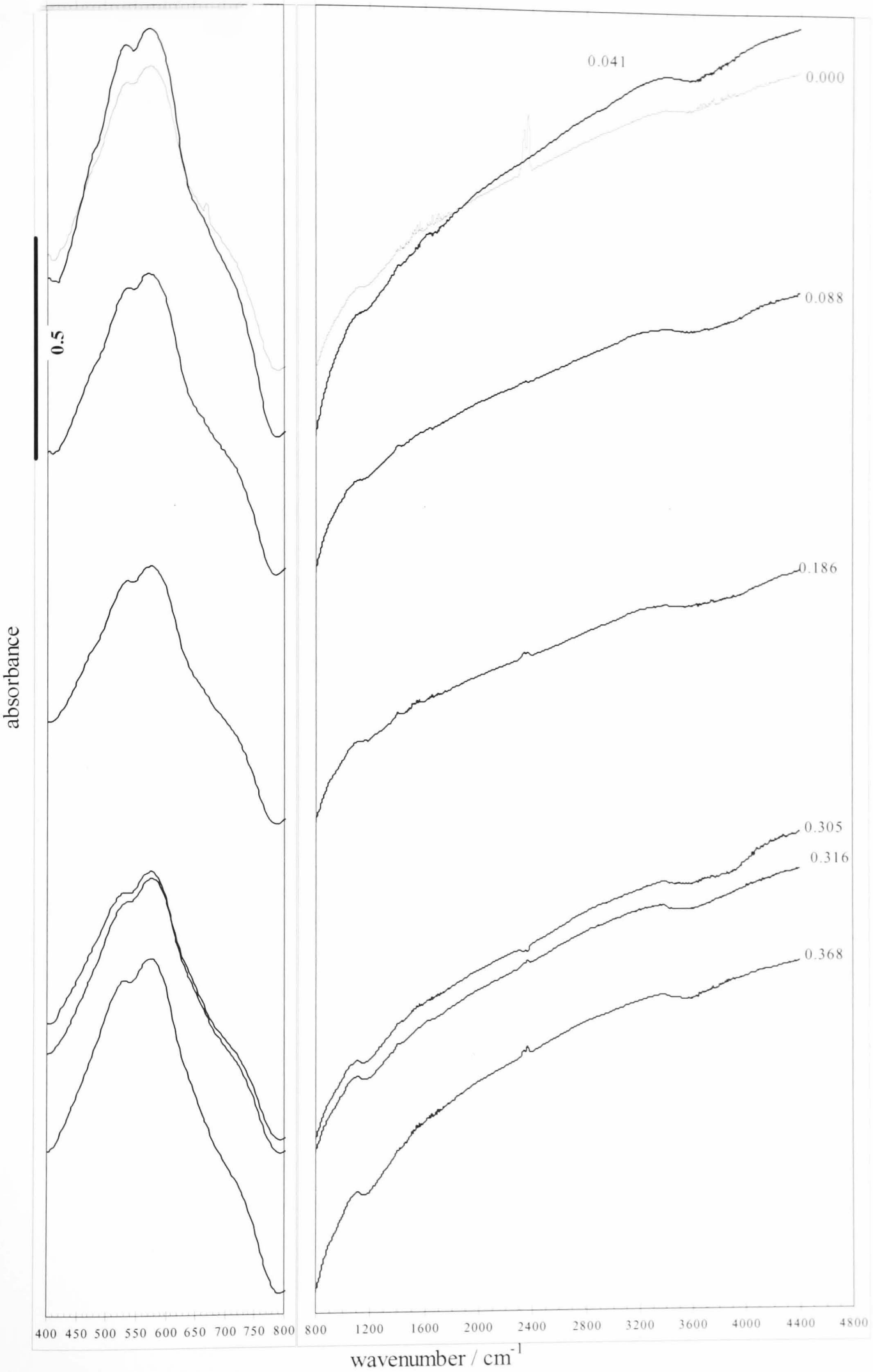

Fig. 5.21 Selected FTIR spectra of R2 material in the homogeneous phase stepped down the page in proportion with the insertion levels. Left: octahedral vibrations, Right: OH vibrations

Unlike the cases with SBP-A and Faradiser M, the octahedral vibrations of R2 did not shift to lower energies, and their shape did not alter throughout the insertion range, except from s = 0.637 when H fully located. In the homogeneous phase, this constancy could probably be an indication of isotropic expansion. IR activity requires a net change of dipole moment, which requires asymmetric vibrations105. An isotropic expansion that maintains the significant amount of the microtwinning is unlikely to disturb the initial bonding configuration; hence, no alteration of position or shape was observed.

5.2.3 Limited H Location

Changes in the FTIR spectra between s = 0.39 and s = 0.63 are only slightly noticeable in the OH vibrations range, Fig. 5.22. Hence, the changes undergone by the structure at this stage did not alter the initial octahedral framework. Fig. 5.22, as compared with Fig. 5.21, shows slight curvatures in the H location bands indicating a *limited* H location. Figs. 5.23 – 5.25 display the net peak area of the OH vibration bands and show clearly some increase between s = 0.39 and s = 0.63.

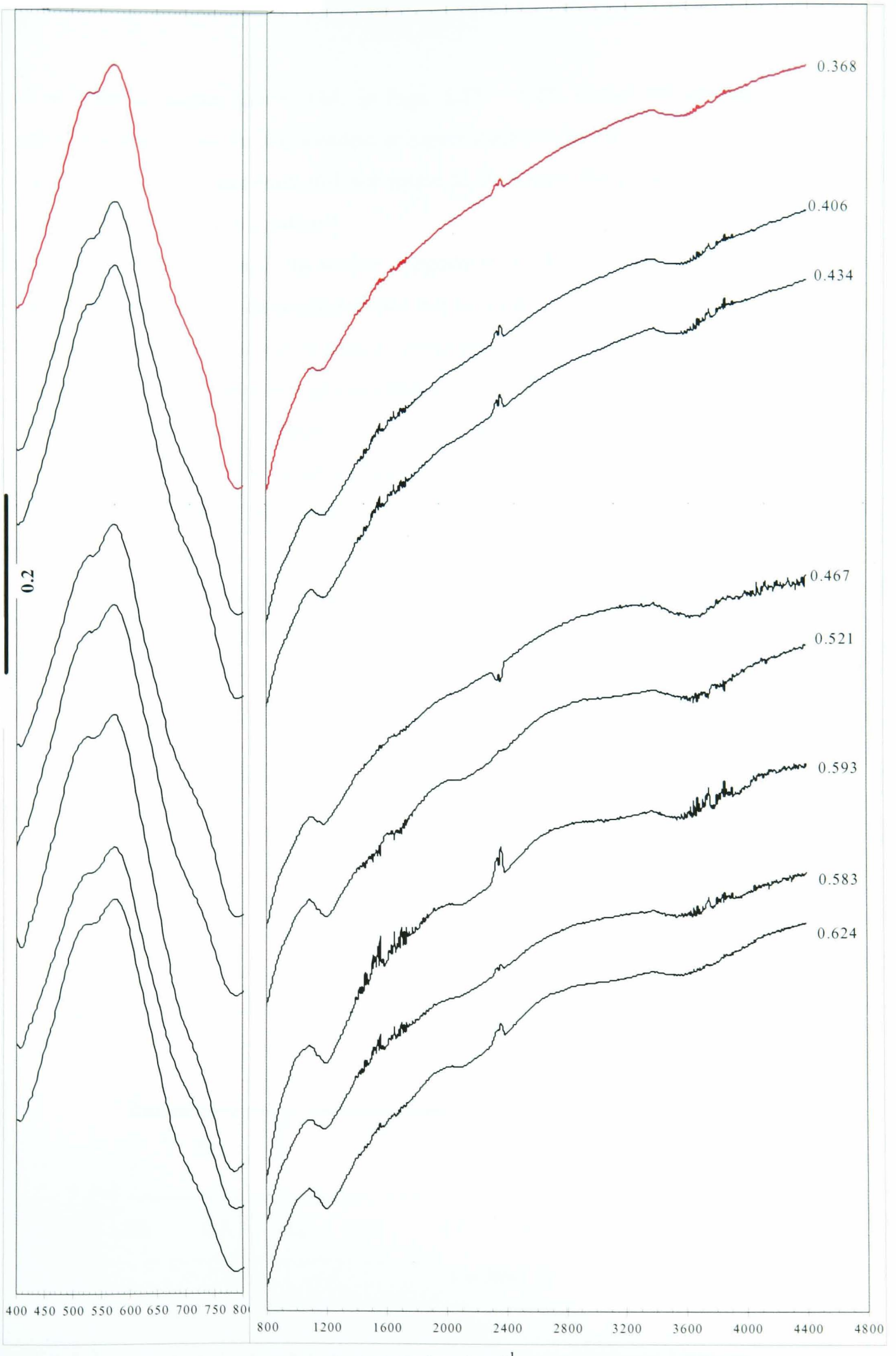

Fig. 5.22 Selected FTIR spectra of R2 material in the first heterogeneous phase stepped down the page in proportion with the insertion levels. Left: octahedral vibrations, Right: OH vibrations

The break of slopes at s = 0.63, in Figs. 5.23 – 5.25. makes the limited H location clearly distinct from the *full* location at higher insertion levels.

If the octahedral framework did not rotate to fix/locate the protons, then what is the origin of the limited H location?

A possible answer, which the author suggests to be likely, is the formation of minute amount of the final H-insertion product due to local over-insertion. During this stage, each material is presumably a binary composition of the material at s = 0.39 (similar structure to the starting material) and that at s = 0.63 (with a demicrotwinned structure without H location, see section 5.3). However, due to the synthesis conditions, an excess of protons was released spontaneously at the surface of the manganese dioxide making it possible for the particles at the surface to reach higher insertion level than those in the bulk.

So, if some particles reached, say s = 0.7, these particles would be from a different phase (see below) where H is located, hence the limited location.

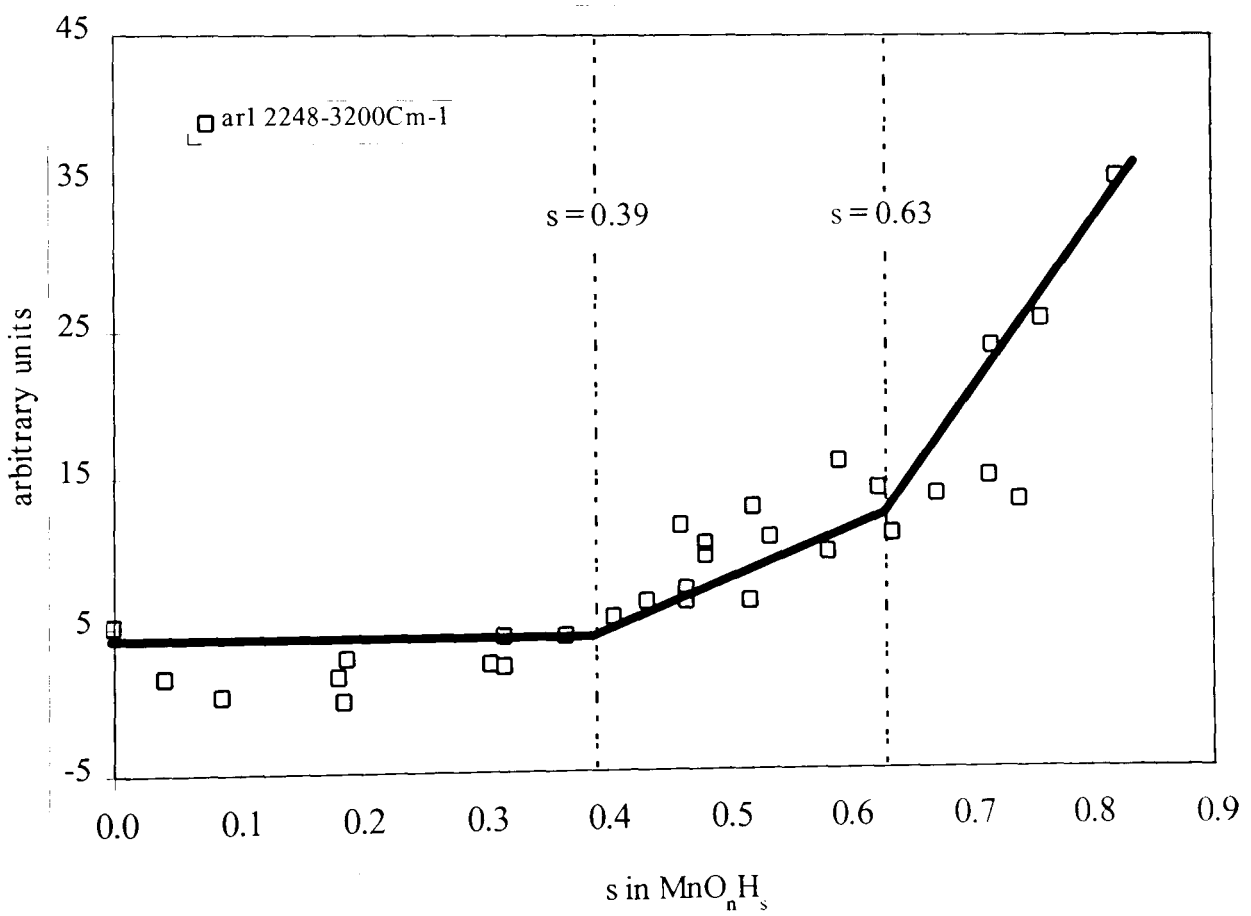

Fig. 5.23 Integrated peak area of the band between 2248 and 3200 cm^{-1}.

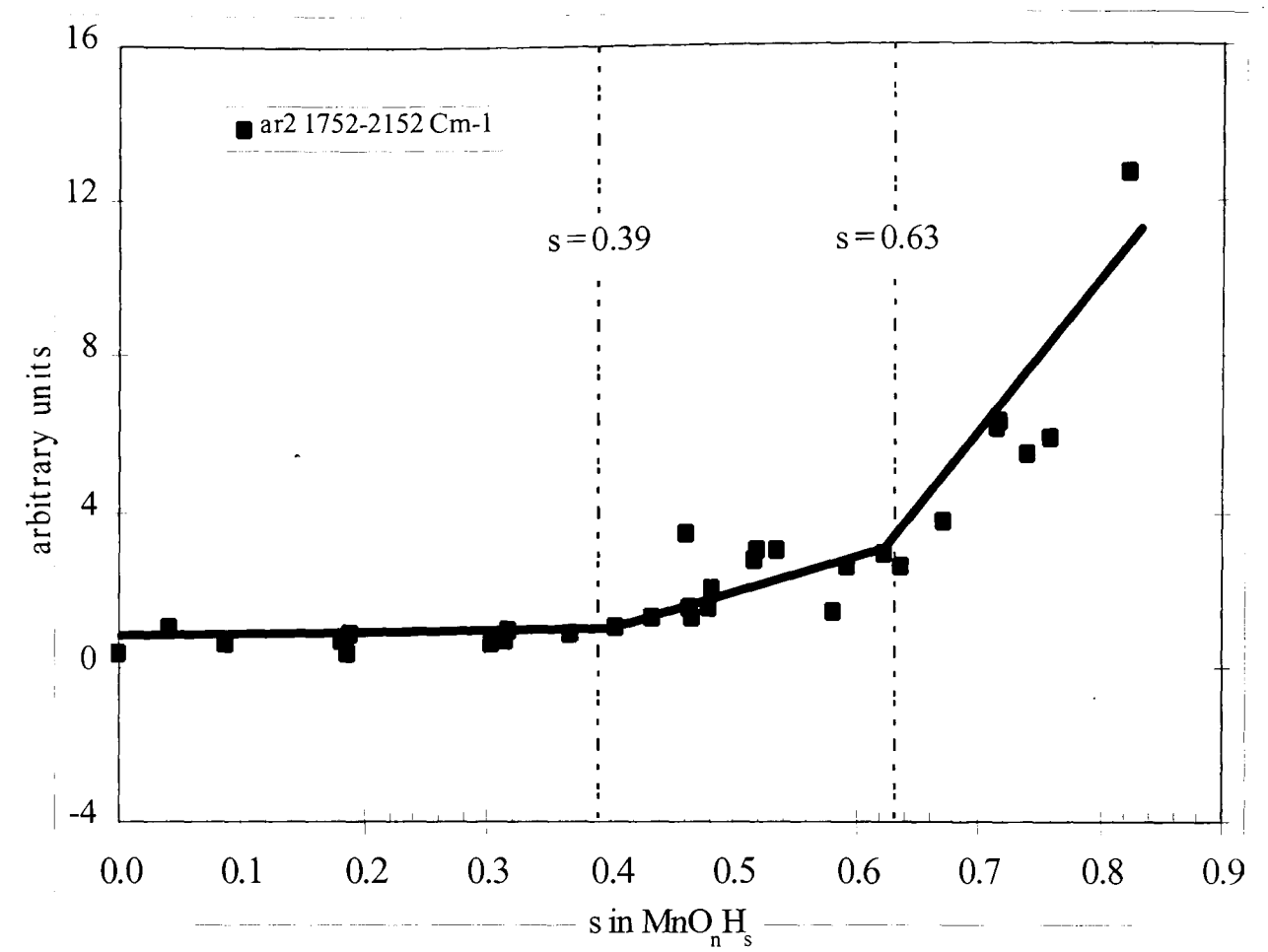

Fig. 5.24 Integrated peak area of the band between 1752 and 2152 cm^{-1}.

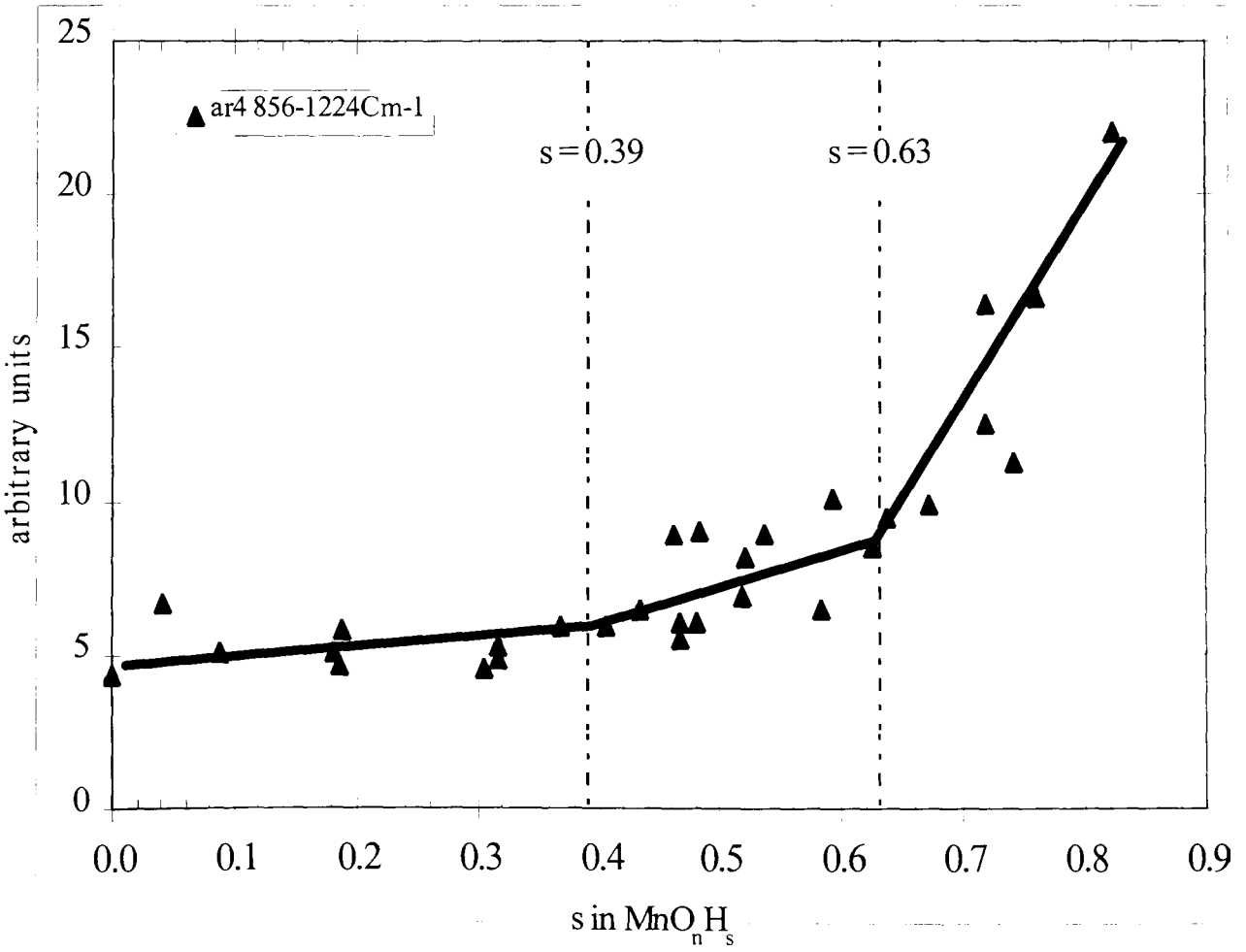

Fig. 5.25 Integrated peak area of the band between 856 and 1224 cm^{-1}.

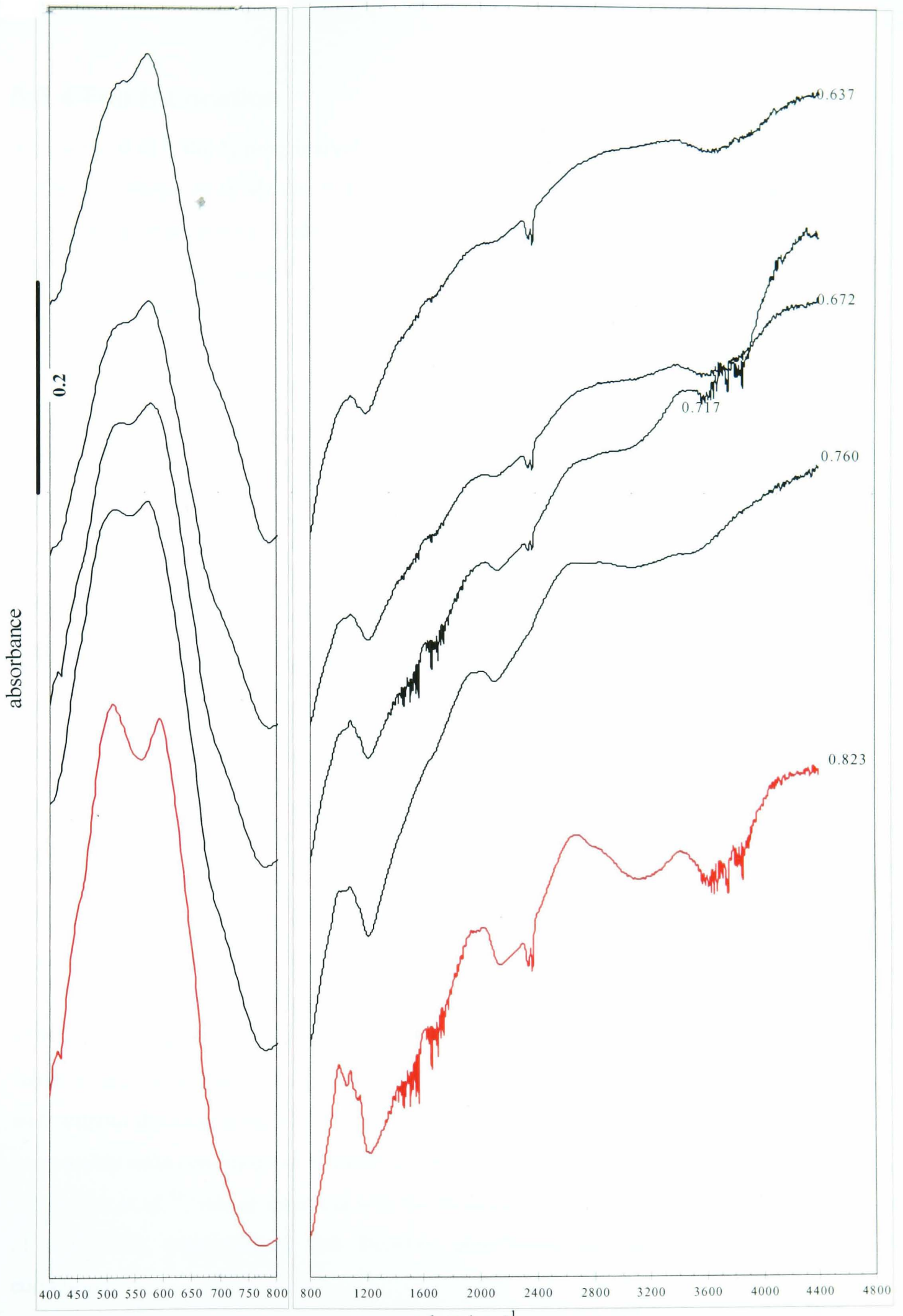

Fig. 5.26 Selected FTIR spectra of R2 material in the second heterogeneous phase stepped down the page in proportion with the insertion levels. Left: octahedral vibrations, Right: OH vibrations

5.2.4 Full H Location

Above s = 0.637, the H progressively located causing an increase of the net peak area of OH vibrations, as is shown in Figs. 5.23 – 5.26. The octahedral framework also marks the H location by a tendency to reverse the intensity ratio of the doublet at 520 and 570 cm^{-1} causing a progressive increase of the peak at 520 cm^{-1}. This change is an additional evidence of heterogeneous behaviour. The H-inserted samples, at this stage, can be –ideally- described as binary mixtures of a material without H location at s = 0.63 and the theoretical final product with H located and $s = s_{max} = 0.897$.

Every time some hydrogen was inserted, the mixture was changed to one containing more final product, hence the increase of OH band areas.

Again, the most H-inserted sample with s = 0.823 exhibits some differences with the rest of the set in Fig. 5.26. Clearly, manganite impurity bands at 1088 and 1152 cm^{-1} are present in the spectrum.

5.2.5 Comparison with previous FTIR Work

The FTIR spectra of the samples subjected to XRD study by Fitzpatrick and Tye[42] have been published[13], and are now considered for comparison with the results of this work.

As it was mentioned in section 5.1.5, differences in the H-insertion procedures caused differing results between the two works. Starting from the same material, both works trace the same spectrum shown in Fig. 5.27. The difference being essentially the high local CO_2 present in the spectrum of this work.

The differences in FTIR spectra encountered between this work and previous works on SBP-A and Faradiser M have led to multiplication of the spectra of this work by a factor to aid comparison, see section 3.3.5. For R2 the two sets of spectra compare well without the need to multiply by a factor. This is likely to be a consequence of the comparably mild conditions of H-insertion in both works. Nevertheless, the spectra of Fitzpatrick et al.[13], whose insertion was the mildest, have lower absorbance than that of this work, suggesting a link between absorbance and severity of insertion conditions.

Fig. 5.28 compares the spectra at $s \approx 0.37$ where the H-insertion proceeded homogeneously in both works with a structure similar to that of R2, in which H is mobile. The spectra are almost identical confirming the similarity of the local

environment and the absence of OH bond. At s = 0.4, when the first heterogeneous phase in this work started, the spectra became only slightly different as shown in Fig. 5.29. This is because of formation of a minute amount of the final phase, in which H is not fully located. At the end of this stage (s = 0.63), further amount of the final phase was formed leading to the limited H location in this work. At s = 0.63, the H-insertion by Fitzpatrick et al.[13] remained in the same homogeneous phase but early H location is visible as in Fig. 5.30. Thus, the spectra are expected to be similar with a difference in the amount of located H; as Fig. 5.30 confirms. Above s = 0.64, H was fully located in both works and the spectra are expected to be similar. It is worth mentioning that the H location started in a homogeneous phase and continued in a heterogeneous phase from s = 0.7 according to the authors[13]. In this work, of course, the full H location proceeded heterogeneously. The spectra are thus expected to be similar as it can be seen in Fig. 5.31. The similarity did not mask the main difference due to the difference in manufacturing procedures, namely the presence of manganite impurity in this work, which is indicated in Figs. 5.31 to 5.33. Also, the absorption bands suggest that there is more H located in the spectra of this work where H located at an earlier insertion level.

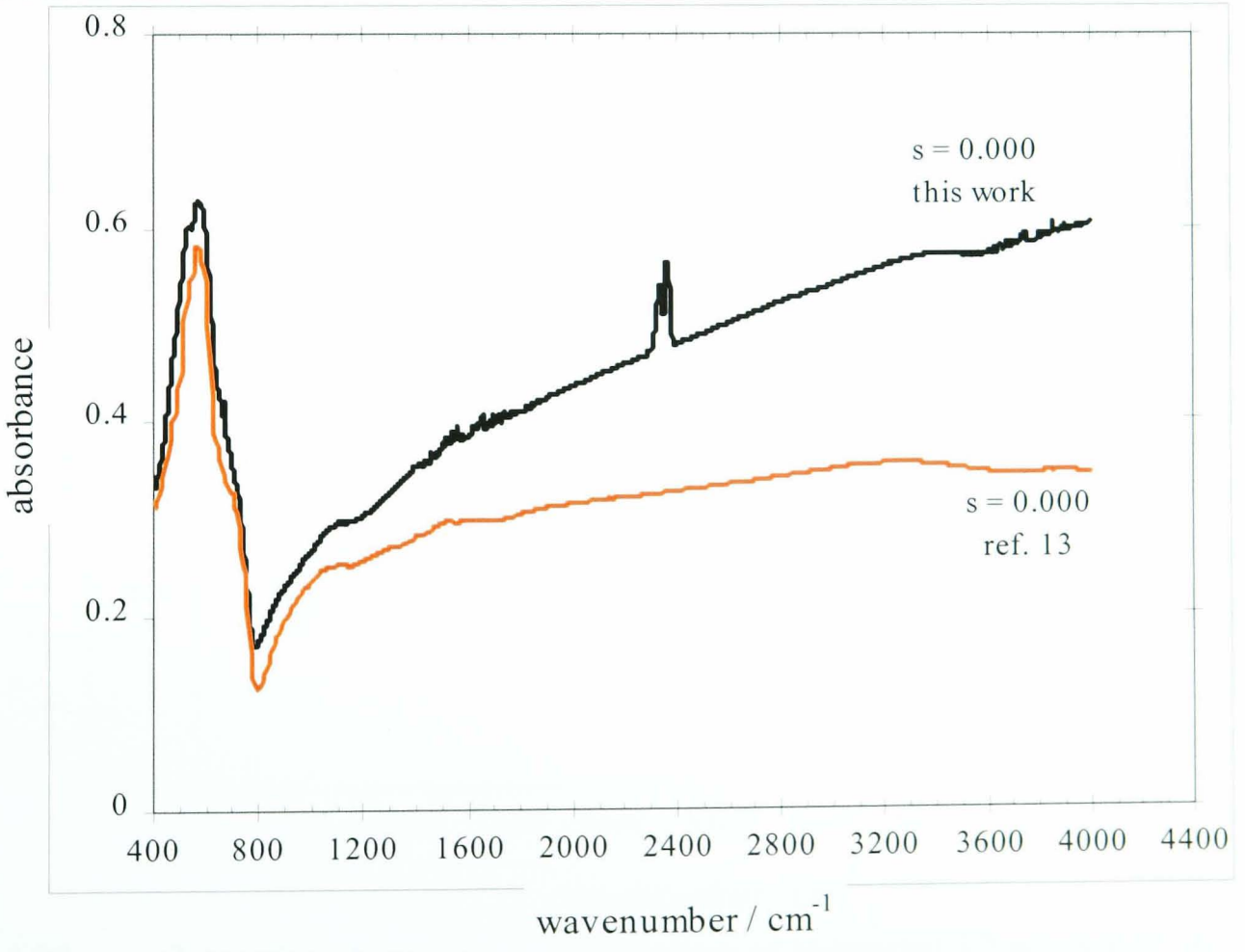

Fig. 5.27 Comparison between the FTIR spectrum of R2 starting material in this work with that in ref. 13.

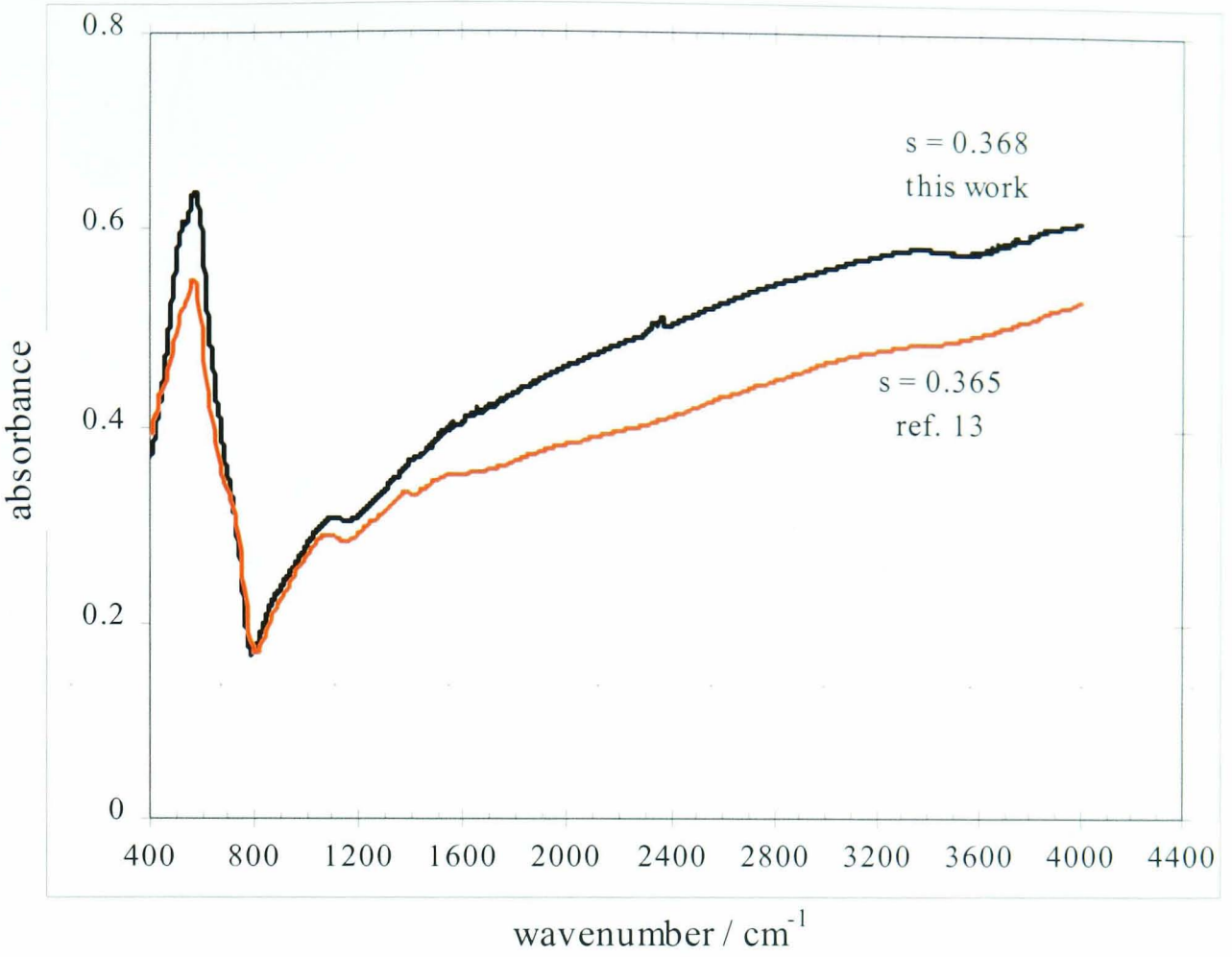

Fig. 5.28 Comparison between the FTIR spectra of H-inserted R2 at s ≈ 0.37 in this work with ref.13. Both are in homogeneous phase with mobile H.

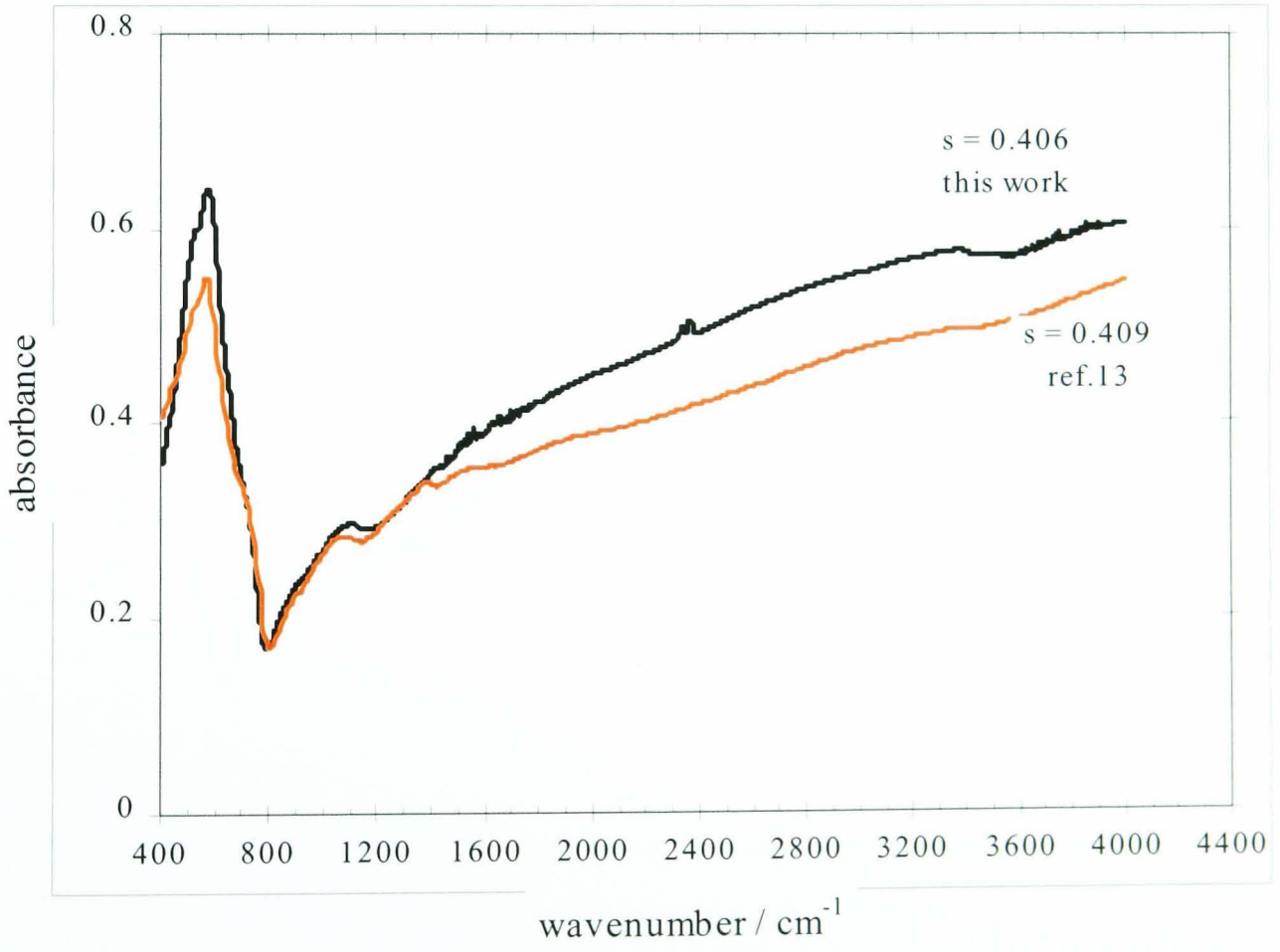

Fig. 5.29 Comparison between the FTIR spectra of H-inserted R2 at s ≈ 0.41 in this work: heterogeneous with limited H location with ref.13: homogeneous mobile H.

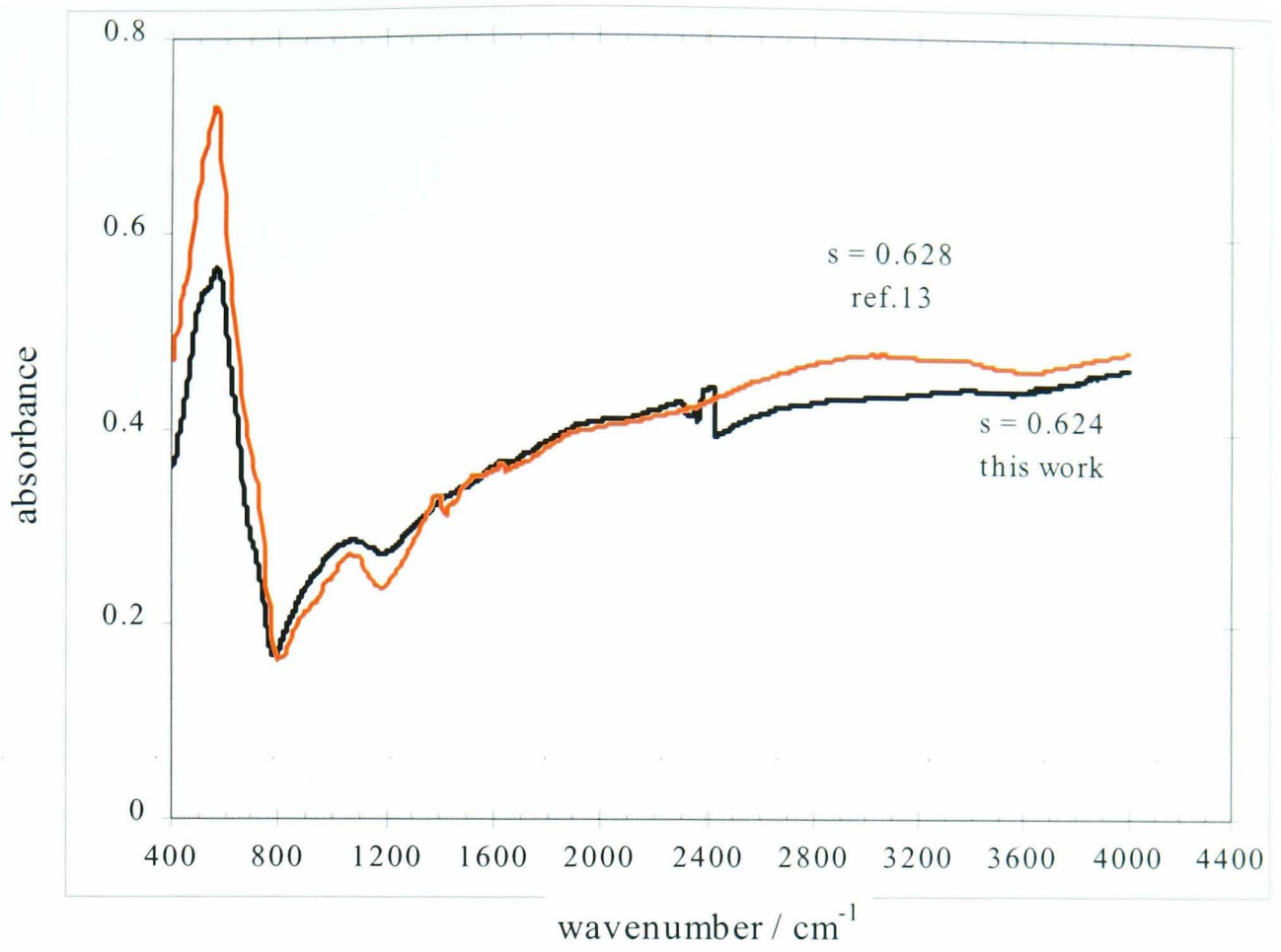

Fig. 5.30 Comparison between the FTIR spectra of H-inserted R2 at s ≈ 0.62 in this work: heterogeneous, limited H location with ref.13: homogeneous, early H location.

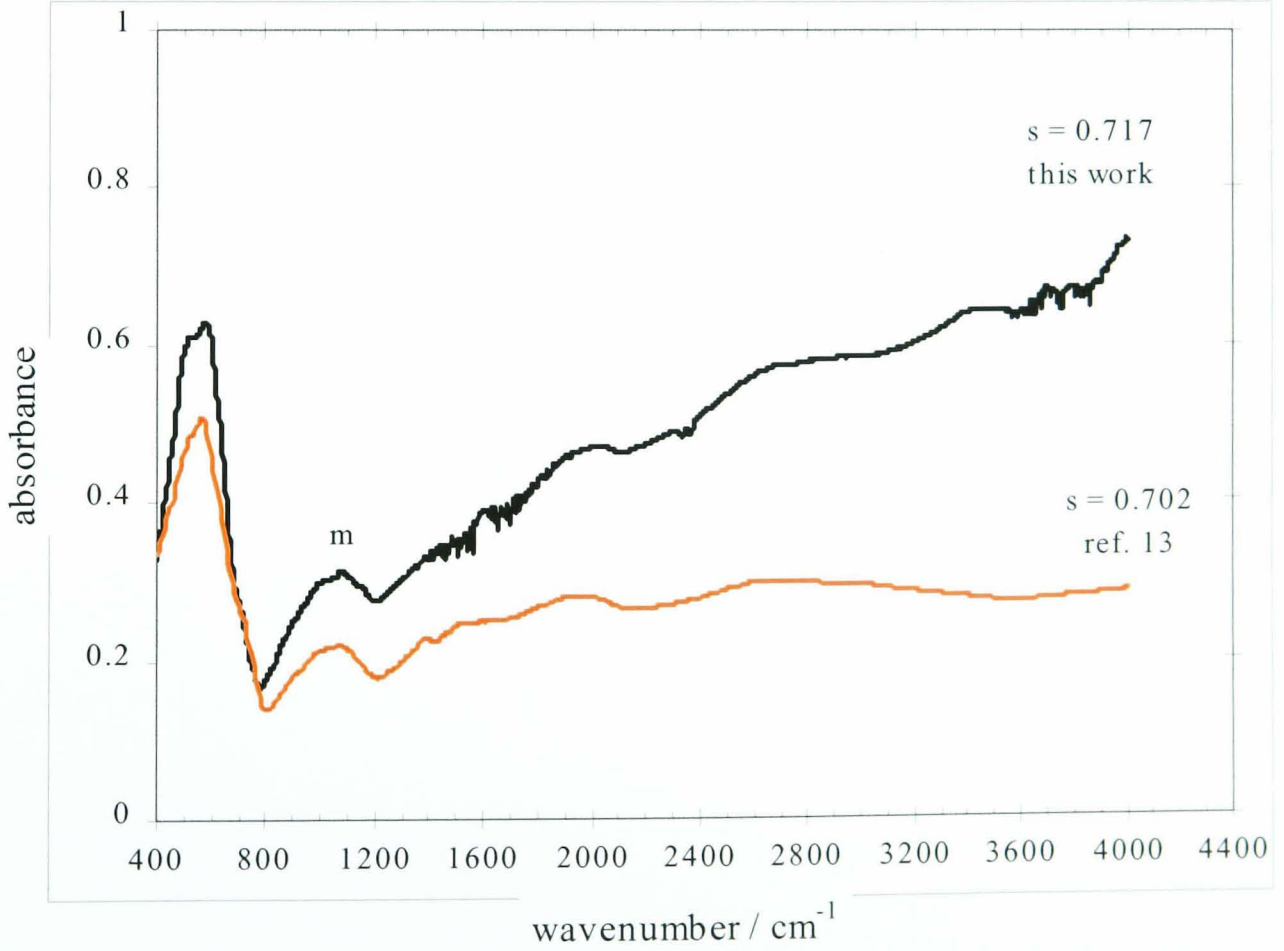

Fig. 5.31 Comparison between the FTIR spectra of H-inserted R2 at s ≈ 0.71 in this work with ref.13. Both have full H location in a heterogeneous phase, m: manganite absorption.

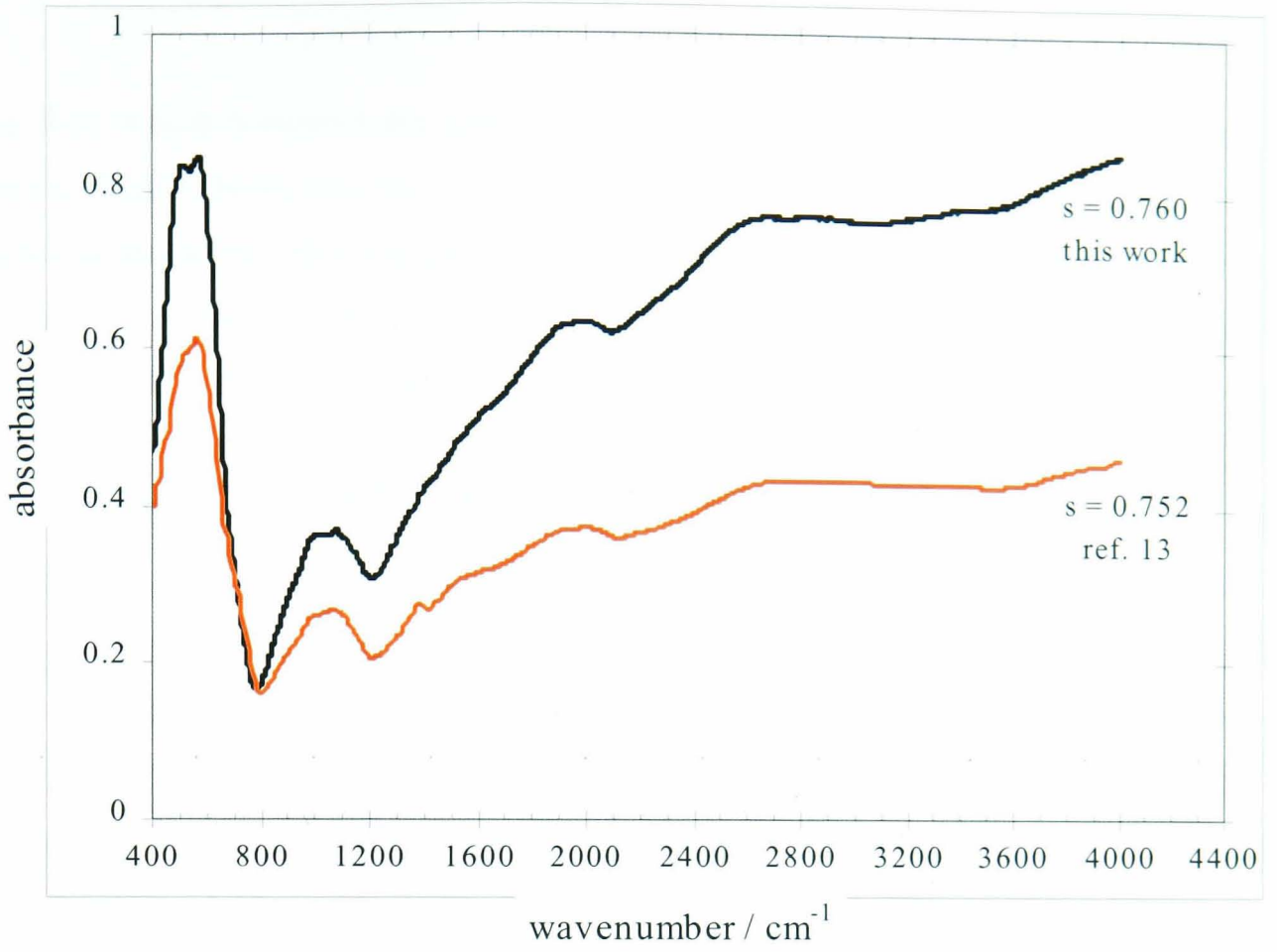

Fig. 5.32 Comparison between the FTIR spectra of H-inserted R2 at s ≈ 0.76 in this work with ref.13. Both have full H location in a heterogeneous phase, m: manganite absorption.

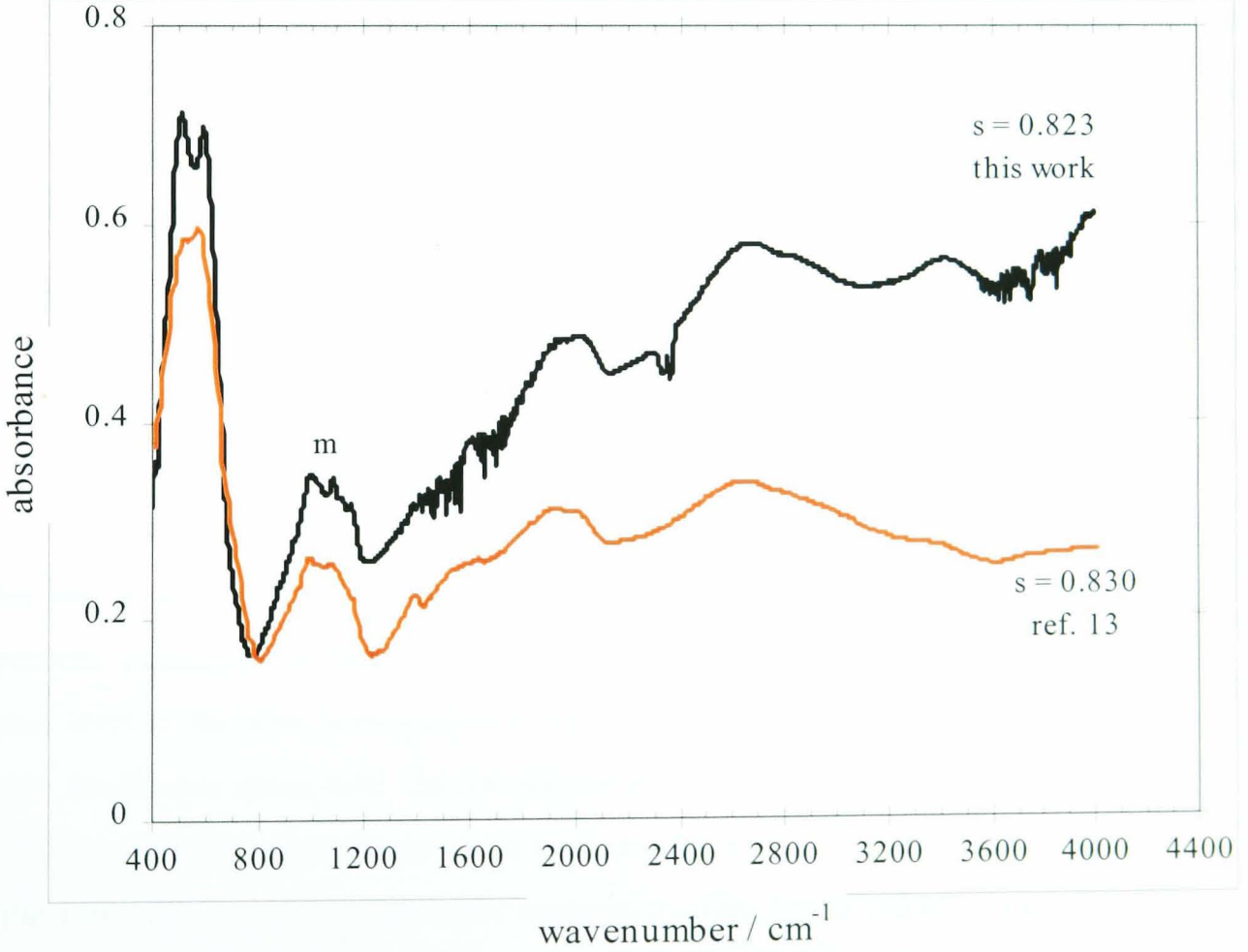

Fig. 5.33 Comparison between the FTIR spectra of H-inserted R2 at s ≈ 0.82 in this work with ref.13. Both have full H location in a heterogeneous phase, m: manganite absorption.

Fig. 5.33 which compares the spectra of manganite-contaminated samples from both works, clearly shows that the similarity remained and the manganite contribution is higher in this work. This manganite contribution is probably responsible for the larger OH absorption bands in the spectrum of this work and suggests that insertion level of s = 0.823 could be only apparent.

5.3 Discussion of the H-insertion into R2

The XRD study has revealed three distinct regions of H-insertion into R2: a homogeneous region from the starting material up to a composition of s = 0.39, followed by two heterogeneous regions delineated by s = 0.63. The FTIR has shown that no OH band was present in the homogeneous region and that limited H location occurred in the first heterogeneous region while full H location was evident in the second heterogeneous region.

In the light of the discussions of the H-insertion into SBP-A and Faradiser M, this section will be discussing the H-insertion into R2.

The expansion-rotation approach (section 3.1.1) was developed for low microtwinned material and enabled the H-insertion into SBP-A and Faradiser M to be interpreted. In both cases, the H-insertion caused an initial anisotropic expansion whose extent and direction depended on the amount of microtwinning. In Faradiser M, which is thought to be untwinned, the expansion was immediate, large and anisotropic in the *b* direction.

With SBP-A, which is lightly microtwinned, limited anisotropic expansion occurred in the *a* direction.

R2 is, however, highly microtwinned and the XRD study has demonstrated an expansion in the first region of the insertion; see Figs. 5.3 to 5.6. The question now is whether the expansion in R2 was anisotropic too and if so in which direction?

The percent expansion of the 021, 121, 221 and 002 lines was plotted against the insertion level in the first homogeneous region, in Fig. 5.34 to 5.37. The slopes are shown in the figures along with the correlation coefficients of the Least Mean Squared lines. Three out of the four slopes range between 4.2 and 4.8 (average 4.5) suggesting a similar rate of line shift; i.e. isotropic expansion. The fourth slope of 6.6 shown for the 002 line can be argued to be different on the ground that in fact it represents the 002 and the 061 lines. Microtwinning causes these two lines to merge as a single line[18] and hence shifts them away from their true position. Due to the high reactivity

of hydrazine hydrate employed for the H-insertion, some local overinsertion leading to some partial demicrotwinning is postulated. This demicrotwinning would shift the lines in the direction opposite to that predicted by Table 1.2. The arrows in Figs. 5.3, 5.5 and 5.6 illustrate this shift. Since the shift is high for the 002 line, partial demicrotwinning throughout the homogeneous region would alter the slope away from its true value. One might then be able to conclude that expansion was isotropic.

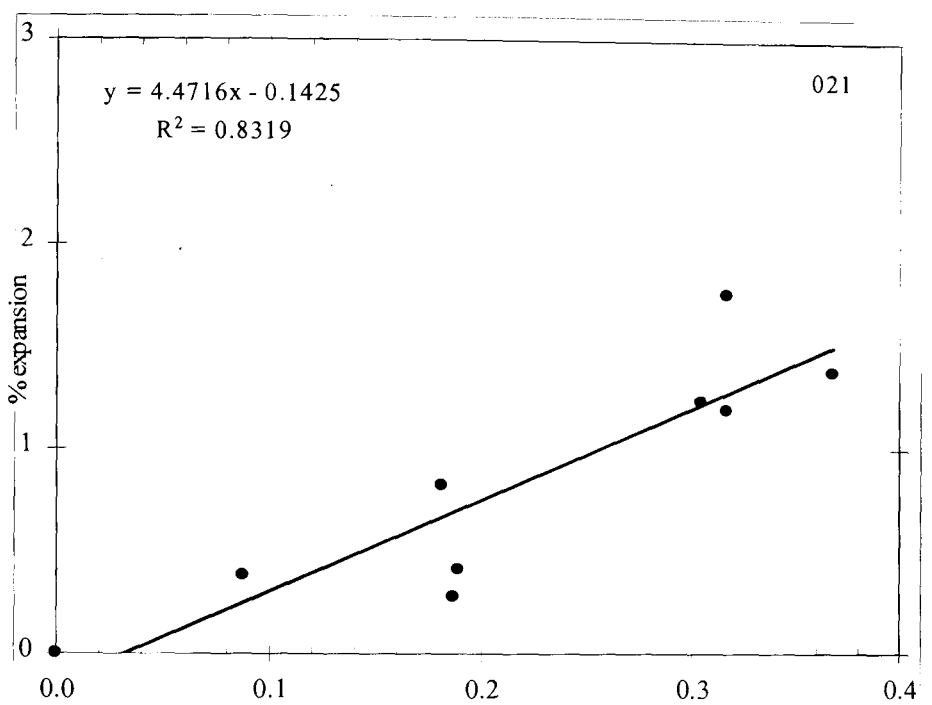

Fig. 5.32 Percentage expansion of the 021r line against insertion level in the first homogeneous region of R2.

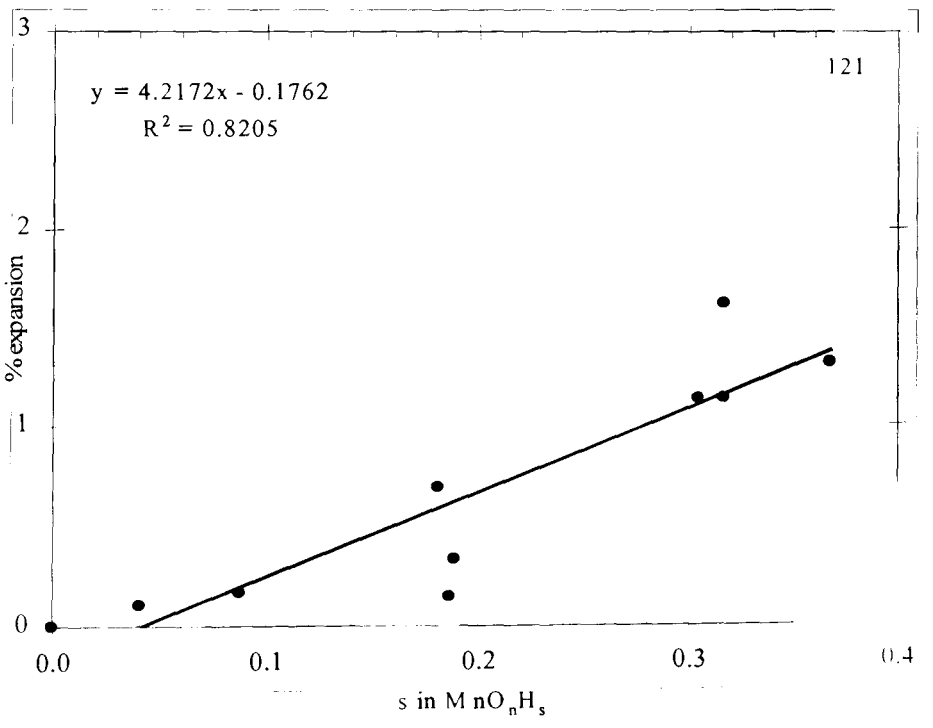

Fig. 5.33 Percentage expansion of the 121r line against insertion level in the first homogeneous region of R2.

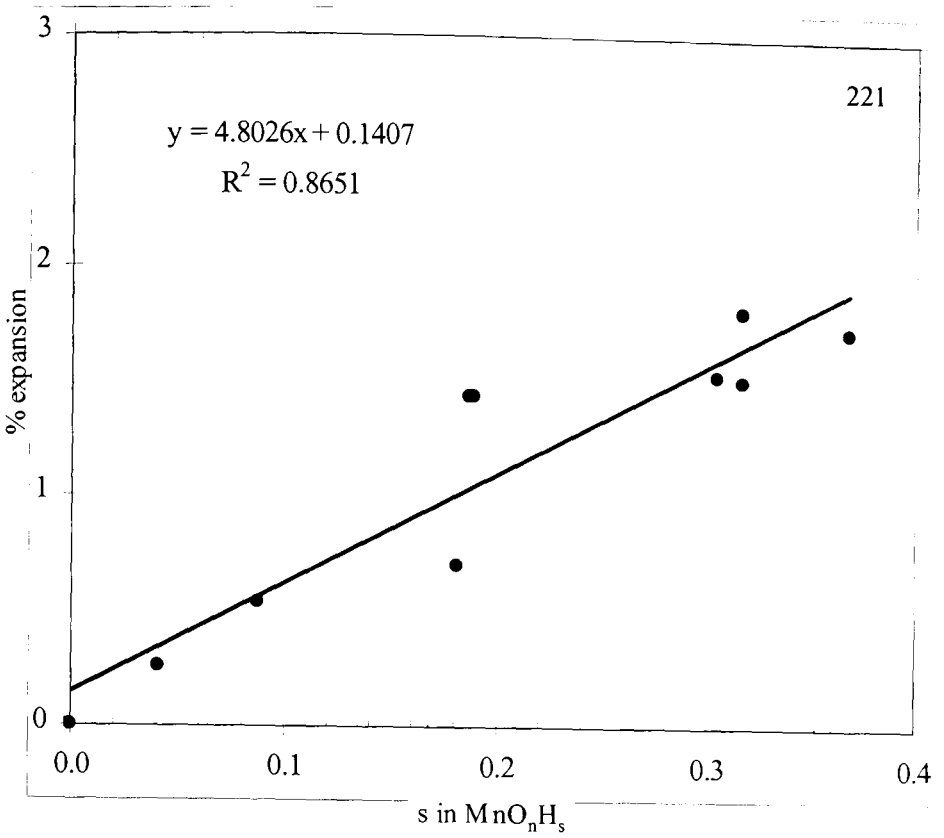

Fig. 5.34 Percentage expansion of the 221r line against insertion level in the first homogeneous region of R2.

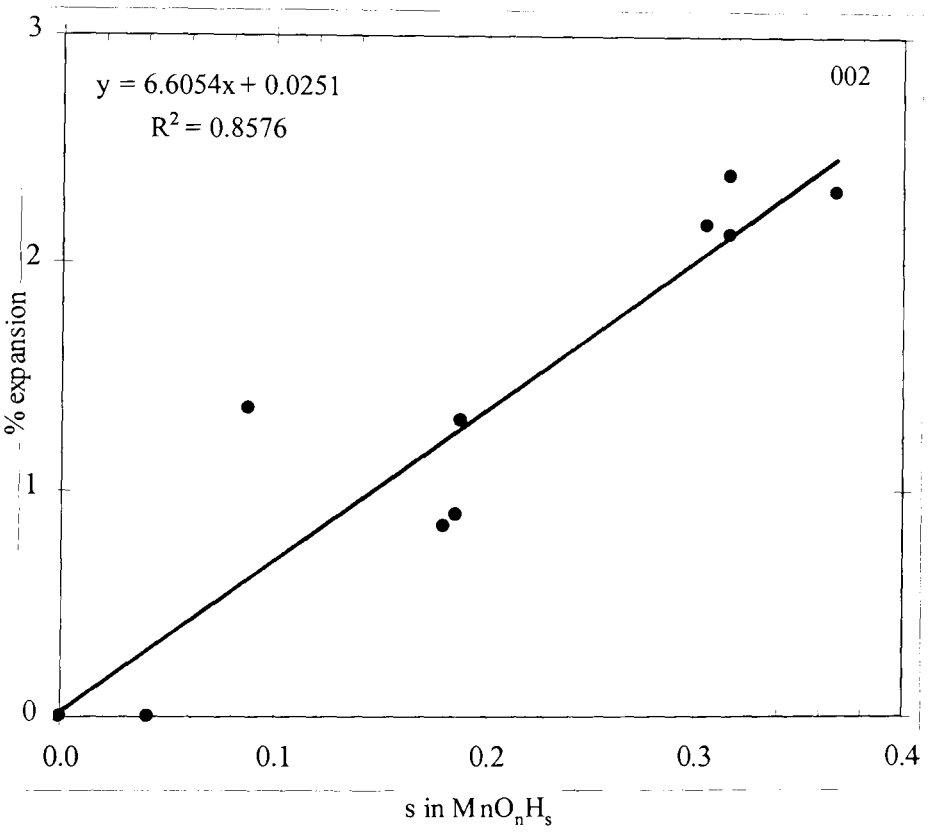

Fig. 5.35 Percentage expansion of the 002r line against insertion level in the first homogeneous region of R2.

Bearing in mind that the insertion was interpreted essentially in terms of *a* and *b* dimensions (Chapters 3 and 4), the *c* dimension was practically constant in the anisotropic expansions but can not be so if the expansion was isotropic. Isotropic

expansion in the homogeneous stage has been suggested previously[42] and is now thought to be necessary to maintain the heavy microtwinning of this material.

Thus, from s = 0.00 to s = 0.37 (at least), the H-insertion into R2 proceeded in a single homogeneous phase in which the initial structure expanded isotropically and no sign of new phase was detected by the XRD.

The FTIR, in this region, shows no sign of OH bond indicating that the H must be mobile in the structure as it was the case in both SBP-A and Faradiser M in their first stages of H-insertion.

In Chapter 3, it has been shown that SBP-A material demicrotwinned following a limited anisotropic expansion along the *a* axis which increased the *a* dimension of the starting material to a value close to that of the final product. In this Chapter, the initial isotropic expansion might have increased the *a* (and possibly the *c*) dimension significantly (with regard to the final product). The *b* dimension, however, is unlikely to have increased enough especially since the extensive microtwinning was maintained and the *b* dimension has a longer way to go (the gap between the *b*'s of the starting and final materials is bigger).

It is therefore suggested that in the first heterogeneous region ($0.39 \leq s \leq 0.63$), the structure partially demicrotwinned and the *b* dimension expanded further. Full demicrotwinning would lead to the emergence of additional XRD lines, which clearly did not appear in Fig. 5.7.

The lines shift in this region supports this suggestion. The shifts in this region (Fig. 5.3, 5.5 and 5.6) are in the opposite direction to that predicted by Pannetier[18] for microtwinning (see Table 1.2). The shift in Fig. 5.4 is in the opposite direction to that expected for microtwinned 221 but in the direction expected from demicrotwinned 240 line. The reader is reminded that 221 and 240 merge into a single line and shift in opposite direction (Table 1.2) as a result of microtwinning[18].

The break of the slopes at s = 0.39, in Fig. 5.3 – 5.6, indicates that this expansion in the first heterogeneous region must be different from that (isotropic) of the homogeneous region. Lines 021 and 002, which includes the 061, are the most shifted; both 021 and 061 are parallel to the *a* axis and cut steeply the *b* axis suggesting anisotropic expansion in the *b* direction.

Above s = 0.63, additional XRD lines merged and developed (Fig. 5.8) in the remaining range of the H-insertion. The appearance of new lines was assigned to full demicrotwinning of the structure since microtwinning reduces the number of XRD

lines. This stage was also characterised by full H location as revealed by the FTIR spectra (see Fig. 5.23 – 5.26). Since H location requires the structure to rotate so as to change the tunnels shape, the end members of this heterogeneous stage would be the following: the final product which is a fully demicrotwinned groutite-like material with full H location and a ramsdellite-like material which is partially demicrotwinned with limited H location.

Absence of H location within a homogeneous phase banned investigation for preferential H-insertion into ramsdellite or pyrolusite parts, which has been carried out for SBP-A (section 3.3.4) and Faradiser M (section 4.3.4).

Similarly to the SEM findings for SBP-A and Faradiser M, the particles of R2 cracked and broke up as anisotropic expansion occurred along the *b* axis. Examination of SEM pictures revealed that particle cracking or break up did not take place before s = 0.406, the first available sample from the heterogeneous phase. Fig. 5.36 shows the smooth surface of R2 starting material that remained uncracked during the homogeneous stage up to s = 0.368, Fig. 5.37.

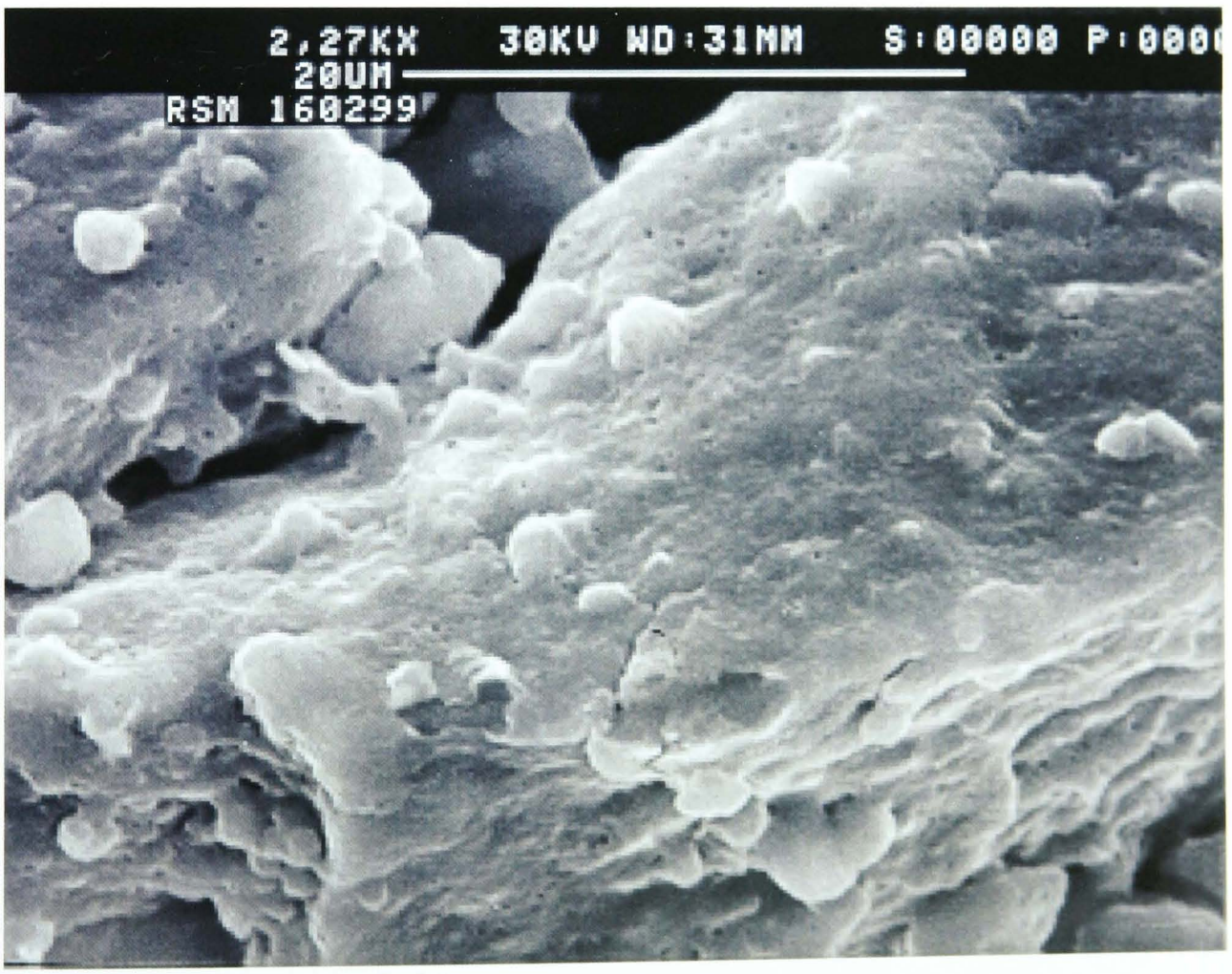

Fig. 5.36 SEM picture of a particle of R2 starting material (s = 0.000). Medium magnification was sufficient to demonstrate the smooth surface of the material.

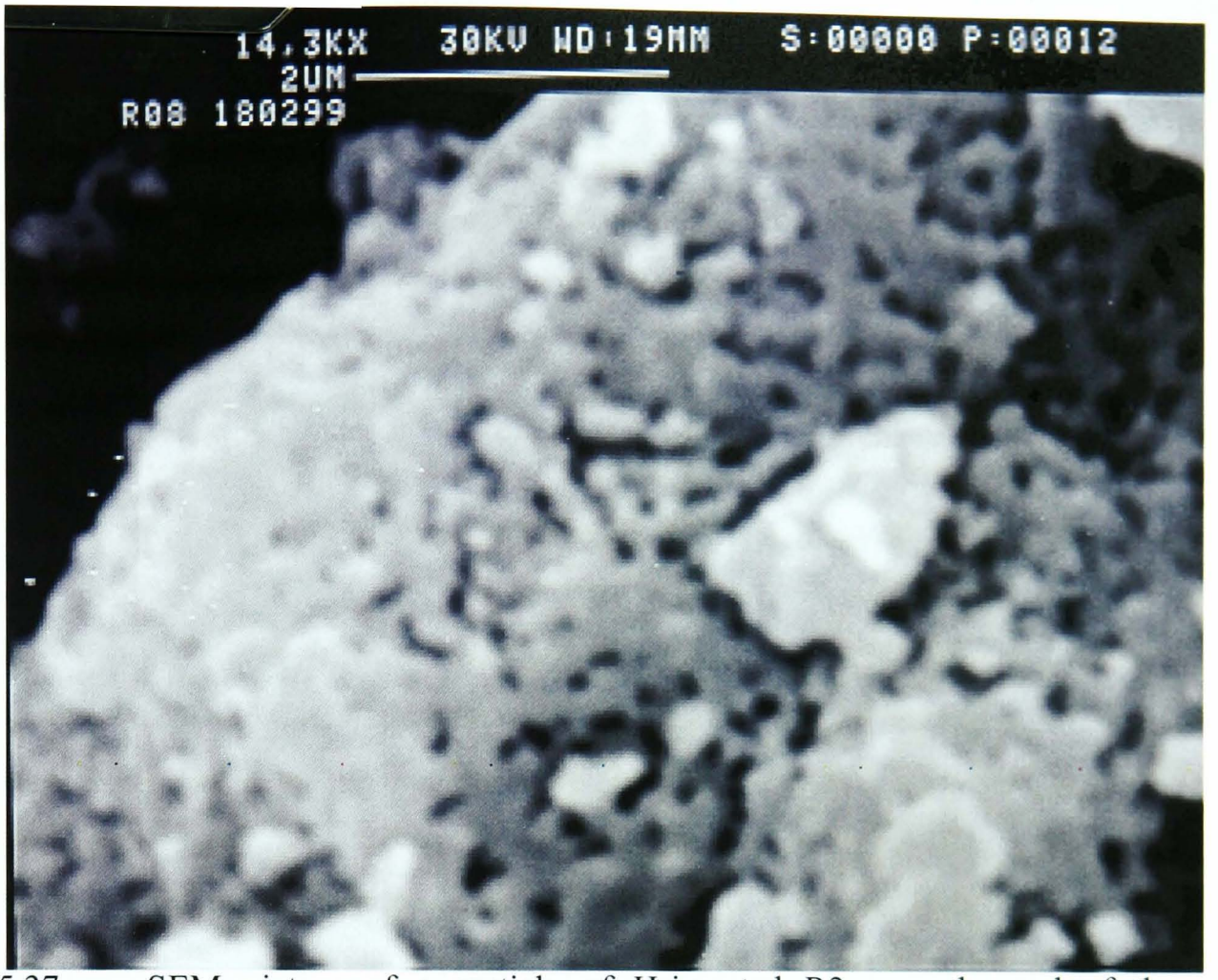

Fig. 5.37 SEM picture of a particle of H-inserted R2 near the end of the homogeneous phase (s = 0.368). High magnification shows that the surface of the particle remained unbroken.

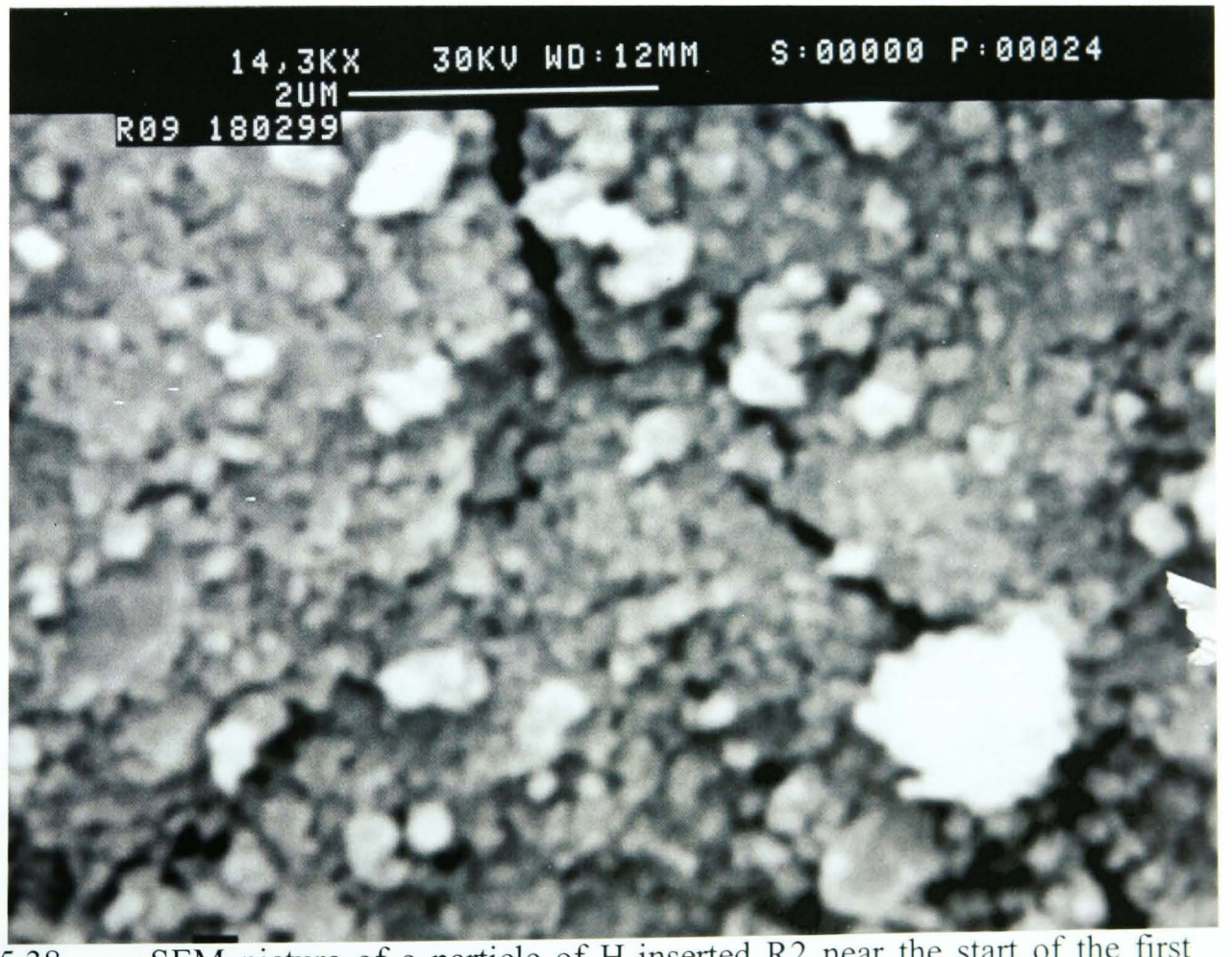

Fig. 5.38 SEM picture of a particle of H-inserted R2 near the start of the first heterogeneous phase (s = 0.408). High magnification shows that the particle was cracked.

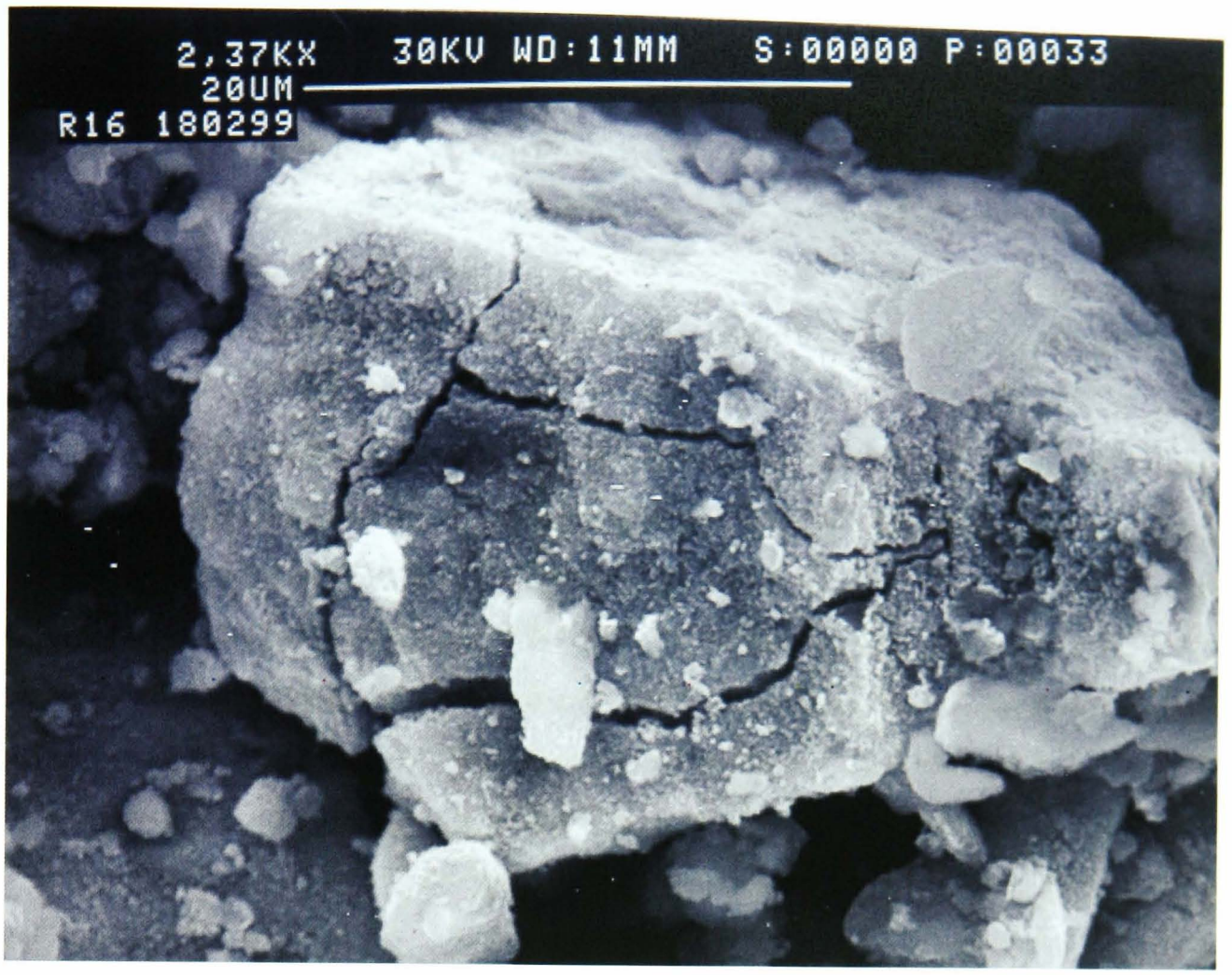

Fig. 5.39 SEM picture of a particle of H-inserted R2 near the end of the first heterogeneous phase (s = 0.624). Medium magnification was enough to reveal the severe cracking.

At the onset of the of the first heterogeneous phase, cracking of the structure became evident and increased upon further H-insertion as shown in Figs. 5.38 and 5.39.

From the above discussion, it can be suggested that the partial demicrotwinning was across the 021 planes as it is twinning across these planes which prevent rotation. Twinning is real across 061 planes and rotation is possible even in the presence of 061 microtwinning. In other words, the 061 is a plane of symmetry while the 021 is not. Figs. 6.22 and 6.23 are a good demonstration of this statement.

The FTIR between s = 0.39 and s = 0.63 has shown a limited H location (Fig. 5.23 – 5.25) which was confined to a fraction of overinserted material while H remained mobile in the main bulk which represents the position under ideal H-insertion conditions.

Above s = 0.64, the H-insertion proceeded in a heterogeneous phase as the XRD indicates (Fig. 5.8) in which demicrotwinning was completed. H was also fully located in this stage as the FTIR reveals (Fig. 5.26). Towards the end of the H-insertion, manganite impurity has been precipitated by a side reaction.

An additional possible consequence of the manganite impurity is a misleading insertion level s. The pure manganite phase would tend to increase s. So, the insertion levels of manganite contaminated samples are only apparent and the true values are lower.

5.4 Conclusion

- H-insertion into R2 material proceeded in three stages: i) homogeneous phase from 0.00 to 0.39 in s, characterised by *isotropic* expansion of the structure, then ii) first heterogeneous phase from s = 0.39 to 0.63. At this stage, the structure partially demicrotwinned across the 021 planes and expanded *anisotropically* in the *b* direction. iii) Second heterogeneous phase where demicrotwinning completed and hydrogen located in the distorted tunnels of the structures.
- The three-stage mechanism is a consequence of the kinetics imposed by the H-insertion method described in Chapter 2. In this H-insertion method, the high reactivity of hydrazine hydrate led to spontaneous release of protons on the surface of the manganese dioxide causing a gradient of H-insertion between the surface and the bulk. This gradient caused diffusion of the inserted species into the bulk during the homogeneous stage. By s = 0.39, the diffusion was no longer fast enough to maintain homogeneous equilibrium; as a result, the particles on the surface engaged into a heterogeneous transformation consisting of breaking the twinning boundaries. From s = 0.63, the structure demicrotwinned completely and the inserted H located in the distorted tunnels as the final stage of the H-insertion. This stage was also accompanied by precipitation of pure manganite that altered the response of the true final H-insertion product (XRD, FTIR and insertion level).
- SEM pictures showed that the particles of R2 remained unbroken until an insertion level of about 0.4 when early cracking was detected. Above this level up to s = 0.63 cracking became more severe suggesting that the demicrotwinning phase led to particle break up.
- Milder H-insertion conditions[42] extended the homogeneous stage to about s = 0.7, the onset of the final stage. The H, however, still located at s = 0.63. The manganite impurity was also substantially reduced.

- The essential difference between the two works is that the H-insertion procedure followed in this work caused partial demicrotwinning before H location, while in the previous work[42] H location occurred with demicrotwinning.

6 Additional Techniques

6.1 Electrode Potential Measurement

6.1.1 Introduction

The electrode potentials of the three γ-manganese dioxide materials and their H-inserted forms have been measured by the procedure outlined in section 2.7. The potentials are given with reference to the standard hydrogen electrode (SHE) scale at pH = 5.6, the value for the buffered electrolyte used (Fig. 2.8). An attempt is made here to correlate the potential data to the interpretation of the XRD and FTIR data presented in the previous chapters.

R2 (and its H-inserted derivatives) has been the subject of many studies[e.g.21,39-41,43,44,47,51,83] for electrode potential. Potential of other EMDs closely related to R2 and used in primary batteries have also been studied, such as an EMD from the Australian Manganese Company Ltd[106] and an EMD produced by a Spanish battery manufacturer, CEGASA S.A[107]. These numerous studies, which agree over a good range of H-insertion, suggest that the potential of R2 could be taken as *typical* for EMD. For this reason, only the potential of R2 material has been taken from the literature for comparison with the new data reported here.

6.1.2 Electrode Potential of R2 and H-inserted Materials

The potential of R2 samples against H-insertion level is plotted in Fig. 6.1.

The line drawn through the data points in Fig. 6.1 confirms the stages of the insertion discussed in Chapter 5. The first section of the line covering $0.00 \leq s \leq 0.39$ is close to the first part of an S-shaped curve characteristic of homogeneous insertion[44]. The middle section ($0.39 \leq s \leq 0.63$) of the potential curve is horizontal indicating heterogeneous insertion between fixed phases over this range. The members of the potential determining reaction are shown as $s = 0.39$ and $s = 0.63$; two fixed compositions with two fixed Gibbs free energies leading a constant Gibbs free energy change (ΔG)- hence the horizontal section. Above $s = 0.63$, the potential data points drop as in the last part of the S-shaped curve characteristic of homogeneous

insertion[44]. The potential of R2 is therefore in good agreement with the three regions of the H-insertion described in Chapter 5.

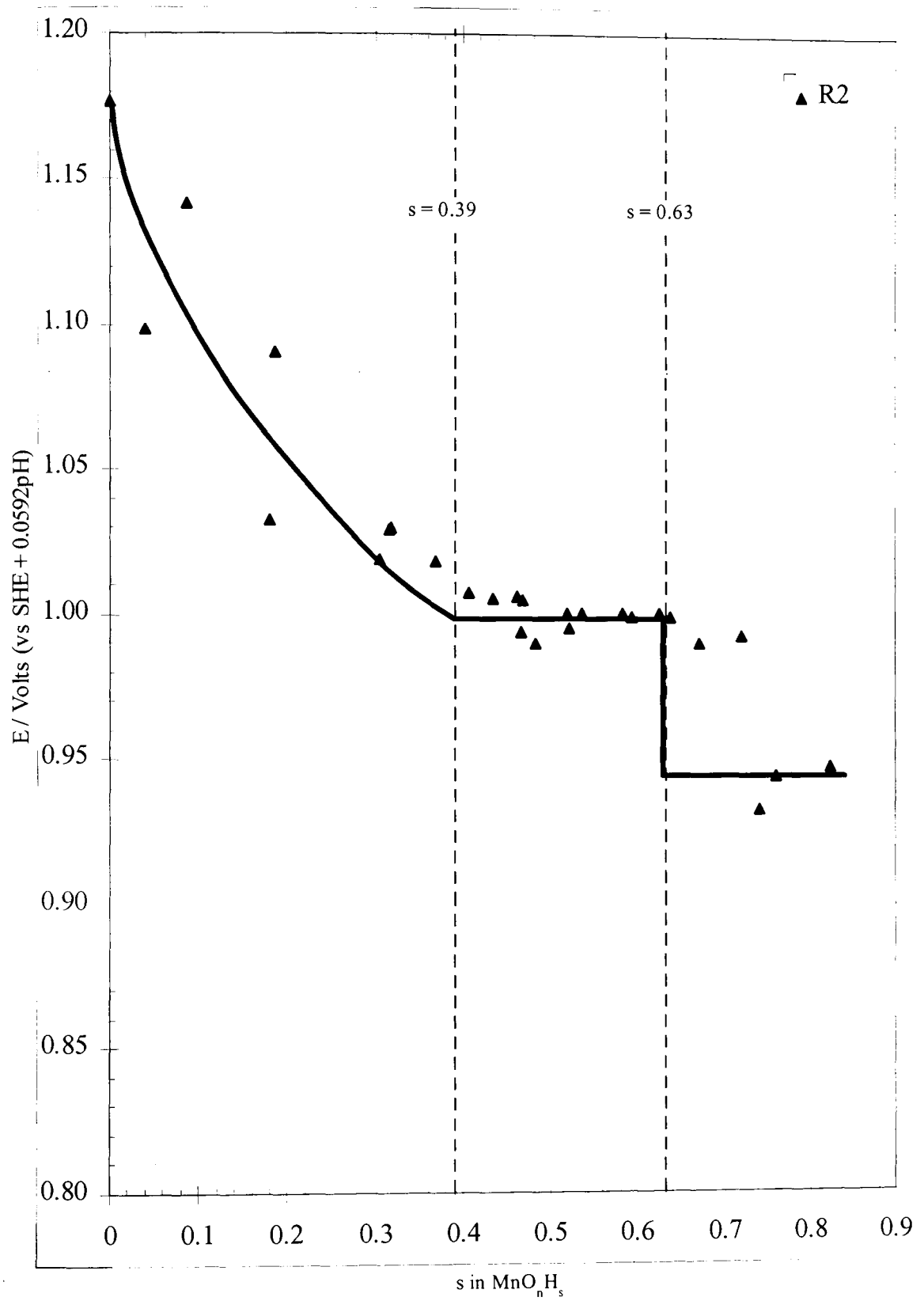

Fig. 6.1 Variation of the potential of R2 materials with H-insertion level.

6.1.3 Electrode Potential of Far. M and H-inserted Materials

The potential of H-inserted Faradiser M samples is plotted against insertion level in Fig. 6.2. The two homogeneous regions on either sides of s = 0.69 (Chapter 4) are not

distinguishable in the potential data. The first region exhibits a typical homogeneous fall but the fall in the second is limited. This could be due to the restricted extent of the second stage ($\Delta s = 0.2$).

This limited fall means that the potential determining reaction has not changed much.

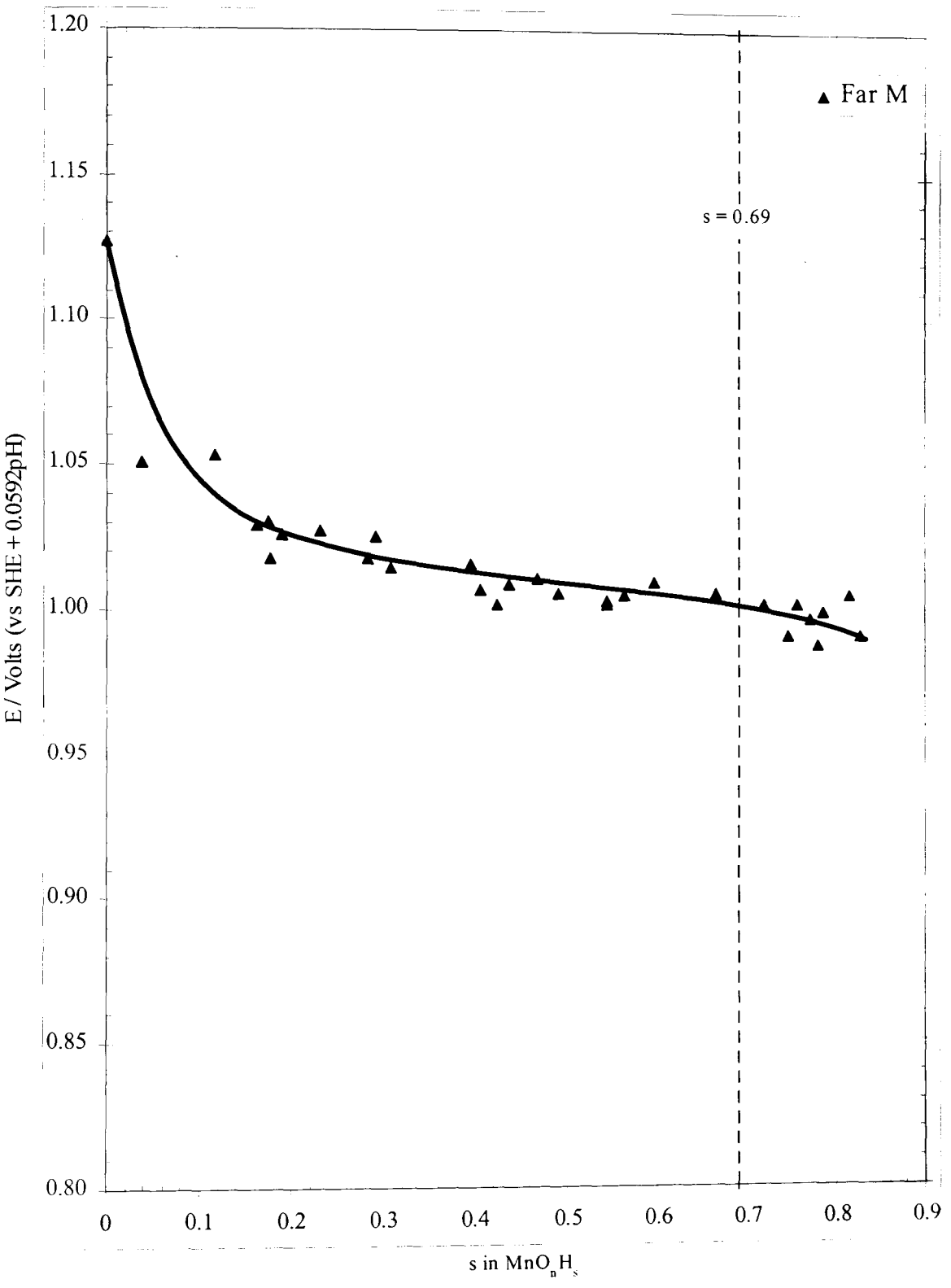

Fig. 6.2 Variation of the potential of Faradiser M materials with H-insertion level.

6.1.4 Electrode Potential of SBP-A and H-inserted Materials

The electrode potential of SBP-A samples against insertion level is plotted in Fig. 6.3. The XRD study in Chapter 3 has demonstrated three regions of H-insertion into this material. These are two homogeneous separated by a heterogeneous region between s = 0.28 and s = 0.68. Many figures in that chapter show these regions unambiguously, see Figs. 3.5-3.8. Considering this fact, the potential data trace would be expected to show two homogeneous falls on either sides of a flat segment covering the heterogeneous phase.

The potential of SBP-A, however, continues to slope through the heterogeneous stage. Continuous slope for SBP-A potential has been reported previously[21] for the samples studied by MacLean and Tye[37] but no explanation was suggested. Some interpretation of this rather unexpected behaviour is discussed in the following lines. The homogeneous stages are considered first.

The potential drop from the starting material down to s = 0.28 can easily be accepted as due to the first homogeneous insertion. The same argument applies for the curve drawn above s = 0.68.

The heterogeneous region ($0.28 \leq s \leq 0.68$) is now considered. The condition to obtain a *horizontal* line in this region is that the solid state H-insertion occurs between two *fixed* phases. Two fixed phases would have two fixed Gibbs free energies whose difference gives a fixed potential (horizontal line) as was the case for R2 between s = 39 and s = 0.63 in fig. 6.1. Given that the insertion was heterogeneous in this stage (Chapter 3), the absence of a horizontal line in the potential data *must* mean that there were no fixed phases; i.e. one phase at least was changing throughout this insertion range.

One possibility is that some over insertion occurred at the higher phase. The potential in this case would be defined by the higher phase (s = 0.68) and a set of materials with $s = (0.28 + \varepsilon)$ where ε is a small positive number that increased slightly with s.

6.1.5 Comparison with the Literature

The R2 material is the one that has received the most studies of the three materials investigated in this work. Observation of the literature reveals that the potential data of Maskell et al[44] on R2, is a good choice for comparison because it has been used for the same purpose by different authors[21,43,83,106]. Although these data were obtained by

electrochemical reduction of the material in Leclanché electrolyte, it has been shown to be (at least partly) consistent with other data obtained by chemical insertion and measured in KOH medium[21,43]. Maclean[21] measured the potential of the R2 samples of Fitzpatrick[42] in KOH solution. MacLean's data were almost identical to those of Maskell et al[44]. Holton et al.[43]'s data were obtained in 30% (w/w) KOH electrolyte and only matches the reference data[44] up to s = 0.4 due to a stability problem in the concentrated alkaline solution.

Donne et al.[106] have also shown that Maskell[44]'s data compare well up to s = 0.4 with their Australian EMD, which was reduced electrochemically in KOH electrolyte.

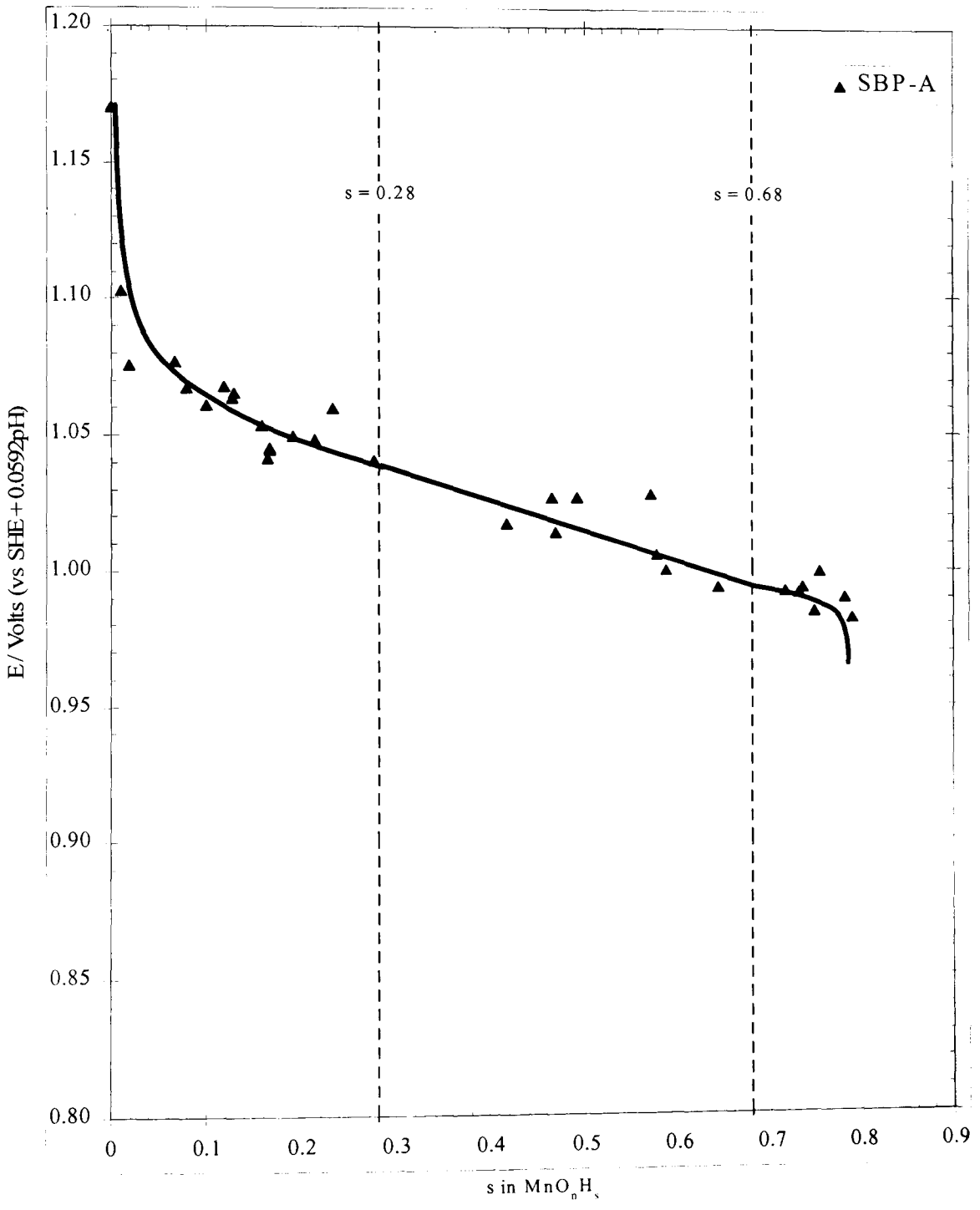

Fig. 6.3 Variation of potential of H-inserted SBP-A materials with insertion level.

Fig. 6.4 compares the potential data of R2 from the present work with Maskell's[44] data. The figure shows that both sets are similar (with a constant difference) up to s = 0.3. In this range, the H-insertion proceeded in a single homogeneous phase in both works. The compared data[44] followed the classical S-shape driving down to lower potentials while the data of the present work engaged into a horizontal line reflecting the heterogeneity of the H-insertion between s = 0.39 and s = 0.63.

Above s = 0.63, the potential fall is not entirely consistent with the expectation of heterogeneous H-insertion due to the potential values between s = 0.63 and s = 0.72. The remaining data points are on a fairly horizontal line consistent with the heterogeneous H-insertion shown by the XRD patterns (Chapter 5). Maskell's data continued as the homogeneous H-insertion route.

The kinetics of the H-insertion suggests an explanation of the difference between the two sets of data. In this work, protons were released spontaneously on the surface of the manganese dioxide due to the high reactivity of hydrazine hydrate used as a source of protons. Therefore, H-insertion reaction at the surface was fast and the kinetically limiting step was the diffusion of the protons into the bulk. This slow diffusion could be due to the low temperature (~ 1° C) effect on the diffusion coefficient of proton. Thus, a significant concentration gradient arisen between the surface and the bulk leading eventually to two different phases hence the heterogeneous behaviour.

In Maskell's work[44] however, the slow electrochemical discharge extracted only a small quantity of protons which had the time to diffuse throughout the manganese dioxide prior to the next discharge. In this regime the kinetically limiting step would be the release of protons (the discharge), not their diffusion into the bulk. In other words, there was no concentration gradient between the surface and the bulk of the material, hence the homogeneous behaviour.

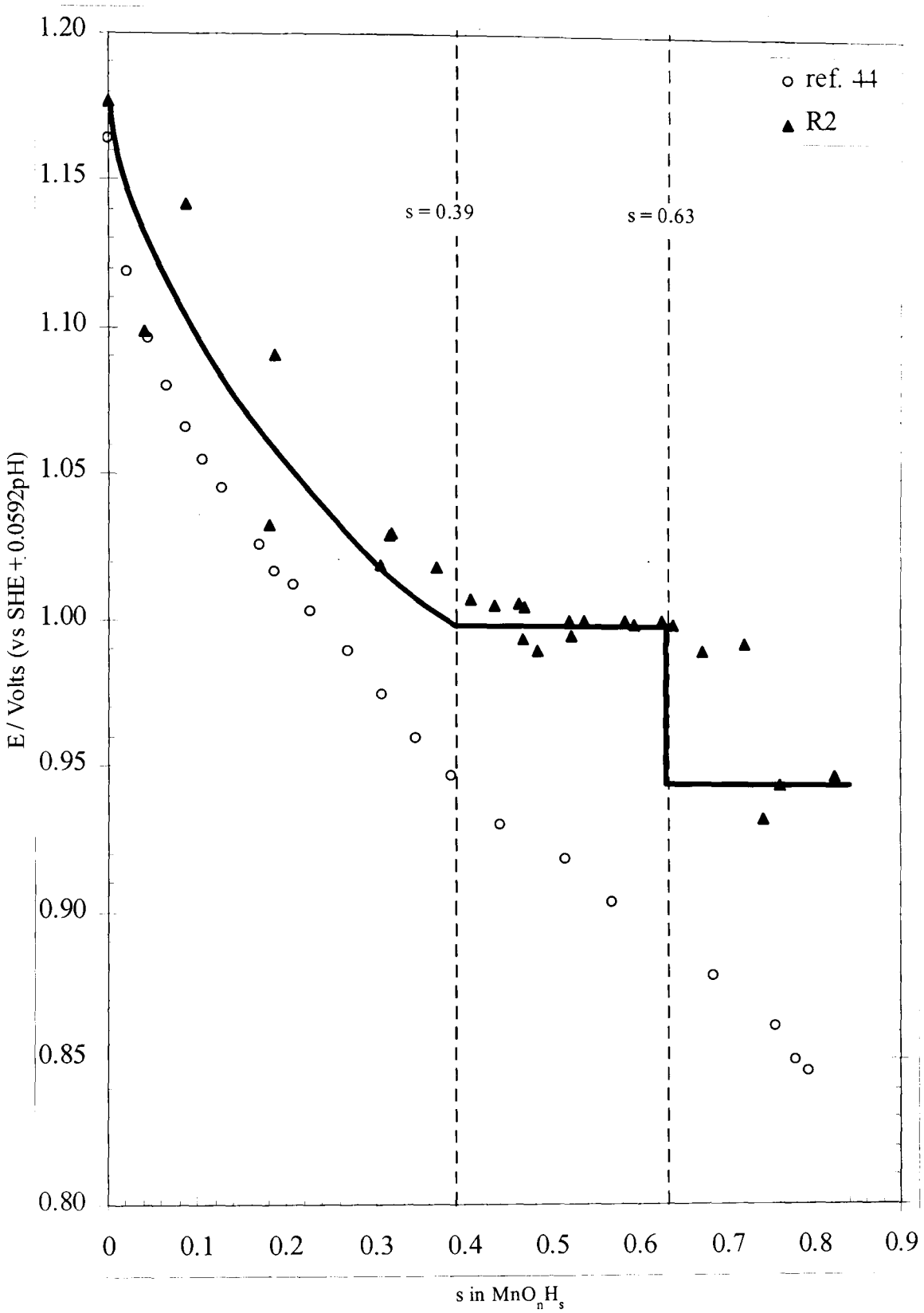

Fig. 6.4 Comparison between the potential of R2 against insertion level in the present work with Maskell's[44] data on the same material.

6.2 FTIR Study at Low Temperature

6.2.1 Introduction

Research at low temperature is sometimes associated with cryogenics, where extremely low temperatures are sought, since there is no hard dividing line between ordinary refrigeration and cryogenics[108]. This explains the dominance of IR studies in liquid inert gases in the literature, as in some recent papers[109-113]. Other low temperature studies[96-100] have also been carried out in liquid inert gases. In addition, IR research at low temperature seems particularly to be less practised: only 9 entries are shown in the Directory of Low Temperature Research in Europe*[114].

However, many papers, which report on some IR studies at temperatures far enough from the absolute zero, are available[115-123]. These and similar papers, are more relevant to this investigation which has been performed close to liquid nitrogen temperature ($\geq$ -180 °C).

From the previous three chapters, it has been established that the H-insertion, into the γ-manganese dioxide materials studied, commences with mobile H which locates at a particular insertion level depending on the material. The aim of this low temperature FTIR spectroscopy study was to investigate OH bond formation upon cooling.

Infrared spectroscopy study at low temperature ($25 \geq T \geq -180$ °C) has been carried out for the starting and selected non H-located H-inserted γ-manganese dioxide samples of SBP-A and Faradiser M as well as a few samples with located H. All R2 samples with and without H located have also been studied at low temperature. The reasons for these choices are discussed below and the experimental details are described in section 2.6.

In the following section the spectra at low temperature are presented and interpreted in a later section, in the light of both the literature and the observations of the results.

6.2.2 The FTIR Spectra at Low Temperature

Although the FTIR spectra was recorded between 400 and 4400 cm^{-1}, only the data above 800 cm^{-1} was significant since the vibrations below this frequency are due to the octahedral framework (see chapter 3). The NaCl windows of the variable temperature

* This directory was published in 1992. The author was unable to find a more recent similar reference.

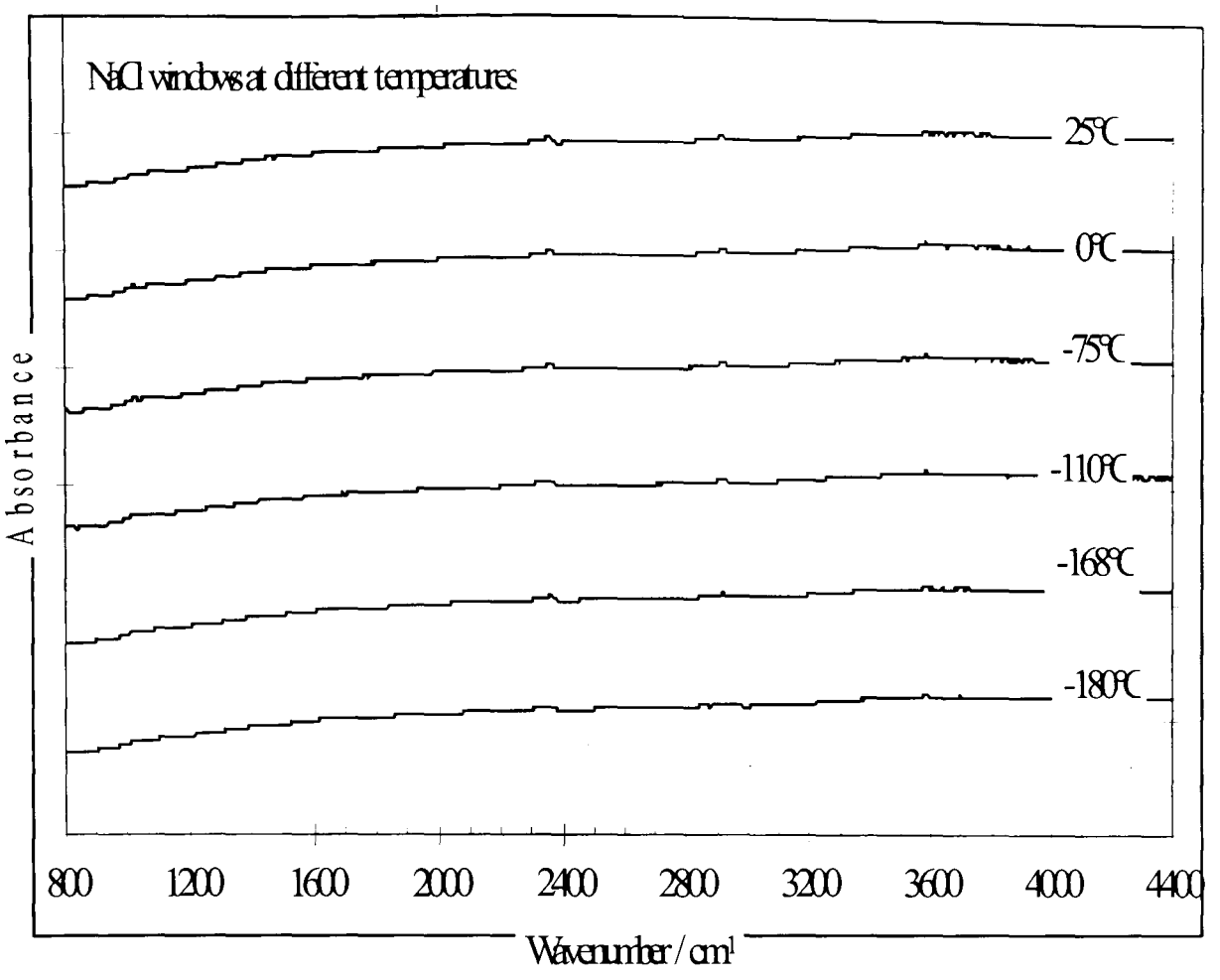

Fig.6.5 FTIR spectra of the NaCl windows of the VTC at different temperatures.

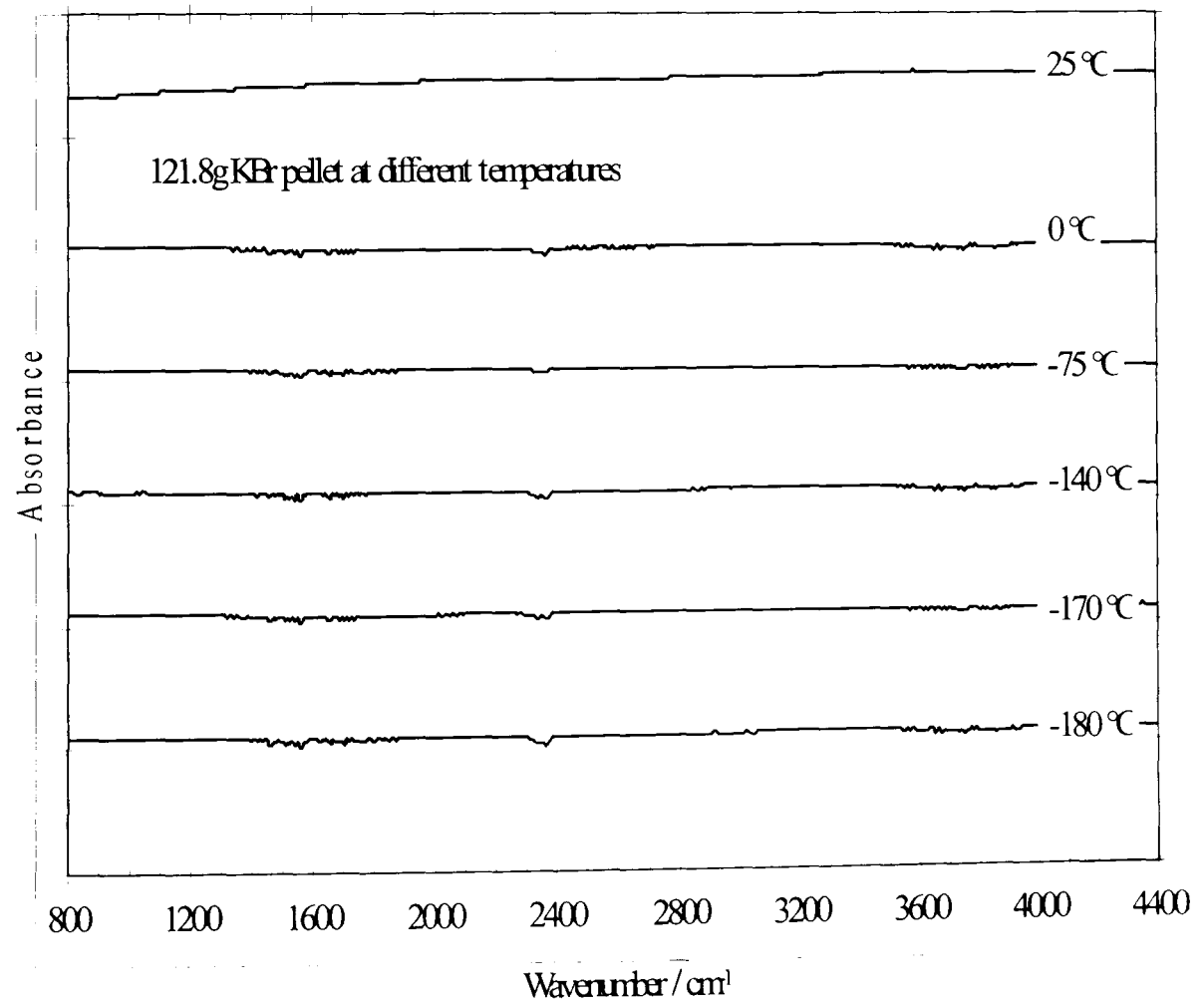

Fig.6.6 FTIR spectra of a KBr disc at different temperatures.

cell (VTC) absorb below 500 cm^{-1} preventing examination at such wavenumbers. Fortunately, the wavenumber range available was sufficient to reveal the changes to the spectra brought about by cooling to near liquid nitrogen temperature.

Prior to scanning sample pellets, the spectra of both the NaCl windows (empty cell) and a blank KBr pellet were recorded over the whole range of temperatures. This was to check for possible fogging of the windows or the KBr discs that might have introduced errors in the spectra of the manganese dioxide samples.

Examples of the low temperature spectra of the NaCl windows and the KBr pellets are given in Figs. 6.5 and 6.6. Only when these spectra were free from any features, were the manganese dioxide samples scanned as described in section 2.6.

The FTIR Spectra of H-inserted SBP-A at s = 0.276, and Faradiser M samples at s = 0.666 have been recorded in the temperature range $-180 \leq T \leq 25$ °C. These insertion levels are the highest before H located in both materials at room temperature, hence they have the highest chance to reveal changes related to H location induced by cooling. The spectra at different temperatures are shown in Figs. 6.7 and 6.8. The spectra remained virtually unchanged. The features marked CO_2 in the figures resulted from a difference of the local CO_2 concentration between the spectra of the manganese dioxide samples and that of pure KBr at the time of scanning. Although no absorption band was developed in either material at these suitable insertion levels, spectra of higher insertion levels (with H located at room temperature) were recorded, see Figs. 6.9 and 6.10. No significant change in FTIR absorption was induced by low temperature.

Similar spectra were acquired for R2 material at the insertion level of s = 0.624, just before H location at room temperature (section 5.2.2). The spectra are shown in Fig. 6.11. These spectra very significantly exhibited absorption bands which appeared and developed at temperatures from about –165 °C and below. These bands were fully reversible: upon heating the bands diminished before vanishing completely at about –165° C. Therefore, an extension of the study to the remaining H-insertion levels was applied to aid establishing at which insertion level these bands appear, how far they develop and how they interact with existing room temperature bands.

Four sets of spectra at significant insertion levels are presented on Figs. 6.12 to 6.15. These are the starting material with no insertion (s = 0.000), the material affected only by the reaction medium (propanol and hexane, see section 2.2.4) with no added

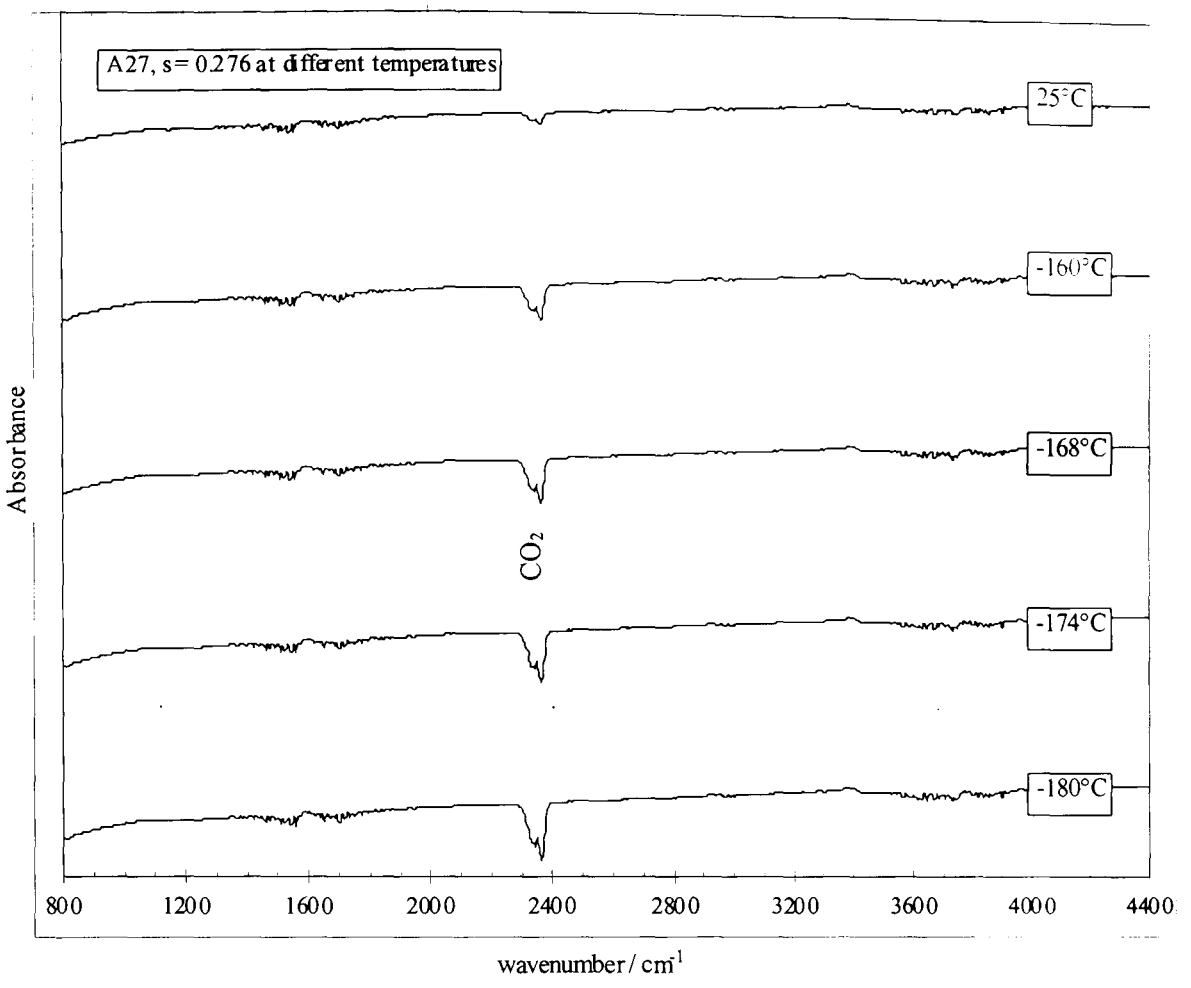

Fig.6.7 FTIR spectra of H-inserted SBP-A, just before H location at room temperature (s = 0.276), at different temperatures.

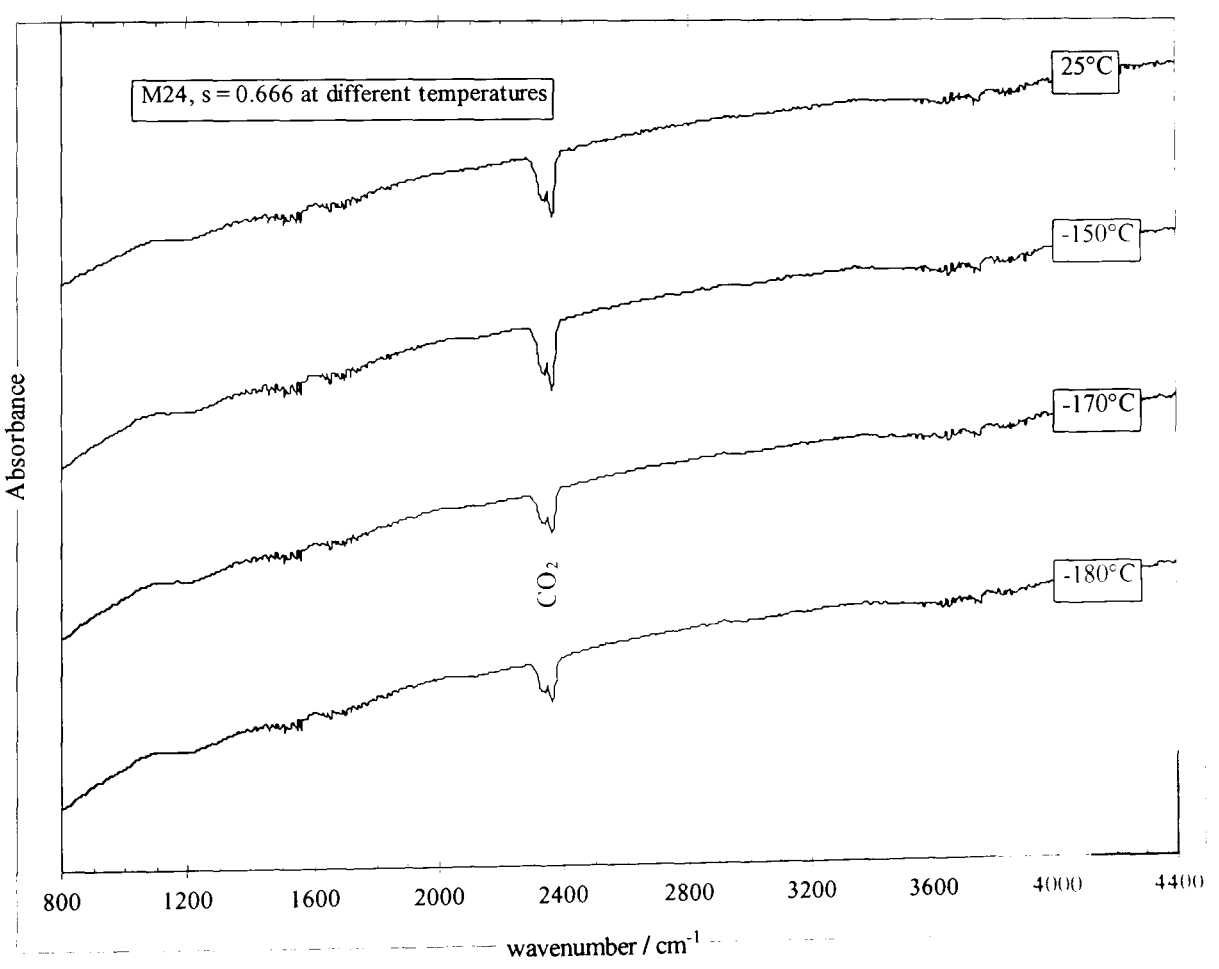

Fig.6.8 FTIR spectra of H-inserted Faradiser M, just before H location at room temperature (s = 0.666), at different temperatures.

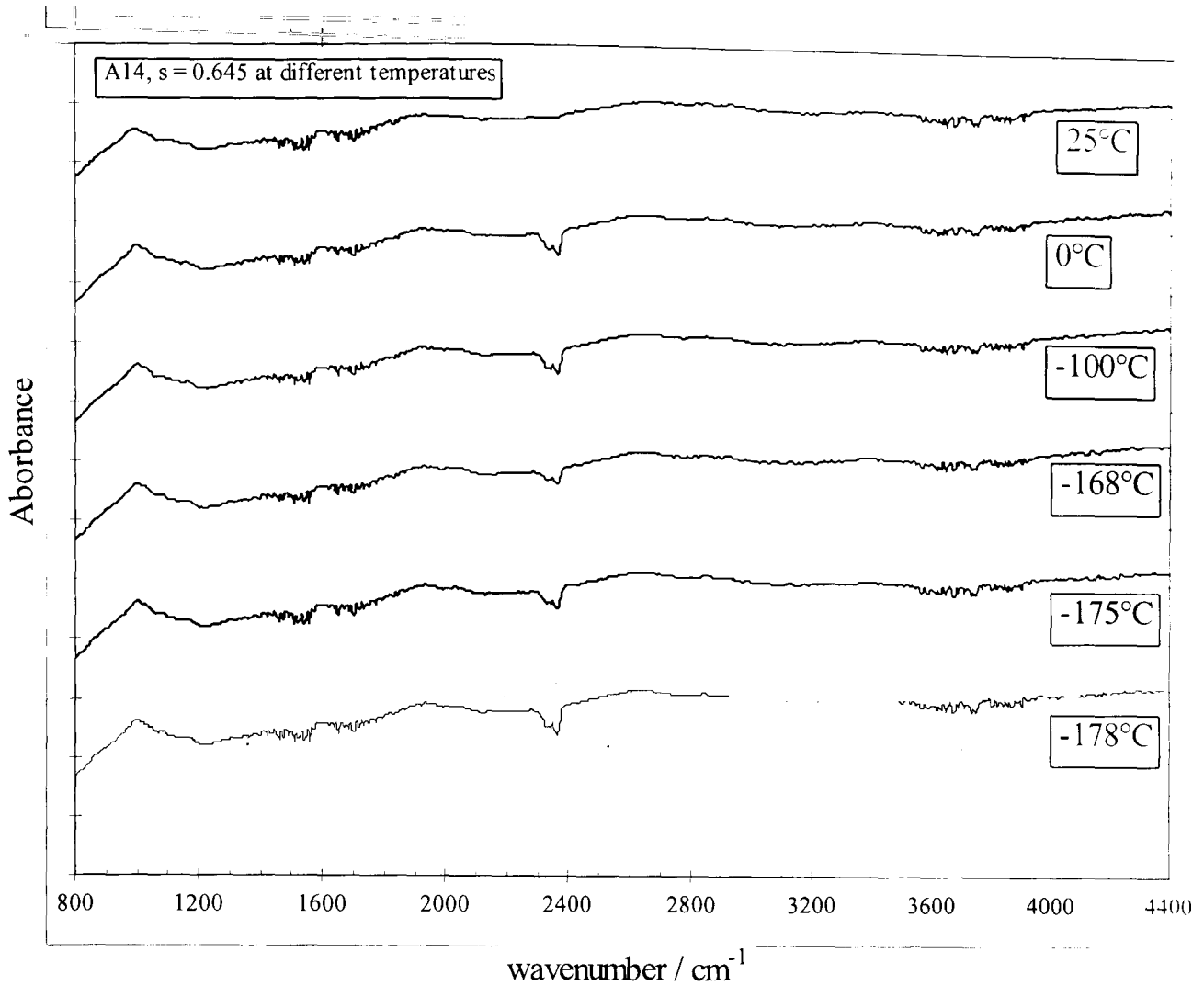

Fig.6.9 FTIR spectra of a highly H-inserted SBP-A sample (s = 0.645), with H location at room temperature, at different temperatures.

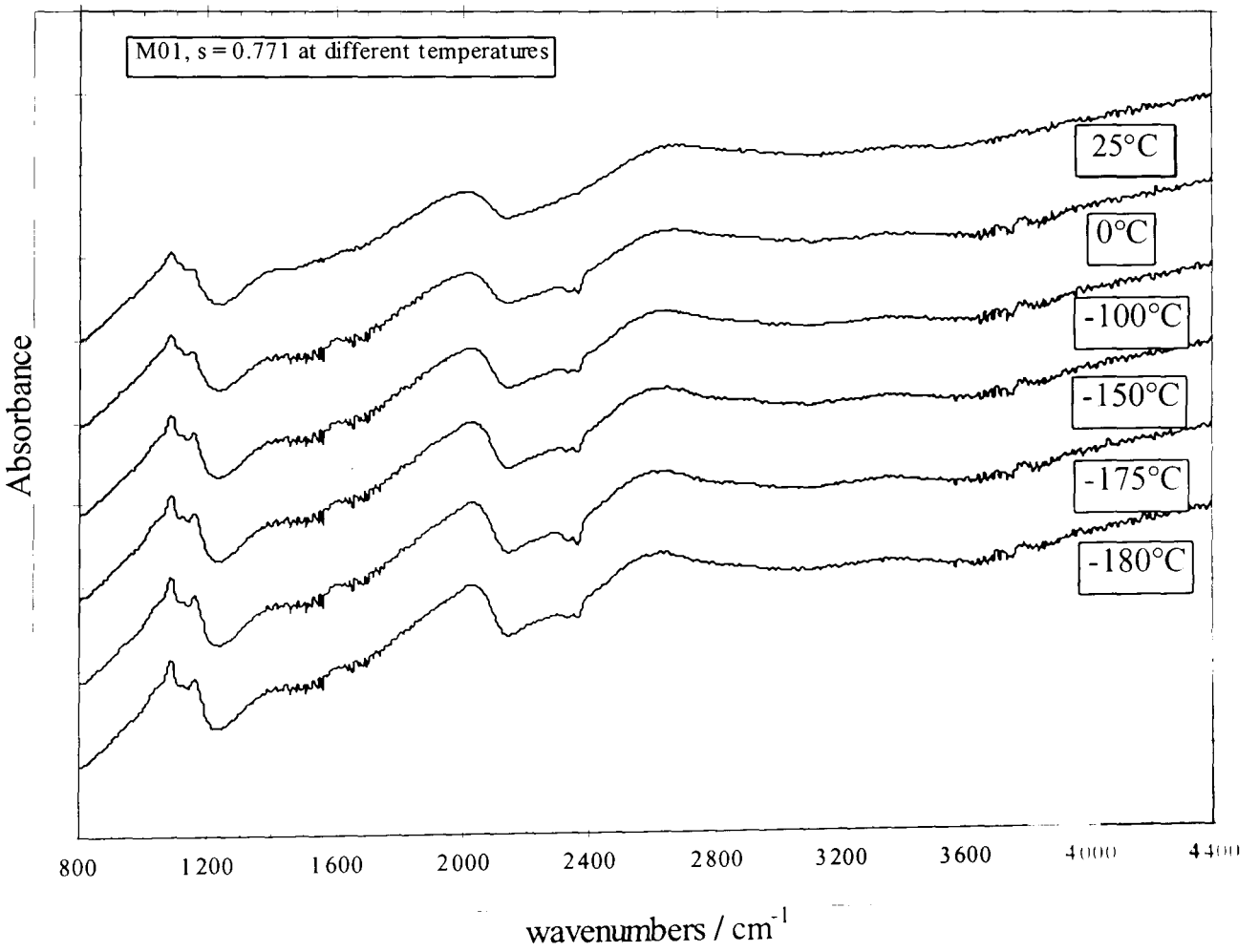

Fig.6.10 FTIR spectra of a highly H-inserted Faradiser M sample (s = 0.771), with H location at room temperature, at different temperatures.

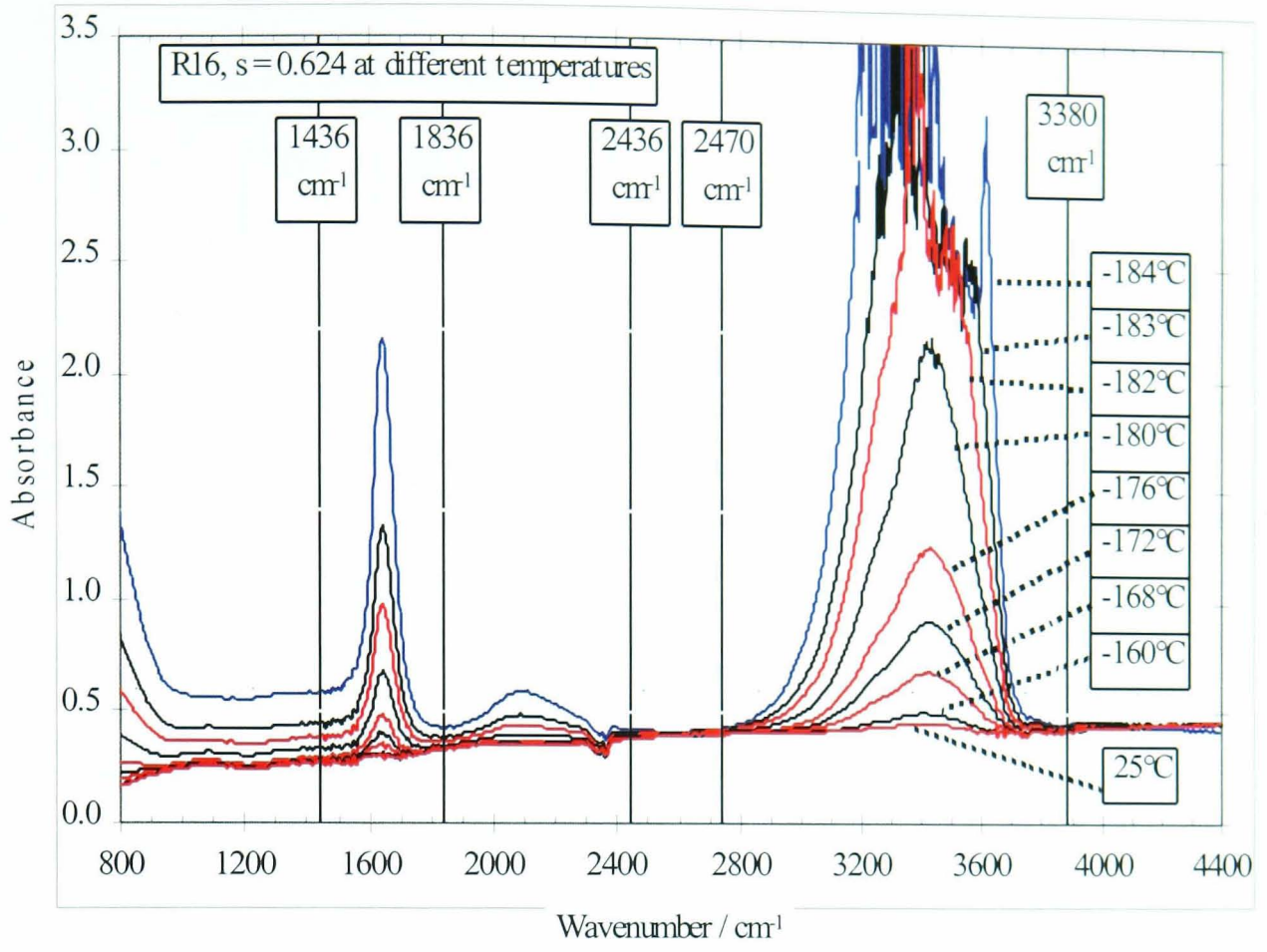

Fig.6.11 FTIR spectra of H-inserted R2 material, just before H location at room temperature (s = 0.624), at different temperatures.

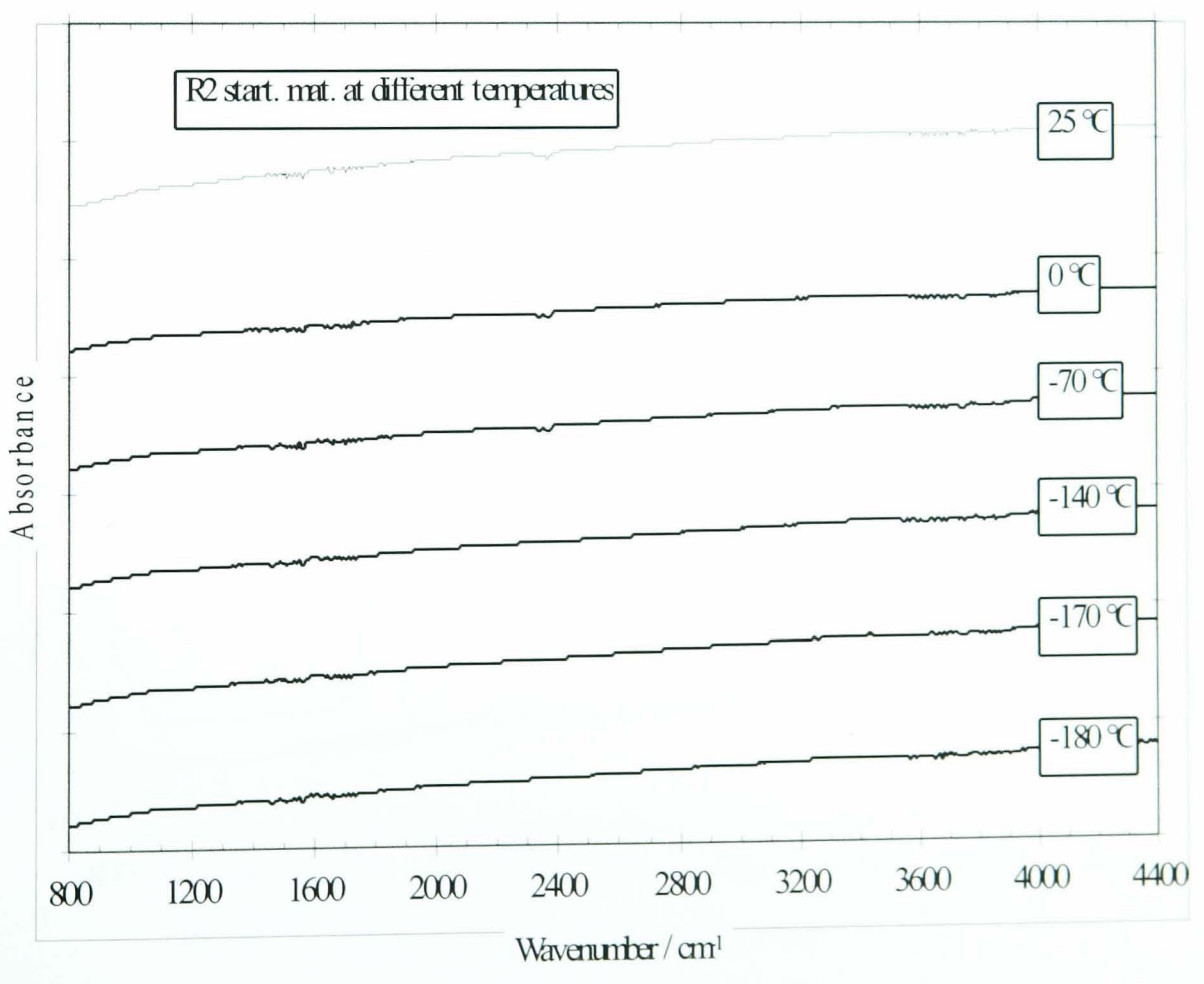

Fig.6.12 FTIR spectra of R2 starting material at different temperatures.

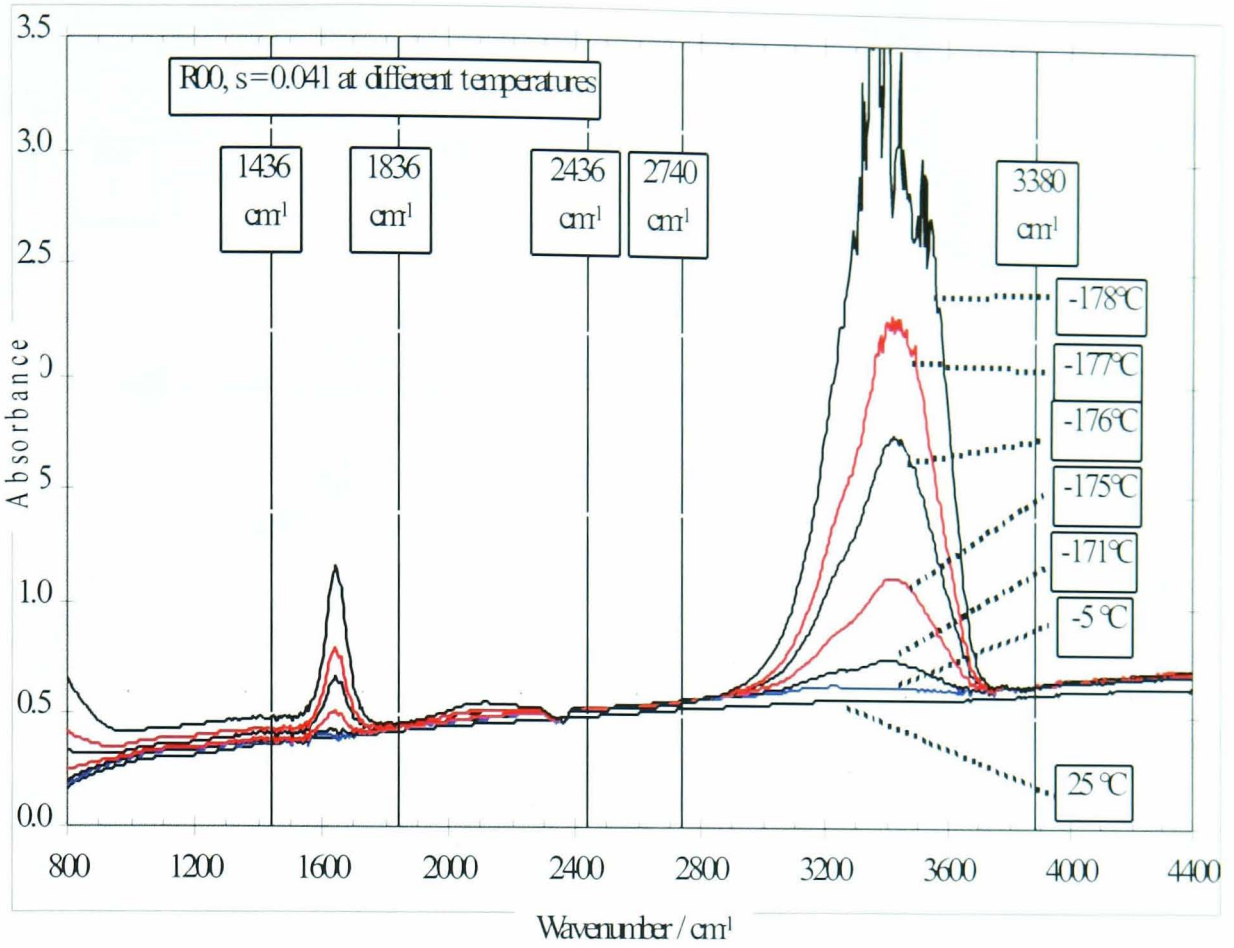

Fig.6.13 FTIR spectra of slightly H-inserted R2 material, H from solvent (s = 0.041), at different temperatures.

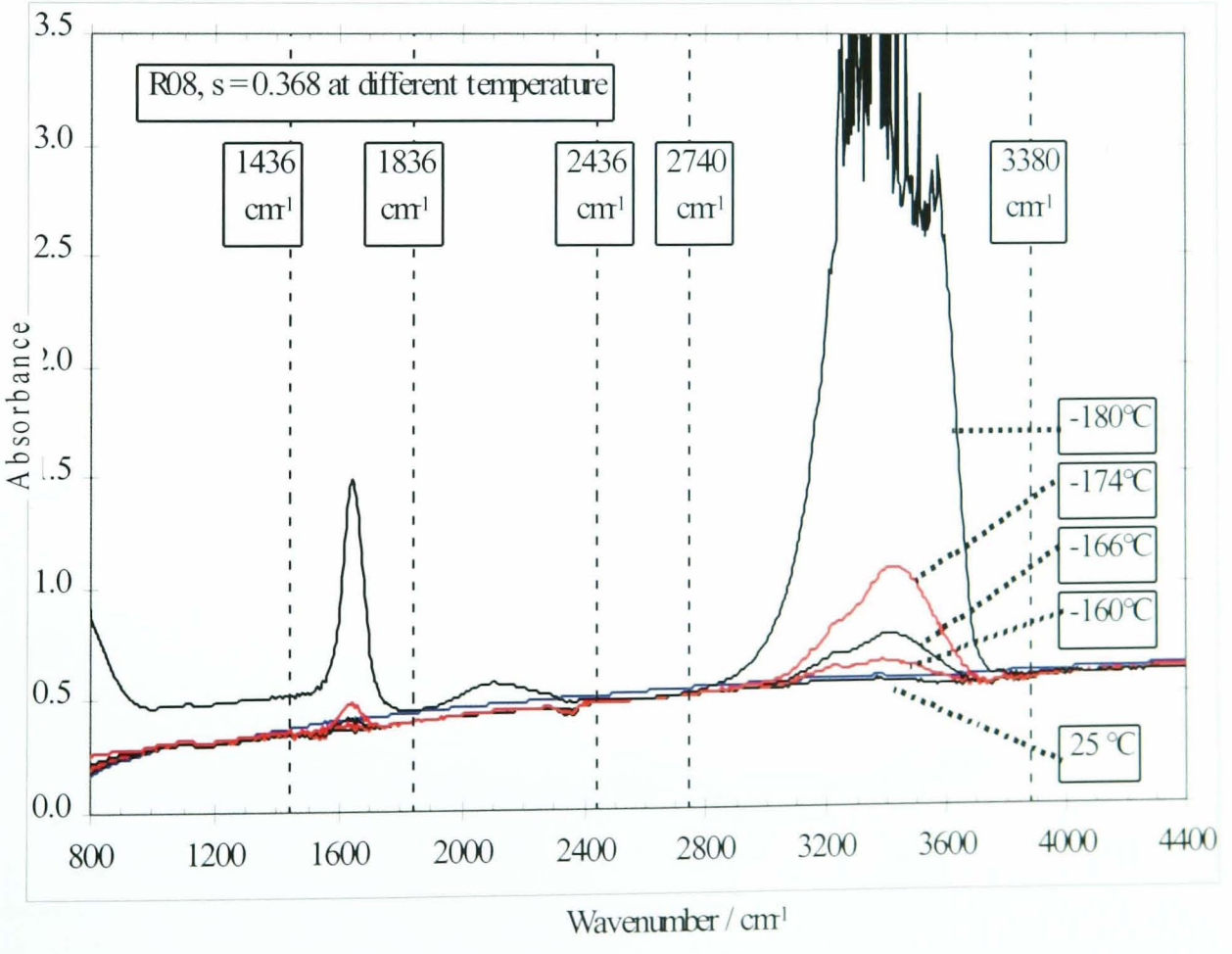

Fig.6.14 FTIR spectra of H-inserted R2 material (s = 0.368) at different temperatures.

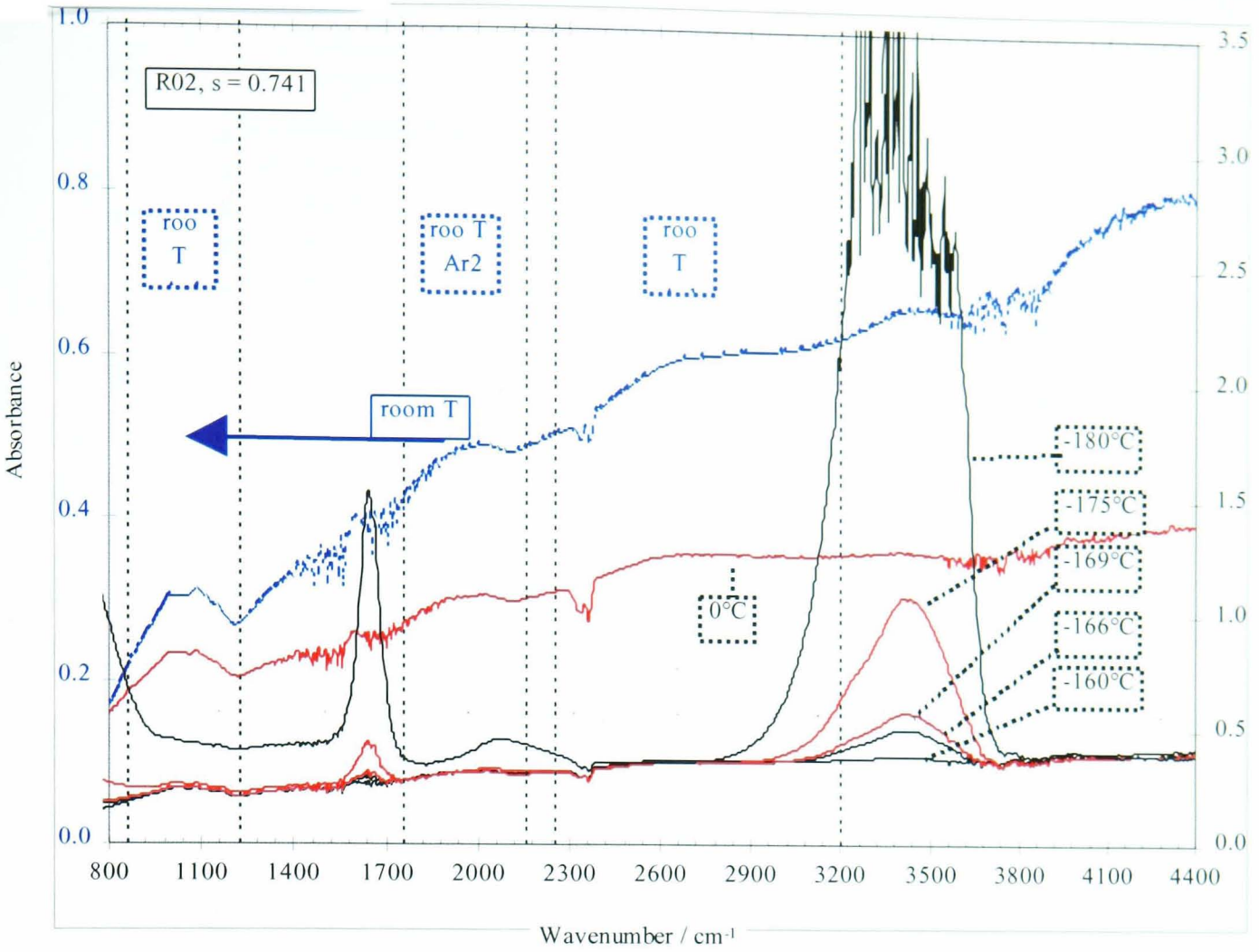

Fig.6.15 FTIR spectra of a highly H-inserted R2 material (s = 0.741) with H located at room temperature, at different temperatures.

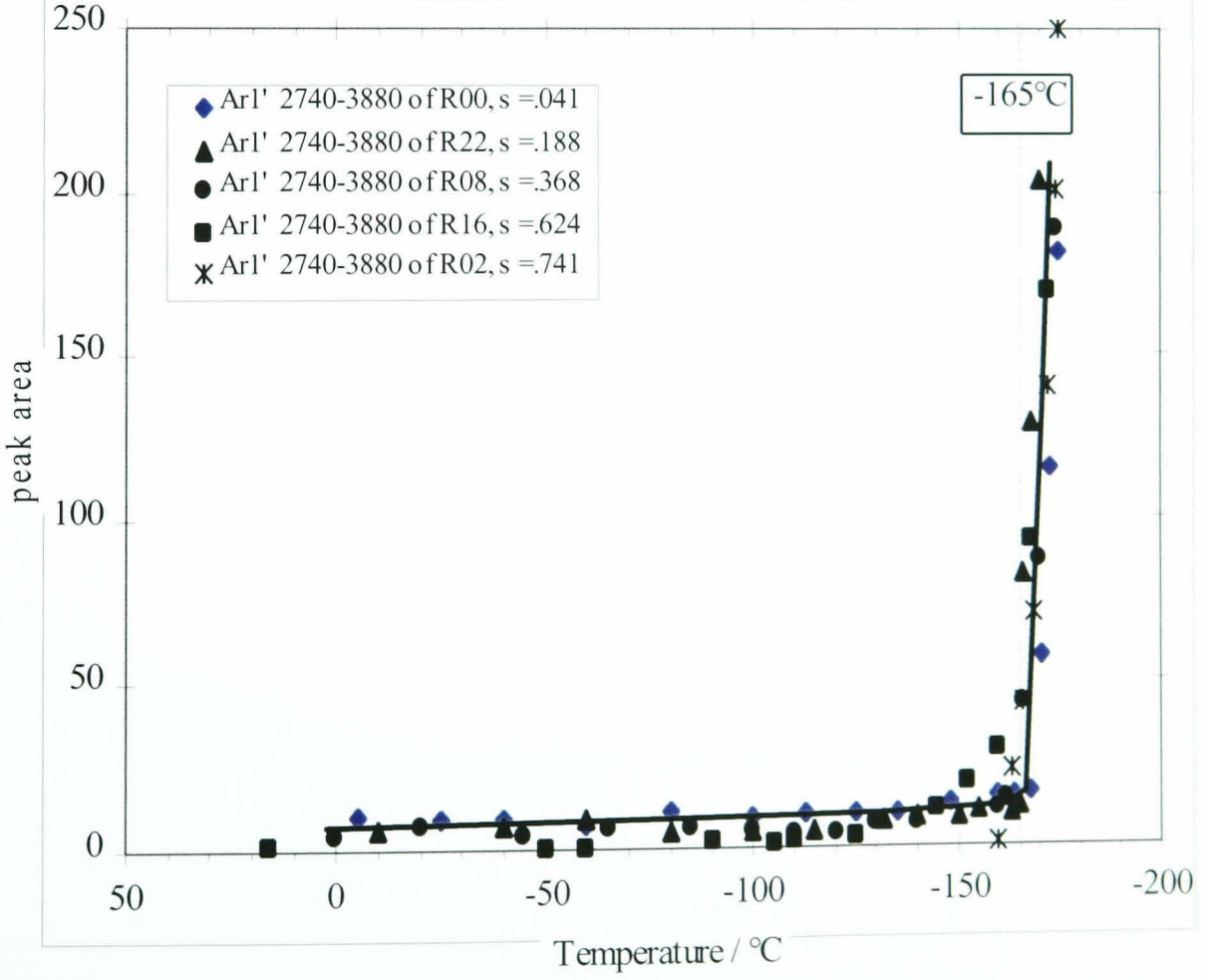

Fig.6.16 Integrated peak area of the low temperature band between 2740 and 3880 cm^{-1} vs. temperature.

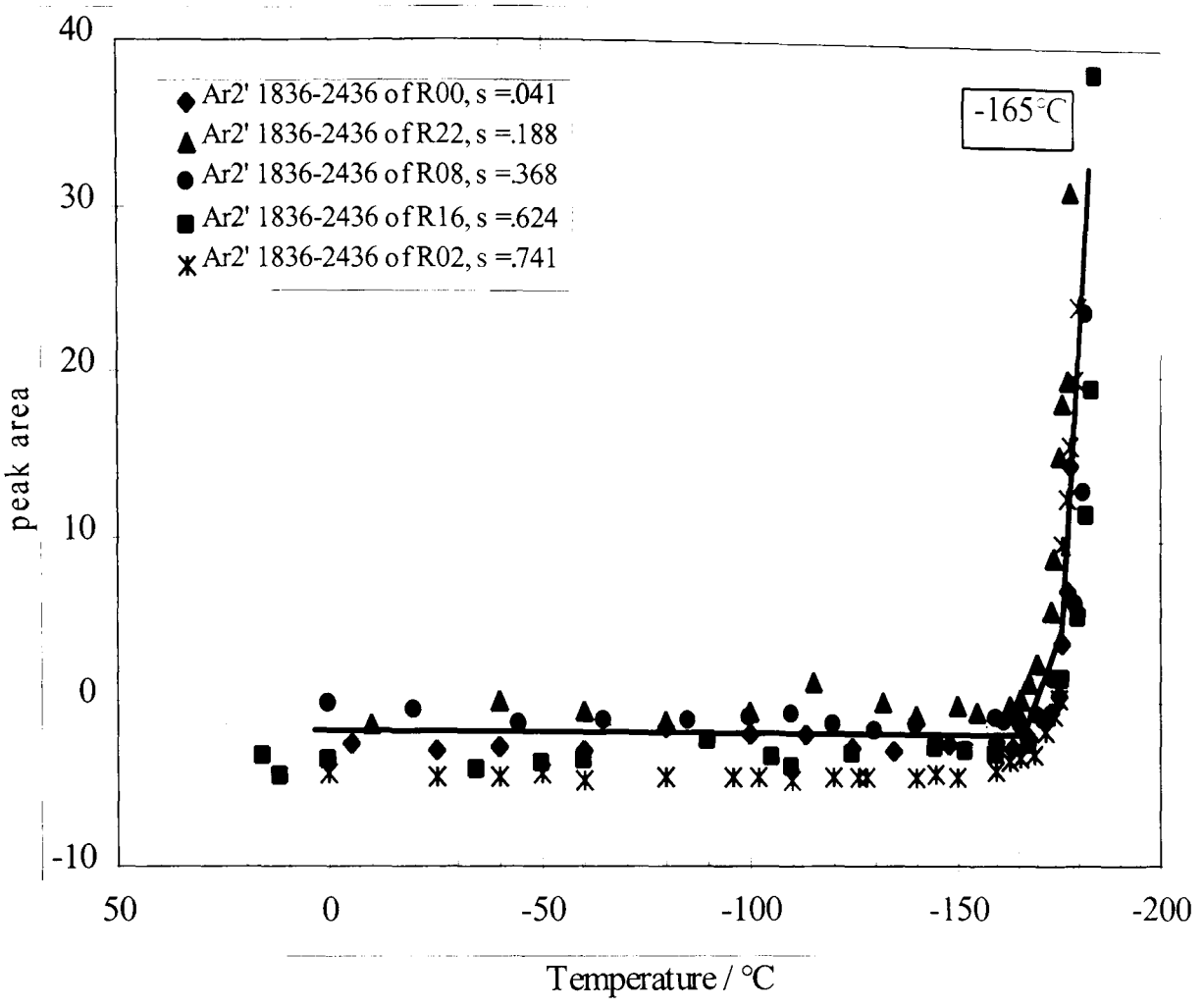

Fig.6.17 Integrated peak area of the low temperature band between 1836 and 2436 cm^{-1} vs. temperature.

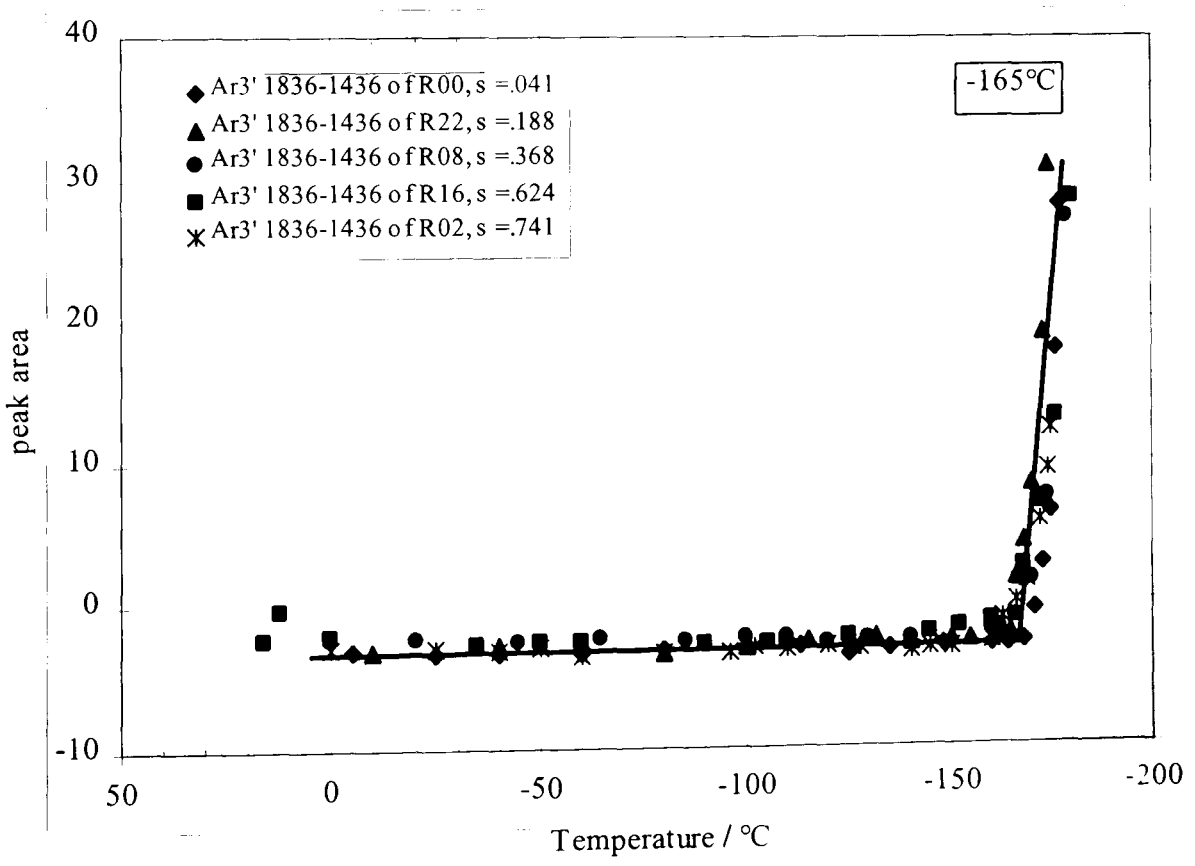

Fig.6.18 Integrated peak area of the low temperature band between 1436 and 1836 cm^{-1} vs. temperature.

reactant (s = 0.041), a material from the first phase of the H-insertion (s = 0.368) and a material from the last phase where H is located at room temperature (s = 0.741).

Except for the starting material, all the spectra exhibited three absorption bands from about -165 °C, and the bands were enhanced as the temperature decreased. These bands are centred at approximately 3400, 2100 and 1650 cm^{-1}.

Integrated band areas have been calculated in the same way as for the spectra at room temperature (section 2.5.7) to enable the evolution of the absorption bands with temperature to be followed. Figs. 6.16 to 6.18 show the integrated band areas against temperature for different insertion levels. The reader is reminded that that these absorption bands were fully reversible; i.e. upon heating from liquid nitrogen temperature, the bands diminished gradually before disappearing at about –165° C. The band boundaries are different from those applied at room temperature to account for the difference in position. The band peaks at room and low temperatures are compared in Table 6.1.

Table 6.1 Approximate positions of the main FTIR absorption bands for H-inserted R2 above 800 cm^{-1}.

Band	Mode	room temperature	low temperature	Shift
Ar1	νOH	2650	3400	750
Ar2	2γOH	1950	2100	150
Ar3	γOH	1000	1650	650

ν: stretching mode, γ: out-of-plane bending mode, 2: first overtone

Fig. 6.15 is of particular interest. It displays the spectra at different low temperatures of a highly H-inserted R2 material along with the room temperature spectrum where O-H bond is already present. This figure provides an opportunity to examine the behaviour of the room temperature OH vibration bands at low temperatures. An expanded region of Fig. 6.15 showing the change in the room temperature vibrations is displayed in Fig. 6.19. Fig. 6.19 shows clearly that the room temperature bands shift to higher frequencies upon cooling. The bands coded Ar1 and Ar2 overlap with the low temperature-induced absorptions. The band coded Ar4, however, shifts without overlapping with other bands, offering an opportunity to examine quantitatively the behaviour of room temperature bands upon cooling. The shift of Ar4 was found to be essentially from the low frequency side; i.e. it is a narrowing rather than a shift.

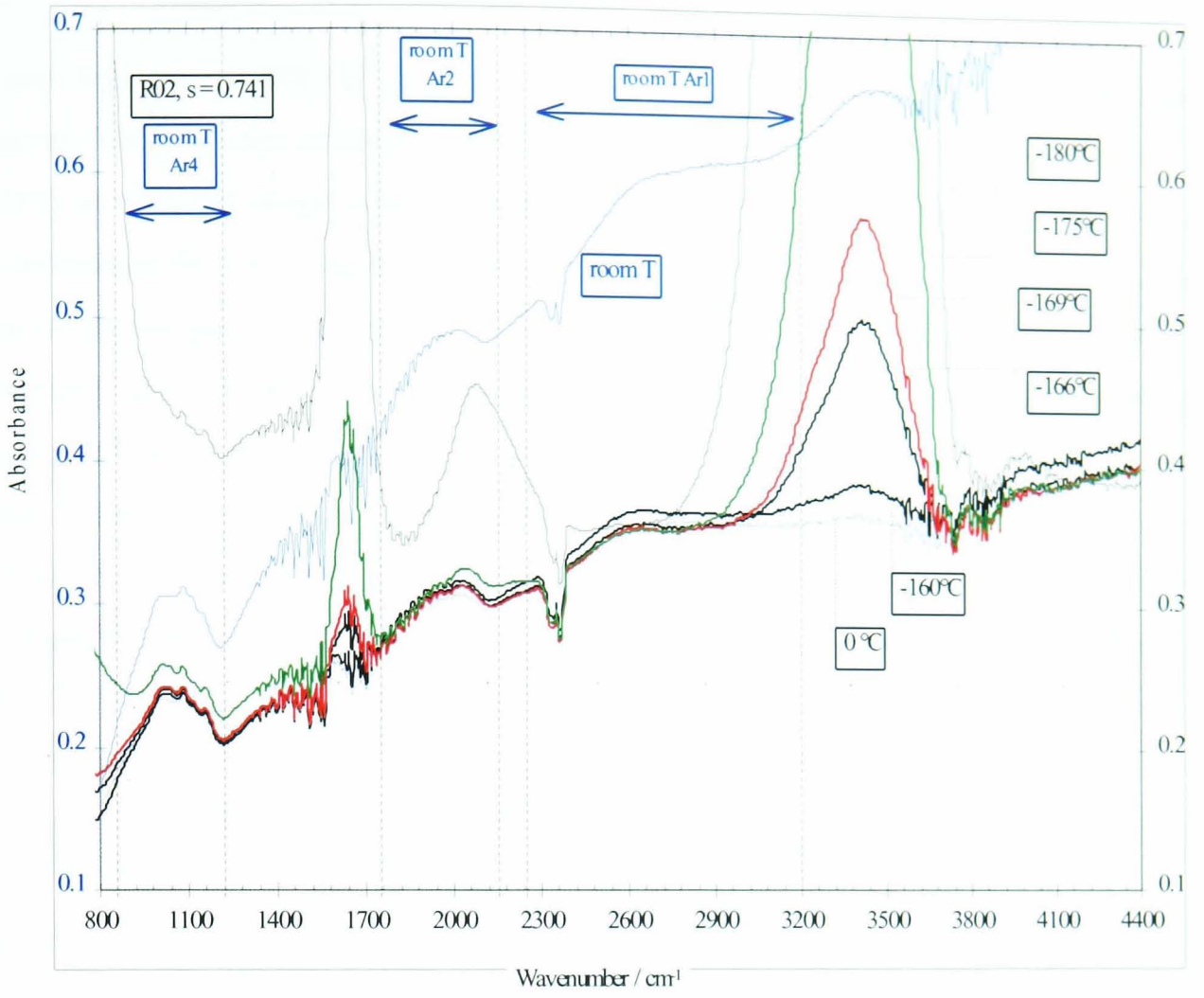

Fig. 6.19 Evolution of the room temperature OH vibrations bands at low temperature.

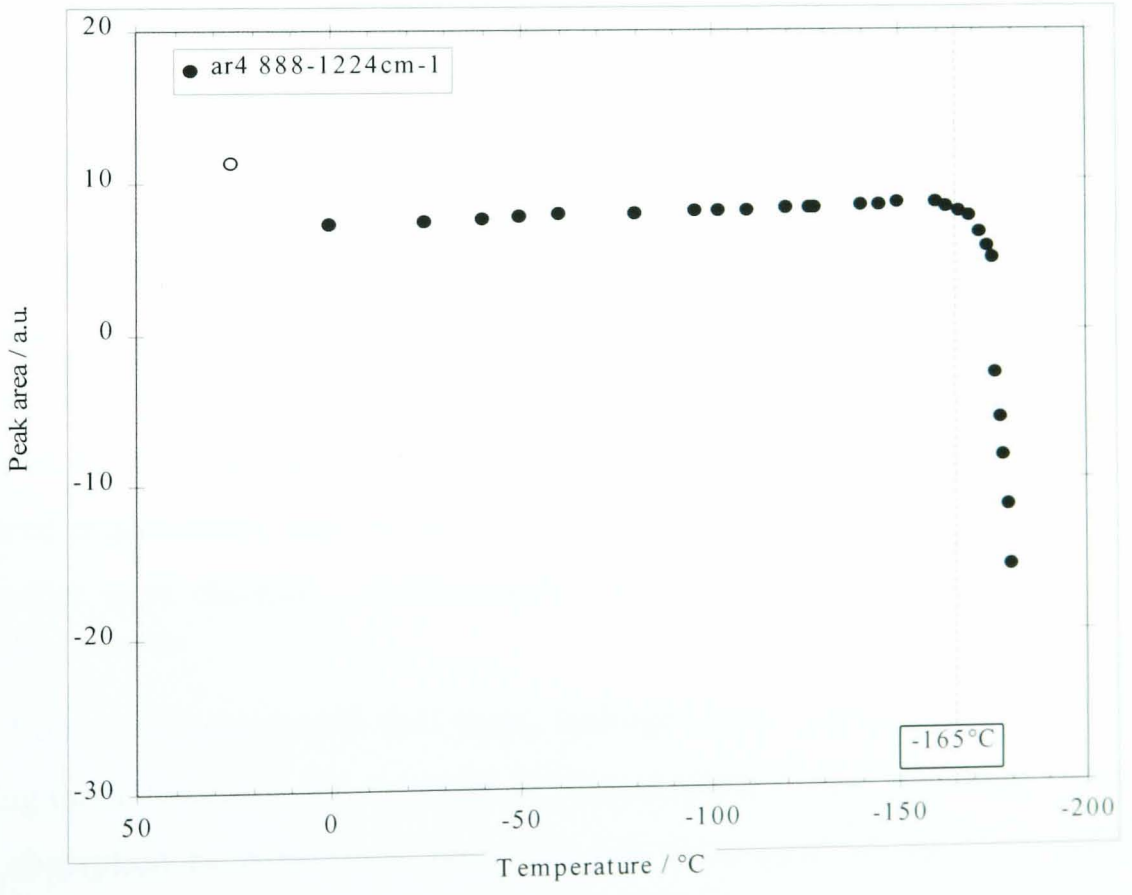

Fig. 6.20: Evolution of the room temperature peak area Ar4 of a highly H-inserted R2 material (s = 0.741) at low temperatures.

A new boundary at 888 cm^{-1} was then chosen as the low frequency end for Ar4. The area of Ar4 has been evaluated for the spectra of the same H-inserted sample (s = 0.741) at different temperatures starting from 25° C down to about –180° C. The boundaries of the 25° C spectrum are 856 to 1224 cm^{-1}.

The results are plotted in Fig. 6.20. Fig. 6.20 demonstrates that from around –165° C, the band, initially present at room temperature, decreases severely upon cooling. Again, this fact was perfectly reversible.

Thus, at low temperatures, some absorption bands appeared exclusively in H-inserted R2 materials. These bands increased with cooling. The room temperature IR bands in R2 samples, with H located, decreased severely as the temperature decreased below –165° C.

The low temperature effects were fully reversible.

6.2.3 Interpretation of the FTIR Spectra at Low Temperature

The interpretation of the low temperature spectra presented above is now considered. The literature has not aided this interpretation as much as it did with the room temperature spectra or the XRD study. This is because of two main differences between the results of this work and those of the cited literature. The first is that what has been widely reported on was the effect of temperature on *H bonding*. *H bonding* involves two atoms: one covalently bonded and the other hydrogen bonded to the H. This is not the situation in the room temperature spectra of H-inserted R2 in this work below s = 0.64; i.e. prior to H location. The second difference is that the only structure in this work exhibiting new vibration bands at low temperature was the heavily microtwinned R2, while no such a defect is mentioned for the materials studied in the cited literature. An additional noteworthy point is that the low temperature effects as investigated in this work were fully reversible. Upon heating, the absorption bands disappeared progressively and the room temperature spectra before and after cooling a sample pellet were identical. Unfortunately, there is no mention about this in the literature[109-113,115-124].

Starting from a compound with O-H bond, hydrogen bond formation H···O-H means weakening the initial OH bond. In terms of infrared spectroscopy, this means a shift of the OH absorption band to lower frequency and an increase of the band width[124]. Conversely, elimination of the hydrogen bond in H···O-H is expected to sharpen the absorption band and shift it to higher frequency. Desseyn and Slootmaeckers[116] study

on hydrogen bonding has shown that in the absence of hydrogen bonding, the OH bond becomes sharper and shifts to higher frequency. In a recent paper from Desseyn et al.[122], the effect of pressure on hydrogen bonded structures has been reported to be strongly due to change of angles rather than change of distances caused by high pressure.

Cooling down a substance reduces the thermal agitation of their particles and hence decreases the entropy. For lightly H-inserted γ-manganese dioxides, solid solution is formed between mobile H in the gaseous state and the MnO_6 octahedra chains (Chapter 1). Upon cooling, the mobility of the H is reduced and so is the entropy of the system. The thermodynamics requirement for a process to occur is a decrease of its Gibbs free energy ($\Delta G < 0$) which is related to the entropy (S), temperature (T) and enthalpy (H) by:

$$G = H - TS \qquad (6.1)$$

To compensate for the decrease in temperature and entropy, which alone would lead to higher G, O-H bond is formed with a sufficiently negative enthalpy to give a lower Gibbs free energy. There is thus a balance between the enthalpy of formation of the O-H bond and the temperature decrease. The lower is the temperature, the lower would the enthalpy be; i.e. upon cooling the O-H bond increases in concentration and/or strength to maintain the balance.

Many investigations[e.g.16,18, 42,46] have reported that only O2 oxygens (see section 1.2.2) can form OH bonds in the ramsdellite/groutite-like structure due to the reduced electrostatic repulsion between the Mn atoms and the hydrogen on these sites. There is also an additional requirement for H to bond with O2 and hydrogen bond with O1[37]. That is rotation to change the tunnel shape so that O2 and O1 are brought closer together. This is achieved by sufficiently decreasing the angle β between the apical oxygens and the *b* axis (see section 3.1.1).

As the low temperature is not expected to change the tunnel shape of the octahedra, the only way of forming O-H bond at low temperature would be by bringing the H closer to the O2 sites.

These bonds are expected to be largely covalent involving only the O2 particularly in the non-rotated octahedra where the O2 and O1 are sufficiently far apart for the O1 not to hydrogen bond. This must be the case for $s < 0.63$. Moreover, since all low

temperature bands are in the same position across the whole range of s, these absorption bands must be due solely to O-H bonding.

The absence of OH bands at low temperatures in Figs. 6.7 - 6.10 indicates that the H has not been brought sufficiently close to bond with the O2 in materials SBP-A and Faradiser M, or there is a difference between the concentration of O2 sites. Perhaps. further cooling can induce OH bonding. The experimental equipment available to this work was not suitable for use below liquid nitrogen temperature.

All H-inserted R2 material, in the other hand, bonded to H at temperatures below –165 °C as shown on Figs. 6.11 and 6.13-6.15. Therefore, there must be an arrangement whereby the O2s are reachable. Examination of the main structural difference between SBP-A and Faradiser M, and R2, namely the extensive microtwinning in R2 suggested an explanation for this H bonding. In order to examine the microtwinning effect(s) on the O1/O2 type oxygens, a non-microtwinned structure has been drawn in Fig. 6.21 and the O2/O1 distinguished. Fig. 6.21 clearly shows that the ratio of O2:O1 in normal octahedral chains is 1:1. The two microtwinning planes 061 and 021 are drawn on Figs. 6.22 and 6.23 respectively, and the oxygen distribution between O1 and O2 is discussed.

The 061 twinning encourages H location by generating extra O2 types, where H may be located. The 061 twinning shifts the ratio of O2:O1 from 1:1 to 11:9. Fig. 6.22 demonstrates that 4 out of the 10 octahedra involved in the 061 twinning have their O2:O1 ratio altered. An overall count shows 33 O2 against 27 O1.

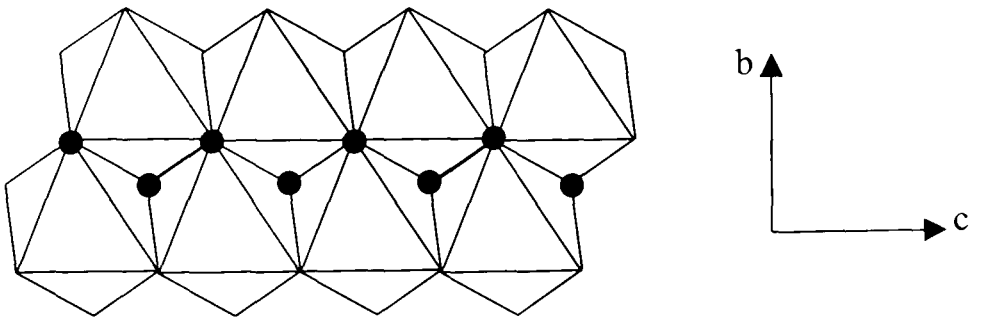

Fig.6.21 Projection on the bc plane of a non-faulted possible idealised ramsdellite chain based on hcp oxygens. The black circles represent O2 oxygens, O1s occupy the remaining corners. The ratio of O1:O2 is 1:1.

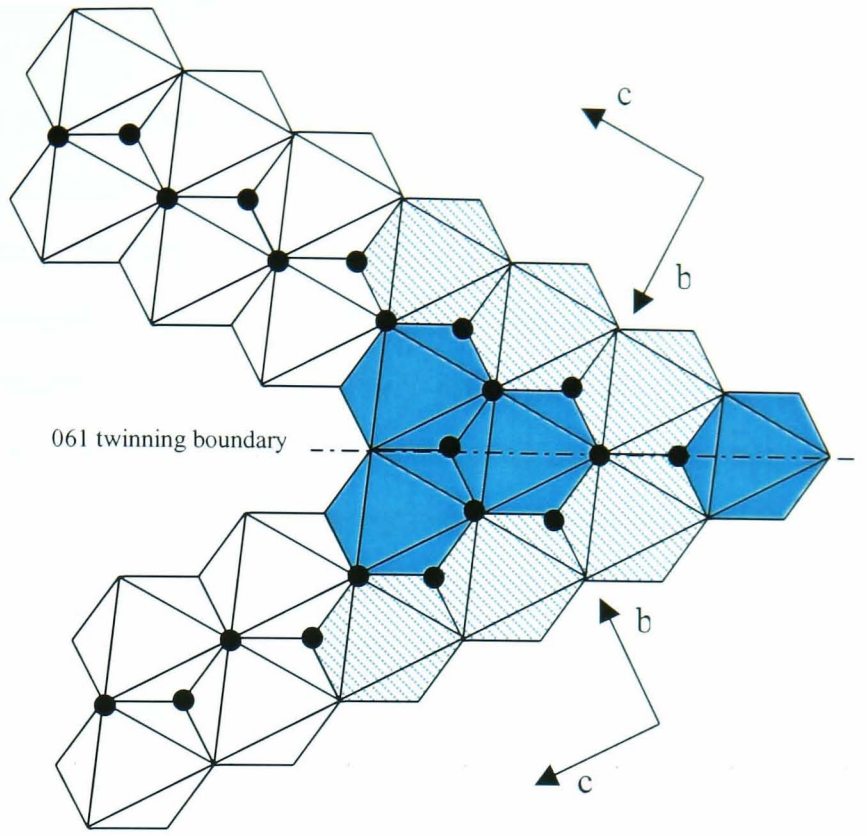

Fig.6.22 Projection on the bc plane of a possible 061 twinning of an idealised ramsdellite structure based on hcp oxygens. The black circles represent O2 oxygens, O1s occupy the remaining corners. The ratio 1:1 of O1:O2 is affected in the coloured octahedra, shaded octahedra are part of the twinning fault but their ratios O1:O2 are not affected. Clear octahedra are unaffected and extending in the c direction. Note the symmetry about the 061 plane.

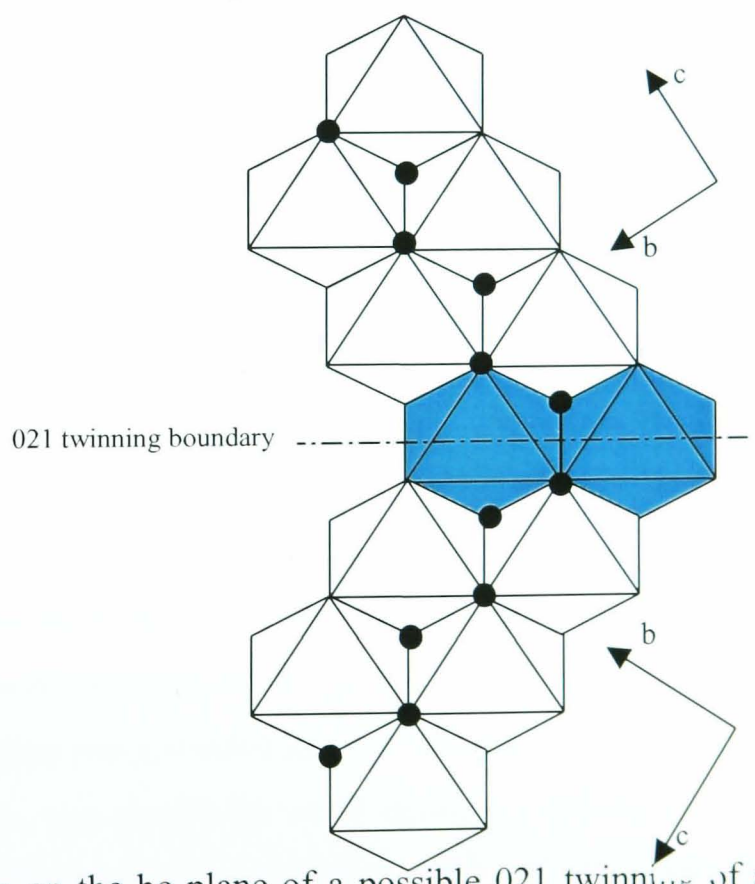

Fig.6.23 Projection on the bc plane of a possible 021 twinning of an idealised ramsdellite structure based on hcp oxygens. The black circles represent O2 oxygens, O1s occupy the remaining corners. The ratio 1:1 of O1:O2 is only *apparently* affected in the coloured octahedra. Note that the 021 plane is not a plane of symmetry.

The 021 twinning plane, however, has a wider angle which is perhaps not significantly narrower than the normal octahedral chains with regard to H bonding. This twinning plane involves two octahedra and alters their O2:O1 ratios to 4:2 and 2:4 leaving the overall ratio unchanged, 1:1 as in normal double chains.

This hypothesis suggests that H bonding at low temperature may be strongly related to the concentration of the 061 twinning planes and not to the 021 twinning planes. An insertion level as low as 0.04 was enough to raise absorption bands in R2 at low temperature (Fig. 6.12) while no absorption band could be detected in the other materials at any insertion level. This can only mean that the concentration of 061 twinning must be highly preponderant in R2. The absence of absorption band at low temperature in SBP-A and Faradiser M is therefore an indication of a low fraction (if any at all) of 061 planes in their microtwinning.

Bearing in mind the discussions of the structural maps of these two materials in Chapters 3 and 4, the suggestion that the slight microtwinning in SBP-A is predominantly across the 021 planes seems reasonable. Faradiser M remains untwinned as no evidence of microtwinning (such as restriction of expansion in the *b* dimension or H bonding at low temperature) was found.

Pannetier[18], who introduced the microtwinning approach to explain the poor XRD of EMD, did not provide a quantitative partition of the microtwinning between the 021 and 061 planes. This study suggests that the low temperature IR can help towards such a partition.

6.2.4 Further Discussion

Although the study by Desseyn and Slootmaeckers[116] aimed to distinguish between inter- and intra-molecular hydrogen bonding, distinctive clues between covalent and hydrogen bonding were also provided. These authors examined the IR spectra at different temperatures and in different solvents of NN'-dihydroxypentyldithiooxamide (NNDHPeDTO) and concluded that in an apolar solvent such as CS_2 under high dilution at 20° C, H bonding was excluded and OH vibration occurred at 3636 cm^{-1}. In 1,4-dioxane, where there was possibility of H bonding between the solute and an oxygen of solvent, the OH vibration was shifted to 3490 cm^{-1} at the same temperature. When a solid state KBr pellet was employed, hydrogen bonding became possible between two different molecules of the solute, and the OH vibration band appeared at 3388 cm^{-1} under 20° C and at 3365 cm^{-1} at –196° C. This shift was due a

strengthening of the hydrogen bond in the solute at low temperatures[116]. The point of presenting these results is to examine the low temperature OH vibration bands present in spectra of H-inserted R2, particularly the large one at about 3400 cm^{-1}.

The low temperature bands at about 3400, 2100 and 1650 cm^{-1} are clearly similar to those observed at room temperature (noted Ar1, Ar2 and Ar4 in Table 3.2) and are due to stretching, out-of-plane and in-plane vibration modes. Figs. 6.19 and 6.20 demonstrate clearly that the room temperature bands shifted to higher frequencies; i.e. strengthen, upon cooling. Contrarily to what Desseyn and Slootmaeckers[116] observed for NNDHPeDTO, cooling weakened hydrogen bonds and strengthened the covalent O-H bonds in R2. Maskell et al.[45] suggested in 1982 that protons in manganese dioxide are bonded to O2 oxygens and hydrogen-bonded to O1 type, i.e. O2–H···O1. Using this notation, the H in the bond O2–H···O1 shifted to O2 at low temperatures. This conclusion is based primarily on the shift to higher IR frequency at low temperature of the bands. Since the 3400 cm^{-1} is by and large the most important band, the discussion is limited to it.

The position of the large band at high frequency (3400 cm^{-1}) indicates strongly that this band is due to stretching of a covalent OH bond without hydrogen bonding. In other words, only the O2 oxygens are involved. This statement is supported by the relative sharpness of this band compared with its shape at room temperature. At room temperature, the presence of hydrogen bonding caused the band to broaden, as is evident in Fig. 6.19 and in the spectra throughout Chapters 3, 4 and 5 are compared. The substantial enlargement of this band upon cooling must be due to a strengthening of the O-H bonds, which generates stronger dipole moments- hence the high absorption.

The appearance of OH band absorption, at low temperature, in a sample as highly H-inserted as s = 0.741 means that there are still some "portions" of the starting structure which is microtwinned across the 061 planes. The decrease of the room temperature bands as the low temperature absorptions developed occurs in addition to the low temperature induced bands and makes it difficult to separate the two phenomena. At this stage, all of the H is presumably located at room temperature in the O2–H···O1 scheme. Cooling to liquid nitrogen temperature strengthened the O2-H on the expense of the H···O1, and adds extra O2-H absorption from the remaining (or residual) pockets (or portions) of the initial structure, as described above.

Below s = 0.63, before H location at room temperature, the low temperature bands force the conclusion that the hydrogen must have been mobile at room temperature. Hydrogen mobility in the manganese dioxide structure was never proven as unambiguously as here, since it was first suggested by Tye in 1976[85].

The low temperature spectra of R2 in particular, also provides an opportunity to throw more light on the widely cited cation vacancy model introduced by Ruetschi[11,12]. Ruetschi's model (section 1.4.3) states that there are some vacancies of Mn^{4+} in the initial structure which are compensated for by four protons in the form of OH^-. Since no absorption band was detected in the spectra of the starting materials, in the range of temperature investigated, the conclusion would be that the low temperature study does not support this model.

6.3 Conclusions

The additional techniques yielded some interesting conclusions both on the electrode potential and the low temperature FTIR studies.

6.3.1 Conclusions From The Electrode Potential

- Electrode Potential of all γ-MnO_2 samples has been successfully studied in a battery situation.
- The potentials were stable indicating stability of the oxyhydroxide compounds.
- The potential of all three materials started off with a homogeneous fall consistent with the homogeneous insertion.
- The potential of R2 switched to heterogeneity (flat line) from s = 0.368 to s = 0.624, then drifted down in an unexpected way but partly supported heterogeneous H-insertion.
- Comparison of the potential of R2 with data obtained by electrochemical discharge test has shown that chemical H-insertion, as carried out in this work, does not simulate the electrochemical discharge beyond s = 0.30.
- The potential of Faradiser M sloped down homogeneously and the H-insertion stages were not distinguishable.
- The potential trace of SBP-A against insertion level was unexpected and points to a continuous phase shift during the heterogeneous stage.

6.3.2 Conclusions From The Low Temperature FTIR

- Cooling down to –180 °C on its own, is not sufficient to induce H location- i.e. no bonding was found in any SBP-A or Faradiser M sample.
- OH bonding at low temperature occurred exclusively in H-inserted R2 presumably because microtwinning across the 061 planes increases the fraction of O2 oxygens.
- For R2 H-inserted materials, low temperature caused the H atom in the bond O2–H···O1 to shift to the O2 oxygen and weaken considerably the hydrogen bond H···O1.
- All low temperature effects were fully reversible.
- Microtwinning in R2 is largely of the 061 type while 021 type probably predominates SBP-A material. SBP-A has probably no 061 twinning.
- Absence of OH bonding in the starting materials, particularly in R2, strongly questions the existence of speculated H in EMD starting materials[6,11,12] and hence the models built upon such a hypothesis.

Low temperature FTIR has also been shown to be a useful technique with considerable benefits for the understanding of the H-insertion of γ-MnO_2.

7 Final Comments and Further Work

7.1 Final Comments

The structural changes undergone by γ-manganese dioxides as a result of hydrogen insertion, have been explained on the basis of ramsdellite and groutite structures. A summary of the H-insertion at room temperature, into the three γ-manganese dioxides studied in this work, is given in Table 7.1 along with a comparison with the literature. This table shows that:

- The H location in SBP-A occurs at a low insertion level (close to s = 0.3) in both this work and in the literature[37]. The H locates as the structure rotates and expands anisotropically in the *b* direction above s = 0.3.
- The concomitance between H location and rotation of the structure was preserved in R2 and Faradiser M materials of this work and took place at s = 0.64 and 0.67 respectively. In comparison papers, however, H located at s = 0.36 in Faradiser[38], and s = 0.63 in R2[13], which corresponds to 0.20 and 0.07 unit of s earlier than the insertion levels where the structures rotated. Furthermore, H located before the structure of R2 demicrotwinned as the literature implies[13,33]. In this work, H location followed demicrotwinning. The early location, during the homogeneous phase, has been interpreted for Faradiser M[38] as an association of proton and electron making them diffuse together through the structure instead of diffusing as two independent entities. The same explanation probably applies to R2 too.
- Given that both Faradiser M and R2 are battery active while SBP-A is not, it is tempting to link the battery activity to the extent of H mobility in the materials.

In this work, the H-insertion into all the materials started homogeneously with structures similar to those of the starting materials and finished in homogeneous phase for SBP-A and Faradiser M, with structures like those of the end products. The two homogeneous phases of SBP-A were separated by a heterogeneous phase between s = 0.26 and s = 0.68. Faradiser M switched spontaneously between the two homogeneous phases. The H-insertion into R2 proceeded heterogeneously with partial demicrotwinning between s = 0.39 and s = 0.63, then heterogeneously again between s

Table 7.1 Summary of the H-insertion stages into SBP-A, Faradiser M and R2 materials at room temperature as carried out in this work and in the literature.

Materials	**Techniques**	**H-insertion stages in this work**			**H-insertion stages in the literature**	
SBP-A	XRD	**homo.** lim. anisotropic ex. along a_r	**heter.** anisotropic ex. along b_g rot. 13.6°	**homo.** isotropic ex. along a_g&b_g	**homo.** ex. along a_r&b_r[37]	**heter.** rot. struct. only the a&b of the most H-inserted material are available[37]
	FTIR	mobile H	located H^{ϕ}		mobile H[37]	located H^{ϕ}[37]
Far. M	XRD	**homo.** lrg. anisotropic ex. along b_r		**homo.** anisotropic ex. along a_g rot. 11.7°	**homo.** lrg. anisotropic ex. along b_r then along a_r[38]	**heter.** rot. struct. as in SBP-A[38]
	FTIR	mobile H		located H	mobile H[38]	located H[38]
R2*	XRD	**homo.** isotropic ex. along a_r&b_r	**heter.** dμTw rot. struct	**heter.** isotropic. ex. along a_g&b_g	**homo.** isotropic ex. along a_r&b_r[21,42]	**heter.** anisotr. ex.[21,42] dμTw[33]
	FTIR	mobile H	l. loc. H^{ϕ}	located H^{ϕ}	mobile H[13]	located H[13]
scale of s in MnO_nH_s →		0		1	0	1

* the lattice parameters of R2 could not been estimated due to the poor quality XRD patterns. Their behaviour was proposed after studying SBP-A and Faradiser M lattice parameters. ϕ: H is located in the product phase only.

dμTw = demicrotwinning, ex. = expansion, homo. = homogeneous insertion, heter. = heterogeneous insertion, lim. = limited, l. loc. H = limited location of H, rot. n = rotated structure with a decrease of n° in the β angle. The relevant reference literature are indicated with superscripts.

= 0.63 and the final product. This observation is in line with the suggested repartition of microtwinning. In Faradiser M, which is untwinned across both the 021 and o61 ramsdellite planes, the transition phase between the two homogeneous stages of the H-insertion was sudden. R2, heavily twinned but only with few 021 types, underwent a shorter 021 demicrotwinning (first heterogeneous) stage than SBP-A, which is lightly twinned but mainly across the 021 ramsdellite planes. Demicrotwinning of the 061 planes in R2 took place in the second heterogeneous stage. The 061 twinning fault can be crossed without causing mismatch to the structure unlike the 021 fault (see Fig. 6.22 & 6.23).

The FTIR at room temperature has shown that H is located in the final stage of the insertion into all materials. This H location took place simultaneously and without preference in the ramsdellite and pyrolusite tunnels of the final structure. These tunnels changed shape so that an O2 of one octahedron is brought near an O1 of a neighbour octahedron, as a result of substantial decrease in the angle β.

Comparison between the XRD patterns of the most H-inserted compounds from SBP-A, R2 and Faradiser M is made in Fig. 7.1 along with the lines of groutite[90] and manganite[93]. If the initial intergrowth of ramsdellite/pyrolusite is maintained throughout the H-insertion (which is likely to be the case), then Fig. 7.1 makes it clear that R2 has a substantially higher pyrolusite content than SBP-A. The structure of highly H-inserted R2 looks intermediate between SBP-A and Faradiser M of similar insertion level. SBP-A's content of pyrolusite is low. The estimate of 0.41 for p in SBP-A[37] and R2[18] must therefore be reviewed, the two material do not seem to have the same Pr. Faradiser M has higher Pr than R2, consistent with the estimated[18] Pr = 0.70.

Similar comparison is made for the FTIR spectra in Fig. 7.2. The spectra confirm the above conclusion about the pyrolusite content. Although all three compounds exhibit groutite and manganite characteristic bands, their proportions were not similar. While Faradiser M has stronger manganite bands, the situation is reversed in SBP-A R2 is intermediate. Hence the order of increasing Pr in the three materials would be SBP-A > R2 > Faradiser M.

The FTIR study at low temperature has indicated that OH bond formation may be largely dependent on concentration of the O2 oxygens which increase with the 061 twinning type. This is why low temperature absorption bands occurred exclusively in

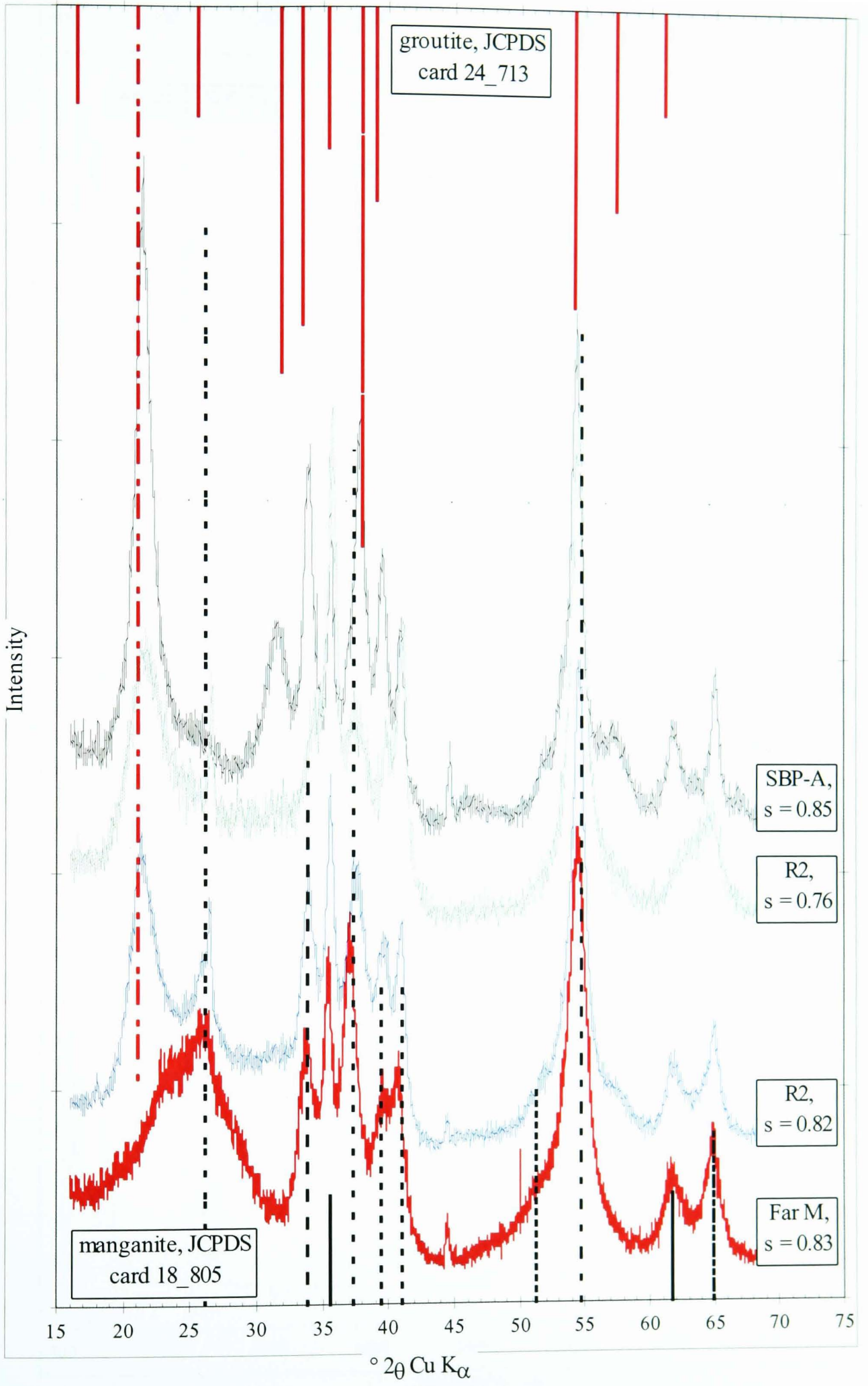

Fig. 7.1: Comparison of the XRD patterns of the most H-inserted materials with the published spectra of groutite and manganite. R2 at s = 0.82 is contaminated with manganite impurity but is shown to aid comparison.

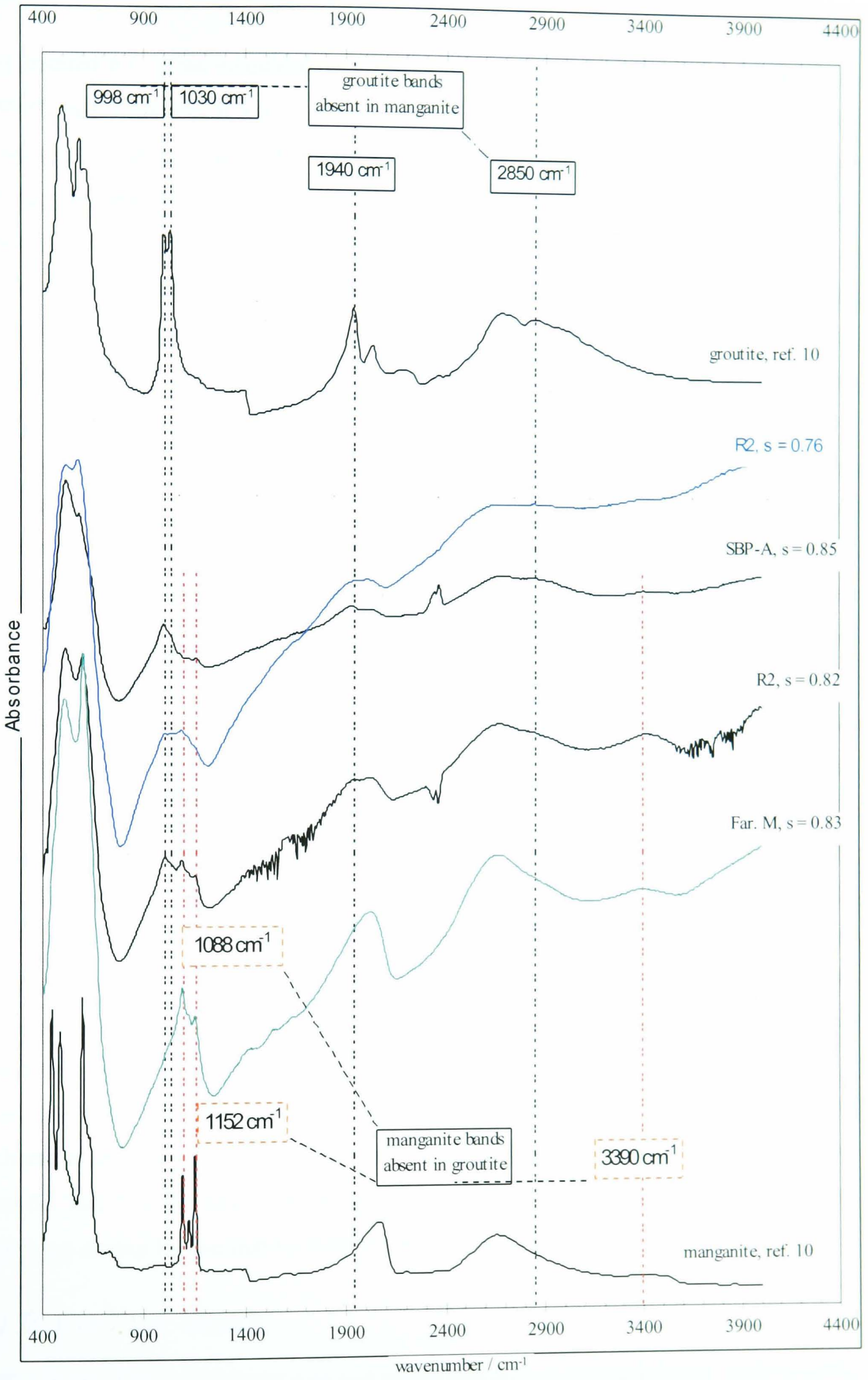

Fig. 7.2: Comparison of the FTIR spectra of the most H-inserted materials with the published spectra of groutite and manganite. R2 at s = 0.82 is contaminated with manganite impurity but is shown to aid comparison.

H-inserted R2. This investigation has proved unambiguously that H is mobile in the MnO_x host structure, at low insertion levels. The same investigation has also revealed that the O1 H-O2 bond vibrations at room temperature are affected upon cooling by weakening the hydrogen bond with oxygen O1 and strengthening the covalent bond with O2. All low temperature effects were fully reversible.

The electrode potential data of R2 and Faradiser M was in reasonable agreement with the insertion stages derived from the XRD studies. The potential of SBP-A, however, did not follow the path expected from the XRD and pointed to a phase shift during the heterogeneous insertion.

Battery activity seemed related to the extent of H-insertion at which the tunnels remained unhinged. R2, which is the most battery active, kept the initial structure up to s = 0.64 before a phase with hinged tunnels started to emerge side by side with the unhinged tunnels structure. In Faradiser M, the tunnels hinged altogether at s = 0.69 where the battery performances diminished considerably. SBP-A, which is classified as battery inactive, lost its unhinged tunnel between s = 0.28 and s = 0.68.

Comparison between the results of this work with those of the selected literature suggested that the kinetic of the H-insertion could explain the differences. In the literature considered, the H-insertion was slow and the limiting step was the release of protons made available for insertion; not their diffusion in the bulk. When severe conditions (e.g. reflux) were applied, the H-insertion was not speeded up and it is suggested that the host material (MnO_x) was affected instead. In this work however, the release of protons was spontaneous and the mild conditions (~1° C and controlled additions of hydrazine hydrate) eliminated effects on the host material and the limiting step was the diffusion of protons into the bulk.

As a final conclusion, it can be stated that Pannetier's school successfully characterised the structure of γ-manganese dioxide by the two-parameter (Pr and Tw) model and Tye's school successfully provided a basis for understanding structural changes during H-insertion by their two-parameter approach (z , β).

7.2 Further Work

This work has reached some new and useful conclusions towards better understanding of the manganese dioxide H-insertion system. However, more research is required to

gain further insight, understanding and control of the H-insertion into γ-manganese dioxide. The following points are particularly recommended:

- Improve the consistency of the experimental data from the different techniques by using the same sample whenever possible. For instance, the XRD can be traced first, then the same sample repartitioned between FTIR pellets, SEM stub and the chemical analysis. Provided that more care is taken when choosing the master sample, this procedure is expected to give more coherent and consistent data.
- Low temperature FTIR study of a set of EMDs differing only by the levels of their 061-type microtwinning. Such a study is expected to help examining the speculated correlation between this microtwinning and the location at low temperature of initially mobile H. The suspension bath series prepared by Preisler[24] is probably a good choice for the suggested EMDs.
- FTIR study of H-inserted Faradiser M and SBP-A at even lower temperatures (e.g. using liquid helium) to investigated location of initially mobile H in these materials.
- Study of the reversibility of the H-insertion into both H-located and non H-located samples by oxidising them chemically or electrochemically under different conditions. Although this work does not suggest that the H-location is reversible, such a study can still yield important results for the battery industry.
- Similar reversibility study of demicrotwinned materials in order to examine the demicrotwinning suggestion[33].
- Further investigation of the electrode potential, especially for SBP-A.
- Additional characterisation techniques such as NMR of proton.

Appendix 1 — *The Program used to collect the temperature reading for H-insertion into γ-manganese dioxide at low temperature (c.f. section 2.2)*

```
DECLARE SUB Box (boxhor, boxver, boxht, boxwd, boxword$)
DECLARE SUB Ibclr (BYVAL BD%)
DECLARE SUB Ibfind (BDNAME$,  BD%)
DECLARE SUB Ibrd (BYVAL BD%, Rd$)
DECLARE SUB Ibwrt (BYVAL BD%, WRT$)
DECLARE SUB Pblock (D$)

DECLARE FUNCTION Ilwrt% (BYVAL BD%, Rd1$, WRT$, BYVAL
CNT&)

     COMMON SHARED Maxl, Max2, filnam$, ans, Num, Coll, Col2, Col3,
Rd1$, Rd2$
     COMMON SHARED Pnt( ), Read1$( ), Read2$( ), Option$( ), DVM1%,
DVM2%, Rest
     COMMON SHARED Tol1, Tol2, V1( ), V2( ), Inst, Xmax


     REDIM Pnt(3000)
     REDIM Read1$(3000)
     REDIM Read2$(3000)
     REDIM Option$(10)
     REDIM V1(10)
     REDIM V2(10)
     REDIM Temp(1000)
```

```
CLS
ans = 1
Num = 9
Col1 = 7
Col2 = 0
Col3 = 14

PRINT "Reading Temperature Data2
OPEN "c:\kt.csv" FOR INPUT AS #4
FOR z = 1 to 1000
        INPUT #4, temp(z)
        PRINT ".";
NEXT z
CLOSE #4

CLS
CALL Ibfind("Dev1", DVM1%)
CALL Ibclr(DVM1%)

COLOR Col1, Col2
CLS
PRINT "Set Inter-Measurment Time"
INPUT "Enter Time Between Measurments", Rest
CLS
PRINT "Set Output Filename:          "
SHELL "dir c:\temp\" + UCASE$(filnam$) + ".csv"

CALL Ibwrt(DVM1%, "NOT1DO")

CLS
OPEN filnam$ FOR APPEND AS #1
```

```
        Stp$ = ""
        time1 = TIMER
        WHILE Stp$ = ""

'******************Get Voltmeter response***************

        IF Rest > 0 THEN SLEEP Rest
        Rd1$ = SPACE$(17)
        CALL Ibrd(DVM1%, Rd1$)
        time2 = TIMER
        time3 = time2 - time1
ans = VAL(Rd1$)*1000000
temper = ans*0.024851
X = X + 1
CLS
LOCATE (1), (1)
PRINT X
PRINT STR$(temper)
PRINT STR$ (time3)
WRITE #1,  X,  time3,  VAL (Rd1$),  temper
Stp$ = INKEY$
WEND
CLOSE #1


PRINT  "  Return to Default Settings "
INPUT  "  Confirm You wish to RESET Voltmeter  (Y/n)  ", conf$
IR UCASE$ (conf$) <> "N" THEN CALL Ibwrt (DVM1%,  "A")


END


SUB Boz  (boxhor, boxver, boxht, boxwd, boxword$)
```

```
' ***** Write boxed word

LOCATE boxver + 1, boxhor + 1
PRINT boxwords

' ***** Draw top of box

LOCATE bozver, boxhor
PRINT CHR$ (201);
NEXT z
PRINT CHR$ (187)

' ***** Draw box sides

FOR z = 1 TO boxht
   LOCATE boxver  + z, boxhor
   PRINT CHR$ (186);
   LOCATE boxver + z, boxhor + boxwd + 1
   PRINT CHR$ (186)
NEXT z

' ***** Draw bottom of box

LOCATE boxver + z, boxhor
PRINT CHR$ (200);
FOR z = 1 TO boxwd
   PRINT CHR$ (205);
NEXT z
PRINT CHR$ (185);

END SUB
```

Appendix 2 Demonstration of the Calculation of the oxidation state of MnO_x and the relationships between x, r, s and n.

Gamma-manganese dioxides (EMD) are non-stoichiometric compounds, their formula is MnO_x with $x < 2$. The deviation from stoichiometry is due to the presence of Mn(III) in the structure of EMD. Thus, the oxidation states of manganese in EMD are III and IV, and the charge balance may be written as:

$$-2x = 4a + 3r \qquad \textbf{(A2.1)}$$

where **a** is the mole fraction of Mn(IV) and **r** the mole fraction of Mn(III)
The material balance would then be:

$$a + r = 1 \qquad \textbf{(A2.2)}$$

only one mole of manganese is included in MnO_x.

From **(A2.1)** and **(A2.2)** it follows that:

$$r = 4 - 2x \qquad \textbf{(A2.3)}$$

When x was evaluated, the insertion level, r, may be calculated. The Method of Vetter & Jeager[53] aims to determine x by the titrations described in section 2.3.2.
After reaction 2.3 had occurred, the titration of the excess ferrous (as done in reaction 2.2), leads to the determination of **k**, the number of mole of ferrous required to titrate MnO_x

$$\mathbf{k = 5\alpha(V_0 - V_1)} \qquad \textbf{(A2.4)}$$

As each mole of MnO_x titrate (2x - 2) mole of ferrous (see reaction (2.3)), the number of mole of MnO_x, **m**, is:

$$m = \frac{k}{(2x-2)} = \frac{5\alpha(V_0 - V_1)}{(2x-2)} \qquad \textbf{(A2.5)}$$

Reaction (2.4), which involves the total amount of manganese, shows that each mole of MnO_4^- titrates 4 moles of Mn^{2+}, i.e.

$$\mathbf{m = 4\alpha V_2} \qquad \textbf{(A2.6)}$$

From **(A2.5)** and **(A2.6)**, it follows that:

$$x = 1 + \frac{5}{8}\left[\frac{V_0 - V_1}{V_2 - \frac{V_1}{4}}\right] \qquad \textbf{(A2.7)}$$

From (A2.3) r is easily calculable.

For the starting material r is noted r_0. Hence, the actual amount of inserted H in an inserted sample (r) would be:

$$\mathbf{s = r - r_0} \qquad \textbf{(A2.8)}$$

The maximum insertion level according to reaction (2.1) would therefore be:

$$\mathbf{s_{max} = 1 - r_0} \qquad \textbf{(A2.9)}$$

The actual insertion level s can also be calculated directly from the oxidation states.

If the oxidation state of the manganese dioxide before H-insertion was x (MnO_x) and after the H-insertion became n (MnO_n), then:

$$\mathbf{s = 2(x - n)} \qquad \textbf{(A2.10)}$$

So, an inserted sample is fully described by MnO_nH_s while for a starting material the formula MnO_x is sufficient. However both forms can describe either materials as $s = 0$ when $x = n$.

Appendix 3

The Oxidation state and lattice parameters evaluation of H-inserted SBP-A samples

Code	s	r	x	a_r	b_r	c_r	a_g	b_g	c_g	β	z
ASM	0.000	0.058	1.971	4.443	9.292	2.849				37.325	-0.784
A00	0.010	0.068	1.966	4.440	9.298	2.850				37.087	-0.750
A15	0.019	0.077	1.962	4.455	9.301	2.851				37.604	-0.578
A16	0.068	0.126	1.937								
A17	0.078	0.136	1.932	4.458	9.298	2.851				37.739	-0.598
A23	0.100	0.158	1.921	4.470	9.300	2.853				38.145	-0.455
A19	0.119	0.177	1.912	4.475	9.309	2.853				38.165	-0.316
A20	0.128	0.186	1.907								
A18	0.130	0.188	1.906	4.466	9.313	2.853				37.783	-0.358
A24	0.158	0.216	1.892	4.489	9.328	2.853				38.333	0.013
A22	0.164	0.222	1.889	4.507	9.333	2.852				38.876	0.255
A07	0.166	0.224	1.888	4.497	9.350	2.856				38.246	0.316
A26	0.166	0.224	1.888	4.507	9.338	2.854				38.786	0.297
A25	0.192	0.250	1.875	4.498	9.318	2.854				38.829	0.008
A06	0.214	0.272	1.864	4.486	9.305	2.849				38.626	-0.246
A21	0.233	0.291	1.855	4.482	9.291	2.852				38.685	-0.429
A27	0.276	0.334	1.833	4.505	9.297	2.851				39.407	-0.118
A28	0.418	0.476	1.762	4.480	9.184	2.854	4.549	10.672	2.876	23.751	18.302
A32	0.465	0.523	1.739	4.483	9.154	2.856	4.538	10.588	2.865	24.221	17.081
A29	0.471	0.529	1.736	4.454	9.299	2.859	4.537	10.619	2.869	23.913	17.564
A33	0.493	0.551	1.725	4.482	9.054	2.849	4.532	10.555	2.864	24.364	16.614
A31	0.571	0.629	1.686	4.493	8.972	2.843	4.530	10.582	2.863	24.066	17.037
A30	0.578	0.636	1.682	4.523	8.699	2.824	4.532	10.658	2.871	23.449	18.187
A08	0.589	0.647	1.677	4.533	8.733	2.829	4.527	10.552	2.865	24.265	16.598
A14	0.645	0.703	1.649	4.473	8.899	2.838	4.532	10.524	2.865	24.630	16.139
A13	0.718	0.776	1.612				4.542	10.526	2.868	24.873	16.132
A02	0.731	0.789	1.605				4.537	10.555	2.866	24.482	16.585
A03	0.735	0.793	1.603				4.537	10.545	2.866	24.574	16.446
A12	0.748	0.806	1.597				4.537	10.544	2.866	24.570	16.433
A05	0.754	0.812	1.594				4.539	10.548	2.866	24.591	16.479
A01	0.782	0.840	1.580				4.542	10.571	2.867	24.460	16.813
A09	0.790	0.848	1.576				4.543	10.543	2.867	24.737	16.386
A04	0.851	0.909	1.546				4.543	10.546	2.867	24.737	16.419

subscripts r and g refer to ramsdellite and groutite structures respectively.

Appendix 4 The Oxidation state and lattice parameters evaluation of H-inserted Faradiser M samples

Code	s	r	x	a_r	b_r	c_r	a_g	b_g	c_g	β	z
MSM	0.000	0.096	1.952	4.398	9.324	2.855				35.216	-0.712
M00	0.037	0.133	1.934	4.397	9.354	2.856				34.680	-0.363
M15	0.117	0.213	1.893	4.411	9.336	2.861				35.461	-0.497
M07	0.163	0.259	1.871	4.388	9.383	2.854				33.777	0.098
M18	0.174	0.270	1.865	4.397	9.433	2.859				33.470	0.656
M13	0.177	0.273	1.863	4.394	9.516	2.860				32.123	1.756
M08	0.190	0.286	1.857	4.392	9.450	2.858				33.011	0.876
M17	0.231	0.327	1.837	4.394	9.417	2.857				33.591	0.450
M09	0.283	0.379	1.810	4.381	9.400	2.851				33.396	0.192
M16	0.291	0.387	1.806	4.396	9.438	2.859				33.331	0.726
M11	0.307	0.403	1.798	4.390	9.561	2.860				31.328	2.379
M19	0.394	0.490	1.755	4.387	9.550	2.859				31.415	2.214
M25	0.405	0.501	1.750	4.396	9.695	2.867				29.780	4.266
M26	0.424	0.520	1.740	4.372	9.719	2.858				28.704	4.661
M20	0.438	0.534	1.733	4.384	9.737	2.864				28.855	4.902
M10	0.467	0.563	1.718	4.374	9.669	2.858				29.394	3.929
M23	0.490	0.586	1.707	4.366	9.843	2.861				27.035	6.550
M27	0.544	0.640	1.680	4.389	9.953	2.873				26.472	8.123
M28	0.545	0.641	1.679	4.389	9.953	2.873				26.472	8.123
M21	0.564	0.660	1.670	4.394	9.665	2.865				30.101	3.840
M22	0.597	0.693	1.653	4.398	9.606	2.865				31.004	3.004
M24	0.666	0.762	1.619	4.403	9.635	2.867				30.775	3.413
M06	0.718	0.814	1.593				4.495	10.546	2.872	23.530	16.664
M02	0.745	0.841	1.579				4.52	10.52	2.87	24.271	16.233
M12	0.757	0.853	1.573				4.51	10.5	2.87	24.181	16.178
M01	0.771	0.867	1.567				4.53	10.5	2.87	24.699	15.907
M04	0.780	0.876	1.562				4.515	10.50	2.872	24.390	15.926
M05	0.785	0.881	1.559				4.53	10.53	2.87	24.491	16.195
M14	0.815	0.911	1.545				4.53	10.54	2.87	24.364	16.455
M03	0.828	0.924	1.538				4.507	10.56	2.860	23.683	16.835

subscripts r and g refer to ramsdellite and groutite structures respectively.

Appendix 5 The Oxidation state of H-inserted R2 samples

Code	s	r	x
RSM	0.000	0.103	1.948
R00	0.041	0.144	1.928
R24	0.088	0.191	1.905
R06	0.181	0.284	1.858
R25	0.186	0.290	1.855
R23	0.305	0.408	1.796
R07	0.316	0.419	1.790
R05	0.317	0.420	1.790
R08	0.368	0.471	1.764
R09	0.406	0.509	1.745
R10	0.434	0.537	1.731
R21	0.462	0.565	1.717
R17	0.466	0.569	1.715
R11	0.467	0.570	1.715
R27	0.481	0.584	1.708
R26	0.483	0.586	1.707
R12	0.518	0.621	1.689
R20	0.521	0.624	1.688
R14	0.536	0.639	1.680
R13	0.583	0.686	1.657
R19	0.593	0.696	1.652
R16	0.624	0.727	1.636
R15	0.637	0.740	1.630
R18	0.672	0.775	1.612
R03	0.717	0.820	1.590
R01	0.719	0.822	1.589
R02	0.741	0.844	1.578
R28	0.760	0.863	1.568
R04	0.823	0.926	1.537

REFERENCES

1. British patent N° 1637, (1866).
2. Leclanché G., *Les Mondes* (Paris), **16**, (1868) 532.
3. *Handbook of Manganese Dioxides Battery Grade*, (edited by Glover D., Schumm B. and Kozawa A.), International Battery Material Association, Brunswick, Ohio, USA (1989).
4. Brenet J., *Rev. Gen. d'Electricite*, **65**, (1956) 61.
5. Gabano J. P., Morignate B., Fialdes E., Emery B. and Laurent J. F, *Zeitschrift für Physikalische Chemie Neue Folge*, Bd. **46**, (1965) 359.
6. Maskell W. C., Shaw J. E. A., and Tye F. L., *Electrochim. Acta*, **27**, (1982) 425.
7. Baur W. H., *Acta Cryst.*, **32** (1976) 2200.
8. Rogers D. B., Shannon R. D., Sleight A. W. and Gillson J. L., *Inorg. Chem.*, **8** N°4 (1969) 841.
9. Baur W. H., *Mat. Res. Bull.*, **16** (1981) 339.
10. Potter P.M, & Rossman G.R., *The Amer. Mineralogist*, **64**, (1979) 1199
11. Ruetschi P., *J. Electrochem. Soc.*, **131,** (1984) 2737
12. Ruetschi P. and Giovanoli R., *J. Electrochem. Soc.*, **135,** (1988) 2663
13. Fitzpatrick J., MacLean L.A.H., Swinkels D.A.J. and Tye F. L., *J. Appl. Electrochem.*, **27,** (1997) 243.
14. Gattowand G. and Glemser O., *Z. anorg. allg. Chem.* **309**, (1961), 20-36.
15. Buerger M.J.. *Z. Krist.* **118**, (1936) 303.
16. Kohler T., Armbruster T. and Libowitzky E., *J. Solid State Chem.*, **133**, (1997) 486
17. West A. R. and Bruce P. G., *Acta Cryst.*, **B38** (1982) 1891.
18. Chabre Y. and Pannetier J., *Progr. Solid State Chem.*, **23,** (1995) 1.
19. Byström A. M., *Acta Chem. Scand.*, **3,** (1949) 163.
20. Dent Glasser L.S. and Ingram L., *Acta Cryst.* **B24** (1968) 1233.
21. MacLean L.A.H., Ph.D Thesis, Middlesex University (1993) London
22. De Wolff P.M., *Acta Cryst.*, **12,** (1959) 341.
23. Vosburgh, W. C., *J. Electrochem. Soc.* **106** (1959) 839.
24. Preisler E., *J. Appl. Electrochem.* **6** (1976) 301.
25. Pannetier, J., *Progress in Battery & Battery Materials,* **11,** (1992) 51.

26. Pannetier, J., *Progress in Battery & Battery Materials,* **13,** (1994) 132.

27. Ripert M., Pannetier J., Chabre Y., and Poinsignon C., *Mat. Res. Soc. Symp. Proceed. Series*, **210** (1991) 359.

28. Ripert M., Poinsignon C., Chabre Y., and Pannetier J., *Phase Transitions*, **2/4** (1991) 205.

29. Ripert, M. (1990), PhD thesis, Inst. Nat. Polytech., Grenoble (France)

30. Preisler E., *J. Appl. Electrochem.*, **6,** (1976), 301.

31. Brenet J., *C. R. Acad. Sc. Paris*, **242** (1956) 3064.

32. Brenet, J. P., Mallesan, J. & Grund A., *C.R. Acd. Sci*, **242**, (1956) 111.

33. MacLean, L.A.H. & Tye, F. L. *J. Sol. State Chem.*, **123,** (1996) 1029.

34. Preisler, E., *J. Appl. Electrochem.*, **19,** (1989) 540.

35. Ruetschi P., *J. Electrochem. Soc.*, **135,** (1988) 2657

36. Picquet, P. C. & Welsh, J. Y., *New Materials & New Processes*, **2** (1983) 12.

37. MacLean, L.A.H. & Tye, F. L., *J. Mater. Chem,* **7** (1997) 1029.

38. MacLean, L.A.H. & Tye, F. L., *J. Mater. Chem,* **11** (2001) 891.

39. Benson P., Price W. B. and Tye F. L., *Electrochemic. Techn.*, **5,** N° 11-12 (1967) 517.

40. Caudle, J. K. G. & Tye, F. L., *J. Chem. Soc., Farad. Trans.*, **69**, (1973) 876.

41. Caudle, J. K. G. & Tye, F. L., *J. Chem. Soc., Farad. Trans.*, **69**, (1973) 885.

42. Fitzpatrick, J. & Tye, F. L., *J. Appl. Electrochem.*, **21,** (1991) 130.

43. Holton, D. M., Maskell, W.C. & Tye, F. L., Powers Sources, **10,** (Ed. L. Pearce), The Paul Press Ltd., (1985) 247.

44. Maskell, W. C., Shaw, J. E. A. & Tye, F. L., *J. Power Sources*, **8**, (1982) 113.

45. Maskell, W. C., Shaw, J. E. A. & Tye, F. L., *J. Appl. Electrochem.*, **12**, (1982) 101.

46. Maskell, W. C., Shaw, J. E. A. & Tye, F. L., *Electrochim. Acta*, **28**, (1983) 225.

47. Tye F. L., Manganese Dioxide Electrode Theory and Practice for Electrochemical Applications, eds. Schumn B., Middaugh R. L., Grotheer M. P. and Hunter J. C., *The Electrochem. Soc. Inc,*. (1985) 301.

48. Allen, T. (1981), *Particle Size Measurement*, Chapman & Hall, London p. 5.

49. Kozawa A., Kalnoki-Kis, T. & Yeager, J.F., *J. Electrochem. Soc.*, **113,** (1966) 405.

50. Larcin, J., PhD thesis, Middlesex Polytechnic (1991) London
51. Jones, J., PhD. Thesis, Middlesex University, (1996) London.
52. CRC, *Handbook of Chemistry and Physics*, 78th Edition, CRC Press Inc. (1997) p 4-61
53. Vetter, K.J. & Jaeger, N., *Electrochim. Acta,* **26,** (1966) 1373.
54. Lingane J. J. and Karplus R., *Ind. Eng. Chem..*, Anal. Ed., **18** (1946) 191.
55. Klug, H.P. and Alexander, L.E., *X-ray Diffraction Procedures for Polycrystalline and amorphous materials*, John Wiley & Sons (1974) 202
56. Gehian, E. D., Picquet, P.C. Spears, C. J. & Tye, F. L., *Progress in Battery & Battery Materials,* **11,** (1992) 56.
57. Reference 55, page 372-373
58. Reference 55, page 361
59. **A**utomated **P**owder **D**iffraction (APD), *Operation Manual of the PC-APD Software*, Version 3.6, Philips Analytical X-Ray, Feburary 1994
60. Chatfield, Christopher, *Statistics for Technology*, Chapman & Hall, London (1983) 148
61. JCPDS Card N° 23 64
62. Schiedt U. and Reinwein Z., *Z. Naturforsch.*, **7B** (1952) 270.
63. Stimson M. M. and O'Donnell M. J., *J. Amer. Chem. Soc.*, **74** (1952) 1805.
64. Stuart B., *Modern Infrared Spectroscopy*, Wiley (1996) 34
65. Fitzpatrick J., Maclean L.A.H., Swinkels D.A.J. and Tye F.L., *J. Appl. Electrochem.*, **27** (1997) 243.
66. Hannah R.W. in *Laboratory Methods in Vabrational Spectroscopy*, 3rd Ed. Eds. Wills, H.A., Van der Maas J.H. and Miller R.G.J., Wiley (1987) 211.
67. Alpert N.L., Keiser W.E. and Szymanski H.A., *IR Theory and Practice of Infrared Spectroscopy*, 2nd Ed. Plenum Press (1970) 330-331
68. George B. and MacIntyre, *Infrared Spectroscopy*, Wiley (1987) 141-143
69. de Faubert Maunder M.J., *Practical Hints on Infra-red Spectroscopy from a Forensic Analyst*, Adam Hilger, London (1971) 7-8
70. Reference 64, p 37
71. Price W.J., in *Laboratory Methods in Infrared Spectroscopy*, 2nd Ed., Eds. Miller R.G.J. and Stace B.C., Heydon and Sons, London (1972) 115-120

72. White R.G, *Handbook of Industrial Infrared Analysis*, Plenum Press (1964) 116-127

73. Graseby Specac Ltd , *Issue 6 of the Operating Manual of the VTC*, Kent (1997)

74. Cahoon N.C., *Trans. Electrochem. Soc.*, **68** (1935) 177.

75. Cahoon N.C. and Heise G.W., *J. Electrochem. Soc.*, **94** (1948) 214.

76. Johnson R.S. and Vosburgh W.C., *J. Electrochem. Soc.*, **99** (1952) 317.

77. Tye F.L., *Electrochemical Power Sources*, Ed. M. Barak, Peter Peregrinus Ltd., London (1980) 50.

78. Goodhew P. J, *Electron Microscopy and Analysis*, Taylor & Francis Ltd., London (1975) 107.

79. reference 78, p. 117

80. Muller J., Tye F.L. and Wood L.L., *Batteries* 2, Ed. D.H. Collins, Pergamon Press (1965) 201.

81. Tye F.L., *Proceeding of the 7th Aust. Electrochem. Conf.*, Eds. T. Tran and M. Skyllas-Kazakos, The Royal Australian Chemical Institute (1988) 37.

82. Larcin J., Maskell W.C. and Tye F.L., *Electrochim. Acta*, **42** (1997) 2649.

83. Larcin J., Maskell W.C. and Tye F.L., *Electrochim. Acta*, **44** (1998) 191.

84. Caudle J., Summer K.G. and Tye F.L., *Power Sources*, 6 Ed. D.H. Collins, Academic Press, London (1977) 447.

85. Tye F.L., *Electrochim. Acta*, **21** (1976) 415.

86. Tye F.L. and Tye S.W., *J. Appl. Electrochem.*, **25** (1988) 425.

87. Tye F.L, *Progress in Batteries & Battery Materials*, **11** (1992) 1.

88. Poinsignon C., Amarilla M., and Tedjar F., *J. Mater. Chem.*, **3** (1993) 1227.

89. Amrilla J.M., Tedjar F. and Poinsignon C., *Electrochim. Acta*, **39** (1994) 2321.

90. JCPDS, card N° 24-713 (groutite)

91. *The Chemistry of the Transition Elements*, Ed. Earnshaw A.and Harrington T.J., Clarendon Press, Oxford (1973) 34-35

92. Maskell W.C., Shaw J.E.A. and Tye F.L., *Electrochim. Acta*, 26 (1981) 1403.

93. JCPDS, card N° 18-805 (manganite)

94. Verdonk L., Hoste S., Roelandt F.F. and Van der Kelen G.P., *J. Molec. Struct*, **79** (1984) 788.

95. Wells A.F., *Structural Inorganic Chemistry*, Clarendon Press Oxford (1987) p.639

96. Fillaux F., Ouboumour H., Tomkinson J. and Yu L.T., *Chem. Phys.*, **149** (1991) 459.

97. Fillaux F., Ouboumour H., Cachet C.H., Kearley G.J., Tomkinson J. and Yu L.T., *Chem. Phys.*, **164** (1992) 311 .

98. Fillaux F., Ouboumour H., Cachet C.H., Kearley G.J., Tomkinson J. and Yu L.T., *Physica B*, **180 & 181** (1992) 680.

99. Fillaux F., Ouboumour H., Cachet C.H., Tomkinson J., Lévy-Clément and Yu L.T., *J. Electrochem. Soc.*, **140** (1993) 585.

100. Fillaux F., Ouboumour H., Cachet C.H., Tomkinson J., Lévy-Clément and Yu L.T., *J. Electrochem. Soc.*, **140** (1993) 592.

101. Tye F.L., *Electrochim. Acta*, **30** (1985) 17.

102. Russel J.D., in *Laboratory Methods in Vabrational Spectroscopy*, 3rd Ed. Eds. Wills, H.A., Van der Maas J.H. and Miller R.G.J., Wiley (1987) 428.

103. JCPDS, card N° 39-375 (ramsdellite)

104. JCPDS, card N° 39-735 (pyrolusite)

105. Colthup N.B., Daly L.H. and Wiberley S.E., *Introduction to Infrared and Raman Spectroscopy*, Academic Press (1964) 8.

106. Donne S.C, Lawrance G.A. and Swinkels D.A.J., *J. Electrochem. Soc.*, **144** (1997) 2949.

107. Alday J., *MPhil Thesis*, Middlesex University 1999

108. McClintock P.V.E., Mederith D.J. and Wingmore J.K., *Matter at Low Temperature*, Blackie (1984) p. 3

109. Nunziante C.S., Dobos S. and Stirling A., *Vibrational Spectroscopy*, **20** (1999) 59.

110. Durig J.R. and Drew B.R., *J. Molec. Struct.*, **560** (2001) 247.

111. Olafsen A., Fjellvag H., Solen S., Atake T., Kawaji H. and Matsuo K., *J. Chem. Thermodyn.*, 31 (1999) 433.

112. Kajihara H., Okamura T. and Koda S., *J. Molec. Spec.*, **192** (1998) 277.

113. Rutkowski K. and Melikova S.M., *J. Molec. Struct.*, **511-512** (1999) 233.

114.McDonald P.C., *Directory of Low Temperature Research and Development in Europe*, Institute of Physics- London (1992)

115.Holzapel W.B., *J. Chem. Phys.*, **56** (1972) 712.

116.Desseyn H.O. and Slootmckers B.J., *Appl. Spec.*, **45** (1991) 118.

117.Granzow B., *J. Molec. Struct.*, **381** (1996) 127.

118.Satoshi K. and Takayanagi M., *J. Molec. Struct.*, **413-414** (1997) 365.

119.Drichko N.V. and Yu G., *J. Molec. Struct.*, **477** (1999) 127.

120.Harmon K.M. and Shaw K.E., *J. Molec. Struct.*, **513** (1999) 219.

121.Bruyneel C. and Zeegers-Huskens T.H., *J. Molec. Struct.*, **552** (2000) 177.

122.Desseyn H.O., Clou K., Keuleers R., Miao R., Van Doren V.E. and Blaton N., *Spectrochim. Acta*, **57A** (2001) 231.

123.Engelen B., Gavrilko T., Panthöfer M., Puchkovsksya and Sekirin I., *J. Molec. Struct.*, **532** (2000) 163.

124.Pimentel G.C. and McClellan A.L., *The Hydrogen Bond*, Freeman (1960) p.70.

125.St. Claire-Smith C., Lee J.A. and Tye F.L., *Manganese Dioxide Symposium Vol. 1 Cleveland*, Ed. Kozawa A. and Brodd R.J., I.C. Sample Office (1975) 132.

126.Valand T., *Electrochim. Acta,* **19** (1974) 639.

127.Atlung S., *Manganese Dioxide Symposium Vol. 1 Cleaveland*, Ed. Kozawa A. and Brodd R.J., I.C. Sample Office (1975) 47.

128.Hunter J.C., *J. Soid State Chem.*, **39** (1981) 142.

129.Reference 55 p. 368

130.Giovanoli R., Bernhard K. and Feitknecht W., *Helv. Chim. Acta*, **51** (1968) 355